UNIVERSITY OF NOTTINGHAM

DOCTORAL THESIS

A Quantum Integrated Light and Matter Interface

Author:
Jonathan NUTE

Supervisor:
Dr. Lucia HACKERMÜLLER

A thesis submitted in fulfillment of the requirements for the degree of Doctor of Philosophy

in the

Quantum Optics and Ultracold Mixtures Group
The School of Physics and Astronomy

March 27, 2017



Declaration of Authorship

I, Jonathan NUTE, declare that this thesis titled, "A Quantum Integrated Light and Matter Interface" and the work presented in it are my own. I confirm that:

- This work was done wholly or mainly while in candidature for a research degree at this University.
- Where any part of this thesis has previously been submitted for a degree or any other qualification at this University or any other institution, this has been clearly stated.
- Where I have consulted the published work of others, this is always clearly attributed.
- Where I have quoted from the work of others, the source is always given. With the exception of such quotations, this thesis is entirely my own work.
- I have acknowledged all main sources of help.
- Where the thesis is based on work done by myself jointly with others, I have made clear exactly what was done by others and what I have contributed myself.

Signed:

Date:

"The rain yields to the stream. The stream cowers before the river. I am the ocean."

Xaero

Abstract

A highly integrated device capable of interfacing light and matter on a chip is presented. 1×10^7 ^{133}Cs atoms are captured from a hot vapour into a magneto-optical trap held close to a chip-mounted single-mode fibre. Sub-Doppler optical molasses cools the atoms and transfers them into a tightly focused $18\,\mathrm{W}$ vertical optical dipole trap which intersects a $30\,\mu\mathrm{m}$ void that has been laser etched through the single-mode fibre. Thus, the optically trapped atoms are tightly confined in the path of fibre-guided photons for maximum overlap. Such a system is capable of writing, reading and storing quantum information and clearly has massive implications for quantum information technologies. The device presented is adaptable, scalable and highly integrated making it the ideal building block for quantum computing.

Developments and modifications made to a system for producing ultracold samples of ^{6}Li , ^{133}Cs and mixtures thereof is also presented. Feshbach molecules have major applications in quantum computing, particularly in the modelling of complex many-body quantum systems. The large dipolar moment of the ^{6}Li-^{133}Cs Feshbach molecule is the largest of all the alkali dimers producing rich long-range anisotropic dipole-dipole interactions. By use of the broad Feshbach resonance situated at $834\,\mathrm{G}$ we associate fermionic ^{6}Li atoms into bosonic $^6\mathrm{Li}_2$ Feshbach molecules. Subsequent evaporative cooling drives a phase transition in the diffuse $^6\mathrm{Li}_2$ gas to produce a $^6\mathrm{Li}_2$ molecular Bose-Einstein Condensate containing up to 1×10^4 atoms, the first to be produced in the UK.

This thesis documents the construction of the quantum integrated light and matter interface (QuILMI) in its entirety from inception to realisation. An enormous amount of work has gone into the design and subsequent development of various vacuum, laser and magnetic systems that work seamlessly in tandem via a programmable control system. The system is now in a position to demonstrate to the world that atom-photon coupling on a chip is the way forward.

For the ^{6}Li-^{133}Cs mixture experiment, a versatile dual-species oven has been meticulously designed, constructed and thoroughly characterised to replace one that significantly malfunctioned and harmed the experiment. The oven is capable of tuning the axial fluxes of ^{6}Li and ^{133}Cs through several orders of magnitude via PID temperature controlled reservoirs. An array of fifteen $0.51\,\mathrm{mm}$ diameter microtubes highly collimate the dual-species atomic beam such that little flux is wasted prolonging the life of both the source and the vacuum ion pumps. This source will return the system to its former glory such that the ultimate goal of realising ultracold ^{6}Li-^{133}Cs Feshbach molecules can once again be pursued.

Contents

Declaration of Authorship i

Abstract iii

1 Introduction 1

2 Theoretical background 8
2.1 Alkali atoms . . . 8
2.2 Interactions . . . 12
2.2.1 Interaction with a static magnetic field . . . 12
2.2.2 Light and matter interactions . . . 16
A two-level atom in a radiation field . . . 16
The Bloch picture . . . 20
Light shift . . . 23
The origin of the scattering and dipole forces . . . 25
The scattering force . . . 26

3 Experimental techniques 28
3.1 Producing an atomic beam . . . 28
3.2 Slowing an atomic beam . . . 32
3.2.1 The magneto-optical trap . . . 34
3.3 Optical molasses . . . 36
3.3.1 The Doppler limit . . . 38
3.4 Sub-Doppler cooling . . . 39
Sisyphus cooling in the Lin $\perp$ Lin configuration . . . 39
Sub-Doppler cooling in the $\sigma^+ - \sigma^-$ configuration . . . 42
3.5 The dipole trap . . . 46
3.5.1 Evaporative cooling . . . 48
3.5.2 Formation of Feshbach molecules via magneto-association 48
3.6 Laser stabilisation . . . 51

3.6.1 Saturated absorption spectroscopy . . . 52
Crossover features . . . 52
3.6.2 Locking to a transition . . . 54
3.6.3 Offset locking . . . 55

4 The ^{6}Li-^{133}Cs mixture experiment 60
4.1 Collimated dual-species oven . . . 60
4.1.1 Design and construction . . . 63
4.1.2 Characterisation . . . 74
4.2 The $^{6}Li_2$ molecular BEC . . . 79
4.3 In-situ measurements of the $^{6}Li_2$ mBEC . . . 85
4.4 Next steps . . . 91
4.4.1 3D degenerate Raman sideband cooling . . . 91
4.4.2 ^{6}Li D_1 grey molasses . . . 92

5 A quantum integrated light and matter interface 94
5.1 QuILMI experimental setup . . . 100
5.1.1 The QuILMI chamber . . . 100
A compact chamber with high optical access . . . 100
A simple and fast chip-mounting procedure . . . 103
Cost-effective, high-transmission fibre feedthroughs . . . 104
MOT coils . . . 106
5.1.2 Laser systems . . . 110
Modified laser setup . . . 110
The magneto-optical trap . . . 111
The dipole trap . . . 116
5.2 Waveguide and fibre chip experiments . . . 120
5.2.1 Evanescent field chip . . . 121
5.2.2 Fliced void chip . . . 123
5.2.3 Fibre chip . . . 125
Chip construction . . . 125
5.2.4 MOT and dipole trap alignment . . . 127
5.2.5 Dipole trap optimisation . . . 130
Trap characterisation . . . 135
5.3 Coupling between atoms and fibre-guided photons . . . 139
5.3.1 Detection as reduced atom number . . . 140

5.3.2 Detection as fluorescence absorption on the single-photon counting module . . . 142
5.4 Next Steps . . . 142
5.4.1 Reducing the dipole beam waist and shape . . . 142
5.4.2 Rotating the chamber . . . 143
5.4.3 Beyond coupling in the fibre . . . 143

6 Conclusions and outlook **145**

A The Hydrogen Atom **147**
A.0.1 Fine structure and hyperfine structure . . . 149

B Nufern NuAMP seeding setup **152**

C Mechanical designs **153**
C.1 Chip-mounting assembly . . . 153
C.2 Coil and optomechanics mounting plates . . . 154
C.2.1 Top plate . . . 154
C.2.2 Bottom plate . . . 155
C.2.3 Middle plate . . . 156
C.2.4 Window plate . . . 157
C.3 Fibre feedthrough Teflon ferrule . . . 158
C.4 Compensation coil brackets . . . 159
C.4.1 Inner compensation coil bracket . . . 159
C.4.2 Outer compensation coil bracket . . . 160
C.4.3 Compensation coil assembly . . . 161
C.5 Nufern NuAMP outcoupler heavy-duty mount . . . 162
C.6 Dichroic mirror holder . . . 164
C.7 Ion pump stand . . . 165

List of Abbreviations

AOM	**A**cousto-**O**ptical **M**odulator
BCS	**B**ardeen-**C**ooper-**S**chrieffer
BEC	**B**ose-**E**instein **C**ondensate
CCD	**C**harge-**C**oupled **D**evice
DFSAS	**D**oppler-**F**ree **S**aturated **A**bsorption **S**pectroscopy
DRSC	**D**egenerate **R**aman **S**ideband **C**ooling
ECDL	**E**xternal **C**avity **D**iode **L**aser
FLICE	**F**emtosecond-**L**aser **I**rradiation followed by **C**hemical **E**tching
FWHM	**F**ull **W**idth **H**alf **M**aximum
HB	**H**ome-**B**uilt
mBEC	**m**olecular **B**ose **E**instein **C**ondensate
MOT	**M**agneto **O**ptical **T**rap
PID	**P**roportional-**I**ntegral-**D**erivative
QC	**Q**uantum **C**omputing
QIP	**Q**uantum **I**nformation **P**rocessing
QuILMI	**Q**uantum **I**ntegrated **L**ight (and) **M**atter **I**nterface
SPCM	**S**ingle **P**hoton **C**ounting **M**odule
TA	**T**apered **A**mplifier
UHV	**U**tra **H**igh **V**acuum
VCO	**V**oltage-**C**ontrolled **O**scillator

Physical Constants

Quantity		Value
speed of light in vacuum	c_0	$2.997\,924\,58 \times 10^{8}\,\mathrm{m\,s^{-1}}$
Newtonian constant of gravitation	G	$6.674\,08(31)\,\mathrm{m^{3}\,kg^{-1}\,s^{-2}}$
magnetic permeability in vacuum	μ	$4\pi \times 10^{-7}\,\mathrm{N\,A^{-2}}$
electric permittivity in vacuum	ϵ	$8.854\,187\,817 \times 10^{-12}\,\mathrm{F\,m^{-1}}$
Planck constant	h	$6.626\,070\,040(81) \times 10^{-34}\,\mathrm{J\,s}$
reduced Planck constant $h/2\pi$	$\hbar$	$1.054\,571\,800(13) \times 10^{-34}\,\mathrm{J\,s}$
elementary charge	e	$1.672\,621\,898(21)\,\mathrm{C}$
electron mass	m_e	$9.109\,383\,56(11) \times 10^{-31}\,\mathrm{kg}$
proton mass	m_p	$1.672\,621\,898(21) \times 10^{-27}\,\mathrm{kg}$
neutron mass	m_n	$1.674\,927\,471(21) \times 10^{-27}\,\mathrm{kg}$
unified atomic mass unit	u	$1.660\,539\,040 \times 10^{-27}\,\mathrm{kg}$
Rydberg constant	R_∞	$1.097\,373\,156\,850\,8(65) \times 10^{7}\,\mathrm{m^{-1}}$
Bohr magneton $e\hbar/2m_e$	μ_B	$927.400\,999\,4(57) \times 10^{-26}\,\mathrm{J\,T^{-1}}$
fine-structure constant $e^2/4\pi\epsilon_0\hbar c$	α	$7.297\,352\,566\,4(17)$
electron gyromagnetic ratio $-e/m_e$	γ_e	$1.760\,859\,644(11) \times 10^{11}\,\mathrm{s^{-1}\,T^{-1}}$
electron g-factor	g_e	$-2.002\,319\,304\,361\,82(52)$
nuclear magneton	μ_N	$5.050\,783\,699(31) \times 10^{-27}\,\mathrm{J\,T^{-1}}$
proton gyromagnetic ratio $g_p e/2m_p$	γ_p	$2.675\,221\,900(18) \times 10^{8}\,\mathrm{s^{-1}\,T^{-1}}$
proton g-factor	g_p	$5.585\,694\,702(17)$
proton magnetic moment	μ_p	$1.410\,606\,787\,3(97) \times 10^{-26}\,\mathrm{J\,T^{-1}}$
neutron magnetic moment	μ_n	$-0.966\,236\,50(23) \times 10^{-26}\,\mathrm{J\,T^{-1}}$
Boltzmann constant	k_B	$1.380\,648\,52(79) \times 10^{-23}\,\mathrm{J\,K^{-1}}$
molar gas constant	R	$8.314\,459\,8(48)\,\mathrm{J\,mol^{-1}\,K^{-1}}$

*It was in the car, during one of our morning trips to school, when I decided to tell my Dad all about what I had been taught about electromagnetic waves. Thoroughly unimpressed, my father turned to me. "Don't be **daft**" he said. "Just think about it, what on earth could be electric or magnetic about light?" So this is for you Dad, almost 200 pages on what is electric and magnetic about light.*

Chapter 1

Introduction

It was 1924 in a hot and stuffy lecture hall at the University of Dhaka (present day Bangladesh), when a man named Satyendra Bose made a critical mistake during a lecture on black-body radiation that would ultimately define an entirely new type of statistics [1]. In an attempt to demonstrate the inadequacy of the Rayleigh-Jeans law, Satyendra made an error akin to thinking that the probability of flipping exactly 1 heads out of two coins is one third. Bose had accidentally treated his particles as being *indistinguishable* and in doing so found extraordinary agreement with experimental results; microscopic particles seemed not to be governed by Maxwell-Boltzmann statistics. This was a truly radical idea and Bose hurried to publish his discovery. However, his article 'Planck's Law and the Hypothesis of Light Quanta', containing a water-tight derivation of Planck's law, was rejected outright by *Philosophical Magazine*. Undeterred, on 4th June that same year Bose sent a letter, with his article attached, to a very popular German physicist who owed him a favour [2, 3]:

> *Respected Sir,*
>
> *I have ventured to send you the accompanying article for your perusal and opinion. I am anxious to know what you think of it. You will see that I have tried to deduce the coefficient $8\pi\nu^2/c^3$ in Planck's Law independent of classical electrodynamics, only assuming that the ultimate elementary region in the phase-space has the content h^3. I do not know sufficient German to translate the paper. If you think the paper worth publication I shall be grateful if you arrange for its publication in Zeitschrift für Physik. Though a complete stranger to you, I do not feel any hesitation in making such a request. Because we are all your pupils though profiting only by your teachings through your writings. I do not know whether you still remember that somebody from Calcutta asked your permission to translate your papers on Relativity in English. You acceded to the request. The book has since been published. I was the one who translated your paper on Generalised Relativity.*
>
> *Yours faithfully,*
> *Satyendra Bose*

Einstein, already a proponent of the idea of quantised light particles [4, 5], obliged and together their paper was published later that year in *Zeitschrift für Physik*.

Einstein, like many others around that time, had already dedicated a lot of time to the problem of deriving Planck's law of black body radiation [4, 5, 6]. Although Planck's law agreed perfectly with experiments, Planck had obtained it in 1900 by purely empirical means [7]. Planck knew that at large wavelengths experimental results were known to follow the Rayleigh-Jeans law, and that at high frequencies, where the Rayleigh-Jeans law broke down[1], Wien's law proved to be accurate. With the knowledge of these limiting cases and further experimental observations, Planck was able to successfully interpolate between the two regimes to reach his landmark result. In 1900, Planck submitted a derivation of his own which included a bold assumption; that energy can only be emitted and absorbed in packets of $\epsilon = h\nu$, an idea that captivated Einstein [5]. However, blissfully unaware that he had just given birth to quantum mechanics, Planck was unable to provide the scientific community a physically sound explanation and admitted that he had made the assumption in order to obtain a positive result "no matter what the cost" [5].

Although numerous attempts had been made, Bose's article was the only derivation of Planck's law that was in his eyes "sufficiently logically justified" [2], and clearly Einstein agreed. In an appreciative adjunct to their 1924 paper, Einstein wrote:

> *"Bose's derivation of Planck's formula appears to me to be an important step forward. The method used here gives also the quantum theory of an ideal gas, as I shall show elsewhere."*

Einstein, driven by his discontent with the asymmetric treatment of matter and light (that matter was thought to be corpuscular while light was considered continuous and wave-like), immediately extended Bose's theory to particles in a non-interacting gas in 1924-1925 [8].

Einstein's extension had an immediate and startling prediction; that under the right conditions atoms would all eventually condense into the lowest accessible quantum state to form a new state of matter - *the Bose-Einstein condensate* (BEC). This was a bizarre and unnerving consequence of the theory; theorists

[1] The failure of the Rayleigh-Jeans law at short wavelengths is famously known as the ultraviolet catastrophe.

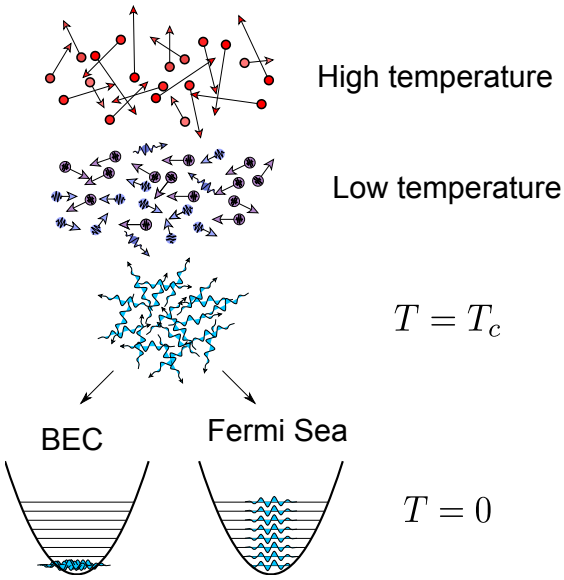


FIGURE 1.1: Cooling to quantum degeneracy. As the temperature of a gas is lowered, the de Broglie wavelength of the constituent particles begins to grow until the particles can no longer be considered point-like. When the particles' de Broglie wavelengths become comparable to the interparticle separation. What happens next depends on whether the particles are bosons or fermions. At a critical temperature $T = T_c$ bosons undergo a phase-transition to form a Bose-Einstein condensate (BEC), a state of matter in which all the particles occupy the lowest possible energy state. Fermions, subject to the Pauli exclusion principle, experience a different low-temperature phenomenon. Instead of a BEC the ultracold fermions form a degenerate Fermi gas in which the atoms fill up the N lowest possible energy states with one atom per state up to the Fermi energy E_F.

around the globe were loathe to accept it and the necessary phase-temperature-density combinations were so ludicrous that experimentalists had no way to test it [9]. The experimental feat was so difficult in fact that it wasn't until 1995, *70 years later*, that the first observations of BEC were made [10, 11, 12]. Using a combination of laser and evaporative cooling, a team in Boulder, Colarado observed the first evidence of Bose-Einstein condensation in a rubidium gas and later that same year a team in MIT observed BEC in a sodium gas. This achievement was so monumental Cornell, Wieman and Ketterle were all awarded the Nobel Prize for Physics in 2001 [13].

The realisation of BEC sparked an explosion of activity in the field of atomic-molecular-optical (AMO) physics, the aftershocks of which we can still feel today. The reason for this is easy to understand; Bose-Einstein condensation is the demonstration of our total and utter control over matter. Using light, magnetic

and electric fields we are able to freely manipulate an atom's internal and external degrees of freedom limited only by Heisenberg's uncertainty principle. The atom is entirely at our mercy.

Ultracold atom experiments have proven to be the ultimate tool for understanding complex many-body quantum systems in one, two and three dimensions. In particular, ultracold atoms find important application in modelling condensed matter systems [14]. By interfering multiple optical dipole traps, one can produce periodic arrays of tightly confining micro-traps called optical lattices which mimic crystalline structures free of defects or impurities. The periodicity and potential walls of the optical lattice can be finely tuned to model whichever system one desires or to drive the system through a quantum phase transition [15, 16, 17]. When the well depth is small, bosons with repulsive interactions will look to minimise their energy by smearing out over the entire lattice producing a superconducting state. As the walls of the potential are increased, a transition is made to the Mott insulator state in which the atoms are tightly confined and they lose their long-range phase coherence. It is also now possible to image single atoms in individual potentials of an optical lattice using quantum gas microscopes [18, 19]. By increasing the well depth in just one or two directions, a three-dimensional lattice can be reduced to sheets of 2D lattices or arrays of 1D lattices opening doors to new physical realms [20, 21, 22, 23].

Ultracold neutral atoms are also exemplary subjects for hyper-sensitive tests of fundamental physics. Quantum electrodynamics and general relativity are being pushed to their limits using neutral atoms with both interferometric and non-interferometric techniques [24, 25]. Atom interferometers in particular are gaining interest in the military and commercial sectors as hyper-sensitive new-age sensors. These systems can be utilised as accelerometers for underwater inertial navigation or as hyper-sensitive gravimeters for the detection of oil under the surface of the earth [26, 27].

Using magnetic fields and a Feshbach resonance one can dictate the interatomic interaction strength [28, 29]. Across a Feshbach resonance, an atom's scattering length can be made to take very large positive or negative values. An important application of this phenomenon is to resonantly couple two free atoms to a bound state forming a Feshbach molecule [30, 31]. With highly tailorable, anisotropic long-range dipolar interactions, Feshbach molecules make

promising candidates for use in quantum computing and precision measurements [32].

This thesis documents work carried out on two experiments: an extremely versatile dual-species ultracold atom experiment and a second dedicated ^{133}Cs experiment for interfacing light with atoms on a chip.

As a result of the work contained in this thesis, the dual-species experiment is capable of routinely producing ultracold samples of ^{6}Li and ^{133}Cs in a tightly focused $1064\,\mathrm{nm}$ $100\,\mathrm{W}$ optical dipole trap. Using the broad ^{6}Li Feshbach resonance situated at $834\,\mathrm{G}$ we drive a phase transition in a diffuse gas of fermionic ^{6}Li to produce a $^{6}Li_2$ molecular Bose-Einstein Condensate of up to 1×10^4 atoms, the first to be produced in the UK. With caesium, 2×10^6 atoms are loaded into the dipole trap ready for evaporative cooling to degeneracy.

^{6}Li -^{133}Cs mixtures are particularly exciting because the Li-Cs Feshbach molecule has an enormous permanent dipole moment (EDM) of $5.5\,\mathrm{debye}$. This EDM is the largest of all the alkali-metal dimers and produces very strong long-range dipolar interactions which potentially have applications in quantum information processing [33]. Lithium and caesium also prove to be convenient to work with experimentally. Large frequency separations between their respective D_1 and D_2 -line transitions means each species only responds to its own respective light field. Hence lithium and caesium can be simultaneously and independently optically trapped in the same chamber without cross-talk. When lithium and caesium mixtures are needed they can be sequentially loaded into a far-detuned optical dipole trap. The ^{6}Li-^{133}Cs mixture experiment has so far been documented in three other theses written by ex-students Dr. Sonali Warriar [34], Dr. Matthew D. Jones [35] and Dr. Asaf Paris-Mandoki [36]. In order to present only new developments, the author has made a concerted effort to minimise overlap with the preceding theses without. However, due to the complexity of the experiment some overlap is necessary for the purposes of clarity and flow.

Brand new for this thesis is our impressive contribution to the Quantum Integrated Light and Matter Interface (QuILMI) project, a multi-institutional collaborative effort with the goal of producing a highly integrated device capable of generating, storing and manipulating light using atoms right down to the single-photon level. The Nottingham Quantum Optics and Mixtures group (this group) led the experimental side of the venture supported by quantum

optics teams at the University of Vienna (led by Dr. Philip Walther) and the University of Jena (led by Dr. Alexander Szameit). Our experimental efforts were accompanied by theoretical contributions from groups led by Dr. Thomas Pohl at the Max Planck Institute for the Physics of Complex Systems in Dresden and Dr. Igor Lesanovsky at the University of Nottingham.

More specifically, the aim of QuILMI was to integrate waveguide optics, light and an ensemble of cold atoms all on a single chip surface with the vision of producing a highly scalable system for holding qubits. This thesis details the successful construction of such a device all the way from inception to realisation. 1×10^7 caesium atoms are captured from a hot vapour into a magneto-optical trap which is held close to a chip-mounted single-mode fibre. Sub-Doppler optical molasses cools the atoms to ~$30\,\mu\mathrm{K}$ and transfers them to an $18\,\mathrm{W}$ vertical optical dipole trap. The dipole trap focus lies inside a micrscale void ($30\,\mu\mathrm{m}$) laser etched through the single-mode fibre. The atoms are held in the void for optimal overlap with fibre-guided photons producing a system capable of writing, reading and storing of quantum information.

The thesis is structured as follows:

- **Chapter 2 - Theoretical background**
  This chapter covers most of the theory required to understand the laser cooling and trapping techniques used in this experiment, namely alkali atoms, interactions with magnetic and electric fields, and light-matter interactions.

- **Chapter 3 - Experimental techniques**
  This chapter uses all of the concepts covered in Chapter 2 to describe the multitude of experimental techniques we employ in the lab.

- **Chapter 4 - The ^{6}Li-^{133}Cs mixture experiment**
  A new dual-species oven is designed, built and characterised for use with future ^{6}Li-^{133}Cs mixture experiments. The experimental setup and procedure used to obtain the $^6Li_2$ mBEC is presented followed by in-situ measurements of the cloud with comparisons to the ideal gas, semi-ideal and Hartree-Fock theoretical predictions. Finally, the steps with which the experiment can move forward are outlined.

- **Chapter 5 - A quantum integrated light and matter interface**
  A compact system for interfacing atoms with light on a chip is presented. An extensive and detailed discussion of the construction process is given followed by experimental results obtained with the various chips that have been investigated.

- **Chapter 6 - Conclusions and outlook**
  Finally, I conclude with a review of the results obtained and discuss future work to be carried out and potential applications of the work contained herein.

Chapter 2

Theoretical background

This chapter exists to arm the reader with all of the basic knowledge needed to understand the laser cooling and trapping techniques used in the two experiments. The discussion begins with alkali metals and the specific elements ^{6}Li and ^{133}Cs . We explore their hyperfine structures and their interactions with magnetic fields. Finally, several important light-matter interactions are explained.

2.1 Alkali atoms

Lithium and caesium are two of the seven group-1 metals in the periodic table which comprise the **alkalis**. All of the group-1 elements have a single valence electron in their outer shell which is easily liberated to form a cation with charge $+1$. The alkalis exhibit astonishingly similar behaviour; they are all shiny, soft metals[1] that are extremely reactive owing to their readiness to lose an electron. Alkali atoms are of particular interest to cold atom physicists because their lone outer electron means their physics closely mimics that of hydrogen, the most simple and understood of all the elements (see Appendix A for a brief overview of Hydrogen and hyperfine structure). Using an atomic species with simple internal structure is a huge advantage when designing a complex cold atom experiment. The alkalis are also popular for cold atom experiments because they harbour closed optical transitions that lie in a convenient spectral range with regard to available laser diodes.

The Schrödinger equation for a neutral atom with a heavy nucleus with Z protons (with total charge Ze) surrounded by Z electrons (each with charge $-e$

[1] At standard temperature and pressure 273.15 K and 100 kPa.

and mass m_e) is written:

$$\sum_{j=1}^{Z}\left\{-\frac{\hbar^2}{2m_e}\nabla_j^2-\left(\frac{1}{4\pi\epsilon_0}\right)\frac{Ze^2}{r_j}\right\}\psi+\frac{1}{2}\left(\frac{1}{4\pi\epsilon_0}\right)\sum_{j\neq k}^{Z}\frac{e^2}{|\mathbf{r}_j-\mathbf{r}_k|}\psi=E\psi \tag{2.1}$$

where $|\boldsymbol{r_j}-\boldsymbol{r_k}|$ is the distance separating two electrons and the term proportional to $1/|\boldsymbol{r_j}-\boldsymbol{r_k}|$ describes the electrons' mutual repulsion. The factor of $1/2$ in front of this term makes up for the double counting. Unfortunately, for any atom with $Z>1$, even helium with $Z=2$, the Schrödinger equation cannot be solved analytically and it is the mutual repulsion term which is to blame. Despite this, we can still make progress with regard to the alkalis by making a clever approximation. First, we notice that the electrons in the filled inner shells of an alkali atom create a spherically symmetric distribution around the nucleus with zero total angular momentum. Secondly, we recognise that the amount of energy required to excite an electron from one of these inner shells greatly exceeds that of the outermost electron. The physics of an alkali atom is thus largely determined by its single valence electron and the atom can be expected to behave like hydrogen with a partially shielded nucleus (charge eZ_{eff} where Z_{eff} is the effective proton number seen by the outermost electron). This is the **central-field approximation**. Hence the Hamiltonian for an alkali atom can be written (ignoring relativistic corrections and spin-orbit coupling) as:

$$-\frac{\hbar^2}{2m_e}\nabla^2\psi+V_{\text{eff}}\psi=E\psi, \tag{2.2}$$

where the potential $V(r)$ has been replaced for $V_{\text{eff}}(r)$, the effective Coulomb potential seen by the outer electron as the inner electrons screen the charge of the nucleus. The wave functions of alkali atoms are very similar to those shown in Figure A.1. D-line transition structure diagrams for ^{6}Li and ^{133}Cs are shown in Figures 2.1 and 2.2 respectively.

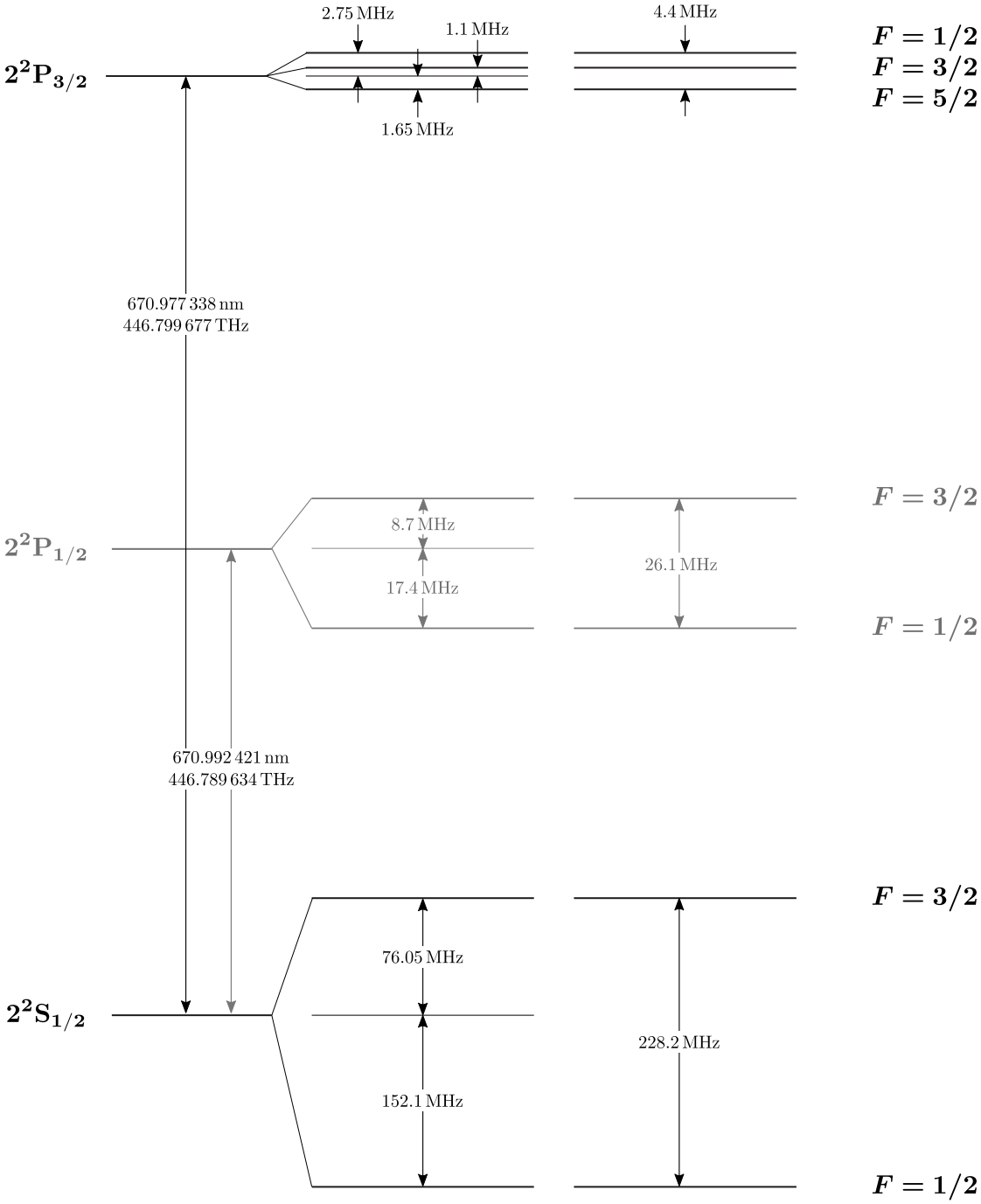


FIGURE 2.1: Lithium-6 D-line transition hyperfine structure complete with frequency splittings between the hyperfine energy levels. Frequency differences are taken from [37]. The frequency shifts within each hyperfine manifold are to scale, but the splittings between the manifolds are not.

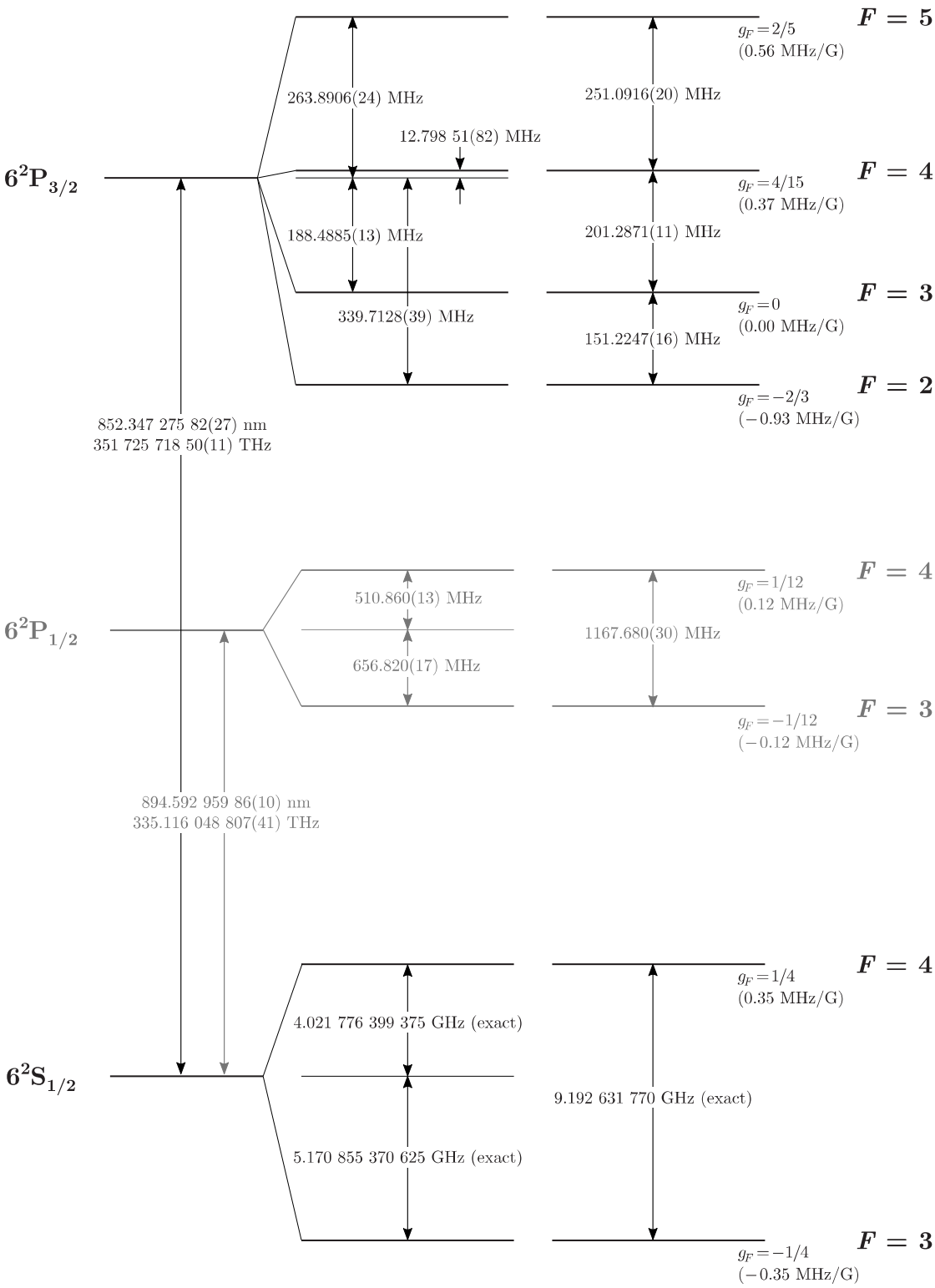


FIGURE 2.2: Caesium-133 D-line transition hyperfine structure complete with frequency splittings between the hyperfine energy levels. Frequency differences are taken from [38]. The frequency shifts within each hyperfine manifold are to scale, but the splittings between the manifolds are not.

2.2 Interactions

2.2.1 Interaction with a static magnetic field

An external static magnetic field B_z[2] interacts with all of the magnetic dipoles of an atom such that its Zeeman sublevels, labelled by their magnetic quantum number m_F, lose their degeneracy. This phenomenon is called Zeeman splitting. The interaction Hamiltonian is written

$$H'_Z = \frac{\mu_B}{\hbar}(g_S S_z + g_L L_z + g_I I_z)B_z, \tag{2.3}$$

where g_S, g_L and g_I are gyromagnetic ratios which relate each of the different angular momenta to the strength of the magnetic dipole they produce. The response of the energy levels to the external field depends on the strength of the external field relative to the internal fields of the atom. We define three regimes: low-field, where the hyperfine structure dominates and the field is treated as a perturbation; high-field, where B_z is large and the hyperfine structure becomes the perturbation; and the intermediate regime, in which the two effects have comparable strength. The total hyperfine Hamiltonian, including hyperfine structure and the external field but excluding the higher order electric quadrupole term is

$$H'_{\text{hfs}} = A_{\text{hfs}}\mathbf{I}\cdot\mathbf{J} + \frac{\mu_B}{\hbar}(g_J J_z + g_I I_z)B_z. \tag{2.4}$$

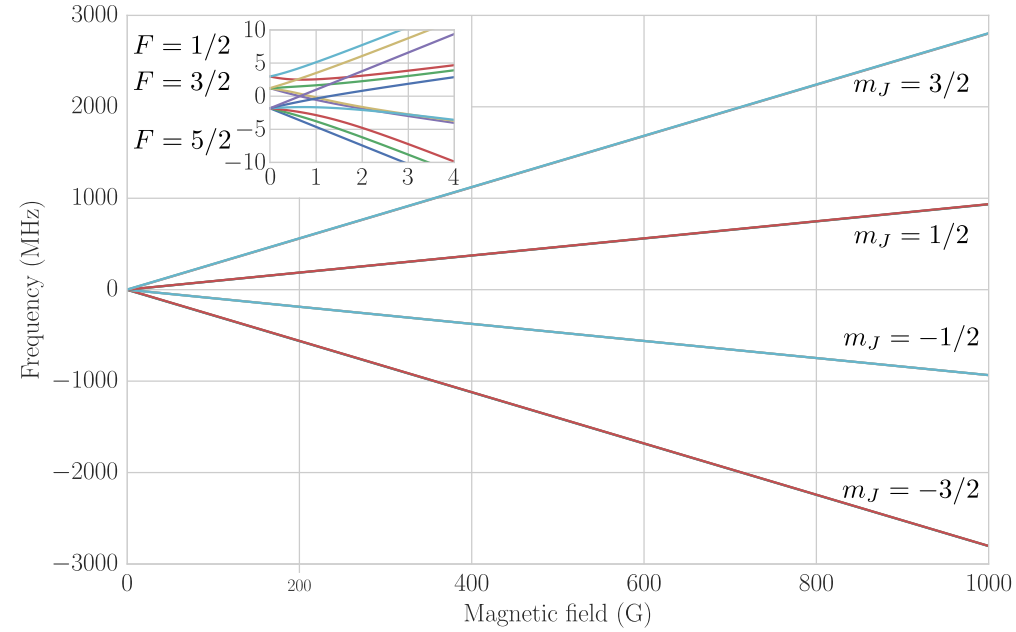
Calculating the eigenvalues of this Hamiltonian is puzzling at first because no matter which basis you choose to work in, there is always an operator whose effects on your states is not immediately apparent. For example, should we wish to evaluate this Hamiltonian in the $|m_J, m_I\rangle$ basis, we see that $I_z|m_J, m_I\rangle = \hbar m_I |m_J, m_I\rangle$. However, the value of $\mathbf{I}\cdot\mathbf{J}|m_J, m_I\rangle$ is not so obvious. Here we enlist the help of **Clebsch-Gordon coefficients** which allow us to evaluate the operators with relative ease. The matrix elements of the hyperfine term in

[2]We may as well align the field to the z-axis to make things easy.

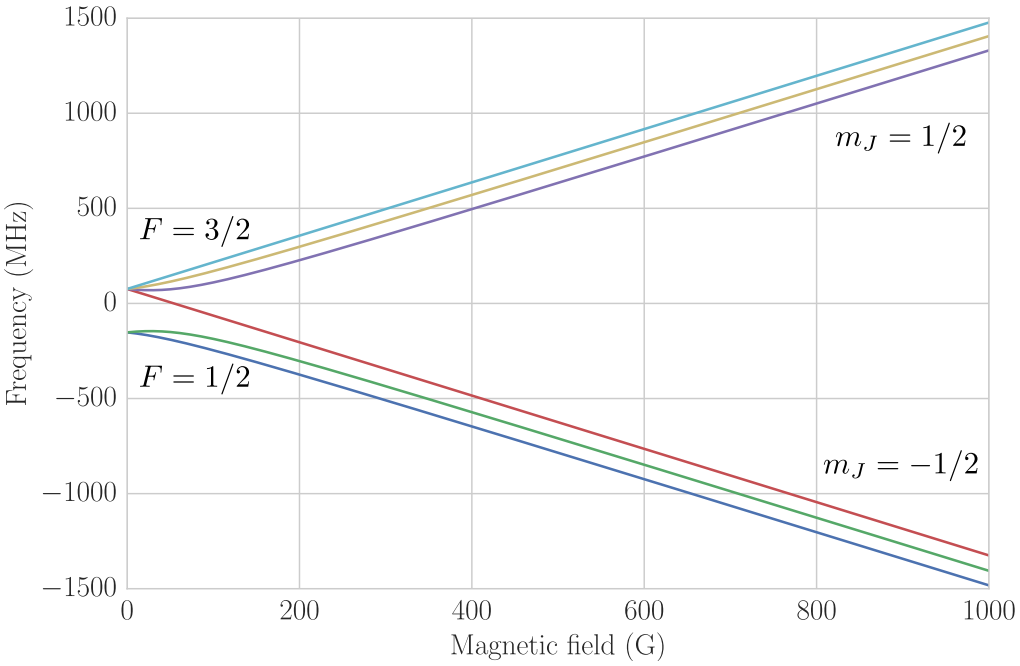
Eq. 2.4 for an arbitrary state with fixed I and J are then

$$\begin{aligned} & A_{\text{hfs}} \langle m_I', m_I' | \mathbf{I} \cdot \mathbf{J} | m_J, m_I \rangle \\ & = A_{\text{hfs}} \sum_{F, m_F} \sum_{F', m_F'} \langle m_J', m_I' | \, F', m_F' \rangle \langle F', m_F' | \mathbf{I} \cdot \mathbf{J} | F, m_F \rangle \langle F, m_F | \, m_J, m_I \rangle \\ & = \frac{\hbar}{2} A_{\text{hfs}} \sum_{F, m_F} \sum_{F', m_F'} C^{I,J,F'}_{m_I', m_J', m_F'} C^{I,J,F}_{m_I, m_J, m_F} (F(F+1) - J(J-1) - I(I-1)), \end{aligned} \tag{2.5}$$

where we have used the identity operator twice and the constants $C^{I,J,F}_{m_I,m_J,m_F}$ are the Clebsch-Gordan coefficients. **Breit-Rabi diagrams** for lithium and caesium are shown in Figures 2.3 and 2.4.

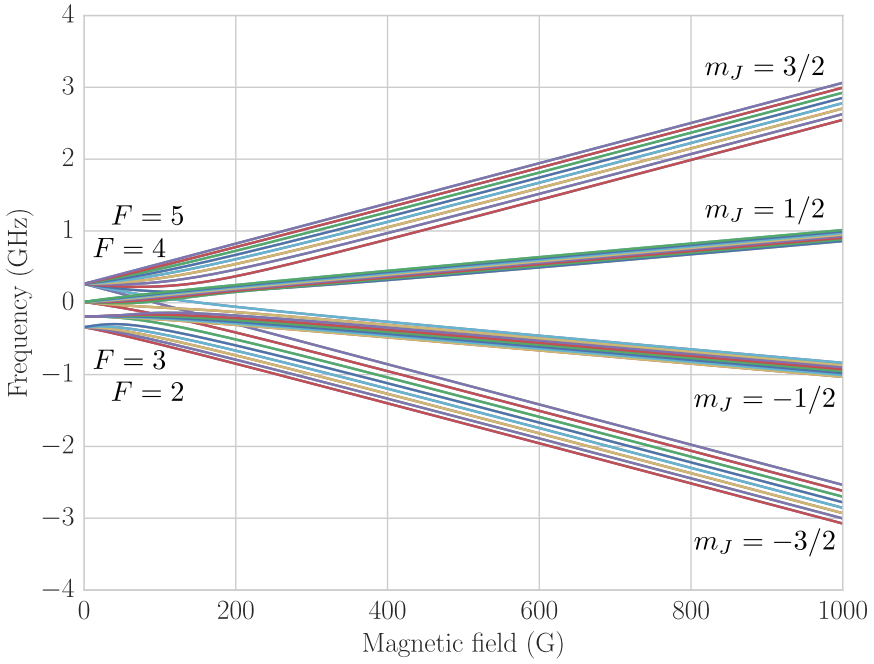


(a)

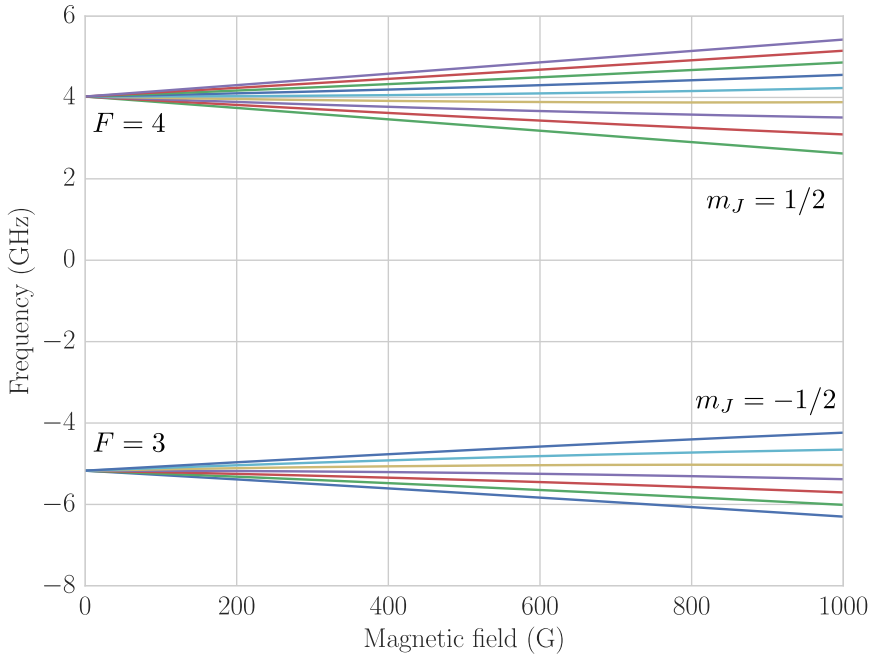


(b)

FIGURE 2.3: Lithium-6's $2^2P_{3/2}$ (D_2 transition) excited level (a) and $2^2S_{1/2}$ ground level (b) hyperfine structure in the external magnetic field range achievable in the ^{6}Li-^{133}Cs mixture experiment. The magnetic field breaks the degeneracy in F and so the levels are grouped according to F in low field and m_J in high field. It takes just a few gauss for lithium's $2^2P_{3/2}$ state to enter the high field regime.



(a)



(b)

FIGURE 2.4: Caesium-133's $2^2P_{3/2}$ D_2 excited level (a) and $2^2S_{1/2}$ ground level (b) hyperfine structure in the external magnetic field range achievable in this experiment. The levels are grouped according to F in low field and m_J in high field. The excited state of caesium eventually reaches the high field regime at 600 G, but even at the maximum field we can produce with our coils, the ground state remains well within the weak field regime.

2.2.2 Light and matter interactions

The interaction between light[3] and atoms is well described by a semi-classical treatment in which the light is treated classically and the atom is treated quantum mechanically. Because radiation only produces a significant effect on an atom if its frequency ω closely matches a transition frequency, we can consider the atom to consist of only two levels, E_1 and E_2 where $E_1 < E_2$. Of course a pure quantum mechanical derivation would be more accurate, but the semi-classical theory is easier to work with and remarkably accurate. In particular, if the analysis is conducted purely quantum mechanically then spontaneous emission pops out as a phenomenological result. With a classical driving field we have to insert it ourselves.

The ways in which light can interact with matter are as diverse as they are numerous. In this subsection we first discover that (in the absence of spontaneous emission[4]) an atom in a radiation field undergoes so-called Rabi oscillations in which the atomic population oscillates between the ground and the excited state at the Rabi frequency Ω. Next, by rewriting the light-atom interaction in terms of the populations and coherences of the density matrix, we obtain three coupled equations known as the *Bloch vector*; a powerful tool for describing the evolution of an atom in a light field of utmost importance in quantum information processing (QIP). By introducing spontaneous emission into the Bloch vector rate equations we form the optical Bloch equations which give us a full description of the atom-field combination. Lastly, we explore how the a.c. Stark effect can perturb the energy levels of an atom and discover the origin of the scattering and dipole forces. The derivations contained herein follow those given in References [39, 40, 41].

A two-level atom in a radiation field

The atom plus field Hamiltonian is written:

$$H = H_0 + H_{\mathrm{I}}. \tag{2.6}$$

[3]Strictly I should use the word radiation, but it is common parlance among cold atom physicists to call radiation of all wavelengths light whether or not it is visible.

[4]Such a situation arises in radio-frequency transitions between atomic hyperfine levels.

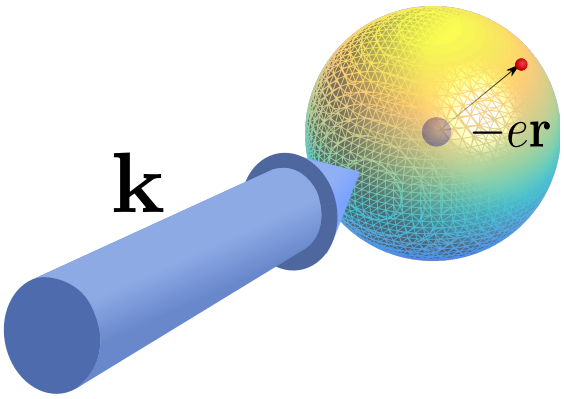


FIGURE 2.5: An atom irradiated with radiation with wavevector $|\mathbf{k}| = 2\pi/\lambda$. The vector $-e\mathbf{r}$ is the dipole moment $\mathbf{d}$.

where H_0 is the standard atomic Hamiltonian

$$H_0 = \frac{\mathbf{p}^2}{2m_e} + V(r), \tag{2.7}$$

and H_I is the interaction Hamiltonian. The eigenvalues and eigenfunctions of H_0 are simply the atomic energy levels and associated wave functions (See Appendix 2.1 for a derivation). The wave function for the level with energy E_n can be written as

$$\Psi_n(\mathbf{r}, t) = \psi_n(\mathbf{r}) e^{-iE_n t/\hbar}. \tag{2.8}$$

Ignoring all of the atomic energy levels but the two we are interested in, the spatial wave functions satisfy

$$\begin{aligned} H_0\psi_1(\mathbf{r}) &= E_1\psi_1(\mathbf{r}), \\ H_0\psi_2(\mathbf{r}) &= E_2\psi_2(\mathbf{r}). \end{aligned} \tag{2.9}$$

The full time-dependent wave function $\Psi(\mathbf{r}, t)$ can then be expressed as a linear function of these eigenfunctions of the with the time-dependence slapped on:

$$\Psi(\mathbf{r}, t) = c_1(t)\psi_1(\mathbf{r})e^{-iE_1 t/\hbar} + c_2(t)\psi_2(\mathbf{r})e^{-iE_2 t/\hbar}, \tag{2.10}$$

which in Dirac notation becomes:

$$\Psi(\mathbf{r}, t) = c_1 \left|1\right\rangle e^{-i\omega_1 t} + c_2 \left|2\right\rangle e^{-i\omega_2 t}. \tag{2.11}$$

Where we have introduced $\omega_n = E_n/\hbar$ and made the time-dependence of the coefficients implicit.

We now look to introduce the effect of the perturbing radiation. Because the magnetic field contribution is so weak we ignore it and deal only with the space and time varying electric field $\mathbf{E}(\mathbf{r}, t)$. We now employ the *dipole approximation* in which we assume that the wavelength of the light is much larger than the extent of the atom so that we can remove the spatial dependence of the electric field $\mathbf{E}(\mathbf{r}, t) \Rightarrow \mathbf{E}(t)$. The interaction Hamiltonian for this perturbation is:

$$H_{\mathrm{I}}(t) = -\mathbf{d} \cdot \mathbf{E}, \tag{2.12}$$

where $\mathbf{d}$ is the *dipole moment* $\mathbf{d} = -e\mathbf{r}$. At this point we describe the oscillating electric field classically such that the interaction becomes:

$$H_{\mathrm{I}}(t) = e\mathbf{r} \cdot \mathbf{E}_0 \cos(\omega t). \tag{2.13}$$

Substitution into the time-dependent Schrödinger equation gives us two coupled differential equations:

$$\begin{aligned} i\dot{c}_1 &= \Omega \cos(\omega t) e^{-i\omega_0 t} c_2, \\ i\dot{c}_2 &= \Omega^* \cos(\omega t) e^{i\omega_0 t} c_1, \end{aligned} \tag{2.14}$$

where we have introduced the angular transition frequency $\omega_0 = (E_2 - E_1)/\hbar$ and the famous **Rabi frequency** defined by the matrix element

$$\Omega = \frac{\langle 1 | \, e\mathbf{r} \cdot \mathbf{E}_0 \, | 2 \rangle}{\hbar} = \frac{e}{\hbar} \int \psi_1^*(r) \; \mathbf{r} \cdot \mathbf{E}_0 \; \psi_2(r) \; \mathrm{d}^3\mathbf{r}. \tag{2.15}$$

We use the dipole approximation again allowing us to take $|\mathbf{E}_0|$ outside of the integral. Assuming the oscillating electric field is aligned to the x-axis, the Rabi frequency can be rewritten:

$$\Omega = \frac{eX_{12} \, |\mathbf{E}_0|}{\hbar}, \tag{2.16}$$

where

$$X_{12} = \langle 1 | \, x \, | 2 \rangle \, , \tag{2.17}$$

is the matrix element of the x-position operator. Since in this experiment highly monochromatic coherent light is used exclusively, it makes sense to study only

light-matter interactions with radiation of this kind. We can rewrite Equations 2.14 as

$$\begin{aligned} i\dot{c}_1 &= c_2 \left\{ e^{i(\omega-\omega_0)t} + e^{-i(\omega+\omega_0)t} \right\} \frac{\Omega}{2}, \\ i\dot{c}_2 &= c_1 \left\{ e^{i(\omega+\omega_0)t} + e^{-i(\omega-\omega_0)t} \right\} \frac{\Omega^*}{2}. \end{aligned} \tag{2.18}$$

We now employ the well-known **rotating-wave approximation** which allows us to neglect the rapidly oscillating terms with $\omega + \omega_0$ since they average to zero over typical interaction times. Excluding these terms, leaving the relatively slowly oscillating terms behind, we obtain the following coupled differential equations:

$$i\dot{c}_1 = \frac{c_2\Omega}{2} e^{i(\omega-\omega_0)t}, \tag{2.19}$$

$$i\dot{c}_2 = \frac{c_1\Omega^*}{2} e^{-i(\omega-\omega_0)t}. \tag{2.20}$$

By substituting Equation 2.19 into the derivative of Equation 2.20 we obtain a second-order differential equation for the probability of being in the upper state:

$$\frac{d^2c_2}{dt^2} + i(\omega-\omega_0)\frac{dc_2}{dt} + \left|\frac{\Omega}{2}\right|^2 c_2 = 0, \tag{2.21}$$

for which the solution for an atom starting in the lower state is

$$|c_2(t)|^2 = \frac{\Omega^2}{W^2} \sin^2\left(\frac{Wt}{2}\right), \tag{2.22}$$

where

$$W^2 = \Omega^2 + \frac{(\omega-\omega_0)}{2}. \tag{2.23}$$

Thus at resonance $\omega = \omega_0$ the population oscillates between the two levels at precisely the Rabi frequency. These are called **Rabi oscillations**. This result is only true for transitions with negligible spontaneous emission such as radio-frequency transitions between magnetic sublevels. When the excited level has significant spontaneous emission the system is governed by rate equations and enters a steady state as we will see in the next section.

The Bloch picture

The Bloch sphere is a powerful analysis tool for the AMO (atomic-molecular-optical) physicist. Following a semi-classical analysis of a two-level atom, one can obtain a beautiful and enlightening representation of the evolution of the system analogous to a magnetic dipole responding to a magnetic field. As well as allowing us to visualise the effect of π and $\pi/2$ pulses, we can build on the Bloch formulation to derive the dipole and scattering forces. We begin with radiation travelling in the positive z-direction whose electric field, polarised along $\hat{\mathbf{e}}_x$, induces an electric dipole moment on the atom which oscillates at the driving frequency. The component of the dipole along this direction is the expectation value:

$$\langle\Psi(t)|\,\mathrm{d}_x\,|\Psi(t)\rangle = -e\,\langle\Psi(t)|\,x\,|\Psi(t)\rangle = -e\int\,\Psi^\dagger(t)x\Psi(t)\mathrm{d}^3\mathbf{r}. \tag{2.24}$$

Substituting in Ψ from Equation 2.10 leads to

$$\begin{aligned}\langle\Psi(t)|\,\mathrm{d}_x\,|\Psi(t)\rangle &= -e\int(c_1e^{-i\omega_1t}\psi_1 + c_2e^{-i\omega_2t}\psi_2)^*x(c_1e^{-i\omega_1t}\psi_1 + c_2e^{-i\omega_2t}\psi_2)\;\mathrm{d}^3\mathbf{r}\\ &= -e\left\{c_2^*c_1X_{21}e^{i\omega_0t} + c_1^*c_2X_{12}e^{-i\omega_0t}\right\},\end{aligned} \tag{2.25}$$

where we have used $X_{11} = X_{22} = 0$[5]. Since $X_{21} = (X_{12})^*$, the right-hand side of Equation 2.25 is a number plus its complex conjugate, thus $\langle\Psi(t)|\,\mathrm{d}_x\,|\Psi(t)\rangle$ must be a real number. The quantities $c_2^*c_1$ and $c_1^*c_2$ are the off-diagonal elements of the **density matrix**:

$$|\Psi\rangle\langle\Psi| = \begin{pmatrix}c_1\\c_2\end{pmatrix}\begin{pmatrix}c_1^* & c_2^*\end{pmatrix} = \begin{pmatrix}|c_1|^2 & c_1c_2^*\\ c_1^*c_2 & |c_2|^2\end{pmatrix} = \begin{pmatrix}\rho_{11} & \rho_{12}\\ \rho_{21} & \rho_{22}\end{pmatrix}. \tag{2.26}$$

The elements ρ_{12} and ρ_{21} are known as the **coherences** and describe the system's response to the applied field at the driving frequency. The elements ρ_{11} and ρ_{22} are the **populations** of the ground and excited states. We make a transformation

[5] X_{ij} is the matrix element $\langle i|\,x\,|j\rangle$ and contains an implicit integration over all space. Now because x is an odd function the integration gives zero for all $i = j$.

into a rotating-frame by defining two new amplitudes:

$$\begin{aligned}\tilde{c_1} &= c_1 e^{-i\delta t/2},\\ \tilde{c_2} &= c_2 e^{i\delta t/2},\end{aligned} \tag{2.27}$$

where $\delta = \omega - \omega_0$ is the detuning from resonance. With these new identities the density matrix becomes:

$$|\Psi\rangle\langle\Psi| = \begin{pmatrix} \rho_{11} & \tilde{\rho}_{12}e^{i\delta t} \\ \tilde{\rho}_{21}e^{-i\delta t} & \rho_{22}\end{pmatrix}, \tag{2.28}$$

and we can rewrite the dipole moment as

$$\begin{aligned}\langle\Psi(t)|\,\mathrm{d}_x\,|\Psi(t)\rangle &= -eX_{12}\left[\tilde{\rho}_{12}e^{i\omega t} + \tilde{\rho}_{21}e^{-i\omega t}\right]\\ &= -eX_{12}[(\tilde{\rho}_{12}+\tilde{\rho}_{21})\cos\omega t - i(\tilde{\rho}_{21}-\tilde{\rho}_{12})\sin\omega t]\\ &= -eX_{12}[u\cos\omega t - v\sin\omega t],\end{aligned} \tag{2.29}$$

where we have defined $u = (\tilde{\rho}_{12} + \tilde{\rho}_{21})$ and $v = -i(\tilde{\rho}_{21} - \tilde{\rho}_{12})$. Thus we see that u and v are the in-phase and out-of-phase (quadrature) components of the atom's response to the driving field. We ultimately want expressions in terms of u and v, but first we need equations for $\tilde{\rho}_{21}$, $\tilde{\rho}_{12}$, $\tilde{\rho}_{22}$ and $\tilde{\rho}_{11}$. Differentiation of Equations 2.27 yields

$$\begin{aligned}\dot{\tilde{c}}_1 &= \dot{c}_1 e^{-i\delta t/2} - \frac{i\delta}{2}c_1 e^{-i\delta t/2},\\ \dot{\tilde{c}}_2 &= \dot{c}_2 e^{i\delta t/2} - \frac{i\delta}{2}c_2 e^{i\delta t/2},\end{aligned} \tag{2.30}$$

which, in terms of only rotating-frame coefficients, become

$$\begin{aligned}\dot{\tilde{c}}_1 &= -\frac{i}{2}(\delta\tilde{c}_1 + \Omega\tilde{c}_2),\\ \dot{\tilde{c}}_2 &= -\frac{i}{2}(\Omega\tilde{c}_2 - \delta\tilde{c}_2).\end{aligned} \tag{2.31}$$

Using $\dot{\tilde{\rho}}_{12} = \frac{d}{dt}(\tilde{c}_1\tilde{c}_2^*) = \tilde{c}_1\dot{\tilde{c}}_2^* + \dot{\tilde{c}}_1\tilde{c}_2^*$ and equivalent expressions for the other density matrix elements we find four equations

$$\frac{d\tilde{\rho}_{12}}{dt} = \left(\frac{d\tilde{\rho}_{21}}{dt}\right)^* = -i\delta\tilde{\rho}_{12} + \frac{i\Omega}{2}(\rho_{11} - \rho_{22}), \tag{2.32}$$

$$\frac{d\tilde{\rho}_{22}}{dt} = -\frac{d\tilde{\rho}_{11}}{dt} = \frac{i\Omega}{2}(\tilde{\rho}_{21} - \tilde{\rho}_{12}), \tag{2.33}$$

which we can rewrite in terms of u, v and the population difference $w = \rho_{11} - \rho_{22}$:

$$\begin{aligned} \dot{u} &= \delta v, \\ \dot{v} &= -\delta u + \Omega w, \\ \dot{w} &= -\Omega v. \end{aligned} \tag{2.34}$$

If we take u, v and w to be the components of the vector $\mathbf{R} = u\hat{\mathbf{e}}_1 + v\hat{\mathbf{e}}_2 + w\hat{\mathbf{e}}_3$ in an arbitrary 3-dimensional space, then Equations 2.34 describe the time-evolution of the vector $\mathbf{R}$ on a unit-2 sphere which can represent any state of the two-level system. Pure states lie on the surface whereas mixed states, probabilistic mixtures of pure states, lie inside the sphere. The Bloch description as it stands is incomplete since we have nothing to represent the spontaneous decay of the excited state. We therefore introduce a damping term to the excited state population evolution[6]:

$$\dot{\rho}_{22} = -\Gamma\rho_{22} + \frac{\Omega}{2}v, \tag{2.35}$$

where Γ is the excited state line-width. This addition generates exponential decay of the excited level population. With spontaneous emission taken into account Equations 2.34 become

$$\begin{aligned} \dot{u} &= \delta v - \frac{\Gamma}{2}u, \\ \dot{v} &= -\delta u + \Omega w - \frac{\Gamma}{2}v, \\ \dot{w} &= -\frac{\Omega v}{2} - \Gamma(w - 1), \end{aligned} \tag{2.36}$$

[6] A long-winded justification of this step can be found in [39]

the steady state solutions of which can easily be found by setting all three to zero:

$$\begin{pmatrix} u \\ v \\ w \end{pmatrix} = \frac{1}{\delta^2 + \Omega^2/2 + \Gamma^2/4} \begin{pmatrix} \Omega\delta. \\ \Omega\Gamma/2 \\ \delta^2 + \Gamma^2/4 \end{pmatrix}. \tag{2.37}$$

Hence, if an optical transition has non-negligible spontaneous emission, an atom in a monochromatic light field will not undergo Rabi oscillations and instead will settle down to a steady state in which the populations of the ground and excited states remain constant. The Bloch description immediately reveals saturation effects. In the limit of a strong field ($\Omega \Rightarrow \inf$) $w = 0$ and so the populations in the upper and lower states will equalise. The **saturation intensity** $I_{\mathrm{sat}}(\omega)$ is the lowest intensity at which point the ground and excited state populations become equal. Although $I_{\mathrm{sat}}(\omega)$ is a function of the frequency, it has a minimum exactly on resonance which is commonly referred to as *the* saturation intensity defined by:

$$I_{\mathrm{sat}} = \frac{\pi}{3} \frac{hc}{\lambda^3 \tau}, \tag{2.38}$$

or equivalently in terms of the Rabi frequency Ω, the linewidth Γ and the intensity I:

$$\frac{I}{I_{\mathrm{sat}}} = \frac{2\Omega^2}{\Gamma^2}. \tag{2.39}$$

It is often favourable to use I and I_{sat} rather than Ω and Γ since the former are real and easily measurable quantities.

Light shift

Similar to how a static magnetic field can shift an atom's energy levels, so too can d.c. and a.c. electric fields. This phenomenon is called the **Stark effect**. Although we do not use any static electric fields in this experiment, we do however, use a lot of oscillating electric fields in the form of laser light. Continuing the analysis from the previous section, we can begin to calculate these **light shifts** using time-dependent perturbation theory. Written in matrix form,

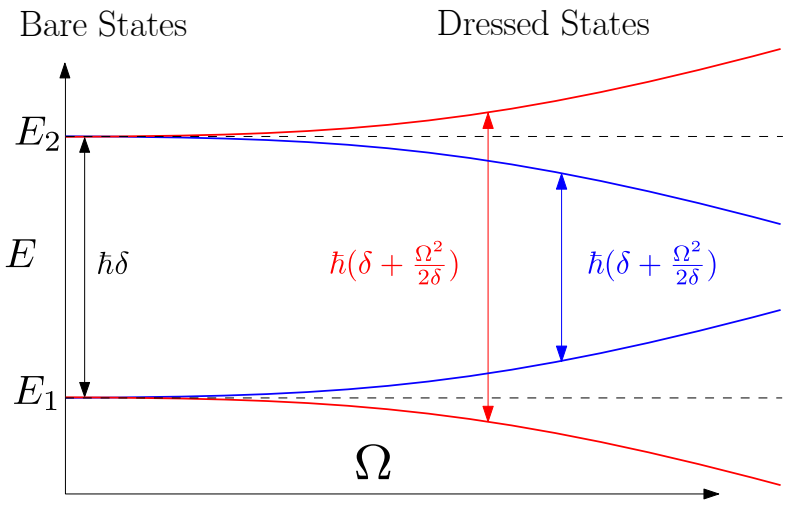


FIGURE 2.6: The light shifted energy states of a two-level atom. The red lines indicate the light shift in response to red-detuned light and the blue lines indicate the response to blue-detuned light.

Equations 2.36 become a time-dependent Schrödinger equation with a rotating-frame interaction Hamiltonian $\tilde{H}_{\mathrm{I}}$

$$i\frac{d}{dt}\begin{pmatrix}\tilde{c}_1\\ \tilde{c}_2\end{pmatrix} = \begin{pmatrix}\delta/2 & \Omega/2\\ \Omega/2 & -\delta/2\end{pmatrix}\begin{pmatrix}\tilde{c}_1\\ \tilde{c}_2\end{pmatrix} = \tilde{H}_{\mathrm{I}}\left|\tilde{\Psi}\right\rangle. \tag{2.40}$$

The eigenvalues of this Hamiltonian are easily found:

$$\lambda = \pm\frac{(\delta^2+\Omega^2)^{1/2}}{2}. \tag{2.41}$$

In the absence of light the unperturbed energies are $\lambda = \pm\delta/2$ corresponding to two states separated by energy δ. The two states are the excited state E_2 and a **dressed state** at energy $E_1 + \hbar\omega$, the ground state energy plus a photon energy. Since light shifts are largely only important when absorption is minimal i.e. $|\delta| \gg \Omega$, the perturbation can be treated as weak such the eigenvalues can be written as the Taylor expansion of Equation 2.41:

$$\lambda \approx \pm\left(\delta/2 + \frac{\Omega^2}{4\delta}\right). \tag{2.42}$$

Thus we conclude the states are shifted from the unperturbed eigenenergies by the light shift $\pm\Omega^2/4\delta$.

The origin of the scattering and dipole forces

When an atom is irradiated with a laser, the oscillating electric field $\mathbf{E}$ induces a dipole moment $\mathbf{d} = -e\mathbf{r}$ on the atom which oscillates at the driving frequency. The dipole moment is related to the electric field by

$$\mathbf{d} = \epsilon_0 \chi_a \mathbf{E}. \tag{2.43}$$

This induced dipole moment then interacts with the electric field that produced it and the resultant interaction energy is

$$U = -\frac{1}{2}\mathbf{d} \cdot \mathbf{E} = -\frac{1}{2}\epsilon_0 \chi_a E^2, \tag{2.44}$$

where the factor of $1/2$ appears because the dipole is induced, not permanent. Taking the negative gradient of the energy to be the force applied to the dipole, we find the z-component of the force to be

$$F_z = -\frac{\partial U}{\partial z} = \epsilon_0 \chi_a E \frac{\partial E}{\partial z} = d\frac{\partial E}{\partial z}. \tag{2.45}$$

As before, we assume the laser is travelling along the z-axis and its electric field is aligned to the x-axis according to $\mathbf{E} = E_0(x, y, z)\cos(\omega t + kz)\hat{\mathbf{e}}_x$. Thus the force is

$$\begin{aligned} F_z &= d \times \left\{ \frac{\partial E_0}{\partial z}\cos(\omega t - kz) + kE_0 \sin(\omega t - kz) \right\} \qquad (2.46) \\ &= -eX_{12}[u\cos\omega t - v\sin\omega t] \times \left\{ \frac{\partial E_0}{\partial z}\cos(\omega t - kz) + kE_0 \sin(\omega t - kz) \right\}, \end{aligned}$$

where in the second line we have substituted in the quantum mechanical expression for the dipole moment from Equation 2.25. Taking the time average of the above expression yields

$$\begin{aligned} \overline{F}z &= \frac{-eX_{12}}{2}\left\{ u\frac{\partial E_0}{\partial z} - vE_0 k \right\} \qquad (2.47) \\ &= F_{\text{dipole}} + F_{\text{scatt}}. \qquad (2.48) \end{aligned}$$

Thus the response of an atom to the oscillating electric field of a laser has distinct in-phase and out-of-phase components. The in-phase component corresponds

to the **dipole force**, and the out-of-phase component corresponds to the **scattering force**. Substituting in our expressions for u and v from the previous section along with the Rabi frequency $\Omega = eX_{12}E_0/\hbar$ we find

$$F_{\text{dipole}} = -\frac{\hbar\delta}{2}\frac{\Omega}{\delta^2 + \Omega^2/2 + \Gamma^2/4}\frac{\partial\Omega}{\partial z}, \tag{2.49}$$

and

$$F_{\text{scatt}} = \hbar k\frac{\Gamma}{2}\frac{\Omega^2/2}{\delta^2 + \Omega^2/2 + \Gamma^2/4}. \tag{2.50}$$

On resonance the dipole force is zero and the atom moves only in response to the scattering force. However, far from resonance, and at high enough intensity such that $|\delta| \gg \Omega$, the dipole force dominates and the scattering force is negligible. In particular, we notice that the dipole force equals the derivative of the light shift in Equation 2.42

$$F_{\text{dipole}} \backsimeq \frac{\partial}{\partial z}\left(\frac{\hbar\Omega^2}{4\delta}\right). \tag{2.51}$$

Thus, the light shifted energy of an atom in its ground state is the potential in which it moves in response to the dipole force. When the light is red-detuned, the dipole potential is negative and so the force acts in the direction of higher intensity and the atom is pulled into the beam. For blue detunings, the reverse is true and the atom is pushed out of the beam. Suffice to say that it is much more practical to produce and use dipole traps of the former kind.

The scattering force

In the previous section I claimed to have derived the scattering force with no justification or explanation before swiftly moving on to describing the dipole force. I intend to clear that up here. Despite having no mass, photons do indeed carry momentum. Einstein's famous equation $E = mc^2$ from Special Relativity is actually incomplete, the full general energy expression including momentum is

$$E^2 = p^2c^2 + (m_0c^2)^2 \tag{2.52}$$

where m_0 is the rest mass of the particle (zero for a photon). Hence the momentum of a photon is related to its energy by

$$p = \frac{E}{c} = \frac{\hbar\omega}{c} = \frac{h\nu}{c} = \frac{h}{\lambda} = \hbar k. \tag{2.53}$$

When an atom is irradiated with resonant light, each absorbed photon gives the atom a momentum kick in the direction of the photon. The subsequent spontaneously emitted photons of the excited atom are distributed randomly into 4π steradians and so on average, over many absorption-emission events, the net effect is an average force that pushes the atom in the direction of the beam. The force is therefore the momentum of a photon multiplied by the scattering rate

$$F_{\text{scatt}} = (\hbar k) \times (\Gamma\rho_{22}) = \hbar k \frac{\Gamma}{2} \frac{\Omega^2/2}{\delta^2 + \Omega^2/2 + \Gamma^2/4}, \tag{2.54}$$

where the excited state population ρ_{22} is found from Equation 2.37 and the definition $\rho_{22} = (1-w)/2$. So we have recovered the same result as in Equation 2.50 through completely different means.

Chapter 3

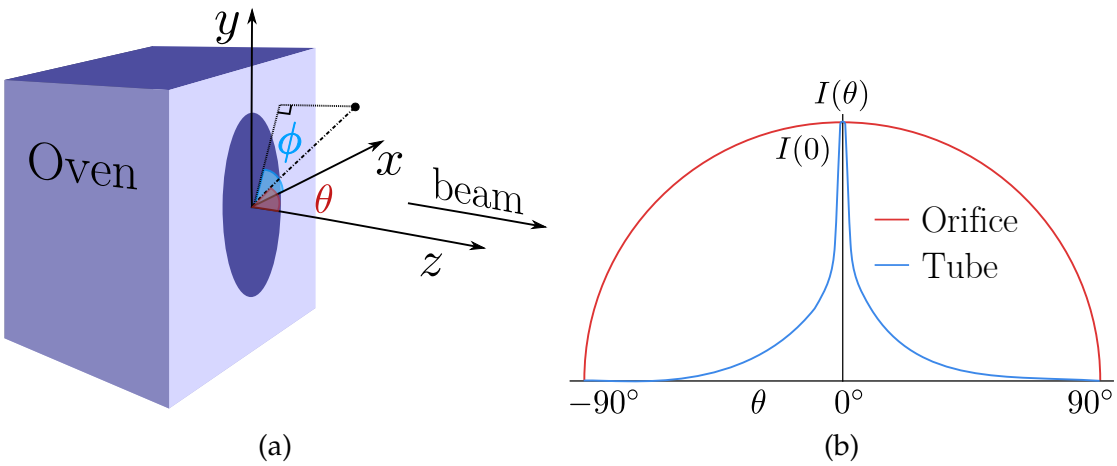
Experimental techniques

In Chapter 2 I discussed how atoms have complex internal structure consisting of discrete quantised energy levels. I also covered how those energy levels can be manipulated using both magnetic and electric fields and how the oscillating electric field of an electromagnetic wave can drive transitions between those levels. Putting all the elements of the previous chapter together one has immense control over an atom's internal and external degrees of freedom. In this section I will discuss the numerous experimental techniques that exploit these physical mechanisms to trap and cool atoms down to temperatures of just a few microkelvin and then even further to a few hundred nanokelvin.

3.1 Producing an atomic beam

Interestingly, ultracold atom experiments often begin from not-so-cold atom sources heated to hundreds of kelvin. Combined with apertures or tubes, these ovens produce beams of atoms travelling at hundreds or thousands of metres per second that need to be significantly slowed in order to be trapped. For instance, in this experiment the most probable velocities of the lithium and caesium gases inside our oven are $1600\,\mathrm{m\,s^{-1}}$ and $340\,\mathrm{m\,s^{-1}}$ respectively.

A simple atom source can be made by allowing atoms to escape from an oven through a small aperture. The emission of atoms from such an orifice is governed by the cosine law $I(\theta) \propto \cos\theta$ where θ is measured from the normal of the aperture [42]. Figure 3.1 shows the coordinate system and the cosine intensity distribution expected from an orifice. The number of atoms $dI(\theta)$ flowing through an orifice of area A per second, into a solid angle $d\omega$ in a direction



(a) (b)

FIGURE 3.1: (a) Diagram illustrating the coordinate system used to study atomic beams. (b) Cross-sections of the beams produced by an orifice and a tube. The beam formed by an orifice has a cosine distribution which is much wider than is desirable for applications within the field of cold atoms. Collimation via tubes significantly reduces the amount of unuseful flux.

making angle θ with the normal to A is given by

$$dI(\theta) = \frac{d\omega}{4\pi} nA\overline{v} \cos\theta, \tag{3.1}$$

where n is the density of the gas and $\overline{v}$ is the mean speed of the atoms [42]. The atoms in the oven have a range of speeds given by the Maxwell-Boltzmann velocity distribution which has a mean speed of

$$\overline{v} = \sqrt{8k_B T/(\pi m)}, \tag{3.2}$$

where m is the mass of the atom and T is the temperature in kelvin. Integrating over the range $0 \leq \theta \leq \pi/2$, $0 \leq \phi \leq 2\pi$ we obtain the throughput, the total number of atoms flowing through the orifice per second:

$$N = \int_0^{2\pi} \int_0^{\frac{\pi}{2}} dI(\theta) = \frac{nA\overline{v}}{4\pi} \cdot 2\pi \cdot \int_0^{\frac{\pi}{2}} \frac{\sin 2\theta}{2} d\theta = \frac{nA\overline{v}}{4} \text{ atoms/s}. \tag{3.3}$$

The conductance of an orifice is C_0:

$$C_0 = 10^{-9} A\overline{v}/4 \, \text{l s}^{-1}, \tag{3.4}$$

which is useful for differential pumping calculations [42].

For cold atom experiments much can be gained from using narrow tubes over orifices. Most of the flux from a beam formed by an orifice is wasted because the cosine distribution has high intensities at large angles θ. Narrow tubes on the other hand produce much narrower distributions with most of the flux contained within a useful solid angle (See Figure 3.1b). Provided we are in the molecular flow regime, the angular distribution $f(\theta)$ of atoms emanating from a narrow tube can be calculated. A beam is considered to be within the molecular flow regime provided $\lambda \geq d$, where d is the diameter of the collimating tube and λ is the mean free path length defined by

$$\lambda = k_B T/(\sqrt{2}\pi P a^2), \tag{3.5}$$

where P is the pressure in Pascals and a is the atomic diameter in metres. The formula for $f(\theta)$ for a tube in the absence of collisions can be obtained from simple geometric considerations and was first given by Clausing in 1930 [43]. However, when collisions are taken into account the precise density distribution along the tube is no longer clear and must be guessed. To obtain $f(\theta)$ taking collisions into account, the density within the tube is assumed to vary along the length of the tube and to stay constant over the cross-section. This turns out to be a very good approximation for tubes with large γ [42] (dimensionless ratio of tube length to diameter). The first theory taking interatomic collisions into account was developed by Giordmaine and Wang [44] in 1960 and independently by Troitskii [45] in 1962. However, the universal Equations 3.6 to 3.10 were produced by Olander and Kruger in 1970 [46]. As a warning, the following equations are extremely complicated and consequently opaque. If true understanding is sought, one is advised to seek the original books and papers referenced in this section. The angular distribution $f(\theta)$ produced by a tube with interatomic collisions considered is given by [42]:

(i) For $0 \leq \theta \leq \theta_0$

$$\begin{aligned} f(\theta) = {} & Z_V \cos\theta + [2/\pi^{1/2}][Z_V \cos\theta \exp(\delta'^2)/\delta'] \\ & \times \{(R(p)/2)\,[\mathrm{erf}(Z_p\delta'/Z_V) - \mathrm{erf}(\delta') \\ & + (2\delta'/Z_V\pi^{1/2})(1 - Z_p)\exp[-(\delta' Z_p/Z_V)^2]\big] + S(p)\Big\}, \end{aligned} \tag{3.6}$$

(ii) For $\theta_0 \leq \theta \leq \pi/2$

$$f(\theta) = Z_V \cos\theta + [2/\pi^{1/2}][Z_V \cos\theta \exp(\delta'^2)/\delta'] S(1). \tag{3.7}$$

The quantities Z_p and Z_V are normalised densities in the planes of the tube entrance and exit which are assumed to vary linearly along the length of the tube. The variables δ and δ' are defined by the expressions $\delta = \left\{ \frac{l}{2\lambda} \left[Z_V^2/(Z_p - Z_V) \right] \right\}^{1/2}$ and $\delta' = \delta/(\cos\theta)^{1/2}$. The error function for any variable x is:

$$\text{erf}(x) = \frac{2}{\pi^{1/2}} \int_0^x \exp(-x^2) dx. \tag{3.8}$$

The quantity Γ is a dimensionless ratio l/d, where l and d are the length and diameter of the tube respectively. When l and d appear explicitly in the formula they are in units of mm and $\mu\mathrm{m}$ respectively. The function $R(p)$ has no clear definition but is given by:

$$R(p) = \cos^{-1} p - p(1-p^2)^{1/2}, \tag{3.9}$$

where $p = \Gamma \tan\theta$. Finally, $S(p)$ is given by the expression:

$$S(p) = \int_0^p (1-z^2)^{1/2} \left\{ \text{erf} \left\{ \delta' \left[1 + \frac{z}{\Gamma \tan\theta} (Z_p/Z_V - 1), \right] \right\} - \text{erf}(\delta') \right\} dz. \tag{3.10}$$

The form of $f(\theta)$ in Equations 3.6 and 3.7 is shown by the blue curve in Figure 3.1b. As well as the angular distribution, it is also important to know the throughput and conductance of such a tube. With l and d still in mm and $\mu\mathrm{m}$ respectively, the total throughput for a tube is given by:

$$N = \frac{2.76 \times 10^9 d^3 P}{l m^{1/2}} \ \text{atoms/s}. \tag{3.11}$$

The conductance of a tube is:

$$C_{\text{tube}} = 1 \times 10^4 \cdot \frac{\pi \bar{v} d^3}{12 l} \ \text{l s}^{-1}. \tag{3.12}$$

Throughput and conductance are simply measures of the rate at which gas is conducted from one chamber to another via the tube. These rates are especially useful for modelling the behaviour of a dual-species oven (See Section 4.1).

3.2 Slowing an atomic beam

In the ^{6}Li-^{133}Cs mixture experiment a dual-species atomic beam is slowed by a **Zeeman slower**, an invention from William Phillips et al. that exploits the Zeeman effect and the scattering force of light for dramatic one-dimensional slowing [47] (see Sections 2.2.1 and 2.2.2). Zeeman slowing involves directing the atomic beam along the axis of a tapered solenoid. The on-axis magnetic field of the solenoid is finely tuned so that atoms in an atomic beam travelling with mean velocity v_p are resonant with a counter-propagating laser along the entire length of the slower. Put another way, the transition frequency ω_T of the atoms at velocity v_p is maintained at the laser frequency ω_L of the counter-propagating laser beam. As a result the atoms continuously scatter photons as they travel down the length of the slower until they emerge slow enough to be trapped in a magneto-optical trap (MOT). Rather than use a single tapered solenoid, we approximate one using 9 concatenated solenoids. A detailed discussion of its construction can be found in the thesis of Dr. Sonali Warriar [34]. Figures 2.3 and 2.4 show precisely how lithium and caesium respond to static magnetic fields.

The design of the ^{6}Li-^{133}Cs Zeeman slower followed some simple analysis [39, 48]. We start by assuming an atom travelling down the slower (along $\hat{\mathbf{e}}_z$) is decelerated at a constant rate:

$$\frac{dv}{dt} = v\frac{dv}{dz} = -a. \tag{3.13}$$

Integration gives the velocity as a function of the displacement:

$$v_0^2 - v^2 = 2az, \tag{3.14}$$

where v_0 is the initial velocity. In the limit of high intensity radiation, the scattering force tends to

$$F_{\max} = \hbar k\frac{\Gamma}{2}, \tag{3.15}$$

which corresponds to a maximum acceleration of

$$a_{\max} = \frac{F_{\max}}{m} = \frac{\hbar k}{m}\frac{\Gamma}{2}. \tag{3.16}$$

As a precaution we suppose the actual deceleration will be less than the theoretical maximum, e.g. $a \sim 0.5a_{\max}$ so the distance needed to bring the atoms to a complete halt would be

$$L_0 = \frac{v_0^2}{a_{\max}}. \tag{3.17}$$

So far we have assumed constant deceleration in the slower, but this is only true if the transition frequency ω_T equals the light frequency seen by the moving atom i.e. $\omega_T = \omega' = \omega_L + kv$. The transition frequency inside the slower changes via the Zeeman effect according to

$$\omega_T = \omega_0 + \frac{\mu B(z)}{\hbar}, \tag{3.18}$$

where ω_0 is the unmodified transition frequency, μ is the magnetic moment of the transition and $B(z)$ is the on-axis magnetic field. Constant deceleration is therefore achieved when the following relation is satisfied:

$$\omega_0 + \frac{\mu B(z)}{\hbar} = \omega_L + kv. \tag{3.19}$$

Rearranging for v and subsequent substitution into Equation 3.17 gives us an expression for the required magnetic field profile along the slower:

$$B(z) = B_0 \left(1 - \frac{z}{L_0}\right)^{\frac{1}{2}} + B_{\text{bias}}, \tag{3.20}$$

where $B_0 = \hbar k v_0/\mu$ and $B_{\text{bias}} = (\hbar\omega_L - \hbar\omega_0)/\mu$. However, we have been conducting this analysis with the objective of bringing the atoms to a halt; to collect the atoms in a MOT a finite final velocity is more useful. Additionally, the final velocity should also be below the MOT capture velocity, the maximum velocity an atom can have if it is to be trapped in a MOT. We therefore tune the B_{bias} term in order to leave the atoms with a velocity below or matching the capture velocity of the magneto-optical trap (MOT). The caesium slower is tuned such that atoms initially travelling under $215\,\mathrm{m\,s^{-1}}$ leave the slower at approximately the magneto-optical trap (MOT) capture velocity of $v_c = 40\,\mathrm{m\,s^{-1}}$. Any lithium atoms initially travelling slower than $900\,\mathrm{m\,s^{-1}}$ are slowed to a final velocity of $200\,\mathrm{m\,s^{-1}}$, just below the MOT capture velocity of $230\,\mathrm{m\,s^{-1}}$. Our slower is configured to switch between two ideal profiles for rapid sequential loading of

lithium and caesium MOTs as shown in Figure 3.2. Details of the switching electronics can be found in [49, 36, 35].

For caesium our slower primarily operates on the $6^2S_{1/2}, F = 4 \Rightarrow 6^2P_{3/2}, F' = 5$ transition. However, because there is a very small probability of a magnetic quadrupole transition to the $F = 3$ state the atoms tend to congregate in this dark state. A weak *repumping* laser is overlapped with the cooling light detuned from the $6^2S_{1/2}, F = 3 \Rightarrow 6^2P_{3/2}, F' = 4$ to get the atoms back into the cooling cycle. We typically use about $30\,\mathrm{mW}$ of cooling light and $0.6\,\mathrm{mW}$ of repumping light in our Zeeman slowing beam and both beams are detuned $95\,\mathrm{MHz}$ from their respective transitions. A level diagram for caesium can be seen in Figure 2.2.

For lithium our slower operates on the D_2 $2^2\mathrm{S}_{1/2} \Rightarrow 2^2\mathrm{P}_{3/2}$ optical transitions. The beam consists of 'cooling' light $120\,\mathrm{MHz}$ detuned from the $2^2\mathrm{S}_{1/2}, F = 3/2 \Rightarrow 2^2\mathrm{P}_{3/2}, F' = 5/2$ transition and 'repumping' light $120\,\mathrm{MHz}$ detuned from the $2^2\mathrm{S}_{1/2}, F = 1/2 \Rightarrow 2^2\mathrm{P}_{3/2}, F' = 3/2$ transition. Cooling and repumping are written in inverted commas because lithium's unresolved excited states (total separation of $4.4\,\mathrm{MHz}$) mean the two beams function equally as cooler and repumper. We typically use about $15\,\mathrm{mW}$ of cooling light and $12\,\mathrm{mW}$ of repumping light. A level diagram for lithium can be seen in Figure 2.1.

Using the Zeeman slower we are able to capture 5×10^7 caesium atoms in the MOT at a loading rate of $5 \times 10^7\,\mathrm{atoms/s}$. We can typically capture 2×10^8 atoms in the lithium MOT at a loading rate of $7 \times 10^7\,\mathrm{atoms/s}$.

3.2.1 The magneto-optical trap

The atoms that emerge from the Zeeman slower are trapped in magneto-optical traps (MOT). MOTs provide both three-dimensional cooling and trapping and, like the Zeeman slower, are based on the interactions of atoms with static magnetic fields and light close to resonance (see Sections 2.2.1 and 2.2.2). Two coils arranged in anti-Helmholtz configuration produce a quadrupole magnetic field with a field zero at the centre point between the two coils. Near to this field zero the magnetic field is weak and so atoms in this region are subject to the weak-field Zeeman effect meaning their Zeeman sublevels are perturbed linearly as a function of the magnetic field. Since the magnetic field gradient about the zero-point varies linearly with radial displacement so too does the Zeeman

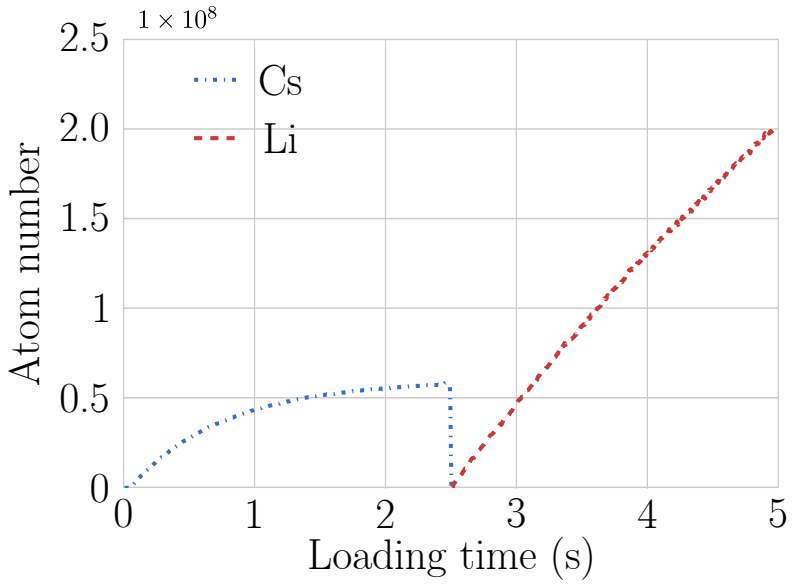


FIGURE 3.2: Sequential loading of lithium and caesium MOTs using our profile-switching Zeeman slower. The lithium MOT atom number plateaus at 6×10^8 after approximately 40 seconds.

shift. The situation for a $J = 0 \Rightarrow J = 1$ atom is shown in Figure 3.3a and the field plus beam arrangement is shown in Figure 3.3b [50].

Consider an atom travelling away from the origin in the positive z-direction in Figure 3.3a. As it travels further from the centre of the trap the $M_J = -1$ state is more red-shifted while the $M_J = +1$ state is more blue-shifted. Since the light is red-detuned, the effect of this is to put the atom more on resonance with the counter-propagating σ^- light than the co-propagating σ^+ light producing a radiation imbalance. This imbalance grows stronger the further the atom gets from the origin. The reverse is true for atoms travelling away from the origin in the opposite direction.

In order for the MOT to function we require *closed transitions*, transitions to states that can only decay back to the original state or that have very low probability of decaying to other states. In this experiment we use caesium's $6^2S_{1/2}, F = 4 \Rightarrow 6^2P_{3/2}, F' = 5$ transition because the $F' = 5$ state is dipole forbidden from transitioning to any states other than $F = 4$. However, there is a very small probability of a magnetic quadrupole transition to the $F = 3$ state and any atoms that end up in this state are lost from the trapping cycle. A weak *repumping* laser resonant on $6^2S_{1/2}, F = 3 \Rightarrow 6^2P_{3/2}, F' = 4$ gets these atoms back into circulation. A level diagram for caesium can be seen in Figure 2.2.

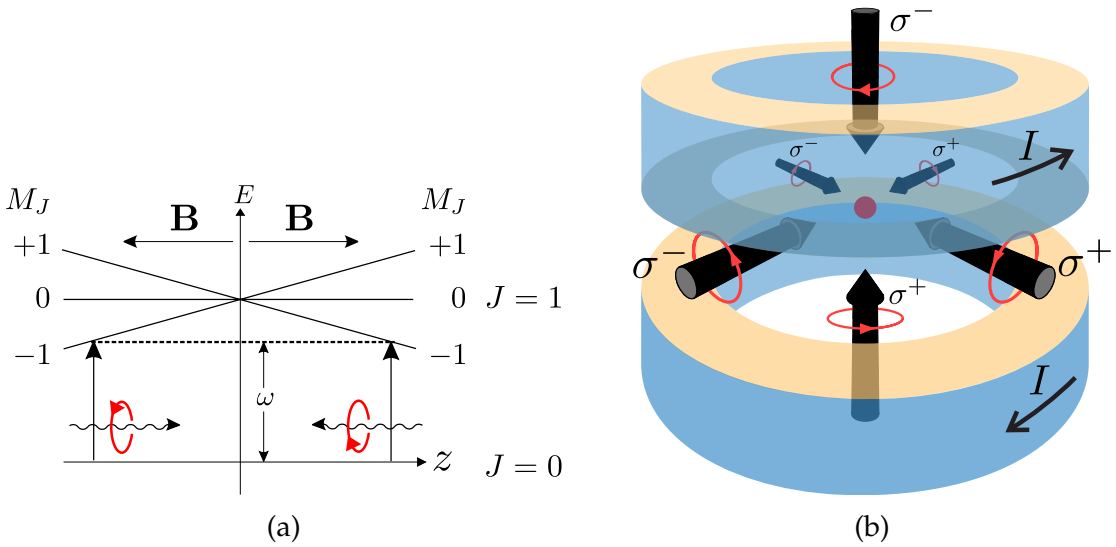


FIGURE 3.3: The magneto-optical trap. Atoms in the MOT feel a force opposite to their velocity that grows stronger with their displacement from the centre of the trap. (a) Diagram illustrating how unbalanced radiation forces are produced for a $J = 0 \Rightarrow J = 1$ system. (b) Diagram of the laser beams and magnetic field arrangement required to produce a MOT.

Lithium is a little trickier to work with because its closely spaced excited states mean we cannot target a single excited state. Therefore we use two equally powerful, equally detuned lasers on the $2^2S_{1/2}, F = 3/2 \Rightarrow 2^2P_{3/2}, F' = 5/2$ and $2^2S_{1/2}, F = 1/2 \Rightarrow 2^2P_{3/2}, F' = 3/2$ transitions. We call the transition from the $F = 3$ state the 'repumper' even though the two beams are both equally cooling and repumping. A level diagram for lithium is given in Figure 2.1.

3.3 Optical molasses

Optical molasses uses the same laser beam arrangement as for the magneto-optical trap (MOT) but is performed in the absence of a magnetic field. A stationary 1-D atom in the field of two slightly red-detuned counter-propagating lasers does not move since the scattering forces from each beam equal each other[1] (See Section 2.2.2). A moving atom however, sees Doppler shifted light frequencies with the beam opposing its motion being closer to resonance. The

[1]Later we see that this is not entirely true and the atom will undergo a random walk due to the recoil velocity of each emission. This phenomenon sets a lower limit to the temperatures achievable in optical molasses.

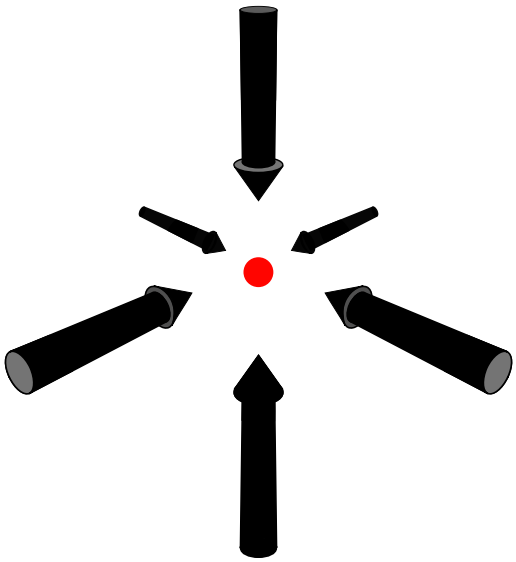


FIGURE 3.4: Beam arrangement for 3-D optical molasses cooling. 3 pairs of counter-propagating lasers cool the atoms in all six directions by way of unbalanced radiation forces.

result is an imbalance of the scattering forces and the atom is slowed in whichever direction it travels until it is brought to a halt (spontaneous emission carries the energy away). Mathematically this is represented as [39]

$$\begin{aligned} F_{\text{total}} &= F_{\text{scatt}}(\omega_L - \omega_0 - kv) - F_{\text{scatt}}(\omega_L - \omega_0 + kv) \\ &= F(\delta - kv) - F(\delta + kv) \\ &\simeq \left(F(\delta) - kv\frac{\partial F(\delta)}{\partial \omega}\right) - \left(F(\delta) + kv\frac{\partial F(\delta)}{\partial \omega}\right) \\ &\simeq -2kv\frac{\partial F(\delta)}{\partial \omega}, \end{aligned} \tag{3.21}$$

where both scattering forces have been Taylor expanded in the limit of low velocity ($kv \ll \Gamma$). The imbalance therefore produces a frictional force proportional to the velocity, just like a particle passing through a viscous fluid. Hence this phenomenon was dubbed **optical molasses** by Chu et. al [51, 52, 53]. By intersecting two more pairs of counter-propagating beams, as in Figure 3.4, we can achieve three-dimensional cooling. This model predicts that atoms caught in the optical molasses will eventually come to a complete halt. Unfortunately this is not a fully realistic model since we have not taken into account heating effects from the scattering forces.

3.3.1 The Doppler limit

There is a theoretical lower limit to the temperatures achievable through optical molasses owing to heating caused by spontaneous emission. This heating derives from the discrete size of the momentum steps the atoms undergo with each emission or absorption event (see Section 2.2.2 for a discussion of the scattering force). We consider once again the 1-D situation of an atom in the field of two counter-propagating laser beams [39, 48]. In each absorption or emission event the atomic momentum changes by $\hbar k$ and so the kinetic energy changes by the recoil energy $E_r = \hbar^2 k^2/2m$. Thus an atom in the light field gains on average $2E_r$ from each scattering event. If we take the scattering rate to be R_{scatt} for a single beam, then provided $I \ll I_{\text{sat}}$, the scattering rate for both beams is $2R_{\text{scatt}}$[2]. The rate at which scattering heats the sample is therefore

$$\frac{dE_{\text{heat}}}{dt} = (2R_{\text{scatt}})(2E_r). \tag{3.22}$$

The 1-D velocity dependent cooling force in optical molasses has the form

$$F_{\text{cool}} = -\alpha v = -2k\frac{\partial F(\delta)}{\partial \omega}v = -\left[2\hbar k^2 \frac{-2\delta}{\delta^2 + \Gamma^2/4} R_{\text{scatt}}\right] v. \tag{3.23}$$

This force generates a cooling rate of

$$\frac{dE_{\text{cool}}}{dt} = \frac{d}{dt}\left(\frac{1}{2}mv^2\right) = vm\frac{dv}{dt} = vF_{\text{cool}} = -\alpha v^2. \tag{3.24}$$

At equilibrium the heating rate equals the cooling rate so we have

$$\alpha v^2 = (2R_{\text{scatt}})(2E_r). \tag{3.25}$$

Thermodynamics tells us the velocity is related to the temperature by $mv^2/2 = k_B T/2$ so we can write:

$$k_B T = \frac{\hbar\Gamma}{4}\left(\frac{2\,|\delta|}{\Gamma} + \frac{\Gamma}{2\,|\delta|}\right). \tag{3.26}$$

[2]We have to be far from saturation so that the absorption from the two beams can be treated as uncorrelated and therefore two beams produce twice as much fluctuation.

This function has a minimum at $|\delta| = \Gamma/2$ which is the **Doppler temperature**:

$$T_D = \frac{\hbar\Gamma}{2k_B}. \tag{3.27}$$

This is the predicted lowest temperature achievable using the optical molasses technique. The Doppler temperatures for ^{6}Li and ^{133}Cs are $141\,\mu\text{K}$ and $126\,\mu\text{K}$ respectively. We perform optical molasses on both species after the magneto-optical trap stage as way of loading our optical dipole traps. When performing optical molasses on the lithium MOT we actually decrease our MOT beam detunings to precisely $-\Gamma/2$, the theoretical minimum. However, the temperature can only reach ~$600\,\mu\text{K}$. For caesium we actually *increase* our MOT detuning as far as we can and the cloud can reach as low as $20\,\mu\text{K}$, much lower than the Doppler temperature. The reason for this is that sub-Doppler cooling techniques work much more effectively at large detunings. This is explored further in the next sub-section. Unfortunately lithium's closely spaced excited states inhibit us again and prevent any sub-Doppler cooling mechanisms from working.

3.4 Sub-Doppler cooling

Initially, experimental observations seemed to agree that the Doppler temperature was a fundamental limit of optical molasses, but as time went on and more precise measurements were made, experiments started to suggest otherwise. In 1988 the National Institute of Standards and Technology Washington group showed that temperatures well below the Doppler temperature could be reached using optical molasses. In 1989 Dalibard and Cohen-Tannoudji [54] released a hugely influential paper that explained how labs across the world were able to cool atoms to temperatures approaching the recoil limit $k_B T_R = \hbar^2 k^2/2m$.

Sisyphus cooling in the Lin $\perp$ Lin configuration

Although this technique is not used in this experiment, a discussion of the cooling mechanism proves useful to the understanding of the more complicated scheme that is employed [50, 48]. Consider the one-dimensional case of two counter-propagating laser beams with orthogonal linear polarisations as shown

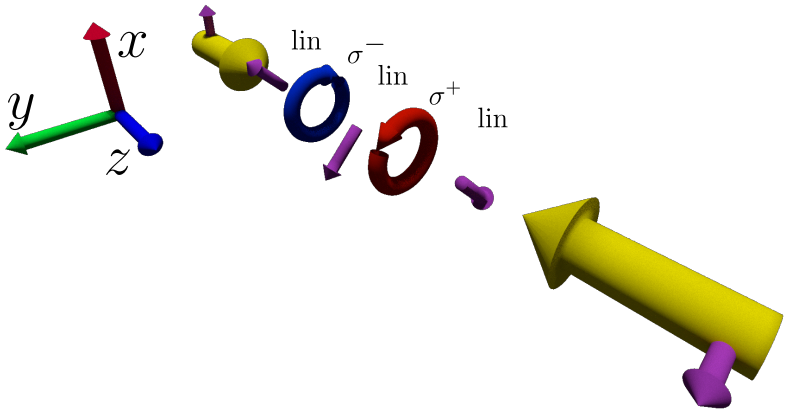


FIGURE 3.5: Polarisation gradient created by the Lin⊥Lin sub-Doppler cooling configuration. Two counter-propagating lasers with orthogonal linear polarisations create a light field with ellipticity that varies in space.

in Figure 3.5. The resulting light field has a polarisation that oscillates from linear to σ^+ to linear to σ^- over half a wavelength. Consider also an atom with a $J_g = 1/2$ to $J_e = 3/2$ transition (Figure 3.6a). In regions of purely σ^+, the ground state population is pumped to the $m_g = +1/2$ sublevel. Similarly, in regions of purely σ^-, the ground state population is pumped to the $m_g = -1/2$ sublevel. Thus in travelling through half a wavelength of the light field, the atoms will shift their entire ground state population from $m_g = -1/2$ to $m_g = +1/2$ and back again.

As well as driving transitions between energy levels, the light field plays a secondary role in light shifting the energy levels. In the low-intensity limit of two laser beams, each of intensity $s_0 I_{\text{sat}}$ (where s_0 is the saturation parameter and I_{sat} is the saturation intensity), the light shifts ΔE_g of the ground magnetic substates are given by

$$\Delta E_g = \frac{\hbar \delta s_0 C_{ge}^2}{1 + (2\delta/\gamma)}, \tag{3.28}$$

where C_{ge} is a Clebsch-Gordan coefficient (see Section 2.1). This relation differs from a typical light shift formula because there are two travelling waves to consider and because the ground state population is split over two sublevels. Because C_{ge} depends on the magnetic quantum numbers and the polarisation of the light field, the light shift is different for each magnetic sublevel.

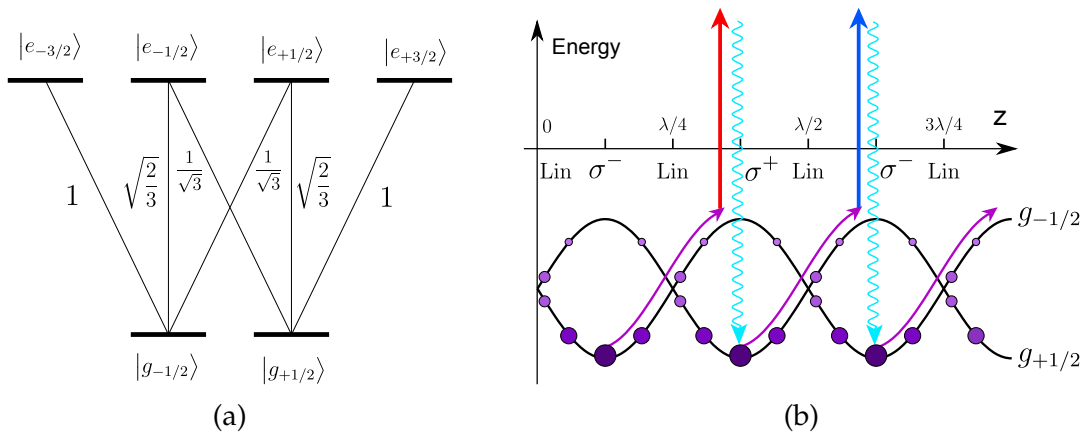


FIGURE 3.6: Atomic Sisyphus effect in the Lin $\perp$ Lin polarisation gradient configuration. Figures adapted from [54]. (a) The atomic level scheme and Clebsh-Gordan coefficients for a $J_g = 1/2 \leftrightarrow J_e = 3/2$ transition. (b) The light shifted energies and steady state populations (purple circles) for a negative detuning. The lowest energy state is always the more populated one.

From Equation 3.28 and Figure 3.6b we see that the light shift for σ^+ transitions from the $m_g = +1/2$ state is three times the light shift for σ^- transitions from the $m_g = -1/2$ state and that the reverse is also true. We also notice that in the regions of linearly polarised light the states are equally shifted. The net result is that the light shifted ground state energies oscillate as a function of z with a period of $\lambda/2$. Thus atoms that find themselves in this arrangement tend to be pumped into the ground state that is more strongly light shifted. If we assume the lasers are red detuned then that state is also the state with the lowest energy.

Now, because it takes a finite amount of time τ for transitions between the ground states, an atom travelling at *just* the right velocity v will experience a friction effect. Suppose an atom starts at $\lambda/8$ in a region of σ^- and propagates at a velocity $v = (\lambda/4)/\tau$ in the positive z-direction towards the region of σ^+ at $\lambda/4$. Following the first purple arrow drawn in Figure 3.6b we see that in travelling from $\lambda/8$ to $\lambda/4$ the atom climbs from the very bottom of the potential well to the top. Now because it takes the atom an amount of τ to complete the ascent, upon reaching the zenith the atom is immediately pumped into the other ground state. The other ground state at $\lambda/4$ sits at the bottom of a new potential well which the atom climbs out of before being pumped back to the original state and the process repeats itself. This perpetual climbing of potential

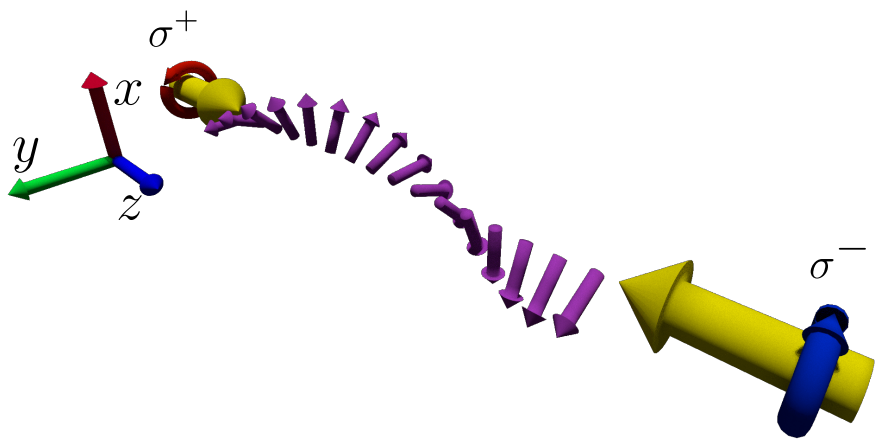


FIGURE 3.7: Polarisation gradient produced by the $\sigma^+ - \sigma^-$ sub-Doppler cooling configuration. This configuration creates a light field with a linear polarisation that rotates in space. The origin is considered to be at the tail of the first purple arrow pointing along $\hat{\mathbf{e}}_y$ on the σ^+ side of the diagram.

hills is somewhat reminiscent of Sisyphus who, according to Greek mythology, was damned to endlessly carry a boulder to the top of a mountain. Upon reaching the summit the boulder would roll back down to the bottom and Sisyphus would have to carry it back up again. It is for this reason that this cooling scheme was dubbed **Sisyphus cooling**. In climbing the potential hills the atom converts some of its kinetic energy into potential energy which is then radiated away as the atom spontaneously decays. Energy is dissipated because the photons that are emitted are of a higher frequency than those that are absorbed.

Sub-Doppler cooling in the $\sigma^+ - \sigma^-$ configuration

The source of cooling in the $\sigma^+ - \sigma^-$ configuration is radically different to the Lin $\perp$ Lin case. Previously, a polarisation gradient caused the ground state Zeeman sublevels to be spatially modulated in energy and optical pumping between the substates generated a cooling effect. In this configuration the ground state sublevels are not spatially modulated so there is no chance of a Sisyphus effect. Instead, atomic motion through the light field causes an unbalanced distribution in the ground state sublevel populations which in turn causes an imbalance between the radiation pressures exerted by the two counter-propagating laser

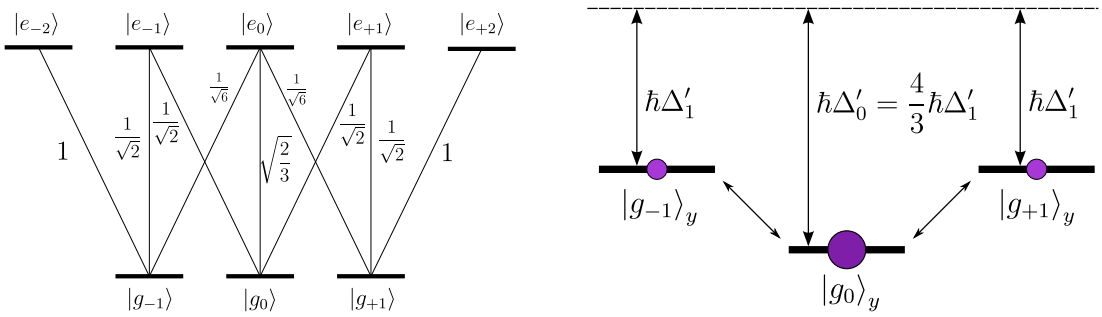


FIGURE 3.8: Sub-Doppler cooling in the $\sigma^+ - \sigma^-$ configuration. Figures adapted from [54].(a) The atomic level scheme and Clebsh-Gordan coefficients for a $J_g = 1 \leftrightarrow J_e = 2$ transition. (b) The light shifted energies and steady state populations (purple circles) for a negative detuning and with the quantisation axis chosen to be along the linear laser polarisation. In this scheme the light shift does not vary with z.

beams. The full explanation of this cooling force is very long and complex so here I will just highlight the key points made by Dalibard and Cohen-Tannoudji in their seminal paper[54].

In this configuration the two lasers have opposite circular polarisations. Here, the laser polarisation remains linear but rotates around $\hat{\mathbf{e}}_z$ forming a helix with pitch λ (Figure 3.7). To uncover the cooling mechanism we turn to a $J_g = 1$, $J_e = 2$ system as it is the simplest system that exhibits cooling.

An atom at rest in the light field

Consider an atom at rest at the origin of Figure 3.7. We see that the light polarisation is perfectly aligned with $\hat{\mathbf{e}}_y$. Taking $\hat{\mathbf{e}}_y$ to be our quantisation axis, clearly only π transitions can be excited and the system will move towards a steady state with sublevel populations governed by the Clebsch-Gordan coefficients in Figure 3.8a. More precisely the atoms will be concentrated in $|g_0\rangle_y$ because the optical pumping rate $|g_{\pm1}\rangle_y \rightarrow |g_0\rangle_y$ proportional to $(1/\sqrt{2})^2(1/\sqrt{2})^2 = 1/4$ is greater than the optical pumping rate $|g_0\rangle_y \rightarrow |g_{\pm1}\rangle_y$ proportional to $(\sqrt{2/3})^2(1/\sqrt{6})^2 = 1/9$. The steady-state populations of $|g_0\rangle_y$, $|g_{-1}\rangle_y$, and $|g_{+1}\rangle_y$ are $9/17$, $4/17$, and $4/17$ respectively. From Equation 3.28 we can see that because the π transition from the $|g_0\rangle_y$ is $4/3$ more intense than the π transitions from $|g_{\pm1}\rangle_y$, the sublevel $|g_0\rangle_y$ will be $4/3$ more light shifted than the sublevels

$|g_{\pm 1}\rangle_y$:

$$\Delta_0' = \frac{4}{3}\Delta_1'. \tag{3.29}$$

As before, we assume a red detuning so the sublevels are shifted down in energy and so $|g_0\rangle_y$ sits lower than $|g_{-1}\rangle_y$ and $|g_{+1}\rangle_y$. We have determined that if an atom is at any point along $\hat{\mathbf{e}}_z$ but still at rest, optical pumping will distribute the populations among the magnetic substates according to the local polarisation direction $\hat{\boldsymbol{\epsilon}}$. Thus, the $|g_0\rangle_\epsilon$ state will be populated most strongly and the sublevels $|g_{\pm 1}\rangle_\epsilon$ will be populated less.

Moving atoms however, experience a rotation of the local polarisation axis, and must be optically pumped in order to follow it. Provided the optical pumping time between the ground states is long, the population of the ground magnetic substates will always lag behind the steady state-distribution appropriate to the local field. This lag introduces non-adiabatic couplings between Zeeman sublevels undergoing different light shifts and we will see soon that this ultimately leads to a population imbalance that generates a friction force.

An atom moving through the light field and a transformation to a moving rotating frame

We consider now an atom travelling along $\hat{\mathbf{e}}_z$ at a velocity v. In the rest frame of the atom the laser polarisation rotates about $\hat{\mathbf{e}}_z$ making an angle ϕ with $\hat{\mathbf{e}}_y$ where

$$\phi = -kz = -kvt. \tag{3.30}$$

It is convenient to make a transformation to a moving rotating frame such that the laser polarisation direction is constant. The effects of the rotation will now manifest themselves in the form of a fictitious magnetic field parallel to $\hat{\mathbf{e}}_z$ with an amplitude such that the Larmor frequency is equal to the rotation frequency. As a result the new Hamiltonian that governs the atomic evolution picks up an inertial term equal to

$$V_{\mathrm{rot}} = kvJ_z. \tag{3.31}$$

To simplify our analysis in the subsequent step, we assume that the splitting of the ground state energy levels is much larger than their widths, i.e. $|\Delta'| \gg \Gamma'$. We will also assume that $|\Delta'| \gg kv$, which permits a perturbative treatment of the effect of V_{rot}. Using perturbation theory the new rotating-frame ground

state wave functions can be calculated:

$$|\widetilde{g_0}\rangle_y = |g_0\rangle_y + \frac{kv}{\sqrt{2}(\Delta_0' - \Delta_1')}|g_{+1}\rangle_y + \frac{kv}{\sqrt{2}(\Delta_0' - \Delta_1')}|g_{-1}\rangle_y\,, \tag{3.32a}$$

$$|\widetilde{g_{+1}}\rangle_y = |g_{+1}\rangle_y + \frac{kv}{\sqrt{2}(\Delta_1' - \Delta_0')}|g_0\rangle_y\,, \tag{3.32b}$$

$$|\widetilde{g_{-1}}\rangle_y = |g_{-1}\rangle_y + \frac{kv}{\sqrt{2}(\Delta_1' - \Delta_0')}|g_0\rangle_y\,. \tag{3.32c}$$

Thus the wave functions have been contaminated with a proportion of the other ground states; since J_z has non-zero matrix elements among the eigenstates of J_y, the inertial term has introduced couplings proportional to kv between the states $|g_0\rangle_y$ and $|g_{\pm1}\rangle_y$. Interestingly, despite a change of basis, the ground state energies and steady-state populations of the new perturbed states are the same as the unperturbed states' and so only the wave functions have changed. Now, importantly, in the perturbed basis $\{|\widetilde{g_m}\rangle_y\}$ the populations of $|g_{\pm1}\rangle_z$, the eigenstates of J_z, are unbalanced (unlike in $\{|g_m\rangle_y\}$). To show this we can calculate the expectation values of J_z in the new basis which is proportional to the population imbalance:

$${}_y\langle\widetilde{g_0}|\,J_z\,|\widetilde{g_0}\rangle_y = \frac{2\hbar kv}{\Delta_0' - \Delta_1'}, \tag{3.33a}$$

$${}_y\langle\widetilde{g_{+1}}|\,J_z\,|\widetilde{g_{+1}}\rangle_y = {}_y\langle\widetilde{g_{-1}}|\,J_z\,|\widetilde{g_{-1}}\rangle_y = \frac{\hbar kv}{\Delta_1' - \Delta_0'}. \tag{3.33b}$$

Weighting these expectation values by their steady state populations (which if we remember were found to be the same as for the stationary atom) gives the steady state value of J_z:

$$\langle J_z\rangle_{\text{ss}} = \frac{2\hbar kv}{\Delta_0' - \Delta_1'}\left(\frac{9}{17} - \frac{2}{17} - \frac{2}{17}\right) = \frac{40}{17}\frac{\hbar kv}{\Delta_0'}, \tag{3.34}$$

where we have used Equation 3.29 to eliminate Δ_1'. Thus we have shown that when an atom moves along $\hat{\mathrm{e}}_z$ in a $\sigma^+ - \sigma^-$ configuration, the two eigenstates of $J_z\,|g_{\pm1}\rangle_z$ have different steady state populations.

Origin of the friction force

From Figures 3.7 and 3.8a we can see that an atom in the $|g_{-1}\rangle_z$ state is six times more likely to absorb a σ^- photon travelling in the negative z-direction than a

σ^+ photon travelling in the positive z-direction. We can also see that the reverse is true for an atom in the $|g_{+1}\rangle_z$ state. If the lasers are red-detuned Equation 3.34 tells us that an atom travelling in the positive z-direction spends most of its time in the $|g_{-1}\rangle_z$ state. Hence the atom is more likely to absorb counter-propagating photons than co-propagating photons leading to unbalanced radiation pressures. Likewise, an atom travelling in the opposite direction spends more of its time in the $|g_{+1}\rangle_z$ and so scatters more counter-propagating σ^+ photons. To sum up, we have seen that the $\sigma^+ - \sigma^-$ configuration causes a population imbalance among the eigenstates of J_z which in turn generates unbalanced scattering forces which ultimately cool the atoms.

Using this sub-Doppler cooling technique temperatures as low as $\sim 30\,\mu\mathrm{K}$ have been achieved with caesium. Unfortunately this sub-Doppler cooling mechanism does not work on lithium because its closely spaced excited state energies prevent us from addressing a single excited state. As a result the minimum temperature we can achieve in the MOT for lithium is a little over $600\,\mu\mathrm{K}$.

3.5 The dipole trap

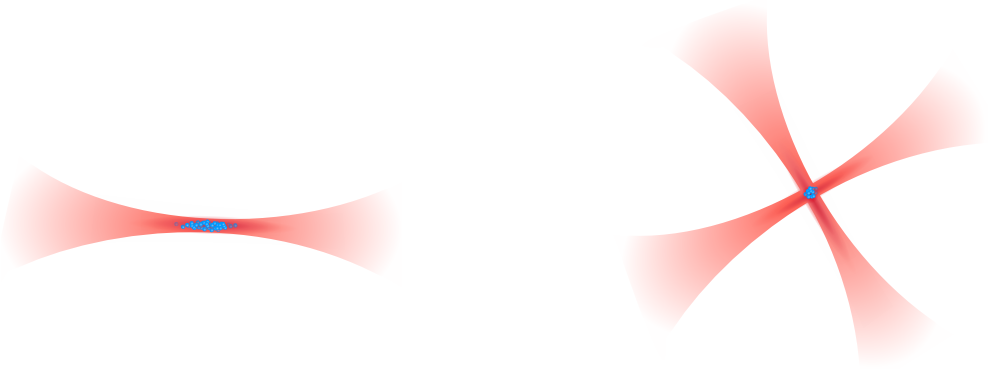
After reaching the lowest temperatures we can achieve using the techniques described above, we turn to the dipole trap for subsequent cooling beyond the recoil limit. As described in Section 2.2.2 the a.c. Stark effect perturbs the ground state energy of an atom as to generate a potential proportional to the intensity of the radiation:

$$U_{\mathrm{dipole}} \simeq \frac{\hbar\Omega^2}{4\delta} \equiv \frac{\hbar\Gamma}{8}\frac{\Gamma}{\delta}\frac{I}{I_{\mathrm{sat}}}, \tag{3.35}$$

in which the atom feels a force

$$\mathbf{F}_{\mathrm{dipole}} = -\nabla U_{\mathrm{dipole}}. \tag{3.36}$$

If the light is red-detuned atoms are pulled to regions of high intensity and the reverse is true for blue-detuned light. Hence, atoms in a tightly-focused red-detuned laser beam are attracted to the focus in both the radial and axial directions. Because of the shallower intensity gradient in the axial direction, and so weaker axial confinement, the atoms form a cigar shaped distribution at the



(a) (b)

FIGURE 3.9: The dipole trap. a) Atoms congregate in the region of focus of a tightly focused, high-intensity, greatly red-detuned laser beam. b) The crossed beam configuration has a smaller trapping region but higher intensity and intensity gradients.

focus of the beam (Figure 3.9). To provide tight confinement in all directions, a second dipole trap can be overlapped with the first so that the atoms congregate at the intersection of the two beams (See Figure 3.9b).

In order to function effectively, dipole traps are typically operated at large red-detunings where the scattering rate can be approximated as [39, 55]

$$R_{\text{scatt}} = \frac{\Gamma}{8}\frac{\Gamma^2}{\delta^2}\frac{I}{I_{\text{sat}}}. \tag{3.37}$$

Since in this limit the scattering rate depends on I/δ^2, but the trap depth depends on I/δ (Equation 3.35), combining a large detuning with a high intensity keeps the scattering rate low while producing a deep enough potential for trapping. Because the trap is conservative, atoms with too high velocities swoop through the trap without dissipating any energy. Therefore, the only way to load the trap is to have the atoms sufficiently cold before placing them gently in the bottom of the trap.

In both experiments we use powerful $1064\,\text{nm}$ or $1070\,\text{nm}$ light to dipole trap our atoms. This light is sufficiently far detuned to effectively dipole trap both lithium and caesium (See Chapters 4 and 5).

3.5.1 Evaporative cooling

In much the same way a cup of tea cools down as the water evaporates, a dipole trap can cool an ensemble of atoms by allowing only the most energetic atoms to escape. When atoms with greater than the mean energy per atom escape from the trap, the ensemble as a whole is effectively cooled. This can be understood using a simple model in which we divide the process into steps. First, the gas starts with a thermal distribution given by the Boltzmann distribution [56]

$$N(E) = N_0 e^{-E/k_B T_1}. \tag{3.38}$$

Now, let us suppose that fluctuations cause a number of atoms to escape. To model this we allow any atoms with energy greater than E_{cut} to escape so that the gas has a truncated energy distribution. Now, if we allow collisions between the trapped atoms to redistribute the energy and establish thermal equilibrium, we find that the new energy distribution has a lower temperature $T_2 < T_1$ owing to the lower mean energy per atom after the cut. Further cooling is represented by repeating this process for lower and lower E_{cut}s. Evaporative cooling by holding the trap depth constant and allowing thermal fluctuations to carry energy away is called **plain evaporation**. **Forced evaporation** is the continuous ramping down of the potential walls in order to force atoms out of the trap. Forced evaporation has to be conducted at a slow enough rate such that the atoms have enough time to rethermalise between "steps".

Forced evaporative cooling is used effectively in Chapter 4 to create a $^6Li_2$ molecular Bose-Einstein Condensate (mBEC). In Chapter 5 a dipole trap is used to increase the atomic density inside an optical fibre. For this purpose achieving BEC is unnecessary and so we only use plain evaporation.

3.5.2 Formation of Feshbach molecules via magneto-association

A **Feshbach resonance** is a phenomenon in which two colliding atoms resonantly couple to a molecular bound state [28, 29, 57]. The origin of Feshbach resonances is rather tricky to uncover. Consider two ground state alkali atoms ($L = 0$) in an ensemble trapped in a dipole trap. Ignoring the harmonic potential produced by the dipole trap and collisions with other particles, we concern ourselves only with the electronic Born-Oppenheimer interaction potentials that

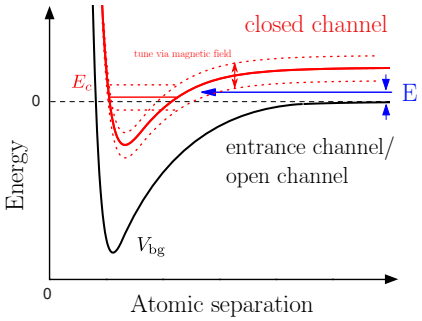


FIGURE 3.10: Two-channel model of a Feshbach resonance. The phenomenon occurs when two atoms colliding at energy E in the entrance channel resonantly couple to a molecular bound state with energy E_c supported by the closed channel potential. If the magnetic moments of the closed and open channel differ it is possible to tune the bound state energy E_c into resonance with the entrance channel continuum energy. Figure adapted from [28].

govern the collisions between the two atoms. All potentials are isotropic for the interaction of two S-state atoms.

At small separations the interaction potential experienced by the atoms is largely determined by the two-electron wavefunction $|\Psi\rangle = |\psi(\boldsymbol{r}_1, \boldsymbol{r}_2)\chi(\boldsymbol{s}_1, \boldsymbol{s}_2)\rangle$ where $\psi(\boldsymbol{r})$ and $\chi(\boldsymbol{s})$ represent the spatial and spin components of the wavefunction respectively. Because the two electrons are identical fermions the wavefunction $|\Psi\rangle$ describing the pair must be antisymmetric with respect to exchange (the Pauli exclusion principle). This is only possible by combining a symmetric spatial wavefunction with an antisymmetric spinor or vice versa. When the spinor is symmetric, the two-particle system is in the triplet state with total spin 1. If the spinor is antisymmetric the spinor is in the singlet state with total spin zero. The interaction potentials that result from symmetric and antisymmetric spatial wave functions are different. Therefore the potential the atoms experience depends on their spin states.

Two of the three sublevels of the triplet state are magnetically responsive, namely the $|s = 1, m_s = \pm 1\rangle$ states (s and m_s are the composite spin and magnetic quantum numbers). The singlet state and the $|s = 1, m_s = 0\rangle$ state do not respond to the presence of an external magnetic field. Consequently, the energies of the $|m_s = \pm 1\rangle$ states can be tuned using an external magnetic field B via the Zeeman effect leaving the other states' energies unchanged.

Typically, at low energies the colliding atoms can only access one interaction

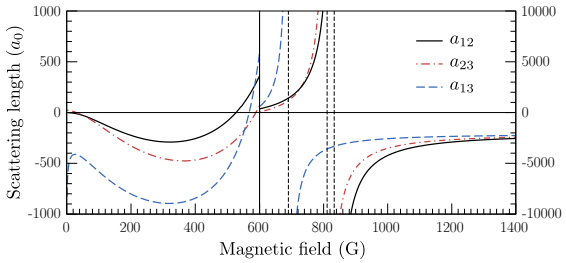


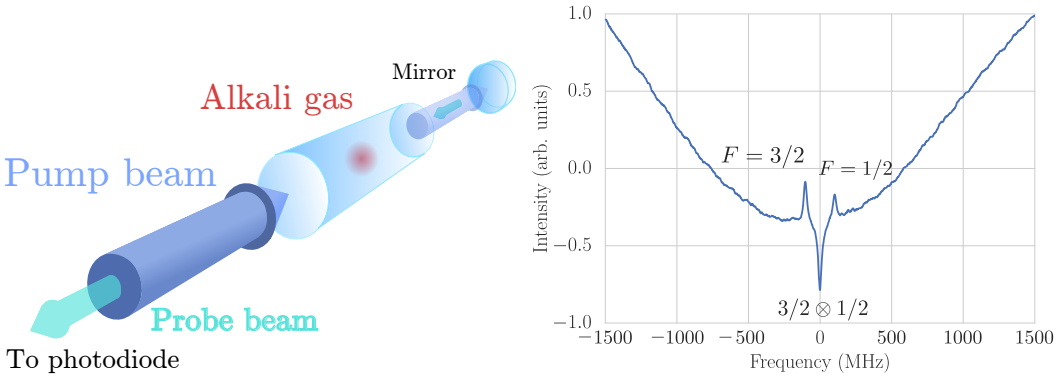
FIGURE 3.11: Scattering length a as a function of magnetic field strength for collisions between the three lowest hyperfine states of ^{6}Li . The states are labelled with 1, 2 and 3 with 1 being the state with the lowest energy (see Figure 2.3b). The vertical dotted lines indicate the centres of the Feshbach resonances. Note that the vertical scale changes at 600 G in order to show the behaviour at low and high field strengths. In this experiment only a 50/50 mixture of atoms in states 1 and 2 is loaded into the dipole trap. The atoms are then associated into molecules via the broad Feshbach resonance at 834 G. Figure adapted from [58].

potential which is named the entrance channel. All other potentials with threshold energies above the continuum energy of the entrance channel are called closed channels. Any with energies below the continuum energy are called open channels. Now provided a bound state in a closed channel potential sits at roughly the threshold energy of the entrance potential, it is possible to magnetically tune the molecular bound state energy into degeneracy with the energy of the two scattering atoms. Even just weak coupling between the two states (via the hyperfine interaction) can cause strong mixing between the two and turn free atoms into molecules. Figure 3.10 shows a diagram of channel description of Feshbach resonances.

The scattering length a is a single parameter which describes the interaction. At negative values of a the interaction is attractive while for positive values the atoms will repel each other. The response of the scattering length to an external magnetic field B in the presence of a Feshbach resonance is given by:

$$a(B) = a_{\mathrm{bg}}(1 - \frac{\Delta}{B - B_0}), \tag{3.39}$$

where B_0 indicates the resonance position, Δ is the resonance width and a_{bg} is the non-resonant s-wave scattering length [28]. The scattering length is plotted as a function of external magnetic field strength in Figure 3.11 for ^{6}Li 's lowest hyperfine levels. The zero-crossing of the scattering length at 534 G was used to calibrate our Feshbach coils [59, 60].



(a) A laser beam passes through an atomic vapour before being retro-reflected back through the vapour (though now much weaker due to absorption) and on to a photodiode where the intensity is measured.

(b) The intensity is measured as a function of the light frequency. The signal shows the familiar Doppler valley a peak at each real transition frequency and a crossover feature at precisely halfway between each pair of transition frequencies.

FIGURE 3.12: Saturated absorption spectroscopy.

3.6 Laser stabilisation

In order for any of the trapping and cooling techniques described in this chapter to work, the lasers involved must have narrow linewidths and be extremely stable. Fortunately, technology has reached a point where robust stable lasers with linewidths of less than 1 MHz are affordable and widely available. Most of the lasers used in this experiment are external-cavity diode lasers (ECDL) using high performance diodes purchased from Eagleyard Photonics. These lasers are then mounted to optical benches which rest on large pneumatic legs to minimise vibrations. Thermal fluctuations are kept to a minimum using peltier devices attached to the diode laser housing controlled by proportional-integral-derivative (PID) feedback loops. In addition to narrow-frequency and stable lasers, we also need to be able to precisely control their frequencies relative to an atom's available transitions. The following section explains how we produce highly frequency stabilised light of whatever frequency is required.

3.6.1 Saturated absorption spectroscopy

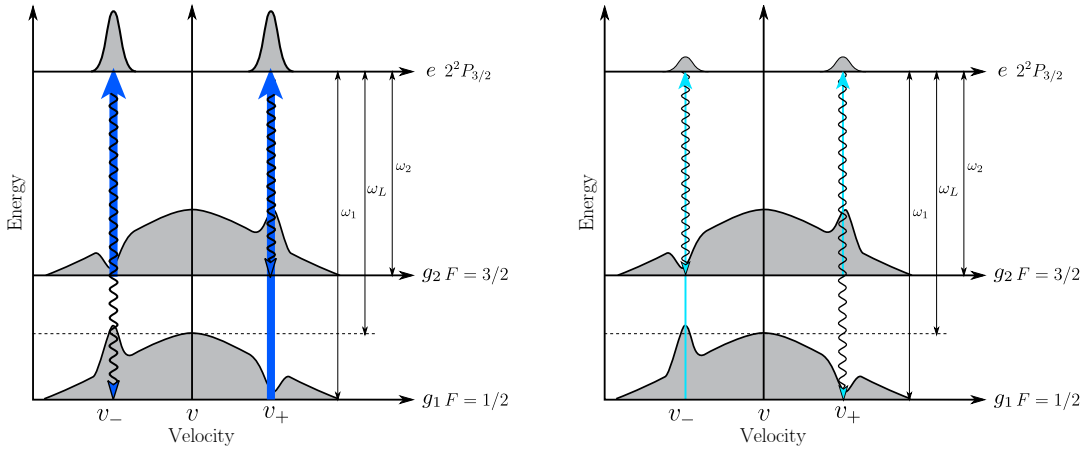
In order to lock our lasers to specific transitions between atomic levels we use saturated absorption spectroscopy (see Figure 3.12a and Section 2.1) to produce spectroscopic signals free from Doppler broadening limitations. A strong pump beam and weak probe beam of equal frequency ω_L propagate in opposite directions through a cell containing atomic vapour and the intensity of the probe beam is measured at a photodiode (Figure 3.12). If we assume a two level atom, then at any arbitrary non-resonant frequency ω_L, the pump and probe beams address two different velocity classes and so there is no interaction. Precisely on resonance however, the two beams address the *same* velocity class i.e. atoms travelling perpendicularly to the radiation. For this particular velocity class the strong pump beam heavily depopulates the ground state which in turn reduces the absorption of the probe beam. The result is a narrow peak that sits at precisely the resonance frequency at the bottom of the Doppler valley in the spectroscopic signal. The raw spectroscopy signal for the lithium D_2 line is shown in Figure 3.12b.

For caesium spectroscopy we pass the lasers through ampoules of caesium vapour kept at room temperature. Lithium on the other hand, has a much lower vapour pressure and so must be heated to $380\,^{\circ}\mathrm{C}$ in its own dedicated chamber. Balanced signals, with the Doppler valley subtracted, are shown in 3.14. When viewing Figure 3.14, it is helpful to also consult the level diagrams shown in Figures 2.1 and 2.2.

Crossover features

The explanation of saturated absorption spectroscopy given above assumes a two-level system. However, real atoms have complex multi-level structure which causes additional features in the spectroscopic signal. Midway between transitions that share an energy level are so-called crossover features which are either peaks or dips depending on whether it is the excited state or ground state the transitions have in common. On the lithium side of the experiment we use a spectroscopy cell with light resonant with the D_2 transition. The ground state population of lithium is split evenly across the hyperfine split $2^2S_{1/2}$ state and

because it has very closely spaced excited state hyperfine levels (4.4 MHz separation), the three levels can be considered to be a single state. Because of this, we observe a dip in the spectroscopic signal as displayed in Figure 3.12b.



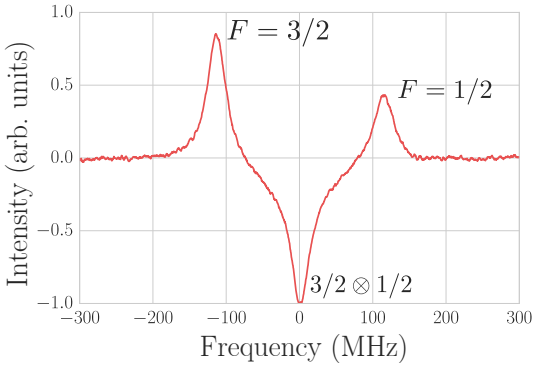
(a) A population-energy-velocity diagram for a lithium gas as the pump beam, at frequency ω_L midway between the two resonance frequencies, passes through the lithium vapour. The pump light excites two velocity classes v_+ and v_- via different transitions. This creates both a 'hole' and a 'lump' in the two ground state populations.

(b) Since the returning probe beam propagates in the opposite direction to the pump beam, it is resonant with the same transitions but for the opposite velocity classes. The probe beam hence sees an enhanced population in both of the states it excites leading to greater absorption.

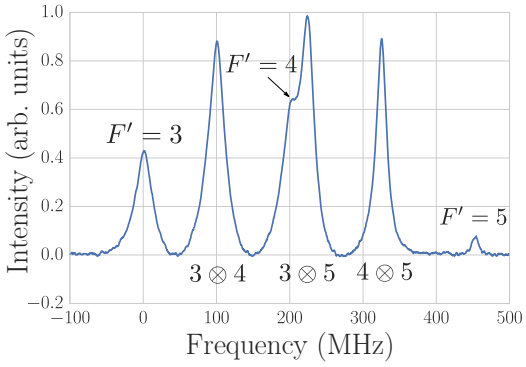
FIGURE 3.13: Physical explanation of the crossover phenomenon in saturated absorption spectroscopy.

To explain the feature it is helpful to break the problem up into two; the effect the pump beam has on the populations of the two ground states g_1 and g_2[3], and the effect this has on the probe beam. If ω_L is midway between the resonant frequencies of the two transitions, the pump beam will burn a hole in the population distributions $P_{g_1}(v)$ and $P_{g_2}(v)$ of each ground state in two different velocity classes. A hole in $P_{g_1}(v)$ for the velocity class for which $\omega_L + \frac{v}{k} = \omega_1$ and a hole in $P_{g_2}(v)$for the velocity class for which $\omega_L - \frac{v}{k} = \omega_2$. The probe beam on its journey in the reverse direction through the cell is resonant

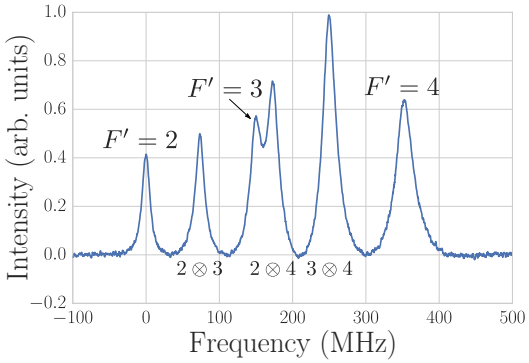
[3]This is sloppy language to say that there are two ground states but because there are no electric dipole transitions from the $F = 3/2$ to the $F = 1/2$ level it has become common among atomic physicists to call them both ground states.



(a) $2^2S_{1/2} \Rightarrow 2^2P_{3/2}$ hyperfine manifold.



(b) $F = 4 \Rightarrow 6^2P_{3/2}$ hyperfine manifold.



(c) $F = 3 \Rightarrow 6^2P_{3/2}$ hyperfine manifold.

FIGURE 3.14: Saturated absorption spectroscopy of the D_2 lines for both lithium and caesium (see Section 2.1 and Figures 2.1 and 2.2).

with the same two velocity classes but for the opposite transitions. The ground state populations of the velocity classes the probe beam is resonant with have been enhanced by the pump beam and so the probe beam is heavily absorbed.

When the energy level shared by the transitions is the ground state, as is the case for caesium spectroscopy, the interaction causes *reduced* absorption at $\omega_L = (\omega_1 + \omega_2)/2$ and so the crossover feature is a peak.

3.6.2 Locking to a transition

In order to lock to an atomic transition we modulate the current feeding the laser diode (typically 100 kHz) at a low amplitude while a piezo device attached to the grating of the ECDL modulates the laser frequency (much more slowly) across the atomic transition. The absorption signal measured by the photodiode

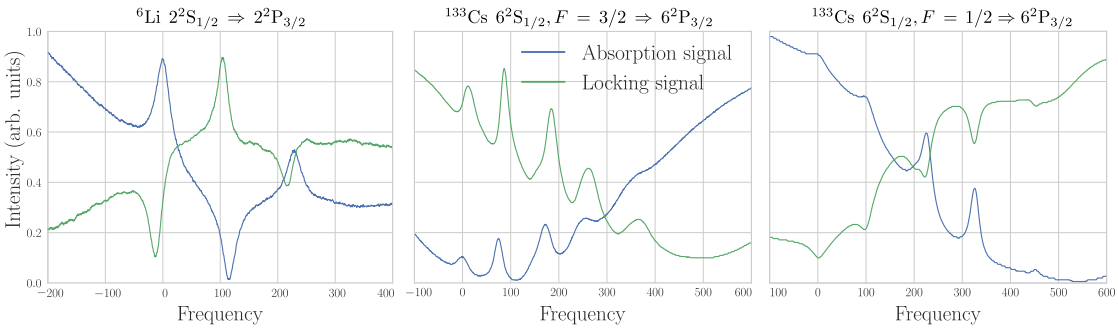


FIGURE 3.15: Locking signals obtained by the frequency modulation technique for each of the transitions we lock to in this experiment. The technique produces a signal with a zero-crossing at the absorption signal peaks which we then lock to the laser to using a PID controller. Although the supposed zero-crossings in the error signals plotted here are not all at the same level, once the piezo frequency scan is reduced in amplitude the signals do pass through zero.

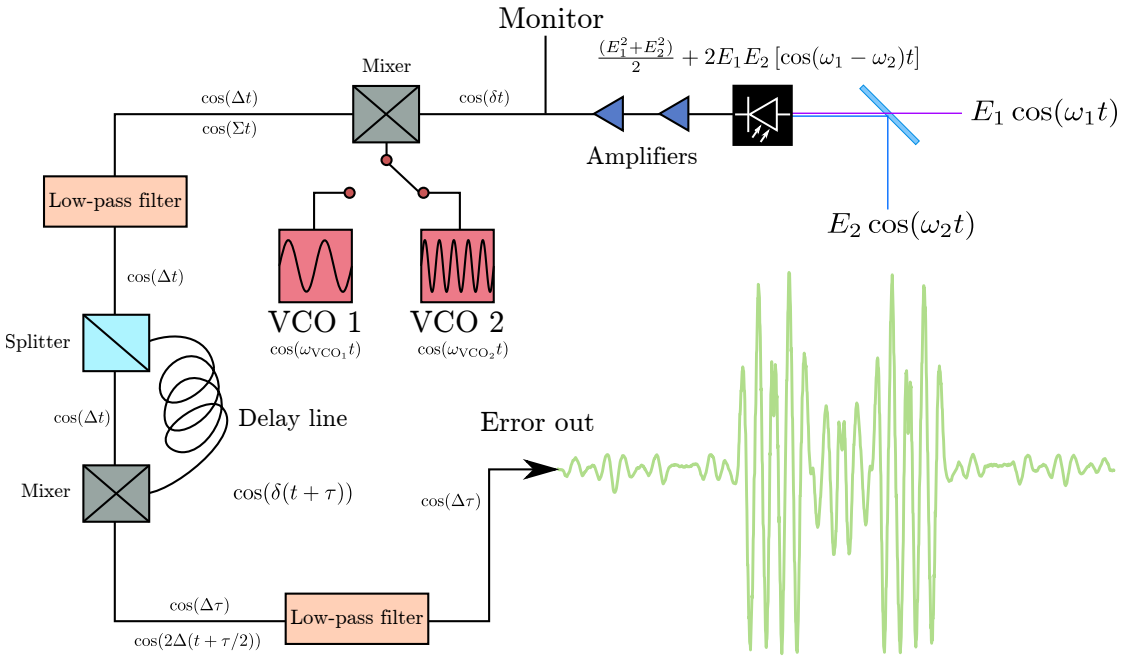
in the saturated absorption spectroscopy setup is then fed to a lock-in amplifier, an electronic amplifier than can pick out very small signals at precise frequencies. Inside the lock-in amplifier the absorption signal is mixed with the original current modulation signal (the $100\,\mathrm{kHz}$ oscillation) and then fed to a low-pass filter. What remains is a DC signal proportional to the derivative of the absorption signal obtained by saturated absorption spectroscopy. This means there are zero-crossings precisely at the absorption peaks which can be used as lock points for a PID controller. All of the signals obtained by this technique in this experiment are shown in Figure 3.15. This type of laser lock is robust against thermal drifts and low frequency vibrations.

3.6.3 Offset locking

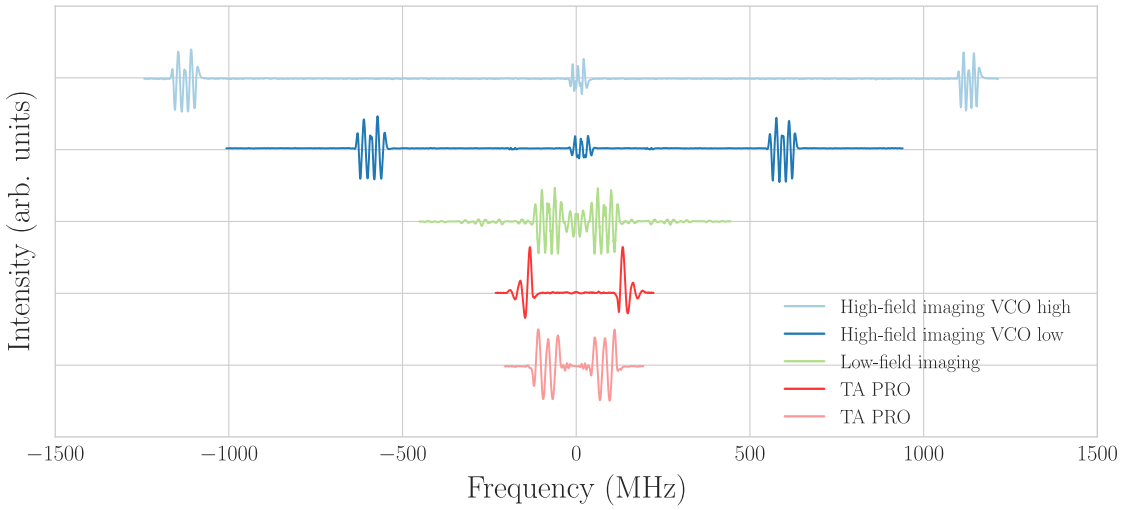
In order to tune our laser frequencies to specific detunings we use **offset locks**. Offset locks allow us dynamically adjust our laser frequencies wide frequency ranges. For instance, once locked our lithium imaging laser can be tuned over a range spanning $600\,\mathrm{MHz}$. The technique begins with overlapping the laser we want to offset lock with another highly stable reference laser which is locked to a known frequency using the techniques described above. The beams are overlapped at a photodiode which measures the intensity of the interfering beams. Figure 3.16a shows the evolution of the electronic signal produced by the photodiode. The measured intensity I_{tot} has components that vary with the

sum and difference of the angular frequencies of the two lasers (plus some DC components that can be ignored). The component that varies with the sum is far too fast for the photodiode to measure so it acts as a low-pass filter. What is left is a signal proportional to the cosine of the frequency difference $\cos(\delta t)$. At this point a voltage-controlled oscillator (VCO) mixes in a signal of angular frequency ω_{VCO} which, in a similar process to before, produces components proportional to both the sum and difference of the two oscillations ($\cos(\Sigma t)$ and $\cos(\Delta t)$). A subsequent low-pass filter removes the high frequency oscillation leaving only $\cos(\Delta t)$. The signal is then split into two and then recombined with one signal having travelled much further than the other. This mixes the signal $\cos(\Delta t)$ with $\cos(\Delta(t+\tau))$ where τ is the delay time cause by the longer path. The resulting signal has a component proportional to $\cos(\Delta\tau)$ and other unwanted higher frequency components which are removed by another low-pass filter. The result of all this signal analysis and manipulation is to produce the signal $\cos(\Delta\tau)$ which is not a function of time and depends only on the beat frequency Δ. This signal can then be used as an error signal for a PID controller hooked up to the laser current controller which can lock the laser at any of the error signal's zero crossings. By tuning the VCO control voltage, the beat frequency Δ can be manipulated which changes the position of the signal's zero-crossings. Thus, a laser locked to a zero-crossing can have its frequency tuned by translating the lock point via the VCO. In this way almost arbitrary laser frequencies can be achieved.

For this thesis two high-field imaging systems, one for each species, were designed and built based on offset locks for the purposes of probing clouds at large magnetic fields. Producing ultracold samples of $^6Li_2$ molecules necessarily requires the use of large magnetic fields in order to utilise the broad Feshbach resonance at $834\,\mathrm{G}$. Similarly, future production of heteronuclear diatomic $^6Li^{133}Cs$ molecules and homonuclear $^{133}Cs_2$ molecules will also require the use of magnetically tunable Feshbach resonances. As seen in Chapter 2, the magnetic field dependence of each magnetic substate of a degenerate hyperfine energy level is different. Thus, via the Zeeman effect, a magnetic field breaks the degeneracy and causes the sublevels to separate in energy. A knock-on effect of this is that transition frequencies between energy levels are also magnetic field dependent and doubly so since they depend on the Zeeman shifts of both



(a) Schematic of the offset lock electronics for the lithium imaging laser. This system generates appropriate laser frequencies for imaging at both low-field (VCO 1) and high-field (VCO 2).



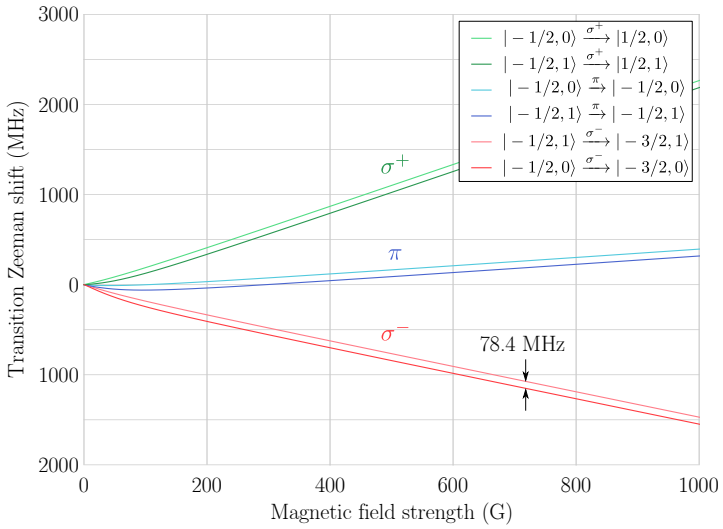
(b) Locking signals and ranges of the various offset locks implemented for the ^{6}Li laser system.

FIGURE 3.16

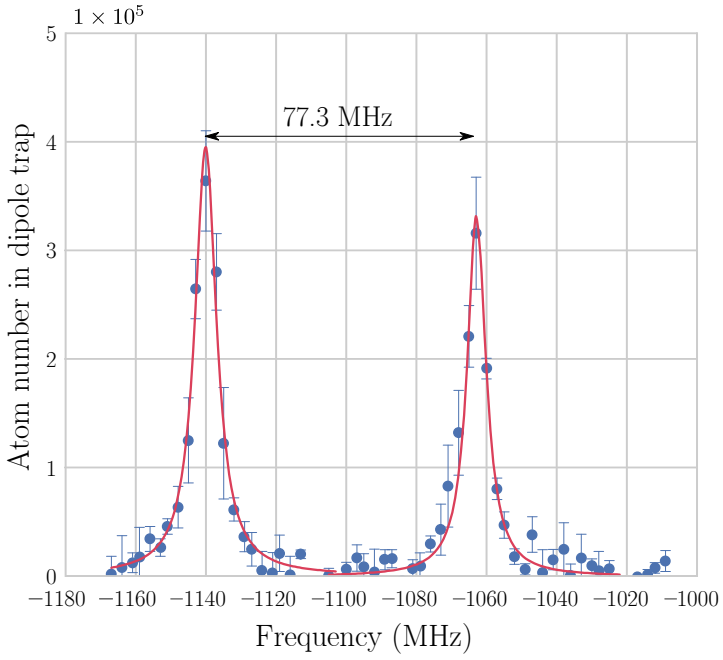
the ground and excited states. Thus these imaging systems have been designed to used VCOs with wide-spanning frequency ranges to compensate for the highly Zeeman shifted transition energies we encounter at large magnetic field strengths. The lithium imaging system boasts an impressive offset range of 0.6-$1.2\,\mathrm{GHz}$ (see Figure 3.16b) while the caesium high-field imaging box can reach upwards of $2\,\mathrm{GHz}$. Figure 3.17 shows the transitions used to image ^{6}Li molecules at high-field. The transitions used are the two lowest lying levels shown in Figure 2.3b.

Detecting Feshbach molecules using zero-field imaging is problematic because it requires that the strong magnetic field used to produce the molecules be rapidly switched off. This process is far from instantaneous due to eddy currents and self-induction and takes several tens of milliseconds. As the field strength decays, the atoms are swept across an enormous range of interaction strengths such that by the time the molecules are actually imaged the measured signal is unlikely to reflect the situation that occurred at the original field. The scattering length a as a function of magnetic field is plotted for ^{6}Li 's two lowest hyperfine states in Figure 3.11. Instead of switching the field off, the zero-crossing at $528\,\mathrm{G}$ can be used to reduce the switching time, but it does not remove the sweep. High-field imaging however, allows us to image the molecules immediately upon formation or after evaporation for accurate and reliable atom number and density measurements. Imaging lithium at high-field also allows us to take advantage of closed transitions for clearly defined, state selective atom number counting. When imaging lithium at zero-field the scattering cross-section is not well defined because a significant number of atoms drop into the $F = 1/2$ state which need to be repumped back up. The same light can also be used to spin polarise the sample by blowing out atoms in a specific m_J state.

Currently, the caesium laser setup only permits imaging at a single frequency, the reference laser frequency locked to the D_2 line $F' = 4 \otimes F' = 5$ crossover (see Figure 2.2 and Figure 3.14). This severely limits us for future mixture experiments which would make use of ^{6}Li-^{133}Cs Feshbach resonances at high magnetic field strengths to produce ^{6}Li^{133}Cs molecules. Although fully constructed, the caesium high-field imaging system is yet to be installed.



(a)



(b)

FIGURE 3.17: High-field imaging of lithium. (a) Available transitions for high-field imaging of $^6Li_2$ molecules and their Zeeman shifts as a function of magnetic field strength. The lithium atoms roughly equally populate the two lowest hyperfine states $|-1/2,0\rangle$ and $|-1/2,1\rangle$ (labelled $|m_J,m_I\rangle$) before they are associated into molecules. One of the two states is then imaged. (b) Lithium atoms in the dipole trap as a function of imaging laser frequency offset for a constant magnetic field of roughly 750 G.

Chapter 4

The ^{6}Li-^{133}Cs mixture experiment

The ^{6}Li-^{133}Cs experiment has the long-term goal of producing ultracold samples of fermionic ^{6}Li and cold ^{133}Cs . Most simply, gases with impurities can be studied by introducing a small amount of the other species to an ultra-cold sample. By use of magnetically tunable Feshbach Resonances, free lithium and caesium atoms can be associated to produce both hetero and homo-atomic molecules. Particularly exciting is the association of fermionic ^{6}Li atoms into bosonic $^{6}Li_2$ Feshbach molecules changing their quantum statistics altogether. Eventually we aim to produce fermionic ^{6}Li^{133}Cs molecules using Feshbach association combined with stimulated Raman passage.

Since the mixture experiment has already been covered in great detail, this chapter only covers modifications to the system and developments not found in the preceding theses [34, 35, 36].

4.1 Collimated dual-species oven

In October 2012 when the author joined the group, the Zeeman slower was a fully-functioning single-species slower for lithium. The slower comprised 9 concatenated solenoids (one disabled for better field matching) and a counter-propagating beam containing detuned cooling and repumping light. Lithium MOTs containing up to 1×10^8 atoms were routinely produced. In late 2014 the lithium oven and Zeeman slower was adapted into a lithium-caesium dual-species oven and Zeeman slower. Rather than tune the field gradient to a compromising profile for mediocre loading rates of each species, we opted to electronically switch between two well-optimised profiles. We were able to demonstrate high loading rates of 6×10^7 atoms/s for caesium and 1×10^8 atoms/s for lithium for rapid sequential MOT production. A full explanation of the old

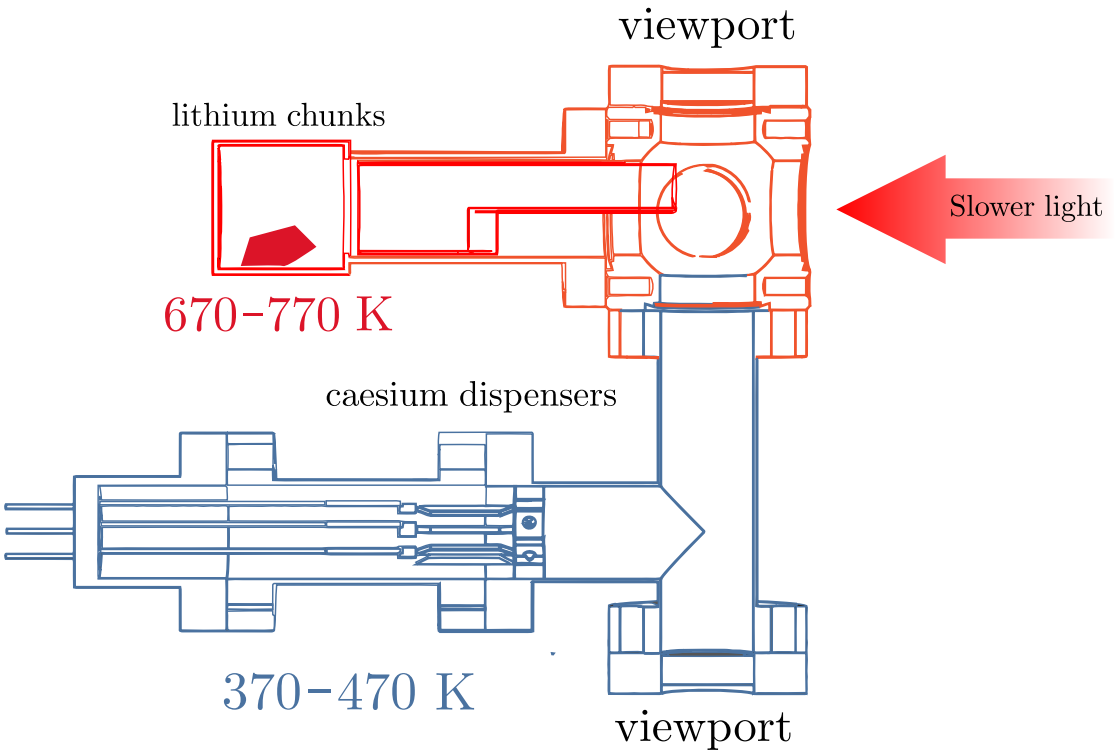


FIGURE 4.1: The old dual-species oven. Poor collimation meant a large wasted fraction of the emitted solid angle and led to the demise of the ion pump.

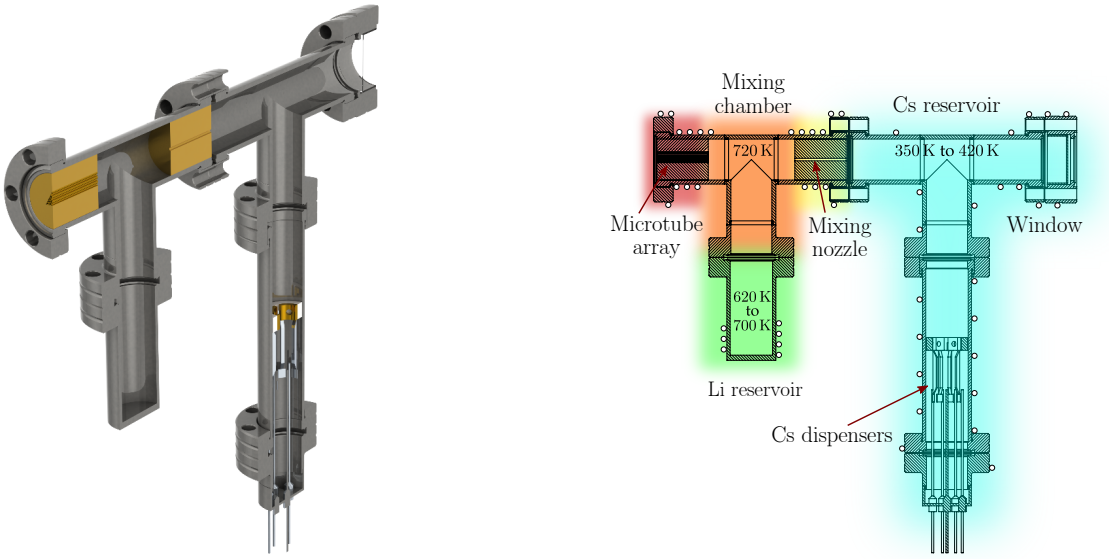
oven and Zeeman slower is given in [36] while a brief overview of the oven is given here.

The old oven design is shown in Figure 4.1. A lithium reservoir heated to roughly $700\,\mathrm{K}$ was connected to a caesium reservoir at approximately $420\,\mathrm{K}$. The lithium chamber was loaded with chunks of 95% ^{6}Li (Sigma-Aldritch) whereas the caesium chamber contained eight ^{133}Cs getters (SAES; model CS/NF/3. 9/12 FT10+10) powered via electrical feed-throughs. The chambers are connected via a CF16 cube and viewports were positioned for optical access in all four transverse directions (to the atomic beam path) for potential 2D cooling. A nozzle with a semi-circular cross-section slotted into the CF16 nipple of the lithium reservoir generated a collimated beam of lithium. The caesium beam was collimated by the entire inner diameter of the CF16 cube and connecting nipple.

The dual-species Zeeman slower and oven functioned well for just a few months before caesium loading was lost entirely (lithium functionality was preserved) and pressures in the oven chamber began to reach as high as $10^{-6}\,\mathrm{mbar}$.

A combination of caesium's high vapour pressure, high mass and a lack of collimation, lead to an atomic beam with a large amount of unusable flux that would eventually deplete the dispensers and coat the inside of the $50\,\mathrm{L/s}$ oven ion pump. The failure of the old atom source prompted work on a new, more rigorously planned, dual-species oven that would avoid the pitfalls of the first. The new dual-species oven would:

- produce highly collimated, overlapped beams of lithium and caesium,
- allow independent control of the atomic flux of each species, and
- produce beams of longitudinal velocity distributions that are well captured by the existing Zeeman slower.



(a) (b)

FIGURE 4.2: The new dual-species oven. (a) A high-quality render of the microtube oven. The microtube array, array holder, mixing nozzle and dispensers are coloured gold for better visibility. The ceramic ring to which the dispensers are attached is coloured white to highlight that they are non-conducting. (b) A labelled diagram of the oven showing the various regions which are heated independently.

4.1.1 Design and construction

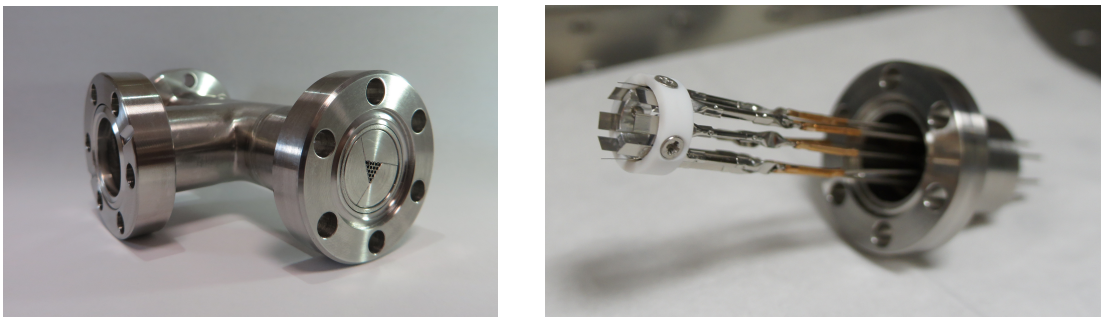
Typical single-species effusive ovens consist of a single heated chamber loaded with the substance in solid or liquid form combined with a beam forming aperture in one of the chamber walls. By varying the temperature of the oven, the pressure inside the volume can be controlled and so the atomic flux can be adjusted. However, if a dual-species atomic beam is required, unless the vapour pressures of the two elements of interest are very similar, simply loading an effusive oven with samples of both will generate a beam with two radically different atomic fluxes. In the case of ^{6}Li and ^{133}Cs , the two species' vapour pressures differ by over *eight* orders of magnitude such that at reasonable caesium fluxes the lithium flux would be too low and at reasonable lithium fluxes the caesium consumption rate would be preposterous.

To solve this problem we use reservoirs containing pure samples of each atomic species connected to a mixing chamber from which the atoms can escape

towards the experiment [61, 62, 63]. By adjusting the reservoir temperatures the throughputs of each species to the mixing chamber can be controlled. Since the throughput at each point in a gas flow system is constant, the reservoir temperatures also adjust the respective fluxes in the atomic beam. In this way, we can tune the oven to produce a two-species atomic beam that delivers roughly equal quantities of each component per unit time. To extend the lifetime of both the caesium source and our ion pump, we use a collimating microtube array which limits the amount of unusable flux produced.

The new dual-species oven is based on one given by Stan et al. [62] and comprises just two chambers: a rear caesium reservoir and a combined lithium reservoir/mixing chamber. The lithium reservoir was integrated with the mixing chamber out of necessity because the maximum temperature rating of the CF16 flanges ($720\,\mathrm{K}$) limits the pressure ratio that would be achievable between a lithium reservoir and the mixing chamber. For proper operation the pressure in the lithium reservoir should be several times larger than the pressure in the mixing chamber which is only achievable at higher temperatures. Eight ^{133}Cs dispensers (SAES Getters model CS/NF/3.9/12 FT10+10) in the caesium reservoir coat the surrounding walls which are then heated to produce a caesium gas. The caesium gas is conducted into the mixing chamber through a $20\,\mathrm{mm}$ long, $1\,\mathrm{mm}$ diameter mixing nozzle made of stainless steel. A $6\,\mathrm{g}$ chunk of ^{6}Li metal (Sigma Aldrich) sits at the bottom of the lithium reservoir which is heated to produce a lithium gas. The atoms in the mixing chamber then make their way towards the experiment collimated by an array of 15 microtubes each with a length of $20\,\mathrm{mm}$ and an inner diameter of $0.51\,\mathrm{mm}$.

The dual-species oven is predominantly constructed using a small number of standard 304L stainless steel CF16 vacuum components making it inexpensive and easy to modify. Annealed nickel gaskets are used at each flange connection except for the caesium window which is made of copper. This is because hot lithium gas is aggressive to copper gaskets and would eat away at them eventually causing a leak. The downside of using annealed nickel gaskets is that they are much tougher to compress which can wear down the knife edges of the flanges. Using 316L stainless steel components was briefly considered in order to slow down 'dulling' of the flange knife edges due to high temperatures and repeated use. However, since we are using microtubes, our lithium and caesium consumption rates are very slow meaning the oven will



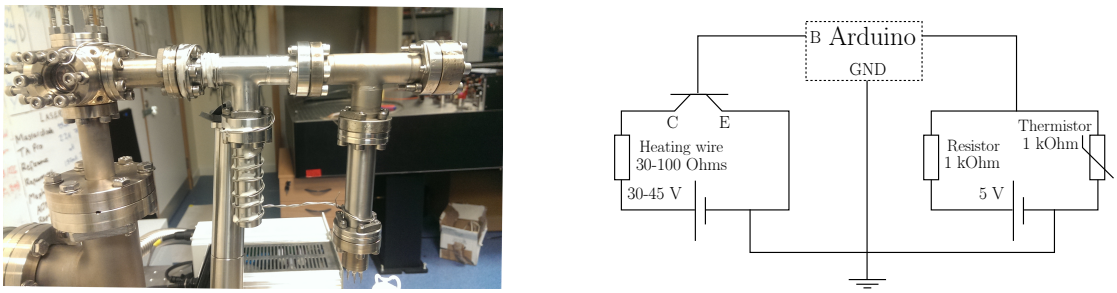
(a) (b)

FIGURE 4.3: The microtube array and the dispensers used in the new dual-species oven. (a) The microtube array sits inside the CF16 tee to minimise the number of potentially leaky CF16 flange connections. The microtubes prevent the oven from producing massive amounts of unuseful flux that would damage the ion pump. (b) Eight dispensers are connected in series using a custom-made ceramic ring.

not be frequently opened and resealed.

The microtube array and mixing nozzle sit inside a custom-made CF16 tee-piece (LewVac). The tee-piece is customised so that the welds connecting the two arms sit close to the junction rather than next to the flanges. This allows the microtube array and mixing nozzle to be slotted inside the tee, alleviating the need for dedicated vacuum flanges to hold them. In our experience CF16 vacuum parts are particularly prone to leaking so this approach was taken in order to minimise the number of CF16 flange connections.

The microtube array holder is made out of a stainless steel cylinder $20\,\mathrm{mm}$ long and an outer diameter as close as possible to the inner diameter of the CF16 tee. Three $11\,\mathrm{mm}$ deep slices were sawn into the cylinder (parallel to its axis) such that the cylinder was divided into four parts: three identical pieces and a triangular prism with a cross-sectional side-length of $5.4\,\mathrm{mm}$. The central prism was discarded and the microtubes were inserted into the void it left behind. The three pieces were then modified such that they could be screwed together. The microtubes are $20\,\mathrm{mm}$ long and have inner and outer diameters of $0.51\,\mathrm{mm}$ and $0.71\,\mathrm{mm}$ (Cooper's needles). The microtube array, holder and custom CF16 tee can all be seen in Figure 4.3. The mixing nozzle connecting the caesium reservoir and the mixing chamber was made by simply drilling an axial $1\,\mathrm{mm}$ through hole in an identical stainless steel cylinder. Combined with the viewport in the caesium chamber, the on-axis mixing nozzle allows us to check



(a) (b)

FIGURE 4.4: The dual-species oven and the temperature control circuit. (a) The oven as it was constructed aside from the main experiment for construction and characterisation. The heating wire is fixed in place using Thermoguss 2000. The cube on the far left has four viewports for analysis of the atomic beam. (b) The temperature control circuit. Only the lithium and caesium reservoir temperatures are PID controlled.

the system for clogging, perform longitudinal analysis on the atomic beam and eventually confirm proper alignment of our Zeeman slower beam.

The various oven sections are heated using external heating wires (ISOMIL-H 73,4V2A10 mineral insulated heating cable) connected to variable power supplies (an Electro-automatik EA-PS 2042-20B for lithium, and a Statron 2225 for caesium). An Arduino Uno running a rudimentary self-written PID control program regulates the current fed to the heating wires via bipolar junction transistors (TIP 120G, NPN type). These transistors were chosen for their ideal switching characteristics ($V_{\mathrm{BE(on)}} = 2.5V$) for use with Arduino Unos ($V_{\mathrm{out(max)}} = 5\,\mathrm{V}$) and their breakdown voltage of ($V_{\mathrm{CEO}} = 60\,\mathrm{V}$) which matches the maximum output voltage of the EA-PS 2042-20B. Under normal operation the lithium and caesium reservoir heating power supplies are set well below the breakdown voltage at $45\,\mathrm{V}$ and $35\,\mathrm{V}$ respectively. At maximum gate voltage ($5\,\mathrm{V}$) the lithium reservoir heating wire dissipates $60\,\mathrm{W}$ while the caesium heating wire dissipates $32\,\mathrm{W}$ (caesium requires less heating due to its higher vapour pressure). Under normal operating conditions the lithium reservoir is kept at $400\,^{\circ}\mathrm{C}$ while the caesium reservoir is heated to $150\,^{\circ}\mathrm{C}$.

Thermistors measure the temperatures of the lithium and caesium reservoirs as voltages which are then fed to the Arduino Uno as input variables for PID control. The error values are calculated ($V_{\mathrm{error}} = V_{\mathrm{set}} - V_{\mathrm{input}}$) and the power supplies are appropriately adjusted via the pulse-width modulated (PWM) output

pins of the Arduino Uno which are used to control the gate voltages of the transistors. Thermocouples are attached to the system next to each thermistor for absolute temperature readings.

Figure 4.4b shows the simple circuit diagram used for temperature control. The small hollow circles in Figure 4.2b show exactly how the heating wire was attached. The temperatures of the mixing nozzle and microtube array are not PID controlled and are instead directly heated using a high-voltage power supply. Precise temperature control of the channels is not necessary: we only require that the nozzle and microtube array are hotter than the rest of the system such that lithium and caesium do not condense inside them and clog them. The temperature of the two channels is typically maintained at $450\,^{\circ}\mathrm{C}$. The heating wires for the mixing nozzle and microtubes were cut, attached and insulated identically such that the two channels would be heated equally when powered in series. The heating wires were fixed in place using Thermoguss 2000 (Harold Patscheider Gmbh), a highly heat resistant ceramic adhesive. The chamber was insulated using a combination of aluminium foil and fibre glass insulation. In order to attach sufficient insulation without the various compartments coming into contact with each other, the fibre glass mesh was moderately compressed before application.

The mixing nozzle and microtube array dimensions were determined by optimising a simple model of the gas flow through the various chambers keeping several important criteria in mind. For optimal operation, the pressure ratio from the caesium reservoir to the mixing chamber should satisfy $P_{\mathrm{Cs,Res}} \gg P_{\mathrm{Cs,Mix}}$. In addition, the partial pressures of lithium and caesium in the mixing chamber should both satisfy $P_{\mathrm{Li,Mix}}, P_{\mathrm{Cs,Mix}} \gg P_{\mathrm{Exp}}$, where P_{Exp} is the pressure

TABLE 4.1: Available microtube dimensions from Cooper's Needles.

Gauge	Outer diameter (mm)	Inner diameter (mm)	N_{mt}
26	0.457	0.305	45
25	0.510	0.305	36
24	0.560	0.381	28
23	0.635	0.406	21
22	0.710	0.510	15

in the experiment. Within this regime the fluxes through the microtube array are entirely controlled by the temperatures of the reservoirs. For the microtube array to collimate effectively, both species need to operate within the molecular flow regime defined by $\lambda \geq d$ where d is the inner diameter of a microtube. Ideally the mean free path length should fall within $l > \lambda > d$ since in this range, where only a few collisions occur within the tube, the axial brightness I_0 is enhanced with only a small increase in the beam half-width [42]. In addition, the available equations of flow are only valid within the molecular flow regime. Although formulae for viscous flow exist, their application requires knowledge of the dynamic viscosities of gaseous ^{6}Li and ^{133}Cs which to date are not known.

The throughput of caesium, $Q_{\mathrm{Cs,Res}}$, from its respective reservoir into the mixing chamber is given by:

$$Q_{\mathrm{Cs,mn}} = C_{\mathrm{mn}}(P_{\mathrm{Cs,Res}} - P_{\mathrm{Cs,Mix}}) \approxeq C_{\mathrm{mn}} P_{\mathrm{Cs,Res}}, \tag{4.1}$$

where C_{mn} is the conductance of the mixing nozzle, $P_{\mathrm{Cs,Res}}$ is the pressure in the reservoir (taken to be the vapour pressure of caesium at the reservoir temperature T_{Cs}) and $P_{\mathrm{Cs,Mix}}$ is the partial pressure of caesium in the mixing chamber (see Section 3.1 for formulae regarding throughputs and conductances of tubes). The second term in equation 4.1 represents the backflow of caesium into the reservoir from the mixing chamber. The throughput of caesium through the microtube array towards the experiment is simply:

$$Q_{\mathrm{Cs,mta}} = N_{\mathrm{mt}} C_{\mathrm{mt}}(P_{\mathrm{Cs,Mix}} - P_{\mathrm{Cs,Exp}}) \approxeq N_{\mathrm{mt}} C_{\mathrm{mt}} P_{\mathrm{Cs,Mix}}, \tag{4.2}$$

where N_{mt} is the number of microtubes, C_{mt} is the conductance of a single microtube and $P_{\mathrm{Cs,Exp}}$ is the pressure in the experiment and is assumed to be zero. Since the throughput is a constant of the system we can equate equations 4.1 and 4.2:

$$Q_{\mathrm{Cs,mn}} = Q_{\mathrm{Cs,mta}} \approxeq C_{\mathrm{mn}} P_{\mathrm{Cs,Res}}, \tag{4.3}$$

so as mentioned before, the beam flux can controlled by the reservoir temperature.

The pressure of lithium in the mixing chamber $P_{\mathrm{Li,Mix}}$ is assumed to be the vapour pressure of lithium at the reservoir temperature T_{Li} and so we have a

similar equation for the lithium throughput:

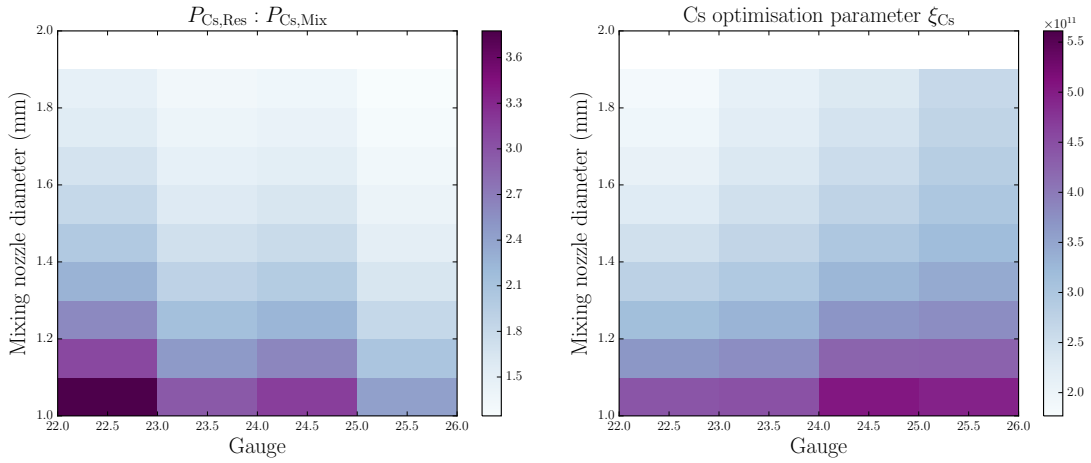
$$Q_{\mathrm{Li,mta}} = C_{\mathrm{mta}} P_{\mathrm{Li,Mix}} \approxeq C_{\mathrm{mta}} P_{\mathrm{Li,Res}}. \tag{4.4}$$

The mixing nozzle and microtube dimensions were optimised almost entirely with respect to the performance of the caesium reservoir. Since lithium is loaded directly into the mixing chamber, provided a negligible amount of lithium flows into the caesium reservoir, its beam properties do not depend on the mixing nozzle. For caesium however, we require that the pumping rate through the microtube array greatly exceeds that of the mixing nozzle such that a large pressure differential can be produced between the two chambers i.e. $P_{\mathrm{Cs,Res}} \gg P_{\mathrm{Cs,Mix}}$. Table 4.1 shows the microtube gauges we had at our disposal with their respective dimensions and number when fitted into the array holder. Figure 4.5a shows the pressure ratio between the two chambers as a function of mixing nozzle diameter and microtube gauge for typical operating temperatures of $T_{\mathrm{Li,Res}} = 650\,\mathrm{K}$, $T_{\mathrm{Cs,Res}} = 370\,\mathrm{K}$, $T_{\mathrm{Mix}} = 720\,\mathrm{K}$. Clearly, for optimal caesium reservoir performance we want to be in the bottom left of Figure 4.5a where the mixing nozzle is narrowest and the microtubes are widest. Wider microtubes come at the cost of collimation and a subsequent increase in unusable flux. To quantify how much collimation is sacrificed we define an optimisation parameter:

$$\xi_{\mathrm{Cs}} = \frac{I(0)^2}{NH^2}, \tag{4.5}$$

where $I(0)$ is the axial intensity, N is the total throughput and H is the beam half-width (FWHM). Figure 4.5b shows ξ_{Cs} as a function of mixing nozzle diameter and microtube gauge and tells us little is lost by using the lowest gauge microtubes.

Looking at Figure 4.5 one would expect even larger pressure ratios and optimisation parameters at mixing nozzle diameters below $1\,\mathrm{mm}$. However, the material hardness (stainless steel) and the availability of appropriate drill bits limited mixing nozzle diameter to >$1\,\mathrm{mm}$. Thus, the mixing nozzle diameter was determined to be $1\,\mathrm{mm}$ and the microtube array gauge was chosen to be 22 (see Table 4.1). The pressure ratio could have been improved by drilling diagonally through the stainless steel cylinder to produce a longer nozzle, but the utility of the on-axis nozzle was deemed too important to lose. Improved channel dimensions could also have been achieved by sliding a microtube with a



(a) (b)

FIGURE 4.5: a) Ratio of caesium's reservoir pressure $P_{\mathrm{Cs,Res}}$ to its partial pressure in the mixing chamber $P_{\mathrm{Cs,Mix}}$ as a function of mixing nozzle diameter and microtube gauge. Chamber temperatures are $T_{\mathrm{Li,Res}} = 650\,\mathrm{K}$, $T_{\mathrm{Cs,Res}} = 370\,\mathrm{K}$, $T_{\mathrm{Mix}} = 720\,\mathrm{K}$. (b) The caesium optimisation parameter ξ_{Cs} as a function of mixing nozzle diameter and microtube gauge. An optimal atomic beam is achieved when ξ_{Cs} is maximised. Each gauge has the number of microtubes have the number listed under Table 4.1. For optimal caesium reservoir operation (large pressure ratio) we want the mixing nozzle to be as narrow as possible and for the microtubes to be as wide as possible. From (b) one can see we can make this choice with at little cost to ξ_{Cs}.

$1\,\mathrm{mm}$ outer diameter through the constriction. This course of action, although clearly superior, was only not taken due to time restrictions.

With a ratio of only 3.77 between $P_{\mathrm{Cs,Res}}$ and $P_{\mathrm{Cs,Mix}}$, we can no longer use the approximation in equation 4.1. Instead, the partial pressure of caesium in the mixing chamber is given by:

$$P_{\mathrm{Cs,Mix}} = \frac{P_{\mathrm{Cs,Res}} C_{\mathrm{noz}}}{N_{\mathrm{mt}} C_{\mathrm{mt}} + C_{\mathrm{noz}}}. \tag{4.6}$$

The axial flux through a microtube with length l (mm) and inner diameter d (µm) was calculated for each species using [42]:

$$I(0) = \frac{4.60 \times 10^{13} d^2 p^{1/2} \mathrm{erf}(1.26 \times 10^{-2} \sigma l^{1/2} p^{1/2} / T^{1/2})}{\boldsymbol{\sigma} m^{1/2} l^{1/2}} \,\mathrm{atoms/sr/s}, \tag{4.7}$$

where p is the partial pressure in Pa, $\boldsymbol{\sigma}$ is the atomic diameter in picometres, T is the temperature in kelvin, m is the mass in kg, and

$$\mathrm{erf}(x) = \frac{2}{\pi^{1/2}} \int_0^x \exp(-x^2) dx. \tag{4.8}$$

The total flux for 15 microtubes was estimated by multiplying the result by 15. Rather than use the atomic diameter $\boldsymbol{\sigma}$, the radius of the interaction is estimated as $r_0 = \sqrt{\sigma/2\pi}$ where σ, the scatting cross-section, is found using the Massey-Mohr formula:

$$\sigma = 7.57 b_6^2(v_p), \tag{4.9}$$

where

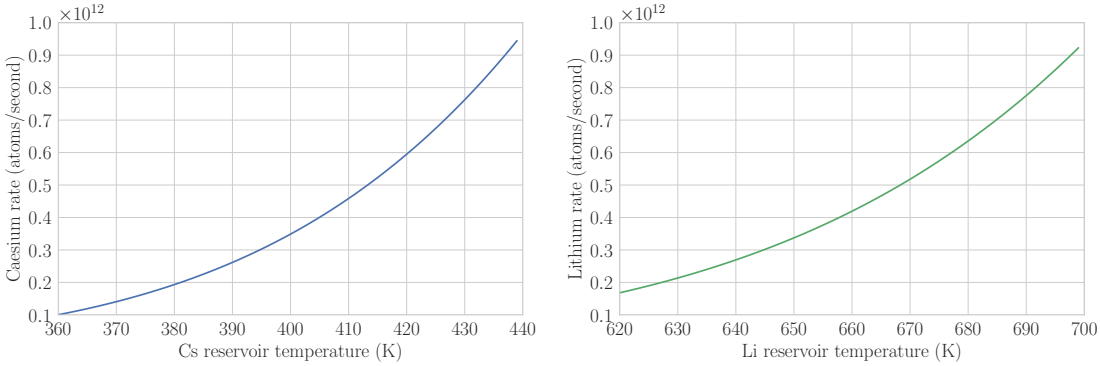
$$b_6(v_p) = 1.033 * \left(\frac{C_6}{\hbar v_p}\right)^{1/5}, \tag{4.10}$$

and v_p is the most probable velocity in the gas given by $v_p = \sqrt{2k_BT/m}$ [64, 65]. The Van der Waals dispersion coefficients C_6 and scattering cross-sections for lithium and caesium are shown in Table 4.2 for a background gas temperature of 720 K.

With the channel dimensions fixed, the optimum operating temperatures were determined by estimating the rate at which atoms would reach the MOTs. Figure 4.6 shows the rate at which lithium and caesium atoms are expected to reach their respective MOTs as a function of their reservoir temperatures. The rates were calculated using equation 4.7 assuming a mixing chamber temperature of 720 K and a MOT captur e area subtending a solid angle of 1.3×10^{-4} sr. For a balanced atomic beam a 200 °C offset between the two reservoirs is ideal

TABLE 4.2: Dispersion coefficients C_6 and scattering cross-sections for lithium and caesium. Coefficients are from Refs. [64, 65] and are given in atomic units ($e^2a_0^5$). The scattering cross-sections are calculated for a mixing chamber temperature of 700 K. The right hand atom is considered to be the background gas.

Atoms	C_6 (a.u.)	σ (Å)
^{6}Li -^{6}Li	1390	777
^{6}Li -^{133}Cs	3065	1979
^{133}Cs -^{6}Li	3065	1065
^{133}Cs -^{133}Cs	6330	2730



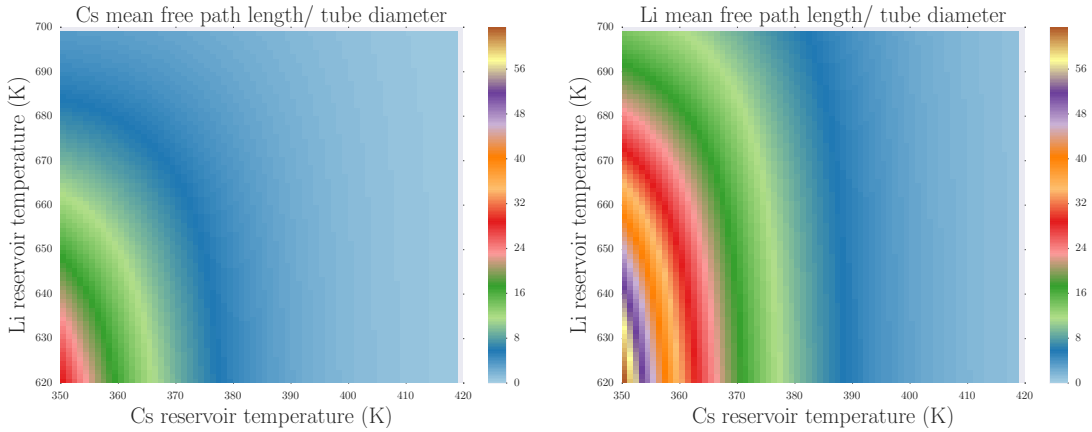
(a) (b)

FIGURE 4.6: Lithium and caesium delivery rates as a function of their respective reservoir temperatures at a fixed mixing chamber temperature of 720 K. By maintaining a constant temperature offset of 260 K between the lithium and caesium reservoirs we can achieve approximately equal atomic fluxes in the atomic beam.

(provided both reservoir temperatures are above the melting points of their respective species and neither reservoir temperature goes beyond those of the channels). When deciding what temperatures to operate the oven at, it is important to know how the mean free path lengths of the two species vary with the chamber temperatures. Provided $\lambda/d_{\mathrm{mtube}} \geq 1$ the oven will operate within the molecular flow regime and our equations for throughput and axial intensity will be valid (all of the equations printed in this section and Chapter 3 Section 1). This ratio is plotted in Figure 4.7 for both species which shows that for all of the temperatures of interest this requirement is well met.

The operating temperatures of the oven also need to fall within a parameter space that minimises the amount of lithium flowing backwards into the caesium chamber. Backflowing lithium is undesirable because the material does not form part of the beam and could potentially react or dissolve into the caesium coating the vacuum chamber walls causing a change in its vapour pressure. A backflow parameter ζ is defined as the mean free path length of lithium in a background of caesium at the caesium reservoir temperature divided by the mixing nozzle diameter. When $\zeta \approx 1$ a lithium atom only travels, on average, one nozzle diameter before making a collision. Thus to ensure suppression of backflow of lithium into the caesium reservoir we require that $\zeta \leq 1$ which is maintained provided the caesium reservoir temperature exceeds $400\,\mathrm{K}$.

In the combined lithium reservoir and mixing chamber, lithium and caesium



(a) (b)

FIGURE 4.7: Ratio between the mean free path length and the microtube diameter as a function of the reservoir temperatures for a constant mixing chamber temperature of 720 K. The ratio must be greater than one for the equations of flux to apply (See Chapter 3 and main body).

are allowed to mix and so reactions and alloy formation can potentially occur. In general, lithium's miscibility with the other alkali metals decreases down the group from sodium to caesium[66]. Above lithium's melting temperature of 180 °C two immiscibility phases are known to exist for the Li-K alloy [67]. Extrapolating from this result and lithium's propensity to separate into two liquids, we can expect that at the operating temperature of the lithium reservoir ($T_{\mathrm{Li}} = 650\,\mathrm{K}$) the ambient caesium gas will have little effect on the liquid lithium sitting at the bottom of the chamber.

With all of these factors taken into account, we can see that optimal reservoir temperatures are $T_{\mathrm{Li}} = 700\,\mathrm{K}$ and $T_{\mathrm{Cs}} = 410\,\mathrm{K}$. At these temperatures we can expect axial fluxes of $I_{\mathrm{Li}}(0) = 1 \times 10^{14}\,\mathrm{atoms/s/sr}$ and $I_{\mathrm{Cs}}(0) = 1 \times 10^{15}\,\mathrm{atoms/s/sr}$.

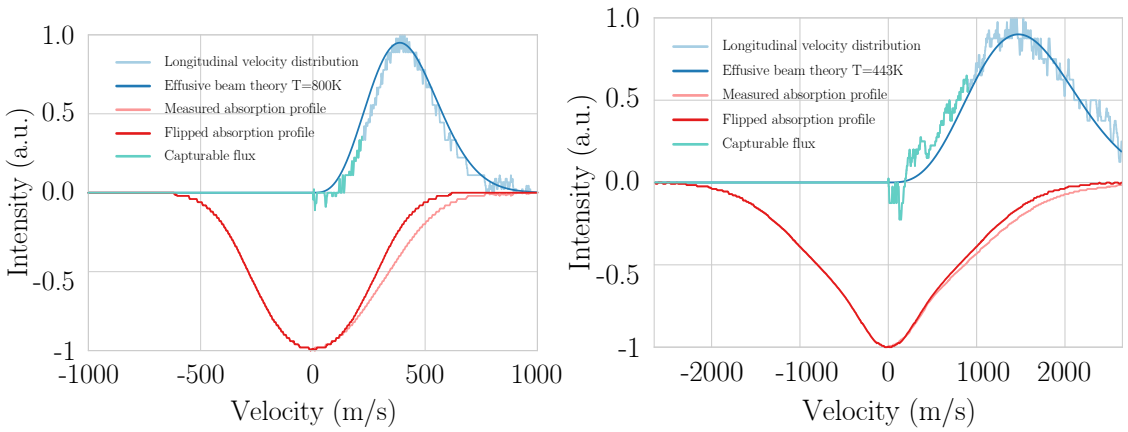


FIGURE 4.8: Longitudinal spectroscopy of the dual-species oven. The absorption profiles shown are averages of 64 measurements. (a) Results for caesium. (b) Results for lithium. The temperatures used for this experiment are given in Table 4.3.

4.1.2 Characterisation

A measurement of the longitudinal velocity distributions was made by performing single-pass absorption spectroscopy through the microtube array and the rear window (Figure 4.8). In turn, for each species we sent a powerful and narrow laser beam tuned to the D2 line longitudinally through the entire oven and measured its intensity on a photodiode after being attenuated by the hot gas. For caesium we used a beam with a $1/e^2$ radius of $1.3\,\mathrm{mm}$, while for lithium we used a beam with a $1/e^2$ radius of $0.83\,\mathrm{mm}$. The intensity of the beam was measured as the frequency of the interrogating beam was tuned across the

TABLE 4.3: The temperatures of the various oven chambers during the longitudinal absorption spectroscopy experiments for each species. The final column shows the theoretically predicted axial intensity for each species of interest during the experiment.

Exp.	$T_{\mathrm{Li,Res}}$ (K)	$T_{\mathrm{Cs,Res}}$ (K)	T_{Mix} (K)	T_{mta} (K)	$I(0)$ (atoms/s/sr)
^{6}Li	604	443	729	623	2×10^{13}
^{133}Cs	430	449	407	497	4.9×10^{14}

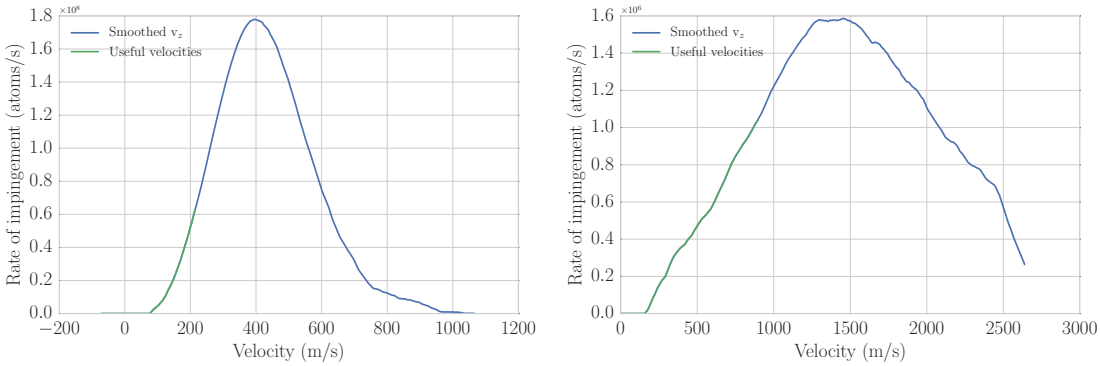
transition using a piezoelectric device inside the laser head. The frequency was tuned over an extreme range so to encompass the entire Doppler valley for post-analysis. However, because of the high optical depth of the gas in the oven the beam intensity had to be much greater than I_{sat} in order for the Doppler valley to not bottom out. This invalidates the results from this experiment somewhat since the intensity of the beam was a function of the travel distance, however the predicted emissivities are reasonable and so can be treated as a rough estimate. In addition, the excited state (ground state for lithium) splittings were considered to be small with respect to the Doppler and pressure broadening for this analysis. For lithium, this approximation is suitable since the total width of the Doppler valley is on the order of several GHz whereas the ground state hyperfine splitting is just $228\,\mathrm{MHz}$. For caesium however, the hyperfine levels of the line are maximally split by about $600\,\mathrm{MHz}$ compared to a $1\,\mathrm{GHz}$ wide absorption signal.

Because the simple single-pass absorption spectroscopy was conducted along the longitudinal axis of the oven, the atomic beam, channel and oven velocity distributions were all measured simultaneously. To simplify the analysis, the channel contributions are ignored. Provided $\zeta \leq 1$ we can assume negligible backflow of lithium into the caesium reservoir and so for lithium only the atomic beam and mixing chamber velocity distributions will manifest themselves. For caesium, two symmetric oven velocity distributions are measured, one for the reservoir and one for the mixing chamber, along with the atomic beam velocity distribution. Table 4.3 shows the temperatures of the various oven sections for both experiments. The measured Doppler valleys are shown in light red in Figure 4.8 with the x-axis converted into a velocity using $v = c\delta/\omega_0$ [39]. Because atoms travelling in the opposite direction to the atomic beam by definition cannot be part of the beam, we can assume that the measured spectroscopic signal at negative velocities is associated only with the oven/ovens. On the other hand, at positive velocities, the signal has contributions from both the oven/ovens and the beam. To obtain the beam distributions on their own, the oven-only distribution is assumed to be symmetric and is subtracted from the total absorption signal. The results of this data manipulation are shown in light blue in Figure 4.8. The results have been fitted with 1D Maxwell Boltzmann distributions for an effusive beam (dark blue) which differ from distributions for a gas only by an extra factor of v since atoms with faster velocities than the mean

leave an oven preferentially. The cyan lines represent the atoms capturable by our Zeeman slower. The lithium absorption profile is particularly Lorentzian which can be attributed to pressure broadening. The caesium data is comparably much more Gaussian.

The temperatures predicted by the fits vary considerably from the mixture chamber temperature in both experiments. For lithium we could understand the reduced temperature as a result of significant cooling from the large amount of caesium flooding in from its respective reservoir. For caesium however, we expect a temperature of at most the microtube array temperature of $497\,\mathrm{K}$. Instead, a temperature of $800\,\mathrm{K}$ is required to fit the resultant atomic beam velocity distribution. Since the mixing nozzle is $20\,\mathrm{mm}$ long, just as long as the interrogated region of the mixing chamber, and should have an average density between that of the caesium reservoir and the mixing chamber, the mixing nozzle contribution could be too large to ignore. However, if the nozzle were to contribute to the absorption profile, its effect would be to enhance the absorption at positive velocities (the atoms in the tube have a positive mean velocity) and to lower the most probable velocity. Hence the issue is more likely to stem from the fact that multiple excited states with significant frequency splittings have been addressed which generate an asymmetric absorption profile to begin with.

Assuming the measured signals are correct however, we can make an estimate for the rate at which capturable atoms reach the MOT. Assuming the MOT capture area is $A = \pi(5\,\mathrm{mm})^2$ and given that the oven (once it is installed) will be $0.78\,\mathrm{m}$ from the centre of the science chamber, the MOT subtends a solid angle of $\Omega = 1.3 \times 10^{-4}\,\mathrm{sr}$. Combining this with our estimates for the axial intensities from the previous subsection and the measured longitudinal velocity distributions we obtain the plots given in Figure 4.9. For this analysis the velocity distribution were smoothed over 150 points (Figure 4.8 shows the raw data). The highlighted green velocity tails indicate the velocities capturable by the slower. Assuming the slower captures 100% of the atoms under the capture speed we obtain estimates for the rate of useful impingement. These are $3.3 \times 10^9\,\mathrm{atoms/s}$ and $3.9 \times 10^8\,\mathrm{atoms/s}$ for caesium and lithium respectively. Considering the lithium MOT loading rate is currently $1 \times 10^8\,\mathrm{atoms/s}$, these estimations are reasonable [36]. It was a genuine concern that the microtubes might limit the axial fluxes too much such that the MOT loading rates would be harmed. This result



(a) (b)

FIGURE 4.9: Smoothed longitudinal velocity distributions from Figure 4.8 scaled such that the total number of atoms equals the number expected to reach the MOT for the chamber temperatures listed in Table 4.3. (a) The rate at which caesium atoms reach the MOT. (b) The rate at which lithium atoms reach the MOT. The highlighted parts (green) of the velocity tails indicate the atoms travelling slower than the Zeeman slower capture velocities for each species ($215\,\mathrm{m\,s^{-1}}$ for caesium and $900\,\mathrm{m\,s^{-1}}$ for lithium). Integrating under the green curves we obtain total useful rates $3.3 \times 10^9\,\mathrm{atoms/s}$ and $3.9 \times 10^8\,\mathrm{atoms/s}$ for caesium and lithium respectively.

therefore give us confidence moving forward with installing the dual-species oven.

The angular distribution of the oven was measured using transverse fluorescence spectroscopy. The transverse optical depth of an atomic beam is far too low for absorptive spectroscopic techniques to work. For caesium a $0.16\,\mathrm{mW}$ beam with a $1/e^2$ radius of $1.3\,\mathrm{mm}$ was used, while for lithium we used a $0.67\,\mathrm{mW}$ beam with a $1/e^2$ radius of $0.83\,\mathrm{mm}$. The beam was aligned perpendicularly by tuning the probe beam exactly on resonance and angling the beam such that the fluorescence was maximal directly in front of the microtube

TABLE 4.4: Temperatures of the various oven chambers for the transverse fluorescence measurements.

Atoms	$T_{\mathrm{Li,Res}}$ (K)	$T_{\mathrm{Cs,Res}}$ (K)	T_{Mix} (K)	T_{mta} (K)
lithium	643	391	804	804
caesium	590	407	761	761

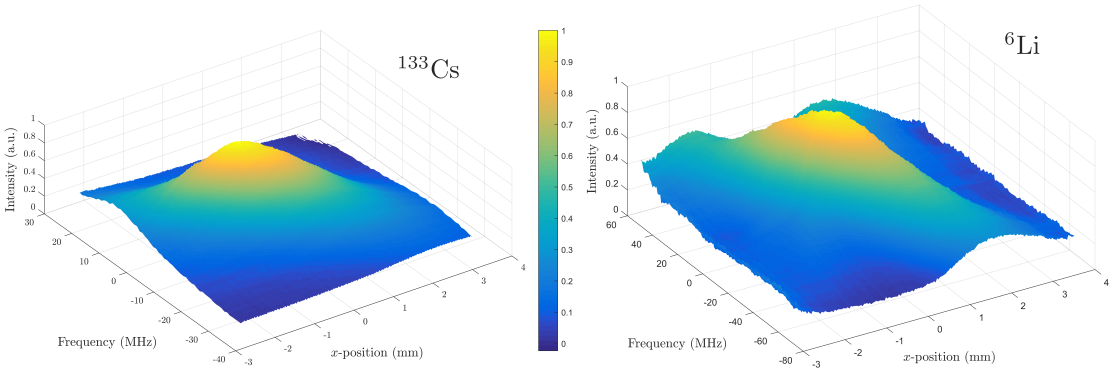
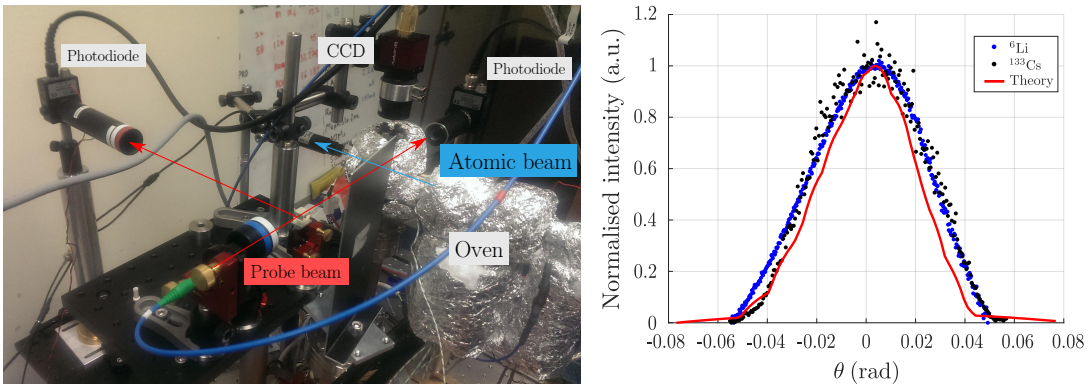


FIGURE 4.10: Density vs position vs frequency plots of the emission from the microtube array.

array. Images of the fluorescence were taken from above through a viewport using a charge-coupled device (CCD) camera (AVT Guppy F038-B) at a range of different laser detunings at a distance of $l = 65\,\mathrm{mm}$ from the microtube array. The temperatures of the oven parts are given in Table 4.4. Surface plots of the fluorescence intensity as a function of space and frequency are shown in Figure 4.10. For caesium the frequencies plotted are expressed relative to the $6^2\mathrm{S}_{1/2}, F = 4 \Rightarrow 6^2\mathrm{P}_{3/2}, F = 5$ transition. For the lithium plot they are given relative to $2^2\mathrm{S}_{1/2}, F = 3/2 \Rightarrow 2^2\mathrm{P}_{3/2}$. By integrating across all the frequencies we obtain an intensity distribution as a function of the x-position which is converted into an angular distribution $f(\theta)$ using $f(\theta) = x/l$. The distributions $f_{\mathrm{Li}}(\theta)$ and $f_{\mathrm{Cs}}(\theta)$ are plotted in Figure 4.11b with a theoretical prediction (red line) obtained using Equations 3.6 and 3.7. The theoretical curve is obtained by calculating the distribution for a single tube and summing the contributions from all the tubes taking into account their spatial distribution shown in Figure 4.12a. The results show good agreement with the theory. Figure 4.12b shows the deposition on the front facing window which has a radius of approximately $5\,\mathrm{mm}$. Since the window is $100\,\mathrm{mm}$ away from the microtube array we have a maximum spread of $\theta = \arcsin(5/100) = 0.05\,\mathrm{rad}$ which is in good agreement with what is shown in Figure 4.12. The fact that the distribution is more or less identical for both species is expected because the mean free path lengths of the two species become very similar at the investigated temperatures.



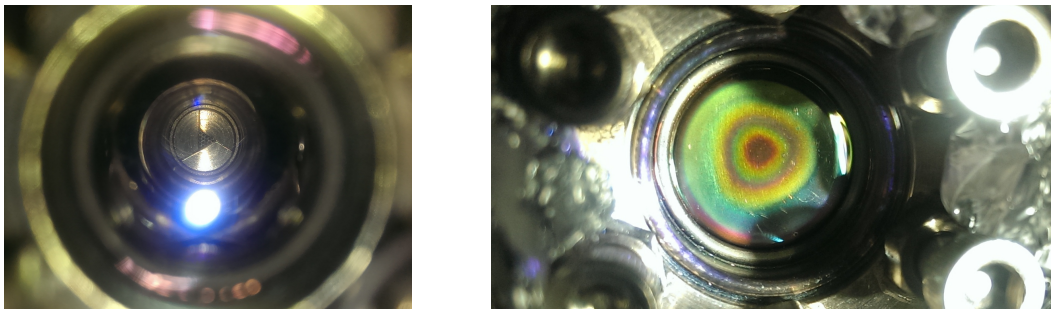
(a) (b)

FIGURE 4.11: (a) The fluorescence experimental setup. (b) The measured angular distribution of the dual-species atomic beam. The red line is a fit using Equations 3.6 and 3.7 taking into account the number of tubes and their spatial distribution shown in (a). The theoretical prediction for the two species was too similar to be visible on the plot so only one line is shown.

4.2 The $^6Li_2$ molecular BEC

The ^{6}Li-^{133}Cs mixture experiment is capable of routinely producing ultracold $^6Li_2$ molecular Bose-Einstein condensates (mBEC). A lithium MOT is loaded from our Zeeman slower which subsequently loads a crossed $1064\,\mathrm{nm}$ $100\,\mathrm{W}$ optical dipole trap. Utilising the broad ^{6}Li Feshbach resonance situated at $834\,\mathrm{G}$ we associate the atoms into $^6Li_2$ molecules before a phase transition in a diffuse gas of fermionic ^{6}Li to produce a $^6Li_2$ molecular Bose-Einstein Condensate of up to 1×10^4 atoms. Although only a brief overview of the experiment is given here, a more detailed description can be found in the theses [34, 35, 36].

The experimental sequence begins with loading a ^{6}Li magneto-optical trap (MOT) operating on the D_2 $2^2S_{1/2} \Rightarrow 2^2P_{3/2}$ optical transitions. We typically load about 2×10^8 atoms (See Figure 4.13) at a loading rate of $7 \times 10^7\,\mathrm{atoms/s}$ from our Zeeman slower. The MOT light configuration consists of three mutually orthogonal retro-reflected beams each with a $1/e^2$ radius of about $12\,\mathrm{mm}$, and a peak intensity of about $3.5I_{\mathrm{sat}}$, where $I_{\mathrm{sat}} = 2.54\,\mathrm{mW\,cm^{-1}}$ is the saturation intensity of the D_2 transition [**Gehm**]. The retro-reflected beams are slightly focused to compensate for the shadows cast by the MOT. Each beam consists of 'cooling' light resonant on the $2^2S_{1/2}, F = 3/2 \Rightarrow 2^2P_{3/2}, F' = 5/2$ transition and



(a) (b)

FIGURE 4.12: (a) The microtube array as seen from the front. (b) The coated window after operation for the first time. The orientation of the microtube array can be seen in the final distribution on the window.

'repumping' light on the $2^2S_{1/2}, F = 1/2 \Rightarrow 2^2P_{3/2}, F' = 3/2$ transition[1]. There is typically $1.25\times$ more cooling light than repumping light. For the MOT loading stage the cooling and repumping beams are equally detuned from the $2^2P_{3/2}, F'$ state by $-40\,\mathrm{MHz}$ (-6.8Γ). With this configuration the atoms are trapped at about $2\,\mathrm{mK}$.

At this point the dipole trap is turned on and the MOT is then cooled and compressed for optimal loading by simultaneously ramping down the beam

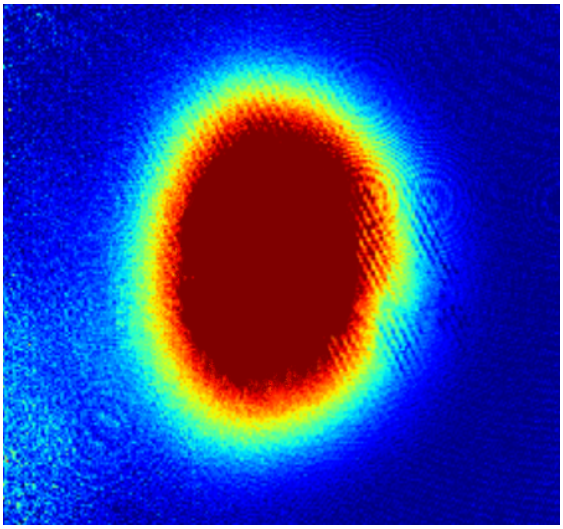


FIGURE 4.13: A lithium MOT containing 2×10^8 atoms

[1]Cooling and repumping are written in inverted commas because lithium's unresolved excited states (total separation of $4.4\,\mathrm{MHz}$) mean the two beams function equally as cooler and repumper.

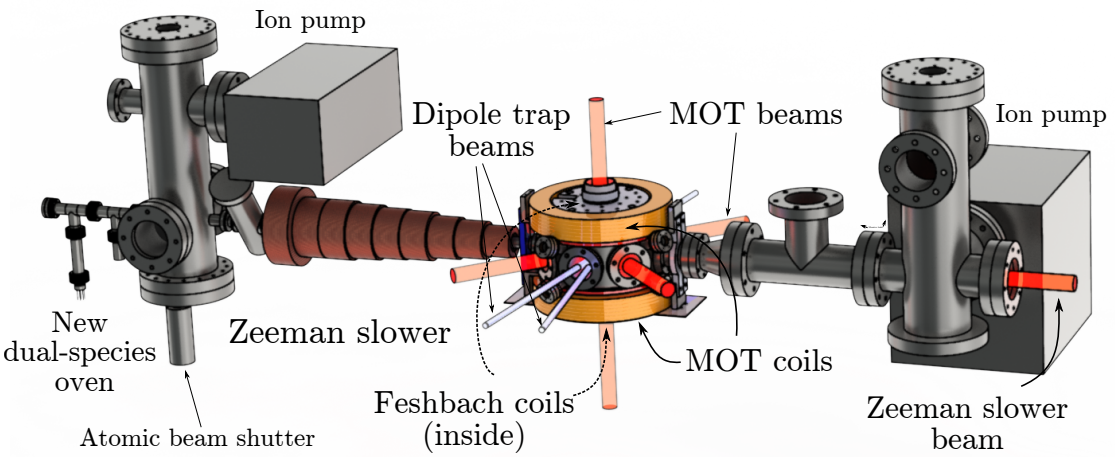


FIGURE 4.14: The lithium BEC experimental setup.

powers and decreasing the detuning while keeping the magnetic field constant. The powers are linearly dissipated until they are completely extinguished, while the detuning is reduced to $0.8\,\mathrm{MHz}$ $(1/7\Gamma)$ which is slightly below the theoretical optimum for optical molasses (Section 3.3). With this step the atoms are cooled to $600\,\mu\mathrm{K}$ in $25\,\mathrm{ms}$ with 90% of the atoms retained.

At the end of compression both the magnetic field and the beams are switched off and $\sim 1 \times 10^6\,\mathrm{atoms/s}$ are loaded into a crossed $100\,\mathrm{W}$ optical dipole trap. The dipole trap laser is focused down to a waist radius of $80\,\mu\mathrm{m}$ at the centre of the spherical octagon and reflected back in after coming out the other side in order to produce an extremely deep trap. The angle between the beams is small, approximately $13.6\,^\circ\mathrm{C}$, so the trap is highly cigar shaped. At full power $(100\,\mathrm{W})$ the trap is $\approx 1.2\,\mathrm{mK}$ deep and the atomic density is on the order of $1 \times 10^{12}\,\mathrm{cm}^{-3}$ (see the thesis of Dr. Asaf Paris-Mandoki [36] for an in-depth analysis of the dipole trap). While the dipole trap is loading, we apply a large magnetic field of $800\,\mathrm{G}$ to drive molecule formation by tuning the scattering length to large positive values just below the Feshbach resonance at $834\,\mathrm{G}$ (see Section 3.5.2). At this field $^6\mathrm{Li}_2$ Feshbach molecules are formed by three-body collisions [68, 69]. The dipole trap is held at $100\,\mathrm{W}$ for one second of plain evaporation before being ramped down gradually in multiple forced evaporation steps as shown in Figure 4.15. At the end of the final evaporation ramp we are left with $1 \times 10^5\,\mathrm{atoms}$ with a significant BEC fraction.

A significant improvement to the experiment made during the time of this

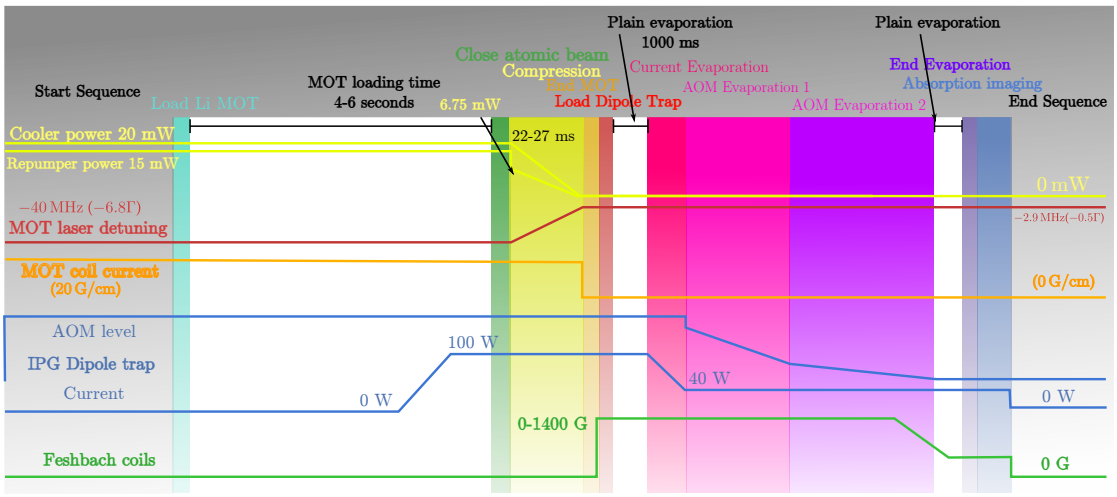


FIGURE 4.15: Diagram of the Mixture experiment.

thesis is the total atom number loaded into the dipole trap. Through rigorous optimisation routines the total atom number has been dramatically increased from 6×10^5 to 2×10^6 as demonstrated in Figure 4.18a. Considerable work was performed in order to obtain this important advance. Dipole trap loading is a highly complex process which depends on a multitude of variables [70]. The most important variables to tune are: cooler and repumper beam alignments, radii, polarisations, powers and detunings; field gradient; offset field strength; Feshbach field strength; source strength; loading time; compression duration; dipole trap beam position, power, shape, crossing and polarisation. For this reason a full multi-dimensional analysis is not possible and so optimisation of the dipole trap is a time-consuming iterative process in which each parameter is optimised individually one after the other. For some pairs of parameters a two-dimensional analysis can be conducted, but most optimisation is performed on a single variable at a time. After many circuits the system is well optimised although we can never be sure that we are not just in a local minimum.

Because an equal mixture of atoms in the $F = 1/2, m_F = 1/2$ and $F = 1/2, m_F = -1/2$ states are trapped, and the atoms are imaged at high field, only half of the trapped atom number is measured in Figure 4.18a. With such a huge boost to the initial atom number, evaporation to degeneracy is now performed more easily.

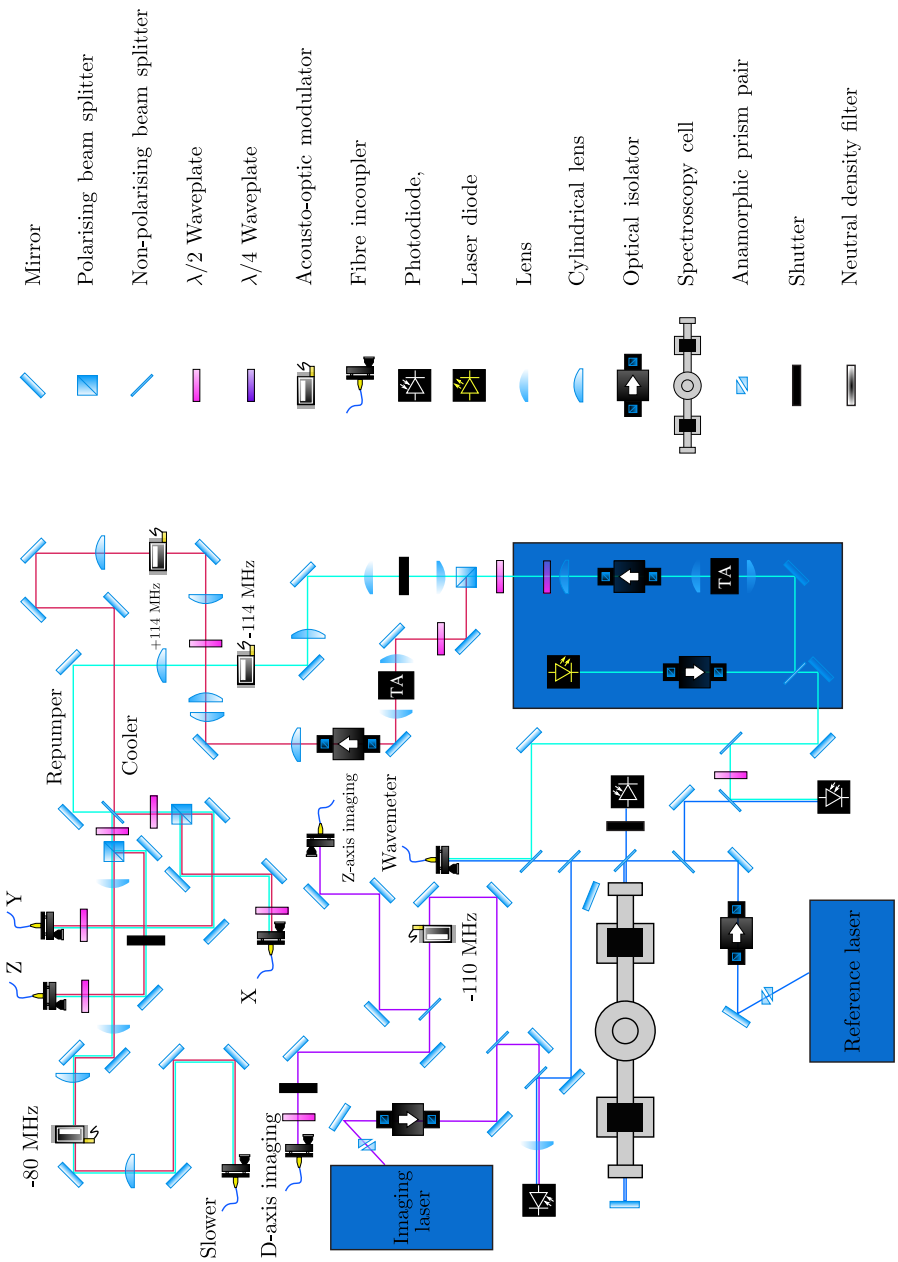


FIGURE 4.16: Lithium optical table setup.

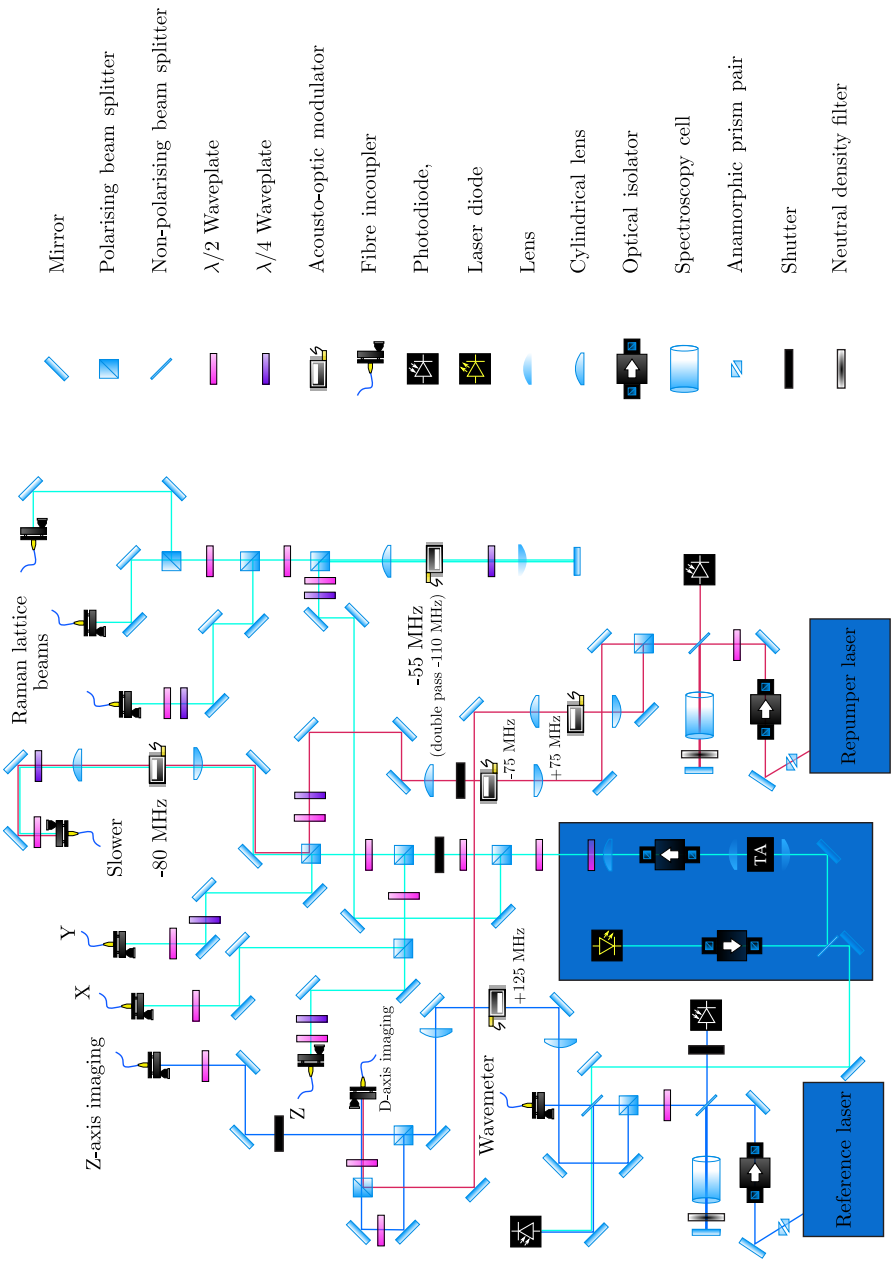


FIGURE 4.17: Caesium optical table setup.

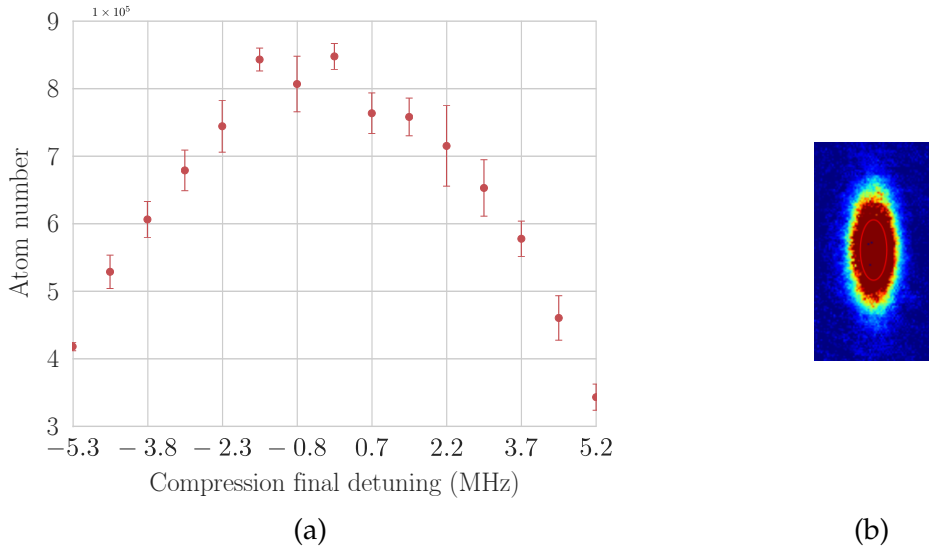


FIGURE 4.18: The lithium dipole trap. (a) The lithium dipole trap atom number as a function of the final compression detuning (multiply by two to account for both states). The optimum detuning corresponds to the theoretical optimum for optical molasses. (b) Absorption image of ~1×10^6 $F = 1/2, m_F = 1/2$ atoms in the dipole trap after ~2 ms of fall time.

TABLE 4.5: ^{6}Li MOT optimal parameters. These MOT parameters are optimised for greatest atom number.

Property	Value
Cooler xyz	20 mW
Repumper xyz	15 mW
Coil current	8.73 A (11.2 G cm^{-1})
Detuning	-40 MHz (-6.8Γ)

4.3 In-situ measurements of the $^6Li_2$ mBEC

In collaboration with Dr. Nathan Welch (University of Nottingham) [71], various models of differing complexity were used to fit the in-situ density distributions of our $^6Li_2$ molecular Bose-Einstein condensates. Over the course of

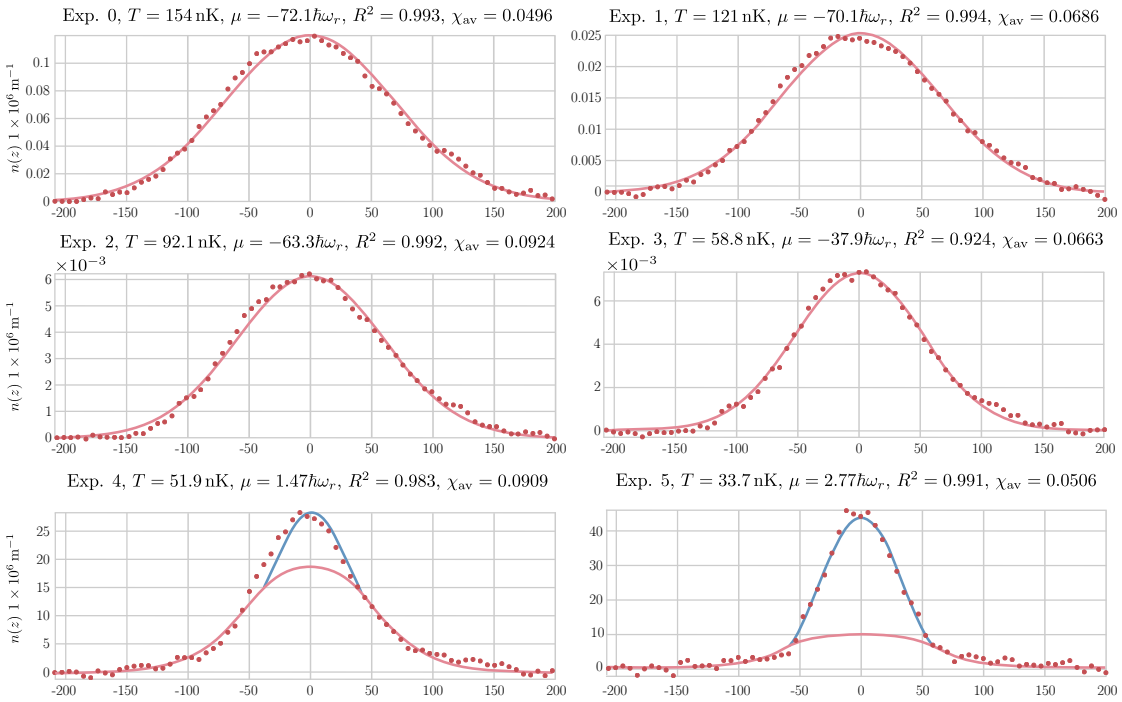


FIGURE 4.19: Fits to experimentally obtained in-situ density distributions of our $^6Li_2$ cloud (red points) using the Semi-ideal model (red and blue lines). The red lines indicate the thermal part of the distribution while the blue lines show the condensed fraction.

several months a significant amount in-situ density distribution data was accumulated for analysis. The measurement process involved evaporatively cooling lithium molecules in our dipole trap (as described in Section 4.2) down to various final trap depths and at different interaction strengths before recording the density profile using high-field absorption imaging. This data was then averaged and handed to Nathan Welch who attempted to fit our clouds with three different models: the ideal gas, the semi-ideal gas and the Hartree-Fock model to compare their validity.

The most important thermodynamic properties of a finite temperature Bose gas are the temperature T and chemical potential μ. However, in a strongly interacting gas like our $^6Li_2$ mBEC the two parameters are coupled to the density distribution in a complex non-linear manner making it difficult to extract them directly from the density. Therefore, in order to obtain them we used several different theoretical models to fit the integrated density distributions of our gas (leaving the temperature and chemical potential to be free parameters)

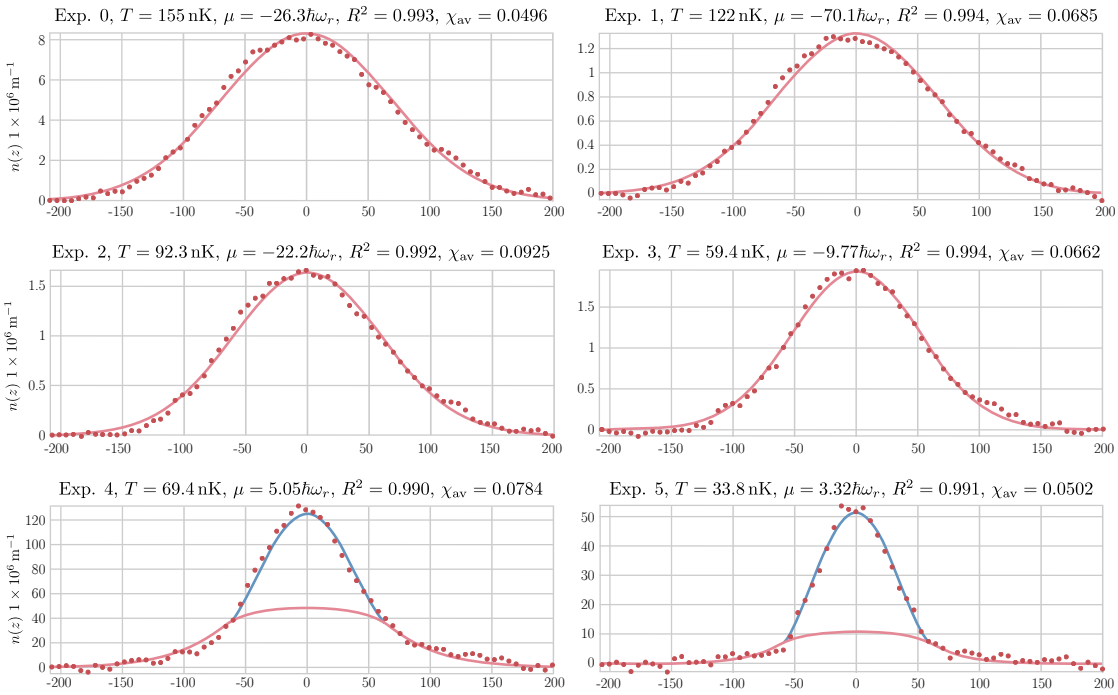


FIGURE 4.20: Fits to experimentally obtained in-situ density distributions of our $^6Li_2$ cloud (red points) using the Semi-ideal model (red and blue lines). The red lines indicate the thermal part of the distribution while the blue lines show the condensed fraction.

and compared the quality of each fit[2]. Then the best fitting model should give us the most accurate estimates for T and μ. In addition, we would also obtain a better estimate for the condensate fraction which is also left as a free parameter. Knowing more about our atom cloud should enable further optimisation of the evaporation process leading to larger final atom numbers, lower temperatures and larger condensate occupations.

Figures 4.19 and 4.20 show the results of this analysis for the semi-ideal and Hartree-Fock models. Absorption images of the cloud in our $1064\,\mathrm{nm}$ optical dipole trap were taken at six different final trap depths. This can be seen in the fitting results as a consistently falling temperature for both fitting schemes. The fit plotted in Figure 4.19 uses the semi-ideal model which treats the thermal cloud as an ideal gas with a distribution described by the Bose-Einstein distribution. Therefore it is more complex and potentially more accurate than the ideal gas model which models the thermal cloud using a simple Maxwell-Boltzmann

[2]In addition to the temperature and chemical potential, two more fitting parameters were required, a normalisation parameter and z_0 which was the position of the trap centre.

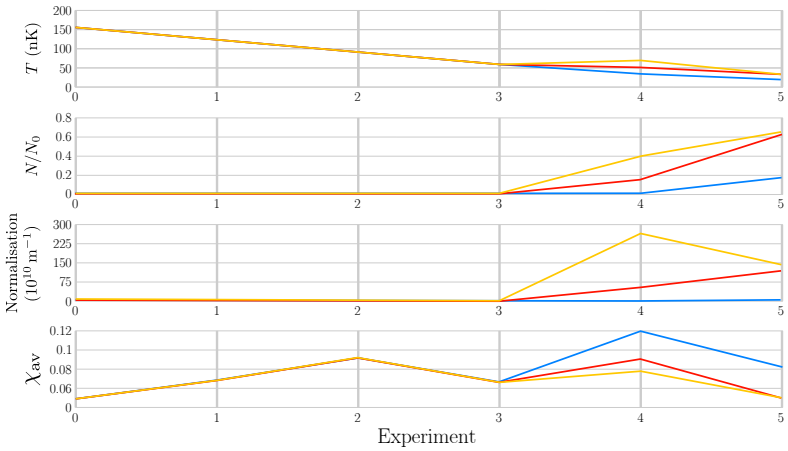


FIGURE 4.21: (a) Temperature (b) condensate fraction (c) normalisation and (d) χ_{avg} for the three models. Figure by Nathan Welch.

distribution. As mentioned earlier the total energy of the cloud reduces from experiment 0 to 5. Because the chemical potential increases as the temperature falls, we can interpret this change as efficient evaporative cooling. In other words only the very hottest atoms are escaping. This trend continues even after μ becomes positive.

Figure 4.20 shows the same experimental data fit to the Hartree-Fock model. This model uses the same Bose-Einstein distribution but takes into account inter-atomic repulsion due to collisions in the thermal cloud. Repulsion from the thermal cloud causes a suppression of the condensate making the condensate density a function of the temperature and chemical potential. The same general trends can be seen in Figure 4.20 as Figure 4.19, however the chemical potential takes on much larger values (less negative) in every experiment. There is a difference going from experiment 4 to experiment 5 in that the chemical potential is actually reduced. This can be interpreted as the trap depth being lowered too far such that below average temperature atoms are escaping leading to inefficient cooling. In addition it can be noticed that the densities measured by the two fitting models differ by over an order of magnitude in some cases. This is necessary in order to fit the shape.

Figure 4.21 shows the results produced by each fitting model as the dipole trap depth was lowered. In addition to T and μ the normalisation fitting parameter and χ_{avg} are plotted. To find the optimal fit for each model the χ^2 fitting parameter was used. To compare the models however, the average value χ_{avg}

was used. Before the emergence of the condensate, all of the models perform equally well in fitting the data. After the appearance of the condensate however, the models begin to diverge. At this point the ideal model has the hardest time fitting the data with errors greater than 10%. The Hartree-Fock model performs the best with the semi-ideal model only slightly behind. Due to the large degree of freedom afforded by the normalisation fitting parameter, it is not clear which model is the most useful in fitting the data. Because the Hartree-Fock method takes into account additional effects that we know should play a significant role in this strongly interacting system, we expect it to be the most accurate model. However, the results do not reinforce this in a conclusive way.

TABLE 4.6: Details of the various semi-analytical finite temperature fitting models.

Model	Condensate	Thermal cloud	Validity
Bi-modal/Ideal gas	Thomas-Fermi	Maxwell-Boltzmann (ignores condensate)	Low T for small thermal cloud but high T for MB distribution
Semi-ideal	Thomas-Fermi	Bose-Einstein (repelled by condensate)	$\mu \gg \max[gn_{\rm th}]$
Hartree-Fock	Thomas-Fermi (repelled by thermal cloud)	Bose-Einstein (repelled by condensate and itself)	all T and $\mu \gg \hbar\omega_{r,z}$

4.4 Next steps

4.4.1 3D degenerate Raman sideband cooling

To go beyond the recoil limit for caesium, we have set up a 3D degenerate Raman sideband cooling arrangement, a complex cooling technique that exploits the tight confinement of atoms in an optical lattice [72].

Atoms are firstly loaded into an optical lattice with the yellow beam configuration shown in Figure 4.22b. An atom begins its cooling cycle polarised in the $|F = 3, m_F = 3\rangle$ ground state in a high-lying vibrational level ν of the lattice. We apply a small magnetic field of only a few tens of milligauss to shift the state $|F, m_F; \nu\rangle$ into degeneracy with the states $|F, m_F; \nu - 1\rangle$ and $|F, m_F; \nu - 2\rangle$. The lattice light then couples these states together (double ended arrows in Figure 4.22a) via 2-photon degenerate Raman transitions[3] so that the atoms hop around freely from to state to state. We then apply pumping light (red arrow in Figure 4.22b) with a strong σ^+ component and a small π component on the $6^2S_{1/2}, F = 3 \Rightarrow 6^2P_{3/2}, F' = 2$ transition such that if an atom finds its way to $m_F = 1$ it is immediately pumped. The subsequent decay favours $m_F = 3$ as a result of the pumping. If the atom is sufficiently tightly bound in the lattice (in the **Lamb-Dicke regime**), it is unlikely to change its vibrational state during the decay, hence the atom is cooled by two vibrational quanta. The atom will cascade down the vibrational levels of the lattice through many repetitions of this cycle until it finds itself in the state $|3, 2; 0\rangle$. Here the weak π light slowly pumps atoms up to $F' = 2$ where they subsequently decay to the dark state $|3, 3, 0\rangle$. This final step suppresses re-absorption heating and reaches lower temperatures than would be achievable with only σ^+ light. This technique should allow us to cool caesium even further from ~30 µK down to ~1 µK for improved dipole trap loading.

[3] A Raman transition is the simultaneous absorption and emission of a photon via a virtual state that can couple two states with an energy difference of $\omega_{L1} - \omega_{L2}$ where ω_{L1} and ω_{L2} are the angular frequencies of two laser fields. A degenerate Raman transition simply means $\omega_{L1} = \omega_{L2}$ and so the photons couple states of the same energy.

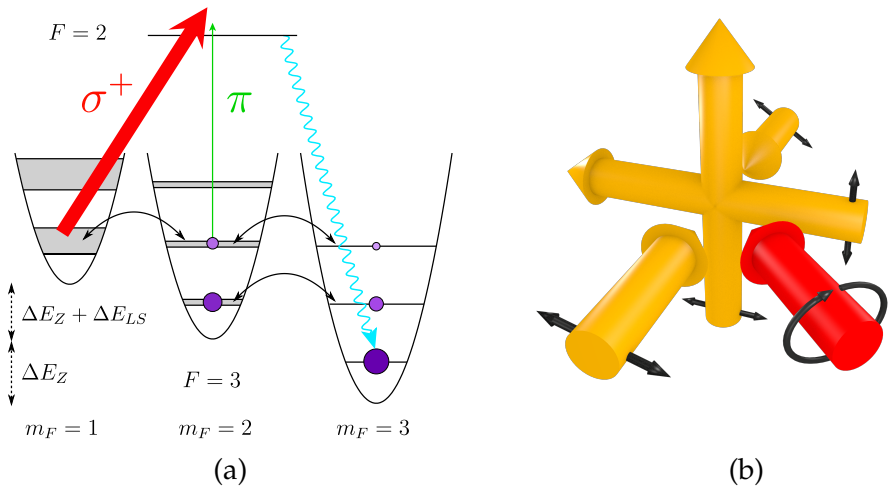


FIGURE 4.22: (a) 3D degenerate Raman sideband cooling scheme. Strong σ^+ light cools the atoms by removing their vibrational energy. Weak π light pumps the atoms into the dark $|3, 3; 0\rangle$ state. E_Z is the Zeeman shift and E_{LS} is the light shift caused by the strong optical pumping. Figure adapted from [72]. (b) Beam configuration for Raman sideband cooling. The yellow arrows depict the lattice beams, the red arrow is the optical pumping beam and the small black arrows indicate the polarisations.

4.4.2 ^{6}Li D_1 grey molasses

Lithium can be cooled to significantly lower temperatures using so-called D_1 grey molasses cooling [73, 74, 75]. This step would be performed immediately after compression for greatly enhanced dipole trap loading. The molasses scheme comprises cooling on the ^{6}Li D_1 transition $2^2S_{1/2}, F = 3/2 \Rightarrow 2^2P_{1/2}, F' = 3/2$ and repumping on the $2^2S_{1/2}, F = 1/2 \Rightarrow 2^2P_{1/2}, F' = 3/2$ transition. Both the cooler and the repumper laser are blue-detuned to the transition with the repumper laser at one fifth of the strength of the cooling laser.

Figure 4.23 shows a proposed optical bench setup that would enable a cost-effective implementation of the technique. Four new ECDLs are required, two for D_1 cooling and D_1 repumping light and two for D_2 cooling and repumping light. With limited table space available, two of the lasers would have to fibre coupled to the rest of the system or mounted on a platform above the rest.

The first addition is a second reference laser locked to the D_1 $2^2S_{1/2}, F = 3/2 \Rightarrow 2^2P_{1/2}, F' = 3/2$ transition that would pass through the spectroscopy cell slightly offset from the current reference laser so that its beam could be picked

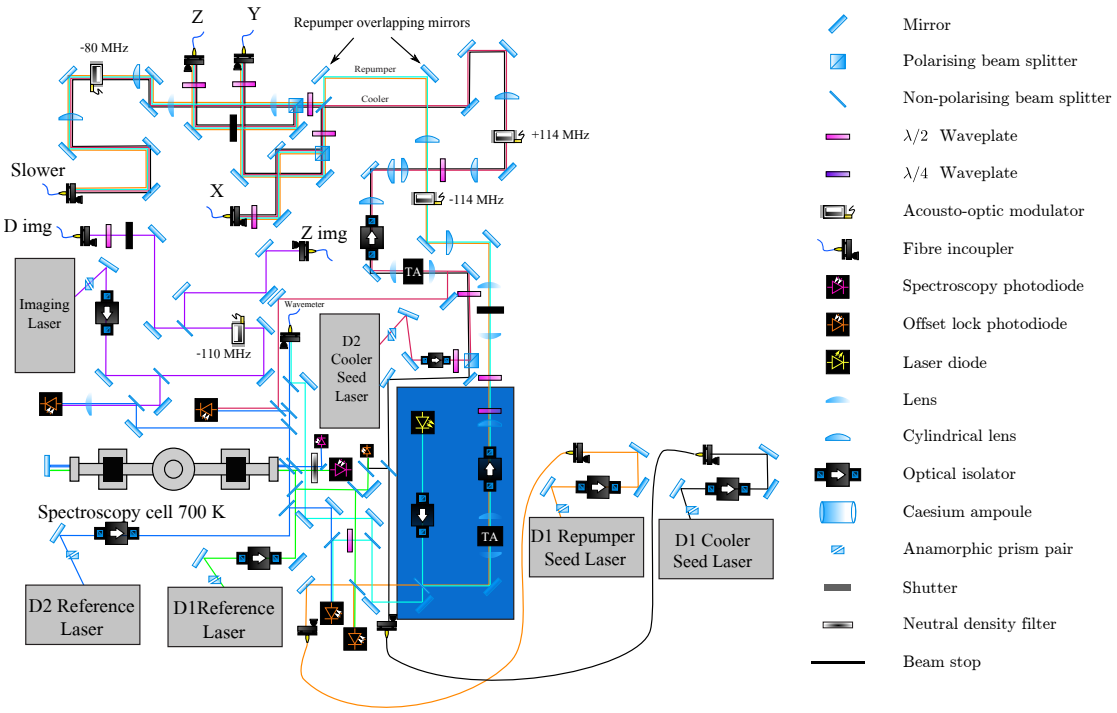


FIGURE 4.23: Proposed setup for grey molasses cooling of lithium. Four new home-built ECDLs are required. Since there is little table space left two would have to be fibre coupled to the rest of the system.

off into a separate photodiode. Separate cooling and repumper seed lasers are used because independent frequency control is important for the grey molasses scheme to work. These are both offset locked to the D_1 reference laser.

Next, in order to acquire the necessary powers in the D_1 beams without spending a significant amount of money on tapered amplifiers, each existing tapered amplifier is doubly seeded with both D_1 and D_2 light. The Toptica TA Pro is seeded with only D_1 light, while the home-built TA is seeded with only D_2 light. Separating the light this way avoids triply seeding the Toptica TA Pro.

As well as providing enough power, double seeding overlaps the D_1 beams perfectly with our existing beams saving money on optomechanics and vital optical access to the chamber. To seed the Toptica TA Pro with an additional laser, one would obviously have to drill a hole in the side of its enclosure. With a standalone D_2 cooler seed laser (also offset locked with the reference laser) we would also have independent frequency control of our cooling and repumping D_2 MOT beams. MOTs containing up to 1×10^9 atoms are reported to have been achieved this way [75].

Chapter 5

A quantum integrated light and matter interface

It is undeniable that classical computing has had an enormous impact on the world. It has been integral to our storming technological progress as a species and has completely changed the way we conduct our everyday lives. Everything from shops, money and business to games, entertainment and news has been digitised and transferred over to the virtual world.

These classical or conventional computers of which we are speaking store and process information which has been encoded into series of 1's and 0's called bit strings. Computers handle this information using transistors combined to perform Boolean operations such as OR, AND and not-AND (NAND) gates [1]. Quantum computers on the other hand process data in a fundamentally different manner. Rather than depending on bits, information is stored in quantum bits or **qubits**. Qubits are quantum objects with two mutually exclusive states which we can label $|0\rangle$and $|1\rangle$. Since the states $|0\rangle$and $|1\rangle$are orthonormal, they form a *basis* so any arbitrary qubit state $|\psi\rangle$can be represented as a linear combination of the two. In Dirac notation this is written:

$$|\psi\rangle = \alpha\,|0\rangle + \beta\,|1\rangle), \tag{5.1}$$

where the prefactors α and β can take on any value (subject to the normalisation condition). Thus the qubit is able to partially exist in both states at once. In the language of quantum mechanics we say the qubit exists in a *superposition* of the states $|0\rangle$ and $|1\rangle$. The computational power of qubits is not immediately

[1]The NAND is a particularly important gate because every binary logic operation can be formed out of combinations of NANDs.

obvious, however, for particular problems it has been shown to be much greater than that of classical bits [76].

It has been 36 years since the quantum computer's inception in 1980 by the works of Paul Benioff [77] and Yuri Manin [78] and in that time enormous leaps forward have been made in both a theoretical and practical sense. Quantum computers hold promise for efficiently solving problems that conventional computers take an unreasonable amount of time solving. In the late 1960's and early 1970's computer scientists devised a method of classifying problems by their computational difficulty[79]. They decided to measure the time taken to solve a problem by the number of elementary steps taken by the algorithm used to solve it. In the language of complexity theory, an algorithm is called *polynomial-time* if the running time grows polynomially with the input size, (e.g. n^2 or $n^{1.5}$). Problems of this nature lie in the complexity class P and are efficiently solved by conventional (classical) computers. Problems which require algorithms that take an exponentially increasing amount of time as the problem size grows, but whose solutions can be checked in polynomial time, belong to the class NP which stands for *non-deterministic polynomial time*. Living in a subset of the NP complexity space are the so-called NP-complete problems. These are *the most* computationally difficult problems to solve and even a quantum computer is predicted to take more than a polynomial number of steps in order to crack them.

Now, the class of problems for which quantum computers are theorised to provide significant speed-up in solving, is the BQP class which stands for *Bounded-error Quantum Polynomial time*. The BQP class includes all P problems and some but not all NP problems. To date, only a handful of quantum algorithms have been discovered that would allow a quantum computer to solve an NP problem in P time. However, one very important quantum algorithm that has been discovered is Shor's algorithm [80] which solves the problem of factoring an n-digit number. The factorisation of enormous numbers happens to be a *very* common method of data encryption; no message would be safe if a quantum computer existed. In addition to code-breaking, a massively important application for quantum computers would be the simulation of quantum systems, just as Benioff [77] and Feynman suggested many years ago [81]. This is particularly true in the fields of chemistry and biochemistry where the interactions involved are of monstrous complexity.

Photons are archetypical qubits. They can be polarised into one of two polarisation states or prepared in a superposition of the two and since they are discrete, they can exist, not exist or again live in a superposition. These then represent two ways in which information can be encoded using photons. Single-qubit operations on photons are also brilliantly cheap and simple to employ through the use of waveplates, beamsplitters and photodetectors. However, performing two-qubit operations using photons is difficult because of the fact that photons do not interact with other photons. Fortunately, it was discovered by Emanuel Knill et al. [82] that through careful use of measurements it is possible to circumvent this issue at the cost of some determinacy. Here presents a major issue of scalability. As the number of two-qubit gates increases the probability that every gate is successful goes down. Since photons are short-lived, it is vital then that the quantum computer has a way of storing its information until all of its gates have resolved successfully. This is where quantum memories like the system presented in this thesis become relevant [83].

While classical computers are able to freely copy information to store for later use or as a backup, quantum computers are restricted by the **no-cloning theorem**. The no-cloning theorem tells us it is impossible to make a copy of an arbitrary unknown quantum state [84]. The proof is rather simple. Suppose a machine exists takes two qubits as its input, a qubit in state $|\psi\rangle$, which we wish to clone, and another in the blank state $|\xi\rangle$ onto which the clone is imprinted. The machine outputs the original qubit in state $|\psi\rangle$and its clone, also in the state $|\psi\rangle$. Written in Dirac notation we have the following:

$$\hat{U}\,|\xi\rangle\,|\psi\rangle = |\psi\rangle\,|\psi\rangle\,. \tag{5.2}$$

Similarly, given another blank qubit and a qubit in state $|\phi\rangle$ the machine would have output:

$$\hat{U}\,|\xi\rangle\,|\phi\rangle = |\phi\rangle\,|\phi\rangle\,. \tag{5.3}$$

Taking the inner product of equations 5.2 and 5.3 we have

$$\langle\psi|\,\langle\xi|\,\hat{U}^{\dagger}\hat{U}\,|\xi\rangle\,|\psi\rangle = \langle\psi|\,\langle\psi|\,\phi\rangle\,|\phi\rangle \tag{5.4}$$

$$\langle\psi|\,\phi\rangle = \langle\psi|\,\phi\rangle^{2}\,. \tag{5.5}$$

Clearly, this result cannot apply to any arbitrary state. It can only apply

when the states $|\psi\rangle$and $|\phi\rangle$are identical ($|\psi\rangle = |\phi\rangle$) or orthogonal ($\langle\psi|\ \phi\rangle = 0$). In other words, it is only possible to make copies of predetermined states or states with zero overlap. Thus we can conclude that quantum information cannot be cloned. Consequently quantum memories must function in a fundamentally different manner to classical storage systems through the transfer of quantum information onto more long-lived mediums. Building a quantum memory means producing a means to swap information between information carriers and a storage medium. In this experiment photons are used as information carriers and an ensemble of cold caesium atoms are used for information storage.

Ideally a quantum information storage medium should be well isolated from its environment such that the information can be stored for a long time before it decoheres. However, noise resilience usually means the medium is also difficult to manipulate; long coherence times and controllability are naturally at conflict with each other. Systems that are easy to manipulate but decohere quickly are more suited for use in a quantum processor whereas well-isolated systems that are harder to interact with find use as quantum memories [83].

Quantum memories will also find use in extending the range of quantum communication systems. Quantum Key Distribution (QKD) is a system for guaranteeing that information transferred between two parties has not been intercepted by an eavesdropper. In fact several companies around the world already sell QKD systems. However, because photons do not survive for much longer than $1\,\mathrm{ms}$ in an optical fibre, QKD is only useful over distances shorter than $300\,\mathrm{km}$. An efficient quantum memory would allow one to construct a **quantum repeater** in order to boost the QKD signals such that they can be transmitted across the globe.

There has been a huge collective effort in recent years in the search for an ideal quantum memory among the multitude of candidates. The various physical systems being explored include: single atoms [85, 86], atomic ensembles [87, 88, 89], ions [90], spin-chains [91], super-conducting circuits [92, 93], nitrogen-vacancy centres in diamond [94, 95] and optical lattices[96].

The hope and vision is to find the quantum computing equivalent of a transistor that can be multiplied and miniaturised. The challenges involved in the development of such a modular device capable of storing, processing, and transmitting quantum information are immense and to date no satisfactory solution has been found.

This was the aim of the Quantum Integrated Light and Matter Interface (QuILMI) project, a multi-institutional collaborative effort. The Nottingham Quantum Optics and Mixtures group (this group) led the experimental side of the venture supported by quantum optics teams at the University of Vienna (led by Dr. Philip Walther) and the University of Jena (led by Dr. Alexander Szameit). Our experimental efforts were accompanied by theoretical contributions from groups led by Dr. Thomas Pohl at the Max Planck Institute for the Physics of Complex Systems in Dresden and Dr. Igor Lesanovsky at the University of Nottingham.

Based on a sophisticated micro-structured waveguide-atom chip, QuILMI's approach was to solve these issues by interfacing quantum light with highly tailorable ultracold atoms via the evanescent field of a waveguide chip. With the help of single-photon detectors, the system would permit the creation, storage and analysis of quantum states of light down to the single-photon level. With this aim in mind, the specific goals laid out at the start of the project for the individual teams on the QuILMI consortium were:

- to prepare a degenerate cold atom cloud in an optical lattice on a chip surface
- to implement waveguides in the atom chip surface
- to achieve quantum control of tailored photon states for guiding their propagation through the integrated circuit structure and for later analysis of the coupling fidelities
- to demonstrate and characterize coherent photon-atom coupling and (single-)photon storage in the ultracold atomic ensemble
- to develop an integrated detector for single-photon measurements
- to devise new protocols and methods for creating entangled photon states based on atomic interactions

Early theoretical studies and experiments concluded that coupling atoms with the evanescent field of a waveguide was unfeasable due to poor overlap between the light and atoms. In light of these events and early results, a shift in approach was appropriated in order to maximise atom-photon coupling. Two

solutions were devised. The first solution was to etch microscale voids into the waveguide chip using FLICE (Femtosecond-Laser Irradiation followed by Chemical Etching), while the second solution was to laser-drill the void into a length of single-mode fibre. In this way we could produce a volume in which the atoms could be trapped using free-space light and probed by waveguided light in the chip. What is most exciting about this approach is the versatility and miniaturisation potential of the waveguide chip. Virtually any operation can be written directly onto the chip and in a robust and highly compact manner.

5.1 QuILMI experimental setup

The experimental pursuit of the QuILMI project was entirely planned and constructed from the bottom up. Although an entire caesium cold atom experiment already existed, the original idea of modifying the existing setup to facilitate the testing of wave-guide chips proved impractical. The testing of multiple chips required a rapid and easy removal/installation procedure which could only be achieved with a new setup. Hence, the decision to build a new, dedicated QuILMI chamber was made. In designing the QuILMI chamber, a multitude of criteria had to be respected:

(a) The chamber had to be very compact in order to enable an easy and fast baking procedure to quickly obtain pressures of $\sim 1 \times 10^{-10}\,\mathrm{mbar}$.

(b) Ease of access to the science chamber and chip was of paramount importance for rapid testing of the numerous waveguide chips and fibres we would receive.

(c) The mounting procedure for the waveguide chips had to be both fast and simple to perform.

(d) A cheap and robust fibre feed-through solution was needed to couple light with high efficiency both in and out of the vacuum system.

(e) A high degree of optical access was required for the various MOT, imaging and optical dipole trap beams we would need.

5.1.1 The QuILMI chamber

A compact chamber with high optical access

The goal of constructing a small and versatile test chamber was achieved as can be seen from Figure 5.1. This achievement owes itself to a number of manufacturing decisions with this design goal in mind. Firstly, the bare minimum of vacuum components have been used. The system consists of merely a 6" 316L steel Kimball spherical octagon (MCF600-SphOct-F2C8) connected to a VacIon 40 Plus ion pump via a CF40 tee and a 6-way cross[2]. In this arrangement

[2]The two blanked off connections on the 6-way cross provide opportunities for modification in the future.

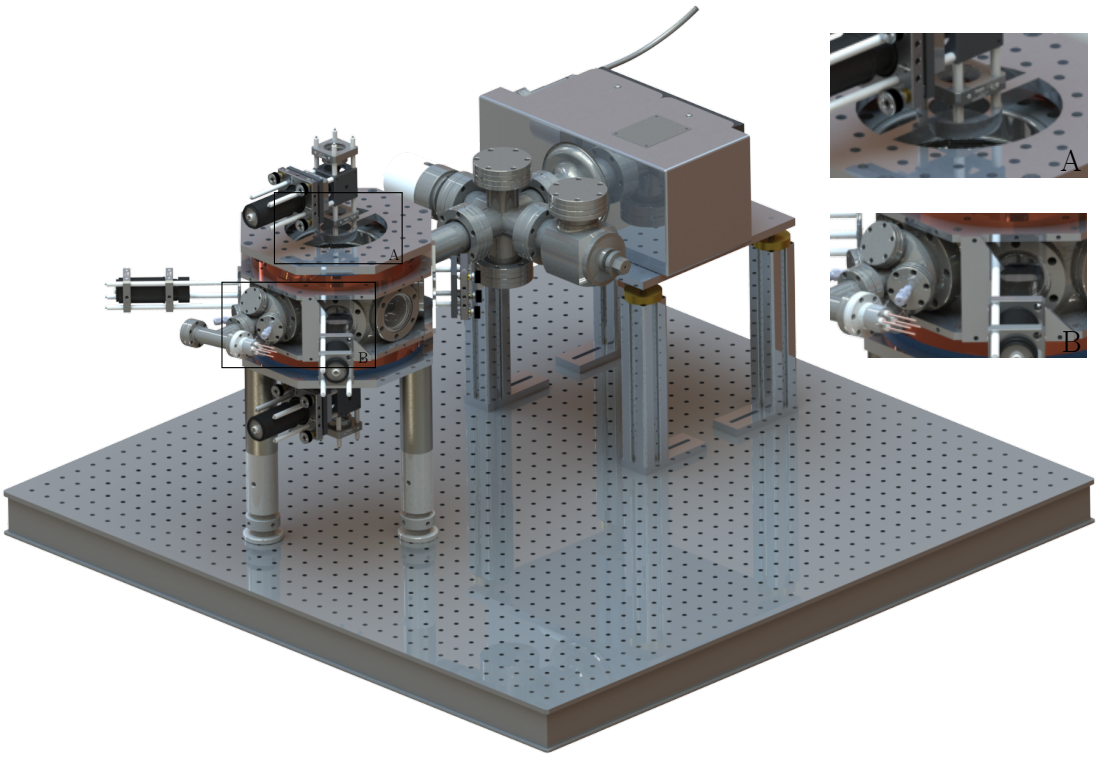
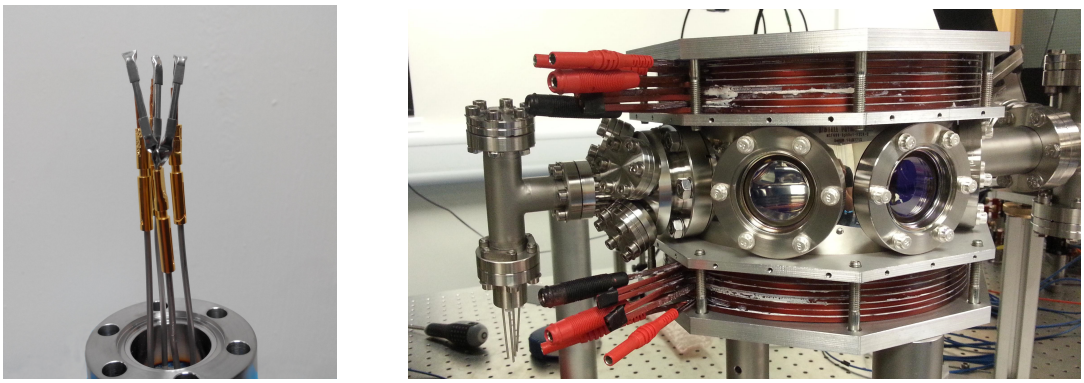


FIGURE 5.1: The QuILMI test chamber with MOT beam optomechanics. Dipole trapping and imaging optomechanics are not shown.

the ion pump has both close-proximity and direct line-of-sight to the MOT and the caesium dispensers (three SAES getters model CS/NF/3.9/12 FT10+10, Figure 5.2a) meaning background caesium gas is pumped with a very high efficiency. This alleviates the need for a space-consuming Zeeman slower to load the MOT.

Figure 5.1 also showcases a new design for the simultaneous mounting of magnetic field coils and optical elements which makes a significant contribution to its compactness. Thin ($6\,\mathrm{mm}$) aluminium plates fastened to the top and bottom faces of the spherical octagon provide, at the same time, surfaces for the coils to be clamped in place, and mounting holes for plates onto which Thorlabs cage system optomechanics can be connected. The coils are mounted between thin aluminium plates and thicker ($10\,\mathrm{mm}$) clamping plates. The top and bottom clamping plates are also multi-functional. Carved centrally into each plate is a large $120\,\mathrm{mm}$ hole for infra-red camera and personnel viewing access. Concentric with this viewing hole, supported by thick ($10\,\mathrm{mm} \times 10\,\mathrm{mm}$ in cross-section)



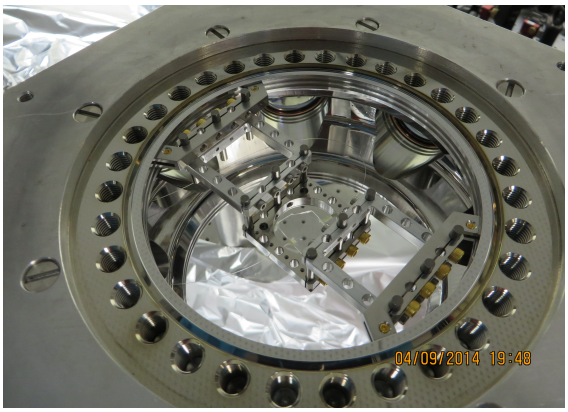
(a) (b)

FIGURE 5.2: The caesium dispensers (a) and a close-up of the science chamber (b) at an early point of development. The dispensers are positioned and orientated inside the CF16 tee (right-hand figure) so that they have direct line of sight to the MOT and ion pump. Typically a current of $4.5\,\mathrm{A}$ is used to produce the caesium vapour. The MOT coils are fitted with common banana connectors for rapid assembly and disassembly. The aluminium plates are highly multi-functional, they: hold the coils in place, act as heatsinks, provide a surface for the supporting legs, and can support the mounting of Thorlabs cage systems onto which optomechanics are fixed.

struts that extend inwards towards the centre of the plate, is a ring shaped platform onto which Thorlabs cage systems can be attached for the vertical MOT, imaging and dipole beam setups (see inset A in Figure 5.1. Furthermore, the top plate is perforated with an abundance of M6 threaded holes for the fixing of any additional equipment while the bottom plate holds two M8 threads for the supporting legs to screw into. Together, these features obviate any requirement of a second breadboard supported above the optical bench as in the mixture experiment. In addition, the viewport mounted cage systems ensure the six MOT beams begin in near-perfect orthogonal arrangement so first signals of MOT are incredibly easy to attain. This makes recovery after opening up the chamber straightforward. The QuILMI mounting plate designs are given in Appendix C.2. One final space-conserving point is that the vertical compensation coils (blue in Figure 5.1) are stacked with the MOT coils (red).



(a)

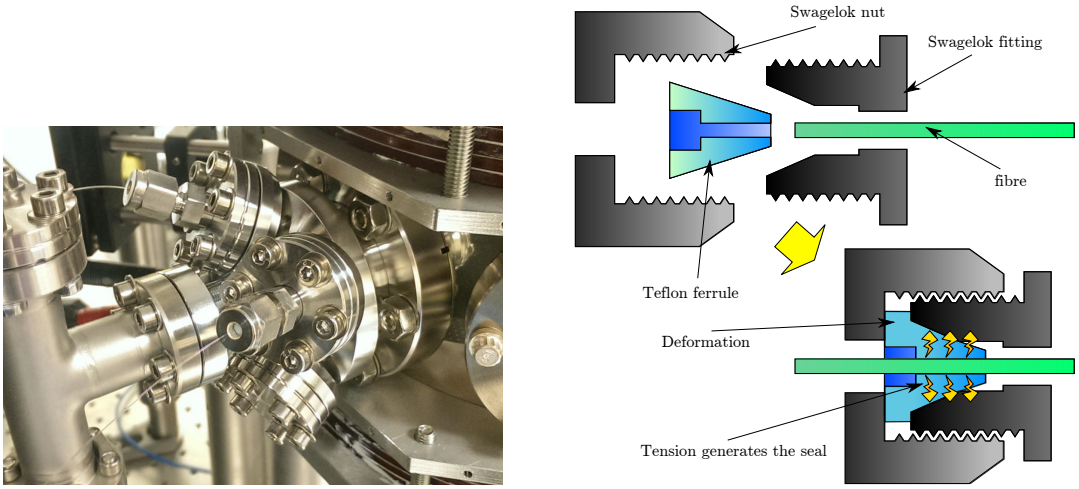


(b)

FIGURE 5.3: The internal chip mounting system. (a) The waveguide chip is glued onto an eV SS-PL-C5X5-R1000 stainless steel plate. (b) The plate is then mounted onto the internal structure by clipping it onto rods protruding beneath the central clamp assembly. Shown in (b) is actually the fibre chip.

A simple and fast chip-mounting procedure

A design that allowed the swift exchange of waveguide chips was essential so that we could rapidly determine the viability of the various chips we would receive from the University of Jena. An internal chip mounting system was devised using Kimball Physics' UHV (ultra high vacuum) internal mounting apparatus attachment system. Two 6" 316L steel 'groove grabbers' (Kimball MCF600-GG), clamped onto ridges carved into the interior of the 6" spherical octagon, provide a split, axially orientated foundation for an internal scaffold made of clamping plate assemblies (2x SS-CPA-C5x5-S1000, 1x SS-CPA-C5x5-R1000 both eV parts), and 316L steel rods. The circular core of the SS-CPA-C5x5-R1000 plate assembly sits concentrically with the axis of the chamber to permit the transmission of vertically orientated optical beams. The steel rods connecting to the central plate assembly protrude slightly beyond the bottom surface such that the waveguide chip, glued using UV-cured UHV compatible DYMAX OP-67-LS epoxy onto an eV parts SS-PL-C5X5-R1000 stainless steel plate, can be attached by tensional and frictional forces alone. The mounting solution is shown in Figure 5.3 and an early blueprint can be seen in Appendix C.1. The transparent chips are mounted horizontally meaning the vertical MOT beams pass through the chip and a *vertical* optical dipole trap is needed. The decision to mount the scaffold on the upper grooves of the science chamber



(a) (b)

FIGURE 5.4: The Swagelok fibre feedthrough system. Two such feedthrough flanges in action (a) and a diagram of the sealing mechanism (b). The fibre is threaded through the ferrule and Swagelok fitting before the nut is fastened and tightened. The inner faces of the Swagelok fitting compress the fibre to form a hermetic seal.

was made in order to facilitate fixing of the waveguide chip with its delicate chip to fibre connections or the fragile fibre chip with its $30\,\mu\mathrm{m}$ hole. Mistakes made at this point of the experiment would have been particularly costly since the lead time of each waveguide chip was on the order of several months. With the MOT formed below the chip, the atoms need to be loaded upwards into the dipole trap *against gravity* necessitating the use of a push beam or another throwing mechanism.

Cost-effective, high-transmission fibre feedthroughs

For the efficient coupling of light into and out of the chamber, compression sealed fibre feedthrough devices based on CF16 Swagelok vacuum flanges (Kurt J. Lesker) and custom-made Teflon ferrules were built. The Teflon ferrule plus Swagelok fitting arrangement is shown in Figure 5.4 with an explanation in the caption. The system follows the method outlined in Abraham and Cornell's short paper [97] with a slight modification due to limitations of available drilling equipment. The hole through which the fibre is threaded is just $100\,\mu\mathrm{m}$ in diameter and drilling such a hole through the entire length of the ferrule proved to be a challenge for our mechanical workshop resulting in many broken drill

bits. The hole was therefore tapped at the wider end of the ferrule at a depth of $5\,\mathrm{mm}$ without any loss of performance.

Our fibre feedthroughs outperform commercial CF-flange fibre feedthroughs in a number of areas. Commercially available products typically mate two separate fibres together leading to high transmission losses at each interface. For our purposes we would have to use a minimum of two flanges meaning a total of four interfaces and unacceptable losses. Since our custom solution keeps the fibre intact and only perturbs the fibre by compressing it, high transmission efficiencies upwards of 98% at each feedthrough have been achieved. Thus the greatest losses arise from the fibre-to-waveguide connections on the chip and the free-space fibre coupling. With two of our fibre in Figure 5.1 installed, vacuum pressures of $1 \times 10^{-10}\,\mathrm{mbar}$ have been reached which is low enough for both the MOT and dipole trap to function well. Furthermore, costs for commercial solutions can easily amount to greater than $1500 per flange connection (Kurt J. Lesker) whereas the fibre feedthroughs presented here can be produced for under $100 per unit. The ferrules should also, in principle, be reusable, but no such test was carried out in this experiment because of an abundance of available ferrules.

The fibres are installed typically with about $30\,\mathrm{cm}$ of slack outside the chamber which can be freely manipulated to connect with the rest of the system without compromising the vacuum or the transmission efficiency. Since the fibres have to be threaded through the fibre ferrules and the Swagelok connections, the fibres have to be connectorised in-situ. For this purpose the fibres are cleaved, unsheathed and fed into Thorlab BFT1 bare fibre terminators fitted with B30126A9 FC/APC connectors (also Thorlabs). These types of connectors hasten the process of switching waveguide chips since they do not require any epoxy which usually require at least 24 hours to set.

These fibre feedthroughs are not entirely without their disadvantages. Baking of the vacuum system, to remove contaminants in order to achieve UHV upon restoration of normal laboratory temperature, must be performed slowly and in such a way as to not raise the temperature of the Teflon ferrules beyond $\sim 80\,^{\circ}\mathrm{C}$. It was discovered first hand that beyond this temperature the ferrules have a tendency to fail upon cooling producing a leak that cannot be plugged by tightening the Swagelok nut. Cooling the chamber even more slowly proved to

be ineffective for preventing the leak. A UHV compatible epoxy such as Vacseal can seal the leak but risks sealing the ferrule inside the nut. Ultimately the chamber was baked while leaving the Swageloks exposed to the air and actively cooled by pressurised air normally used for the floating optical benches. Considering the maximum operating temperature of the optical fibres we use is $85\,^{\circ}\mathrm{C}$, this is a small concession.

Another minor disadvantage is that particles can pass through the small gap between the fibre coating and the fibre cladding. This produces a small leak that is detectable with a leak detector, but ultimately does not threaten the experiment since the pressures achieved are more than satisfactory.

The fibre feedthroughs are connected to a Caburn MMF275-5-133 multi-mini flange attached directly to the science chamber. The multi-mini flange connects five CF16 flanges to a single CF40 flange. One connection is occupied by the atom source leaving four slots for fibre feedthroughs and/or additional optical access. Only briefly explored was to trying to couple multiple fibres through the same Swagelok flange by simply making a number of holes in the Teflon ferrule. Only one test was performed with a ferrule hosting a total of three through-holes but UHV could not be obtained and the idea was not explored further owing to a lack of necessity. Although the first test was a failure, in principle such a device should work and this would need to be investigated in the future when more sophisticated chips with more fibre connections are in use.

MOT coils

The QuILMI MOT coils were constructed using a "pancake stacking" technique in which each layer is wound individually before being stacked together to produce a coil. This method has multiple advantages over conventional winding. Firstly, the method produces very high quality coils with little to no imperfections. Secondly, the building process is easier because each coil is constructed in steps. Using a conventional winding technique an entire coil must be wound and glued in single step which can be logistically trouble-some and physically difficult leading to mistakes and defects. Finally, the coils are easily modified after construction. Adding more layers is as simple as winding an extra layer and gluing it to the rest.



(a) (b)

FIGURE 5.5: The MOT coil winding rig. (a) The whole system including the spool of coated copper wire, winding plate, workshop chuck and a recently completed pancake. (b) Close up of the completed pancake.

The coil winding rig is displayed in Figure 5.5. A large spool of coated $1.55 \times 3.2\,\mathrm{mm}$ cross-section copper wire (Von Roll Thermex 200 Grade 1-BS-EN60317) is slotted onto a vertically mounted post such that the spool can rotate when the wire is drawn. The wire is threaded across the table into the device shown in Figure 5.5b which sits inside the teeth of table-mounted, hand-operated chuck. The device consists of a $154\,\mathrm{mm}$ diameter Teflon coated aluminium base plate mounted coaxially with an aluminium (also Teflon coated) coil former with a thickness of $3.2\,\mathrm{mm}$ and a diameter of $154\,\mathrm{mm}$ (the outer diameter of a CF100 viewport). The wire is threaded into a notch carved into the coil former (top right of Figure 5.5b) and bent round the corner before being lightly clamped into place by one of six Teflon coated clamping blocks. With a good amount of tension between the spool and chuck, the first orbit can be wound while clamping the wire down to keep it in position. Upon reaching the notch a thin layer of 3M Scotch-Weld DP760 Structural Adhesive is applied to a long stretch of the inner surface of the wire to be wound. This adhesive is chosen for its short setting time of 45 minutes and high maximum operating temperature of $230\,^{\circ}\mathrm{C}$. Winding resumes, taking care to loosen the clamping blocks as the wire approaches (to avoid scratching off the coating) and to tighten them back up once it has passed. This process is repeated until the coil layer has as many windings as desired. In this experiment each MOT coil comprises 6 'pancakes' of 15 windings each. Stacked on top of each coil are two additional layers which

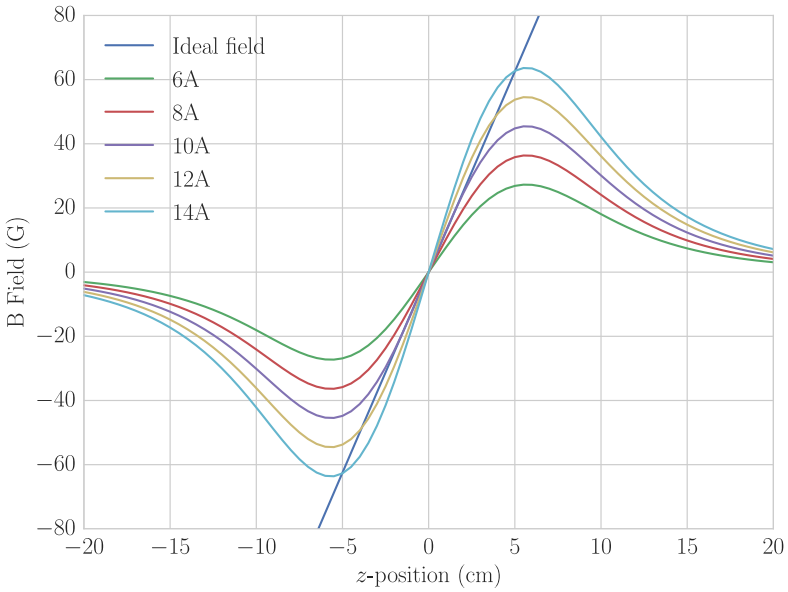


FIGURE 5.6: Magnetic field profile through the axis of the QuILMI MOT coils. The ideal field is $12.50\,\mathrm{G\,cm^{-1}}$, the same field gradient used for caesium in the mixture experiment. The coils are powered by a programmable Electro-automatik EA-PS 3016-20B.

are used as vertical compensation coils for offsetting the zero of the magnetic field in the vertical direction. The finished products can be seen in Figure 5.2b.

Field calculations are shown in Figure 5.6. To smoothen the transition from the mixture experiment to the QuILMI experiment, the coils were designed to produce precisely the same field used for caesium in the mixture chamber of $12.50\,\mathrm{G\,cm^{-1}}$. In practice currents of 8-$11\,\mathrm{A}$ are typically used in this experiment to optimise the position of the MOT relative to the chip which is more important than absolute atom number.

Run continuously at $16\,\mathrm{A}$ while attached to the system the coils eventually reach a steady state temperature of $55\,^{\circ}\mathrm{C}$ which in turn raises the pressure inside the chamber to $1 \times 10^{-8}\,\mathrm{mbar}$. Under normal operating conditions however, the coils are run at lower currents (8-$11\,\mathrm{A}$) and in pulses of 5 to 7 seconds with a few seconds in between so the coils heat up only slightly to roughly $30\,^{\circ}\mathrm{C}$. This is not enough to raise the pressure out of the 1×10^{-10}-$1 \times 10^{-9}\,\mathrm{mbar}$ range and so additional cooling was found to be unnecessary.

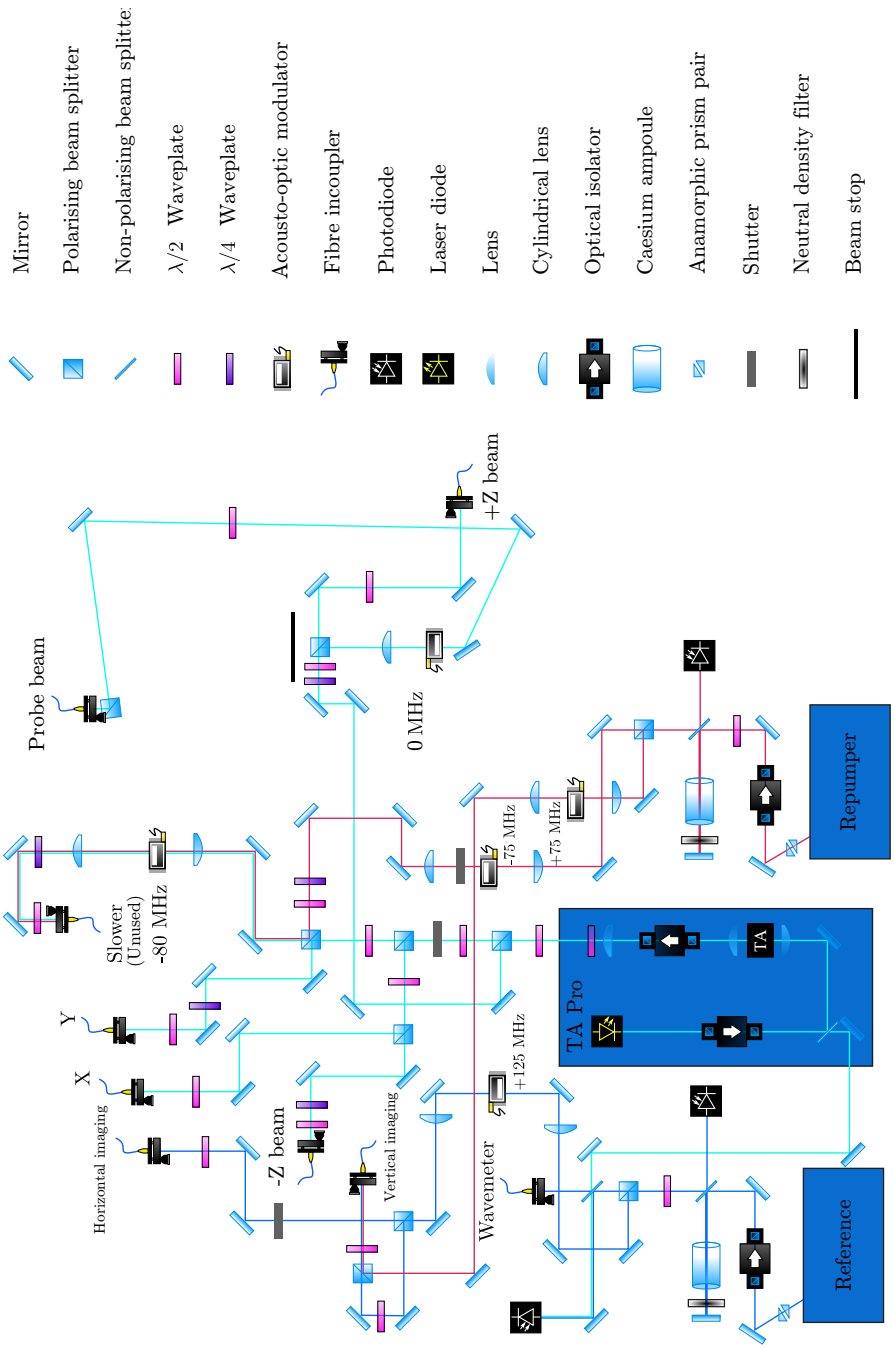


FIGURE 5.7: Laser setup for caesium laser cooling including some modifications for the QuILMI project.



FIGURE 5.8: Photo of the MOT under the evanescent field chip. Roughly 1×10^7 atoms are held about $1\,\mathrm{cm}$ from the chip surface.

5.1.2 Laser systems

Modified laser setup

The laser table setup for the QuILMI experiment is shown in Figure 5.7 and is the same as for the mixture experiment except for a few modifications. The first is that the vertical MOT beam is not retroreflected. Instead, the Raman lattice cooling setup is bypassed and used as a second vertical MOT beam. This arrangement helps us in three ways. Firstly, although the chips used in this experiment are largely transparent, the losses are significant enough to heavily affect a retroreflected beam. Thus, by using independent beams we do not suffer from unintentionally unbalanced beam strengths. Secondly, the intensities of the downward facing $-Z$-beam and the upwardly propagating $+Z$-beam can be independently controlled so we have an extra degree of freedom when aligning the MOT. Thirdly, a shutter in the $-Z$-beam path can extinguish the downward beam before the $+Z$-beam to generate an even greater imbalance of radiation forces that pushes the atoms up into the chip and the dipole trap focus. The final modification is to use one beam path of the Raman lattice cooling setup as a probe beam on the $F = 4 \Rightarrow F' = 5$ transition for the detection of atom-photon coupling in the chip. This arm propagates through the acousto-optic modulator (AOM) for rapid switching. Apart from these modifications the laser setup is the same as reported in theses [34, 35, 36].

The magneto-optical trap

The ^{133}Cs magneto-optical trap operates on the D_2 $6^2S_{1/2}, F = 4 \Rightarrow 6^2P_{3/2}, F' = 5$ optical transition with repumping on the D_2 $6^2S_{1/2}, F = 3 \Rightarrow 6^2P_{3/2}, F' = 4$ transition. We typically load about 1×10^7 atoms at a loading rate of $2 \times 10^6\,\mathrm{atoms/s}$ from a caesium vapour produced by the dispensers. The MOT cooling light beams each have a $1/e^2$ radius of about $12\,\mathrm{mm}$, and a peak intensity of about $5.7 I_{\mathrm{sat}}$, where $I_{\mathrm{sat}} = 2.71\,\mathrm{mW\,cm^{-1}}$ is the saturation intensity of the D_2 $F = 4 \Rightarrow F' = 5$ transition [38]. The horizontal beams are retroreflected while the vertical beams are formed separately. Each retro-reflected beam is ever so slightly focused to compensate for the shadow cast by the MOT. Since decay from $F' = 5$ to $F = 3$ is very unlikely, only weak repumping light ($8\,\mathrm{mW}$) through the y-axis beam is used. The cooling beams are detuned from the $F = 4 \Rightarrow F' = 5$ by $-15.5\,\mathrm{MHz}$ (-2.96Γ) while the repumping beam sits on resonance. With this configuration the atoms are trapped at about $300\,\mu\mathrm{K}$. The magneto-optical trap beam paths are shown in Figures 5.13a and 5.13b while optimal beam powers and coil currents are given in Table 5.1. Figure 5.12 shows the laser frequencies.

Considerable work has been put into optimising the QuILMI MOT. Since the MOT depends on so many variables, a full multi-dimensional analysis is not possible. Optimisation is therefore an iterative process in which each parameter is optimised individually one after the other. For some pairs of parameters

TABLE 5.1: QuILMI MOT optimal parameters. The optimal parameters for the MOT are those that best compromise between total atom number, density, position and temperature.

Property	Value
X cooler	$35\,\mathrm{mW}$
Y cooler	$35\,\mathrm{mW}$
Y repumper	$8\,\mathrm{mW}$
$+Z$ cooler	$35\,\mathrm{mW}$
$-Z$ cooler	$35\,\mathrm{mW}$
Coil current	$8.73\,\mathrm{A}$ ($11.2\,\mathrm{G\,cm^{-1}}$)
Detuning	-15.5 MHz (-2.9Γ)

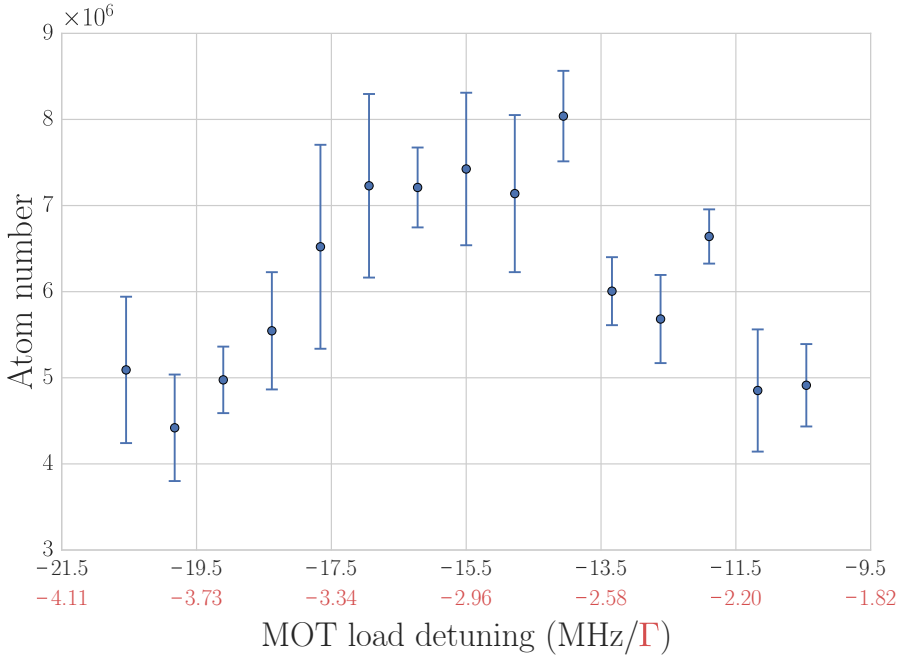


FIGURE 5.9: Atom number measured as a function of the laser detuning (Error bars show the standard deviation after four repeats). The other parameters were as given in Table 5.1. Peak atom numbers can reach ~1×10^7 after full optimisation.

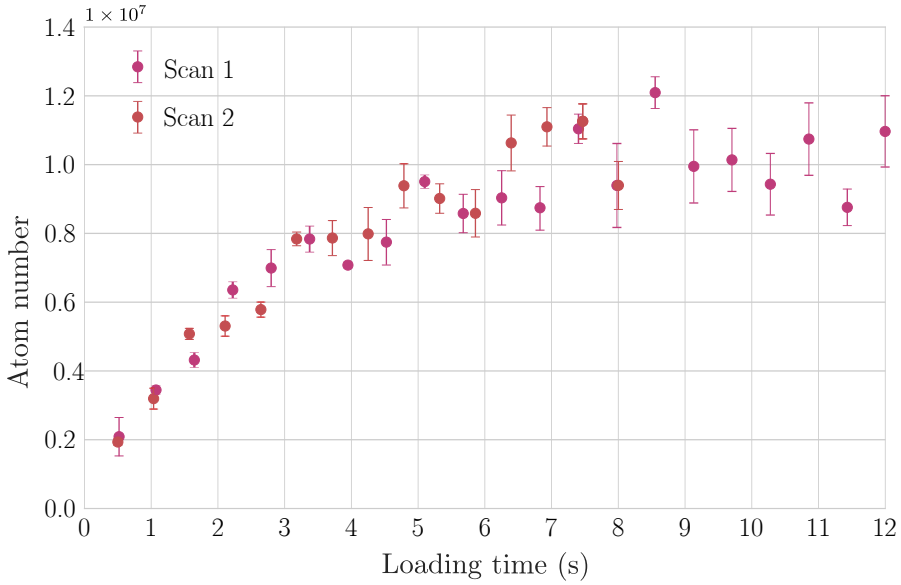


FIGURE 5.10: The MOT atom number as a function of time with optimal settings. The loading rate is approximately 2×10^6 atoms/s.

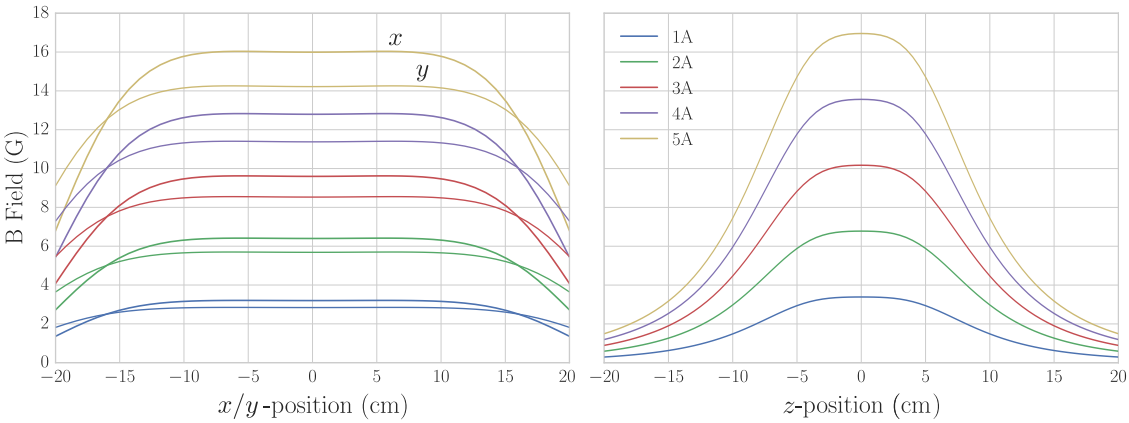


FIGURE 5.11: Fields produced by the horizontal and vertical compensation coils. The y-axis is defined as the axis that runs from the ion pump to the chamber (the same as the slower axis in the mixture experiment). The x-axis coils produce a stronger field for the same current because they have a smaller side-length and corresponding separation (to satisfy the Helmholtz configuration).

a two-dimensional analysis can be conducted, but most optimisation is performed on a single variable at a time. After many circuits the system is well optimised although we can never be sure that we are not just in a local minimum. The MOT is typically optimised for atom number, position and temperature in that order.

The total atom number in the MOT depends on many variables, in no particular order they are: beam alignments and radii, polarisations, cooling beam powers, repumping beam powers, laser detunings, field gradient, offset field strength, source strength and of course loading time. Figure 5.9 shows an example of a typical MOT optimisation analysis in which the atom number is measured as a function of the laser detuning. The optimal detuning is the same as for the ^{6}Li-^{133}Cs mixture experiment. After optimisation the MOT atom number is typically 1×10^7 (Figure 5.10).

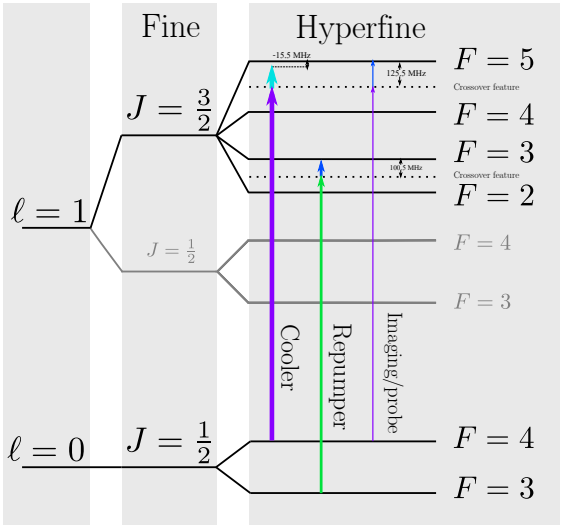


FIGURE 5.12: Frequencies used in the QuILMI experiment. The dark blue arrows represent AOMs while the light blue arrow indicates an offset lock which is VCO tunable. The thickness of the beams give a rough indication of the powers used.

The position of the MOT is controlled by the beam alignment, beam powers, field gradient and offset fields produced by the three sets of compensation coils (one for each axis). The fields produced by the compensation coils are plotted in Figure 5.11. The coils are mounted in the Helmholtz configuration in order to produce a homogeneous field at the chamber centre which displaces the field-zero and thus the location of the MOT. Each horizontal compensation coil comprises 75 windings of $1\,\mathrm{mm}$ diameter coated copper wire around square aluminium brackets (See Appendix C). The x-axis brackets have side-lengths of $40\,\mathrm{cm}$ while the y-axis brackets have side-lengths of $45\,\mathrm{cm}$. The z-axis coils are constructed in the same way as the MOT coils and are glued directly to the MOT coils. Each z-axis coil consists of 2 layers for a total of 30 windings. The compensation coils can be seen in Figure 5.33 and the bracket designs are given in Appendix C.4. The z-axis compensation coil has boosted importance in this experiment since it is used to launch the MOT into the chip and dipole trap. During MOT loading currents of a few hundred mA are typically fed to the compensation coils. For loading the dipole trap the z-axis coil current is ramped up to the maximum of $5\,\mathrm{A}$.

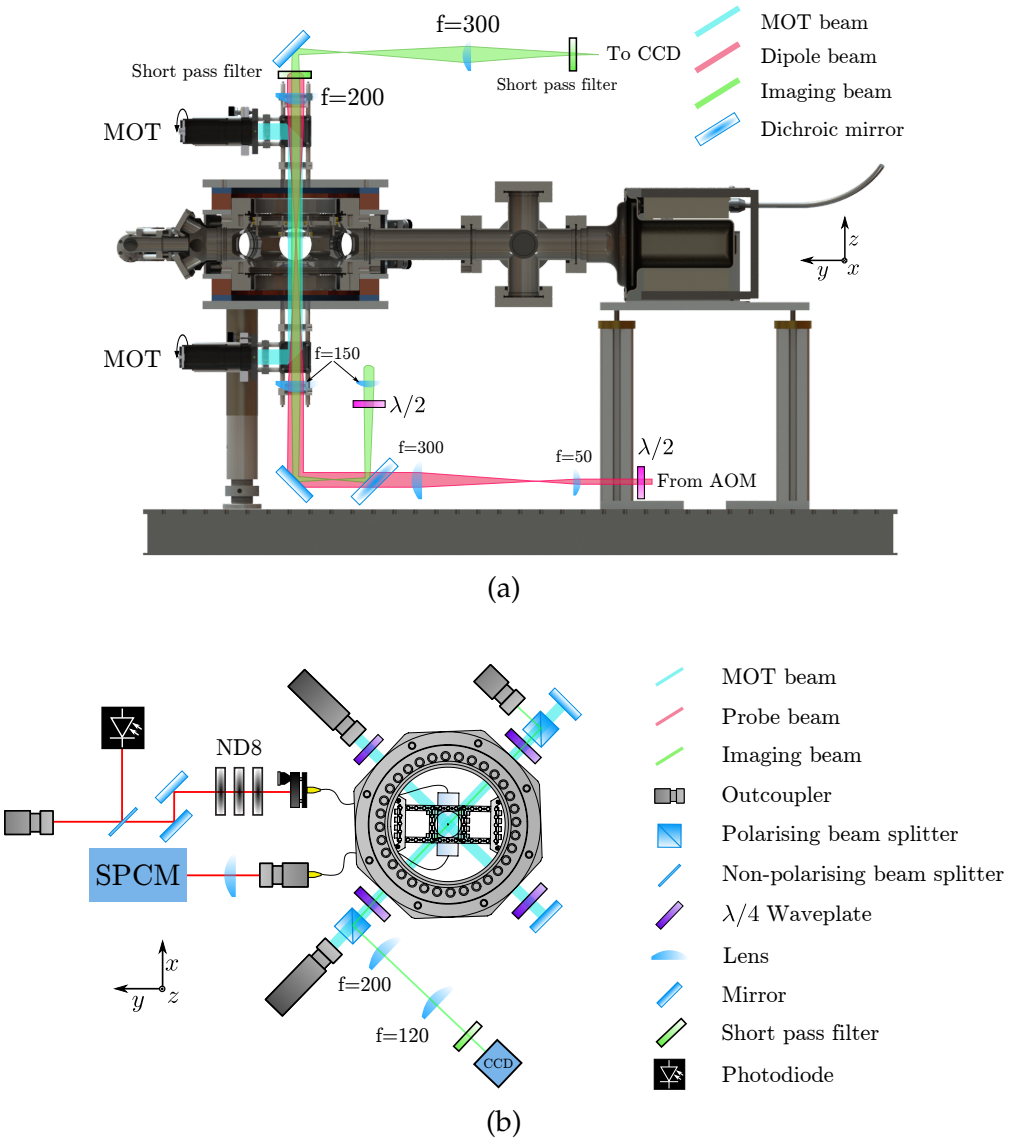


FIGURE 5.13: QuILMI beam setup. (a) Section view of the QuILMI chamber showing the vertical MOT, dipole and imaging beams. The 1064 nm dipole trap light is overlapped with the 852 nm imaging light using a Thorlabs DMLP950R dichroic mirror. The MOT beams are overlapped with the imaging light using a combination of polarising beam splitters, $\lambda/2$ and $\lambda/4$ waveplates and rotation of MOT outcouplers themselves. The vertical imaging magnification is 1.5. (b) Horizontal beam arrangement through the QuILMI chamber and experimental setup for experiments using the single-photon counting module. Both horizontal MOT beams (blue) are retroreflected. Two 1" Polarising beam splitters allow a horizontal imaging beam (green) to be overlapped with one of the MOT beams with little disruption. The horizontal imaging can either be set up along the MOT axis this way or through the two spare viewports. The horizontal imaging magnification is 0.6.

The dipole trap

A ray diagram of the dipole trap optics is shown in Figure 5.14 which includes a zoomed-in view of the beam waist as it passes through the fibre. A beam of 15-50 mW of 1064 nm light from a Coherent Mephisto S is used to seed a 30 W Nufern NuAMP fibre amplifier (See Appendix B). The beam begins collimated out of the fibre outcoupler with a $1/e^2$ radius of approximately 1.2 mm. The beam is immediately fed through a Gooch and Housego AOM (model 133421) for switching and future evaporative cooling purposes. Two 50 mm cylindrical lenses are used to optimise coupling into the first-order which can typically reach about 80%. Unwanted light in the other orders is dumped into a bent copper tube coupled to the table. In Figure 5.14 a -50 mm focal length planoconcave lens expands the beam before it is collimated with a 300 mm focal length planoconvex lens. This was the original design, but due to a lack of achromatic planoconcave lenses an equivalent setup was installed using an achromatic 50 mm focal length planoconvex lens. The beam is therefore focused before being expanded resulting in a slightly longer beam arrangement. After collimation the

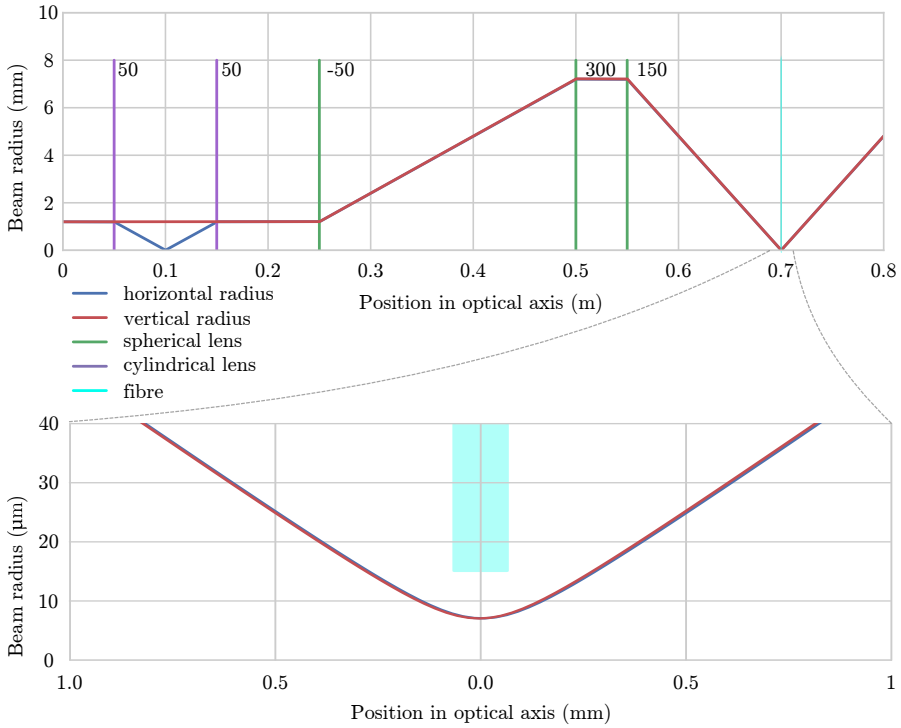


FIGURE 5.14: Ray diagram of the vertical dipole trap arrangement. The lower plot shows a zoomed in view of the beat waist at the point of the fibre.

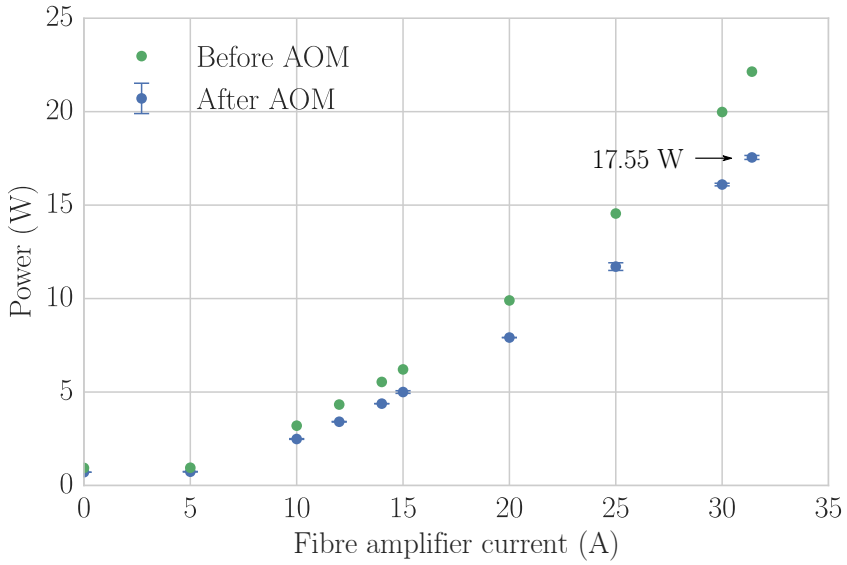


FIGURE 5.15: The Nufern NuAMP fibre amplifier calibration. Although the amplifier is rated as being 30 W, in reality we can only achieve 23 W which is cut by 20% after passing through the AOM.

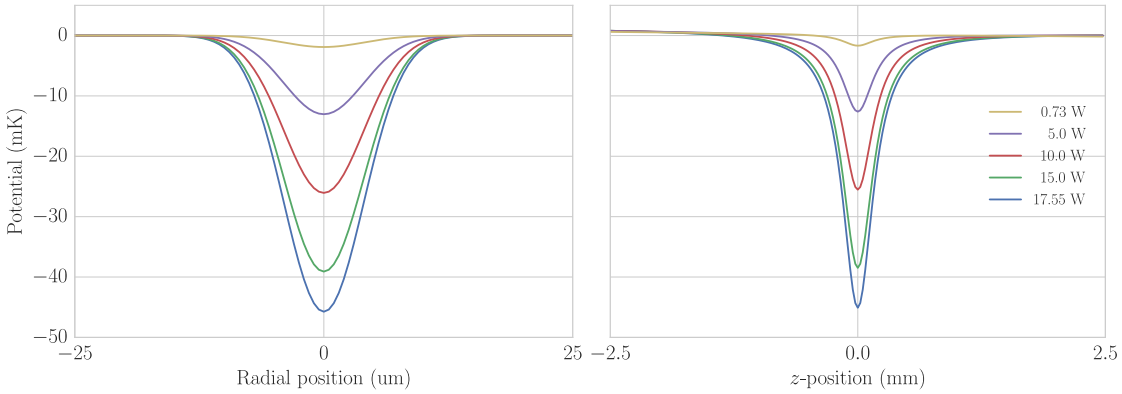
beam hits two large 2" mirrors before hitting a 150 mm focal length planoconvex lens mounted on the lower cage system as shown in Figure 5.13a. The beauty of having the dipole beam collimated before it hits this lens means the focus can be easily translated into the plane of the chip. One of the two 2" mirrors below the chamber is fitted with two New Focus Picomotor piezo linear actuators (model no. 8302) for precise angular control of the dipole beam (needed for piercing the 30 µm fibre hole or the 69 µm fliced void in the waveguide chip). The 150 mm focal lens produces a final beam waist of ~8 µm which is small enough to pass through both the fibre and the waveguide chip.

Although the NuAMP fibre amplifier is rated 30 W, the maximum power we can actually obtain is closer to 23 W[3]. A full power vs current curve is plotted in Figure 5.15 from which one can see that after passing through the AOM we are left with ~18 W. The actual power at the position of the atoms is likely to be lower still due to losses from the optical elements, especially the polarising beam splitter. Figure 5.16a shows the potential produced by the dipole beam produced by the fibre amplifier as a function of power. Because the beam is focused to a narrow waist, low operating powers of ~1 W can still lead to a

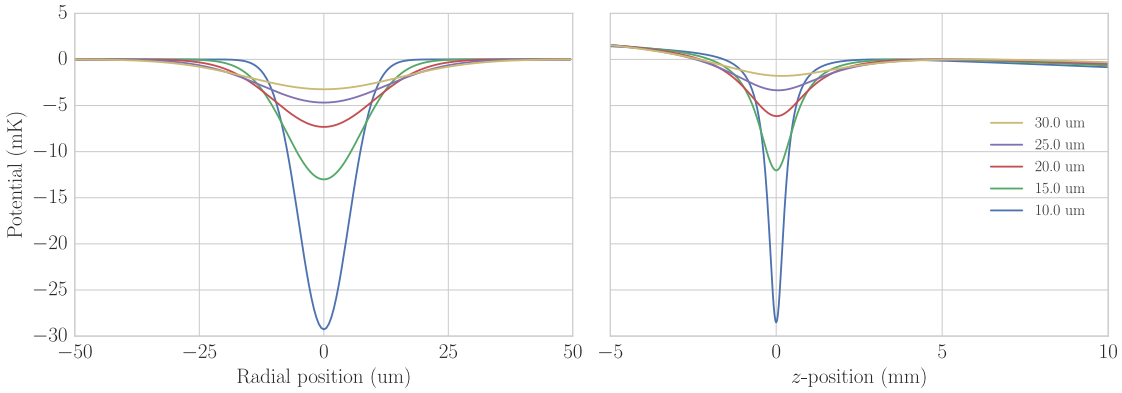
[3]Updating the control program of the Nufern NuAMP should allow us to use higher currents and reach the rated the rated power output according to the manufacturer.

deep trapping potential of $>10\,\mathrm{mK}$.

Unfortunately for our real-world system, such a small waist has not been achieved to date. Recent measurements, taken by reflecting the beam away from the chamber and imaging on a charge-coupled device (CCD) camera, put the $1/e^2$ radius to be $22\,\mu\mathrm{m}$ (see Figure 5.32) which has a drastic effect on the beam's trapping ability. Figure 5.16b shows the trapping potential as a function of beam waist for the maximum power of $17.55\,\mathrm{W}$. Widening the beam waist to $22\,\mu\mathrm{m}$ shrinks the z-axis trap depth by 92% from $45\,\mathrm{mK}$ to $4\,\mathrm{mK}$. This is largely because the trap depth is directly proportional to the beam intensity which has a $1/x^2\exp(-1/x^2)$ dependence on the beam waist [98]. That combined with the gravitationally induced tilt causes a dramatic loss of axial trap depth. Despite this, radially the trap is still $5\,\mathrm{mK}$ deep and vertically still $4\,\mathrm{mK}$ deep. This is still a deep trap for our caesium atoms which are routinely measured to be around $30\,\mu\mathrm{K}$ at the end of optical molasses. In fact for optimal dipole trap loading, one ideally wants a trap at least eight times deeper than the temperature of the atoms [98].



(a) Theoretical potentials produced by an $8\,\mu\mathrm{m}$ waist $1064\,\mathrm{nm}$ dipole beam for the full range of power available to us. Each line is a cross-section of the potential along either the strong (radial) or weak (longitudinal) axis of the trap. It is important to notice that the left-hand graph is in units of $\mu\mathrm{m}$ while the right-hand graph is in units of mm.



(b) Theoretical potentials produced by the $1064\,\mathrm{nm}$ dipole trap at maximum power of $17.55\,\mathrm{W}$ for more achievable waists. Each line is a cross-section of the potential along either the strong (radial) or weak (longitudinal) axis of the trap. It is important to notice that the left-hand graph is in units of $\mu\mathrm{m}$ while the right-hand graph is in units of mm. At a waist of $30\,\mu\mathrm{m}$, more than three times the desired waist, the trap is still $2\,\mathrm{mK}$ deep in the vertical direction.

FIGURE 5.16

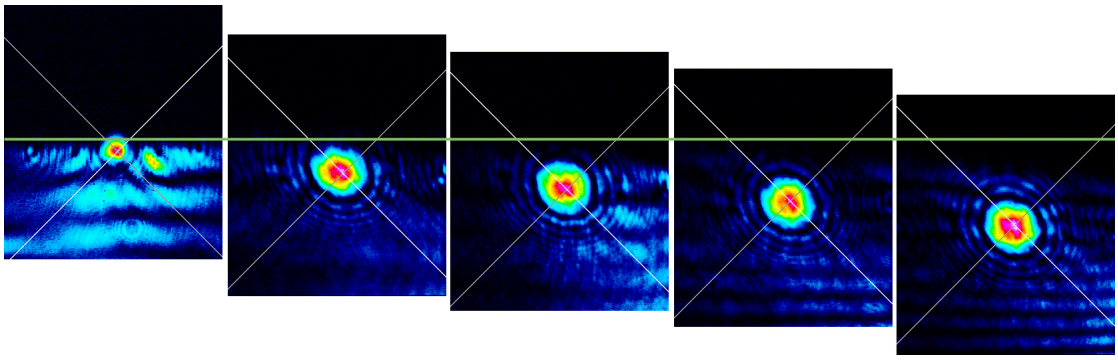


FIGURE 5.17: The extent of the evanescent field in the test waveguide chip. The green line indicates the air-chip interface. Photos printed with permission from Amir Moqanaki of the University of Vienna.

5.2 Waveguide and fibre chip experiments

A number of different waveguide chips have been made for this project by our collaborators Dr. Alexander Szameit and Toni Eichelkraut at The University of Jena using a femtosecond laser. The writing process is as follows. The femtosecond laser is tightly focused inside a transparent fused silica chip and rapidly pulsed as the chip is translated on a high-precision, programmable 3D translation stage. The femtosecond pulses change the refractive index of the glass in the immediate vicinity by an amount proportional to the laser intensity. It is this small change in refractive index that guides the light. However, because the writing process uses a focused gaussian beam, the resultant waveguide cross-section is elliptical which can make mode-matching difficult, especially for connecting a waveguide to a fibre. Furthermore, the pulsed nature of the writing process means the refractive index along the waveguide varies periodically. This effect can be mitigated by writing multiple times with appropriate phase offsets, but it cannot be completely eliminated.

However, these are just small prices to pay for the versatility offered by this technique. Complex waveguide designs such as beamsplitters, interferometers etc. can be written into a chip with an impressive turn-around time. Because the chip can be moved vertically as well as horizontally, the femtosecond-laser is free to explore all three dimensions of the chip for ultimate sophistication and miniaturisation.

The first strategy to couple atoms with photons on a chip was to utilise the

evanescent field of the waveguide mode profile. However, for reasons explained in Subsection 5.2.1, this was quickly abandoned in favour of a more direct approach. The new strategy was to etch a small void in the waveguide using FLICE such that the atoms could be trapped in free-space and probed directly via the waveguide. In addition, the feasibility of a fibre with a laser-eteched void was explored. In the following subsections I will discuss the work and experiments conducted on the various chips.

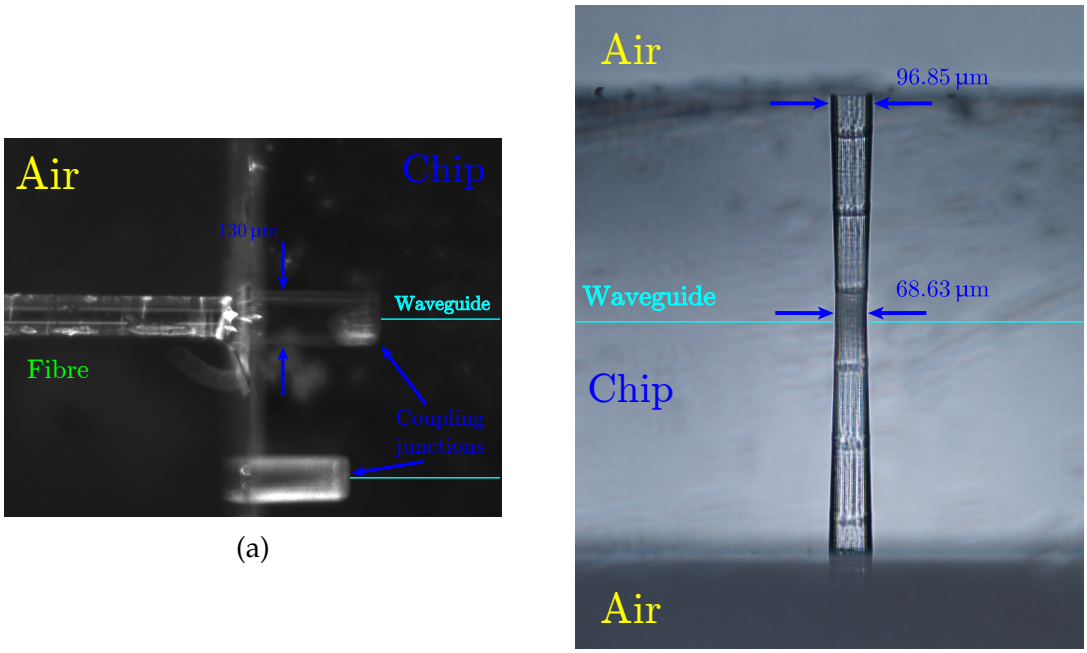
5.2.1 Evanescent field chip

The first chip to be investigated was a $30\,\mathrm{mm} \times 20\,\mathrm{mm} \times 1\,\mathrm{mm}$ test chip with a large number of waveguides written into it. The waveguides themselves ran parallel to the long edge of the chip spaced $200\,\mu\mathrm{m}$ apart and had small, very elliptical, $11\,\mu\mathrm{m} \times 3\,\mu\mathrm{m}$ mode field diameters. The goal of this experiment was to explore the feasibility of atom-photon coupling via the evanescent field of light propagating along a waveguide. For this purpose the waveguides were written at various different depths from the surface of the chip. Prior to receiving the chip in Nottingham, an experiment was conducted at the University of Vienna by Amir Moqanaki. He coupled a few $\mu\mathrm{W}$ of $780\,\mathrm{nm}$ light into each waveguide and measured the extent of the waveguide mode into the surrounding air. Photos from this experiment can be seen in Figure 5.17. From the Figure, one can see the light is well confined; the extent of the evanescent field protrudes beyond the surface of the chip only when the light is coupled into the shallowest waveguide. With this knowledge, we continued to investigate the shallowest waveguide and installed the chip into our newly built chamber. At this point the fibre feedthroughs and MOT had been tested with excellent results but the dipole trap was still under construction. The objective was to simply hold the atoms as close to the chip surface as possible and to measure any interaction between the chip and the atoms.

The test chip arrived with many surface imperfections across each of its faces. This badly affected both the mode profile of the waveguide and the fibre coupling which could consequently only maximally reach efficiencies of approximately 4% per interface. With significant polishing of the chip edge, this was eventually improved to 10%. Poor coupling was entirely expected due to

the highly elliptical mode profile of the waveguide. In addition, the small refractive index , $\Delta n = 0.7 \times 10^{-3}$, between the waveguide and the surrounding chip volume means the waveguides have a numerical aperture (NA) of just ~0.045. For comparison, the NA of a single-mode Thorlabs 780HP fibre is 0.13. This all means the fibre and waveguide must be exceptionally well-aligned in order to couple light from one to the other. Photos of the fibre coupled evanescent field chip can be seen in Figures 5.3a and 5.3b.

With the chip installed, several milliwatts of $852\,\mathrm{nm}$ light was coupled into the fibre connected to the chip. First tests were promising as the MOT was noticeably displaced by the waveguide light. Unfortunately, rather than being from the evanescent field of the waveguide, the perturbing light was merely the uncoupled light escaping at the highly lossy fibre-chip interface. Without any sensitive photodetectors available to investigate absorption the evanescent field chip was abandoned at this point.



(a) (b)

FIGURE 5.18: Annotated photos of the waveguide chip with fliced coupling junctions and voids. (a) The fibre is inserted into the coupling junction and glued into place using a refractive index matching epoxy. The end of the bare fibre abuts the endface of the waveguide (which is invisible with conventional imaging methods and so drawn on). (b) The waveguide is intersected by a void with a 68.63 µm diameter at its narrowest point in which the atoms are held. Original photos taken by Toni Eichelkraut of the University of Jena.

5.2.2 Fliced void chip

From the evanescent field chip experiment we learned two main lessons. That the evanescent field of femtosecond-laser written waveguides can only extend ~2 µm beyond the chip surface and so does not produce significant overlap with cold atoms. And that fibre-waveguide coupling is a challenging and time-consuming process. After significant discussion it was agreed that our collaborators at the University of Jena would begin fabricating chips with features designed to combat these issues:

- **Intersected waveguides**
  Instead of using the evanescent field, the new chip would give waveguided light direct line-of-sight to cold caesium trapped directly at the centre

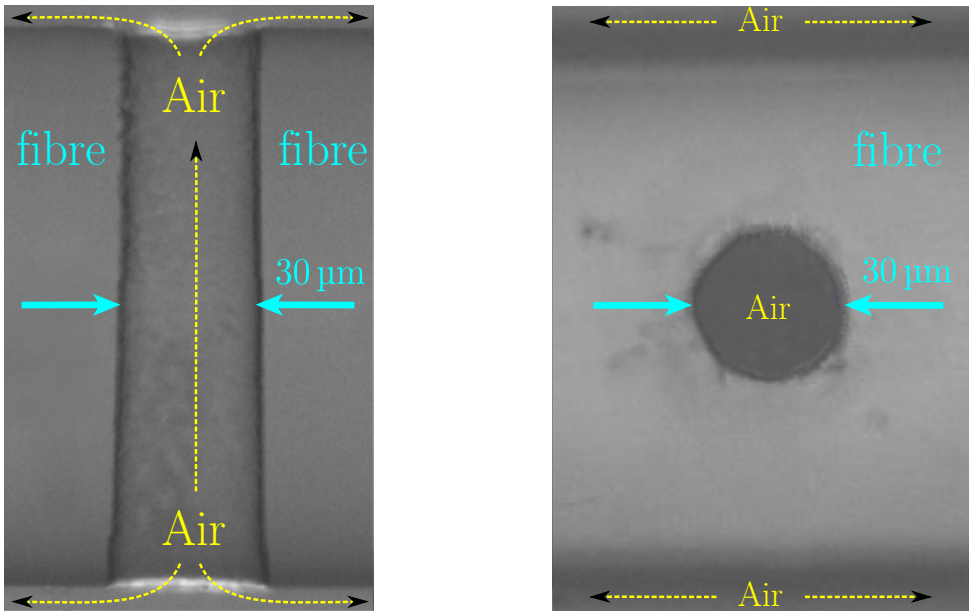
of the waveguide. Using Femtosecond Laser Irradiation followed by Chemical Etching (FLICE) we would etch a microscale void through the waveguide through which atoms could be trapped using a free-space dipole trap.

- **Improved fibre-waveguide coupling**
  Using FLICE, fibre-waveguide coupling junctions could be fabricated. Holes slightly larger than a single-mode fibre were to be etched into the ends of the waveguide. The fibre could then be slotted into the hole and glued in place using a refractive index matching epoxy. This would provide good axial alignment and thus boosted coupling efficiencies. In addition, the waveguides would be written with larger mode profiles that would better match the Thorlabs 780HP single-mode fibres we were using.

The coupling junctions and voids are shown in Figure 5.18.

In practice, the coupling junctions resulted in a lower coupling efficiency than direct endface-to-endface fibre-waveguide coupling. First attempts to fibre couple were disappointing with best results being a mere 10-15% for each facet. Application of the refractive index matching adhesive was also very difficult due to its high viscosity. Even if all had gone well, and one had managed to couple with a high efficiency and apply the glue gently enough, upon setting the glue would expand and move the fibre around relative to the wave guide causing high losses and in some cases eliminating the coupling entirely.

As a precaution, the fliced void chips also carried waveguides without coupling junctions. With a significant amount of polishing we could achieve roughly 40% coupling into one of these waveguides (tested using a waveguide without a void). However, catastrophically high losses were measured at the void such that no transmission could be detected at all with the equipment available at the time. For these reasons a fliced waveguide chip was never fully investigated.



(a) (b)

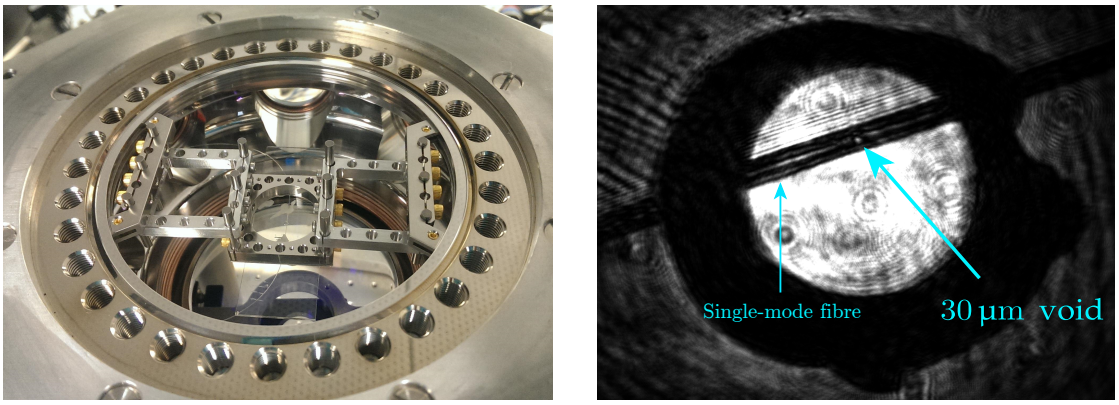
FIGURE 5.19: Photos of the 30 µm laser drilled hole in a Thorlabs 780HP single-mode fibre taken by Workshop of Photonics . (a) A side-on shot of the fibre void. (b) A top down view of the fibre void. A small amount of damage from the drilling process can be seen around the edge of the hole on the fibre surface.

5.2.3 Fibre chip

With poor coupling to the waveguide chips and a long lead time to the next chip (on the order of months), a new chip was designed and built based on single-mode and multi-mode fibres with laser drilled voids. With fibres, we would immediately bypass the problem of poor coupling; the only coupling required would be free-space coupling into and out of the fibre which can reach efficiencies upwards of 80%.

Chip construction

The chip construction was as follows. A 1 mm diameter hole was carefully drilled through a standard off-the-shelf microscope slide with dimensions of 76 mm $\times$ 26 mm $\times$ 1 mm. Before we could attach the fibre, the fibre's protective coating had to be removed. This was first attempted chemically using xylene stripper, but ultimately the best unsheathing method discovered was to use a fibre stripping tool (Thorlabs T08S13 normally used for connectorisation) to 'munch'



(a) (b)

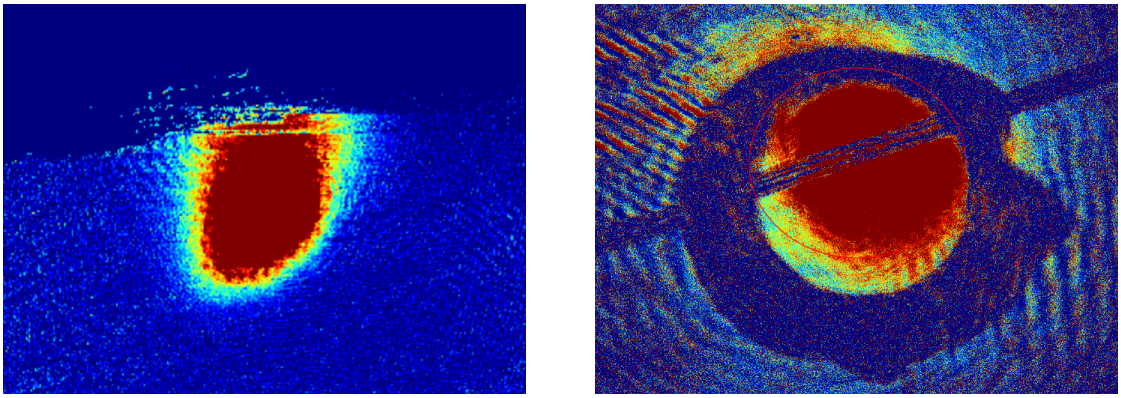
FIGURE 5.20: The mounted fibre chip and a raw image of the fibre suspended over the 1 mm drilled hole taken with the vertical imaging setup. The 30 µm hole is clearly visible from this angle.

and scrape the coating before wiping it down with acetone. The fibre was then suspended over the hole as centrally as possible before being glued into place using UV-cured UHV compatible epoxy (DYMAX OP-67-LS). The fibre plus microscope slide assembly was then sent to a company (Workshop of Photonics) for laser drilling using a high-power femtosecond laser. Four chips were manufactured using this technique with three types of fibre: two single-mode 780HPs, one single-mode polarisation maintaining PM780HP and one multimode HPSC10 (all Thorlabs). Each fibre was drilled with a 30 µm diameter through hole perpendicular to the fibre axis. This hole diameter was chosen as a good compromise between maintaining structural integrity and the required dipole trap beam waist. Only two fibre chips made it back to the laboratory intact, one 780HP and the HPSC10. The others were broken during the drilling process. A likely explanation is that tensional forces from the glue holding the fibre to the microscope slide pulled the fibre apart after the fibre's structural strength had been compromised by the drilling process. This can be avoided in the future by ensuring there is no stress on the fibre during the gluing process. Unfortunately, the HPSC10 fibre was broken due to mishandling in the laboratory. Although the laser drilled hole remained intact, the fibre was accidentally snapped making it too short to be installed. The chip holding the Thorlabs 780HP single-mode fibre was carefully installed into the QuILMI chamber. The 30 µm laser drilled hole can be seen in Figure 5.19 and the mounted fibre chip

is shown in the vacuum chamber in Figure 5.20a. The pale opaque spots on the surface of the chip are the blobs of epoxy used to attach the fibre to the microscope slide and to attach the microscope slide to the steel plate (eV parts SS-PL-C5X5-R1000) for clipping on to the internal mounting assembly. These blobs obstruct the fibre along the designated imaging axis and motivated the decision to overlap the imaging axis with one of the horizontal MOT beams as shown in Figure 5.13b. The original horizontal imaging setup can be seen in Figure 5.33. With the fibre chip installed, the chamber was gently baked for three days at just over $100\,^{\circ}\mathrm{C}$ while making sure the fibre feedthroughs stayed cooler than $80\,^{\circ}\mathrm{C}$. After baking, the pressure read by the gauge on the QuILMI chamber (Pfeiffer IKR-270) was ~$1 \times 10^{-9}\,\mathrm{mbar}$. However, in order to maximise optical access to the science chamber the gauge was installed some way away on the six-way cross in front of the $40\,\mathrm{l\,s^{-1}}$ ion pump. Therefore the reading is very likely to be an underestimation of the pressure at the position of the atoms.

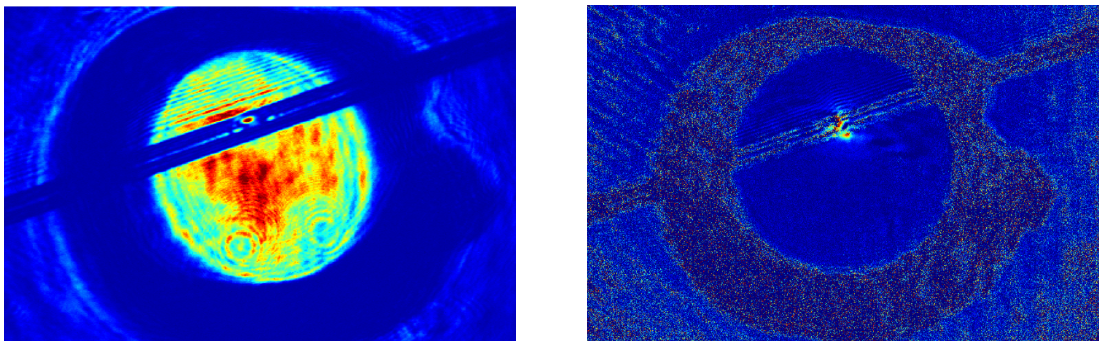
5.2.4 MOT and dipole trap alignment

Positioning the MOT as close as possible under the fibre hole turned out to be a more difficult process than anticipated. Even with both vertical and horizontal imaging and three sets of compensation coils, getting the MOT to appear under the chip on the vertical camera was challenging. This was largely due to the



(a) (b)

FIGURE 5.21: Horizontal and vertical absorption images of the MOT positioned under the fibre. Approximately 1×10^7 atoms are held. (a) Here the MOT can be seen encompassing the fibre and extending well above it. (b) From above we see that the MOT is very well aligned to the fibre and the fibre hole.



(a) (b)

FIGURE 5.22: Aligning the dipole trap. (a) A snapshot of the beam alignment process with the dipole beam highly attenuated and the short pass filter removed (not an absorption image, illumination is from the dipole beam light). The beam waist is minimised before the spot is migrated to the fibre hole. Here the beam is slightly offset from the hole position. (b) An absorption image taken after alignment to the hole. The fibre heavily distorts the image such that we cannot be sure if the beam is passing through the hole.

fact that both the edge of the hole in the microscope slide and the fibre scatter a considerable amount of light, the former being almost entirely opaque. The hole and fibre therefore cast shadows in the $-Z$-beam precisely where the ideal MOT position is. In future experiments, the hole in the microscope slide should be made much larger than the extent of the MOT. A hole diameter of $2\text{-}3\,\mathrm{mm}$ should suffice.

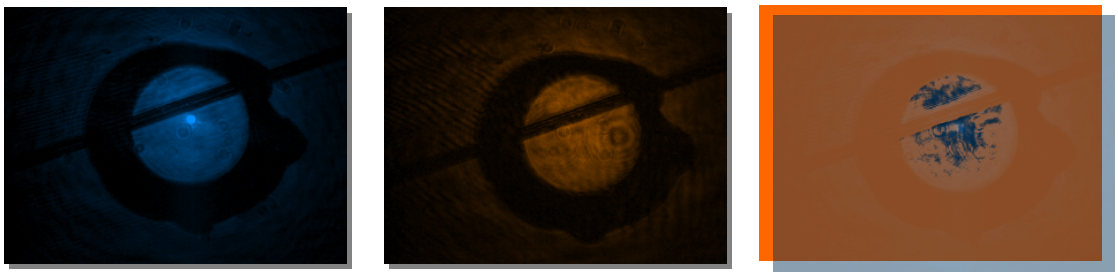
Aligning the MOT to the hole as seen in Figure 5.13 was performed in real time with three imaging systems running simultaneously: horizontal fluorescence imaging, vertical absorption imaging and handheld fluorescence imaging using an infra-red finger camera (Conrad CCD Fingerkamera 1/3" S/W). The hand-held camera was integral to the alignment process as it could be panned around the MOT to give a clear indication of where it was in space. With three viewing angles, the MOT was migrated to the fibre using a combination of beam power adjustment, beam alignment, field gradient tuning and offset field adjustment. Despite it being a non-ideal environment however, large atom numbers ($\sim 1 \times 10^7$) could be trapped as shown shown in Figure 5.13.

Aligning the dipole trap to the microscope slide hole was a comparatively easy process. Since the chip scatters a lot of light, the dipole trap beam position in the plane of the chip is visible on an infra-red camera. With the amplifier

tuned to minimum power (~1 W) and the AOM reducing the power further to ~20 mW, the beam is easily migrated to the hole. Fine alignment to the fibre void however, is significantly more difficult because at this point there is no longer any chip surface with which to track the dipole beam position. With the short pass filter (Thorlabs DMLP950) in the path of vertical imaging beam removed (Figure 5.13a) and a number of neutral density (ND) filters in place for heavy attenuation of the dipole beam, the dipole beam waist can be optimised in the plane of the fibre. With the vertical imaging camera well focused on the fibre, the final 150 mm focusing lens underneath the chamber is translated up and down until the observed beam waist is at a minimum.

The beam is then migrated to the fibre (the beam is visible through the fibre) and translated along the fibre axis to the fibre hole. Illuminated from below, either by dipole beam light or imaging light, the fibre void can be clearly seen by the vertical imaging camera as a light blue dot(Figures 5.20b and5.22a). However, since vertical absorption images are heavily distorted by the fibre (see Figure 5.34) there is no definitive sign of good alignment and from here we proceed using a combination of guesswork and iteration. Before the trap is loaded in this position, it is optimised away from the fibre in free-space where it can be analysed more easily free from optical aberrations.

At a certain point during dipole trap optimisation, it was noticed that the dipole trap beam position seen on the camera did not exactly correspond to the position of the trapped atoms when imaged with resonant 852 nm light. Figure 5.23 shows the displacement. The first image shows the dipole beam position during alignment (bright blue spot) which has been purposely offset from the fibre so that it can be seen more clearly. The second image shows a subsequent absorption image of dipole trapped atoms (dark spot). In the final panel in Figure 5.23 the first image has been overlapped with a negative of the second image revealing a distinct offset between the beam position and the position of the trapped atoms. The cause of this is likely to be chromatic aberrations in the imaging system or the slightly different beam paths of the dipole beam and imaging light. This offset (as viewed on the monitor) was recorded and taken into account for all future attempts to overlap the trap with the fibre hole.



Dipole beam on camera | Absorption image | Overlapped

FIGURE 5.23: Displacement between the beam spot and the trap position. The left hand image shows the position of the dipole beam seen by the vertical imaging camera at low power. The middle image is an absorption image of dipole trapped atoms with the beam path unchanged. The final image is the first image overlapped with the negative of the second image. Looking closely one can notice the blue spot and the orange spot are slightly displaced from one another.

5.2.5 Dipole trap optimisation

After collecting as many atoms as possible in the MOT, the atoms must be cooled to very low temperatures in order to be captured in the dipole trap (a conservative potential). The temperature of the atoms is first optimised in the MOT in the absence of a dipole trap using optical molasses. The optical molasses step involves simultaneously increasing the MOT beam detuning while reducing the magnetic field gradient. This is surprising given that theory predicts that the minimum temperature achievable (the Doppler temperature) should be

TABLE 5.2: Optimal dipole trap loading parameters. Downward arrows indicate a step while horizontal arrows indicate a ramp.

Property	QuILMI	Mixture
Duration (ms)	7	40
Cooler power	max	max
Repumper power (mW)	max $\Downarrow 0.96(12\%) \Rightarrow 0.18(2.3\%)$	max
MOT field ($\mathrm{G\,cm^{-1}}$)	$11.2 \Rightarrow 9$	$12.5 \Rightarrow 12.5$
Detuning (MHz)	$-15.5 \Rightarrow -79$	$-15.5 \Rightarrow -77$
Detuning (Γ)	$-2.9 \Rightarrow -15.1$	$-2.9 \Rightarrow -14.9$
Temperature (K)	$200 \Rightarrow 20$	$200 \Rightarrow 16$
Efficiency	80%	80%
Loading eff.	0.1%	2%

at $-\Gamma/2$. The reason for this is that although Doppler cooling is inefficient at large detunings, *sub*-Doppler cooling mechanisms function better at large detunings. The mechanism behind this is explained in Section 3.4. Strictly speaking, optical molasses should also be performed in the absence of a magnetic field (see Section 3.3). However, we obtain better results by ramping the field down gradually to a shallower gradient. At the same time as ramping the field down the cooling beam power is kept constant and the cooler detuning is increased to $79\,\mathrm{MHz}$ (15.1Γ) which is the maximum detuning possible with our setup. At the start of the optical molasses the repumping power is stepped down to $1\,\mathrm{mW}$ and then ramped down to $184\,\mu\mathrm{W}$. The optimal optical molasses settings for the QuILMI experiment and the ^{6}Li-^{133}Cs mixture experiment are listed in Table 5.2 for comparison. The QuILMI optical molasses settings differ considerably to those used for the same procedure in the ^{6}Li-^{133}Cs mixture experiment. Most apparent is the difference in durations; the QuILMI optical molasses is performed almost six times faster than the mixture optical molasses. Currently with optical molasses we retain $> 80\%$ of the 1×10^{7} initially trapped atoms and cool them to a final temperature at $30\,\mu\mathrm{K}$ in 5-7 ms ready for loading into the dipole trap. Figure 5.25 shows a temperature measurement performed on the atoms after optical molasses using the horizontal imaging setup and the time-of-flight method. The high temperature of $55\,\mu\mathrm{K}$ is simply because the data was taken before optimisation. Typically such a precise measurement of the cloud temperature is unnecessary and one-point measurements suffice for the purposes of optimising dipole trap loading. Figure 5.26 shows how the measured dipole trap atom number changes with the final MOT field gradient. The atom number was measured using absorption imaging along the vertical axis after a short fall time of $1\,\mathrm{ms}$. The dipole trap loading efficiency shown here is low compared to the mixture experiment (See Table 5.2). This is likely because the dipole trap beam used in the mixture experiment has a beam waist that is roughly $4\times$ larger ($80\,\mu\mathrm{m}$ waist instead of $< 22\,\mu\mathrm{m}$) and so can accommodate more atoms.

Since the fibre chip is positioned above the MOT, in order to load the dipole trap a combined optical molasses cooling and throwing process is performed. The control system sequence for a typical atom-photon coupling experiment is shown in Figure 5.24.

At the same time as optical molasses, the MOT is thrown upwards into the chip. The necessity of this step depends on where the MOT is initially loaded.

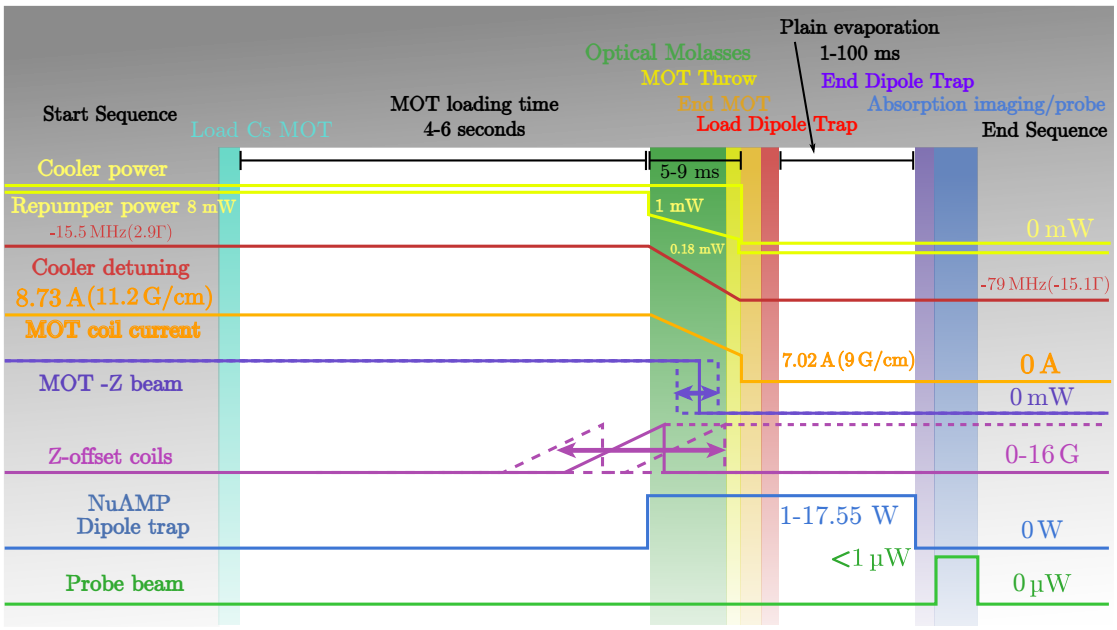


FIGURE 5.24: The dipole trap loading sequence including atom-photon coupling.

In Figure 5.13 the MOT can be seen engulfing the fibre and so very little or no pushing was needed. In general however, the MOT performs better, in terms of loaded atoms and final temperature, further away from the chip surface so a throwing step is necessary.

The MOT throw is performed by ramping the z-axis bias field and extinguishing $-Z$-beam before the $+Z$-beam. The z-axis coil current can either remain at its final value at the end of the ramp or switch to zero. Both methods work, but the latter leads to higher final atom numbers and cooler temperatures. Figure 5.28 shows the temperature of the atoms in the dipole trap as a function of the optical molasses duration while Figure 5.27 shows the temperature dependence on the final z-axis compensation coil current.

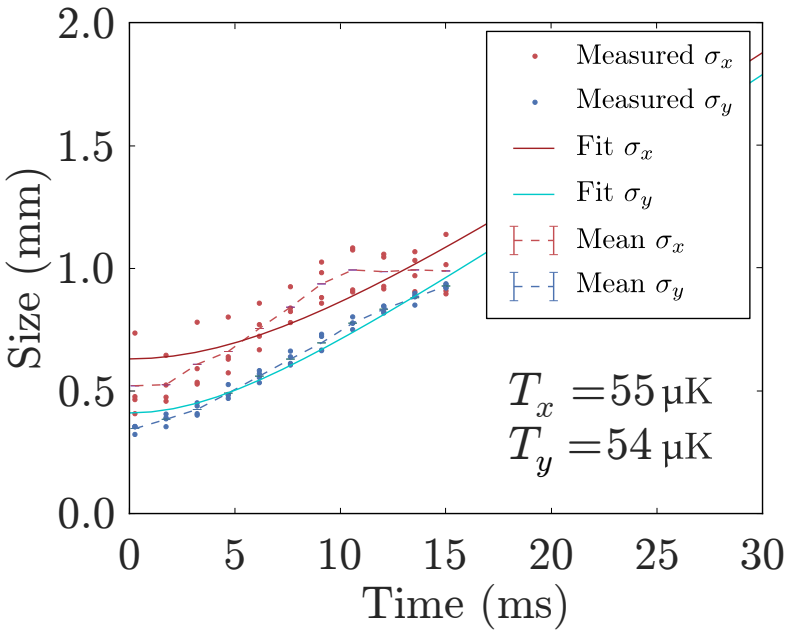


FIGURE 5.25: MOT temperature after optical molasses. The temperature is obtained by fitting the cloud's spatial extent with a Gaussian in both the x and y directions for increasing times t. The standard deviations squared, σ_x^2 and σ_y^2, are plotted as a function of t^2 and the resulting trend has a slope equal to $k_B T/m$.

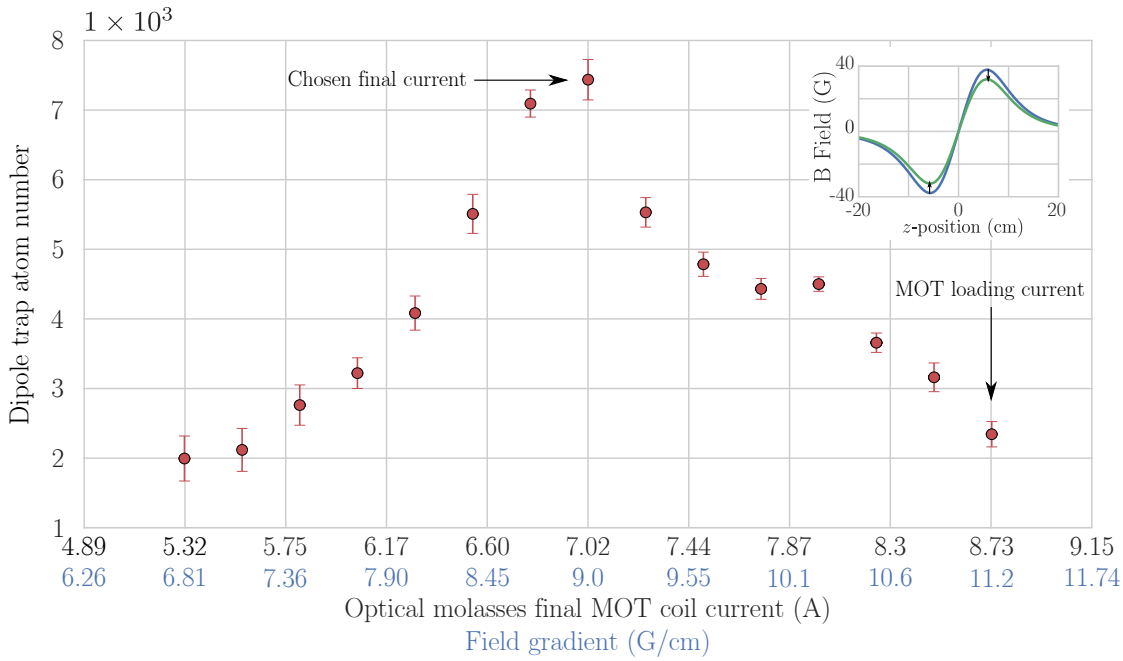


FIGURE 5.26: Atom number in the dipole trap as a function of the final field gradient in the optical molasses step.

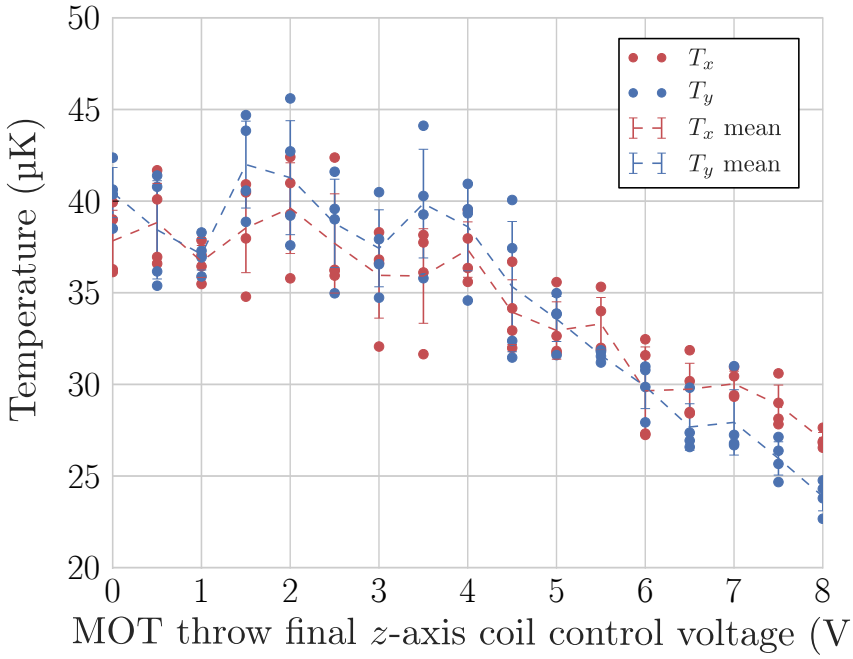


FIGURE 5.27: Temperature in the dipole trap as a function of the final z-axis coil control voltage. Measurements taken after 1 ms of expansion.

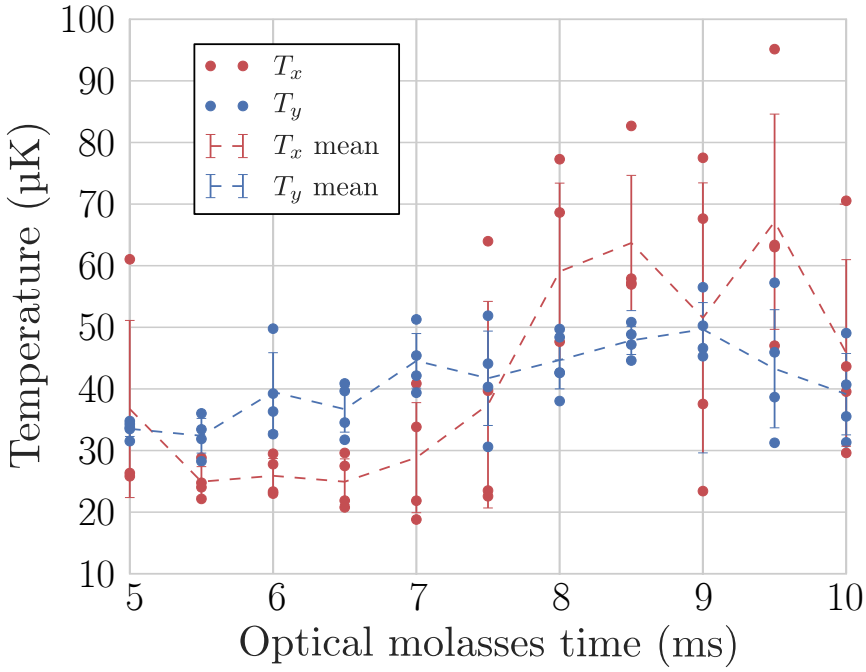


FIGURE 5.28: Temperature in the dipole trap as a function of the optical molasses duration measured using a single point time-of-flight method. The optimal optical molasses duration differs greatly from the mixture experiment procedure which lasts 40 ms. Measurements taken after 1 ms of expansion.

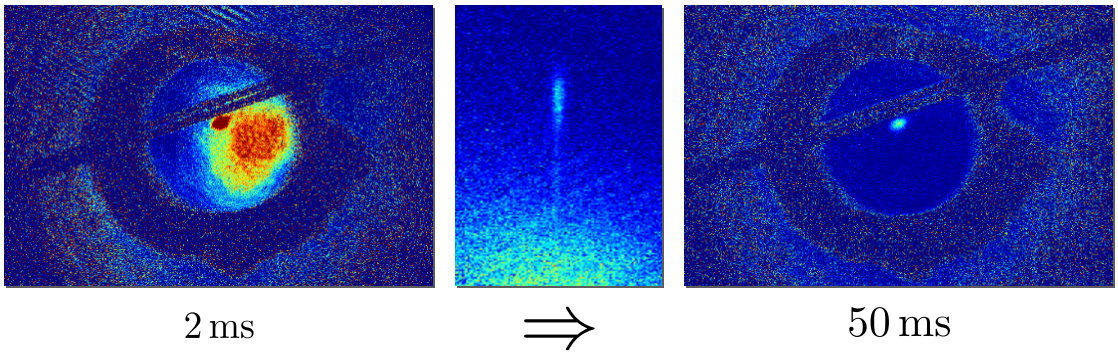


FIGURE 5.29: Vertical and horizontal absorption images (left and right) from a medium power (12 W) lifetime measurement. The dipole trap is displaced from the fibre so that the atom number can be measured as a function of time.

Trap characterisation

After successfully loading the atoms into the vertical dipole trap the lifetime of the trapped atoms was measured. This experiment was performed by simply holding the atoms at a fixed trap power and measuring the number of atoms remaining after increasing lengths of time using absorption imaging. Figure 5.29 shows absorption images taken at different stages of a lifetime measurement at a medium dipole trap strength of 12 W from both horizontal and vertical angles. The results of this measurement, alongside other lower power measurements performed at 7 W and 1 W, are given in Figure 5.30. These measurements demonstrate that we are indeed able to hold the atoms against gravity and reveals the large influence of collisions. The lifetime measurements are fitted with the solution to the equation [70]

$$\frac{dN}{dt} = -\Gamma N - \beta N^2, \tag{5.6}$$

where N is the initial number of atoms, Γ is an exponential loss rate and β is a collisional loss coefficient. Γ describes the single-particle loss rate due to collisions with the background gas while β is a loss rate from inelastic two-body collisions. If the two atoms involved in a collision are not in the absolute lowest ground state ($F = 3$ for caesium), a hyperfine state changing collision can occur releasing a huge amount of energy (relative to typical dipole trap depths of a few mK). When a caesium atom drops from $F = 4$ to $F = 3$ a total of $E = h \times 9.2\,\mathrm{GHz}$ is released as kinetic energy, which is equivalent to $440\,\mathrm{mK}$

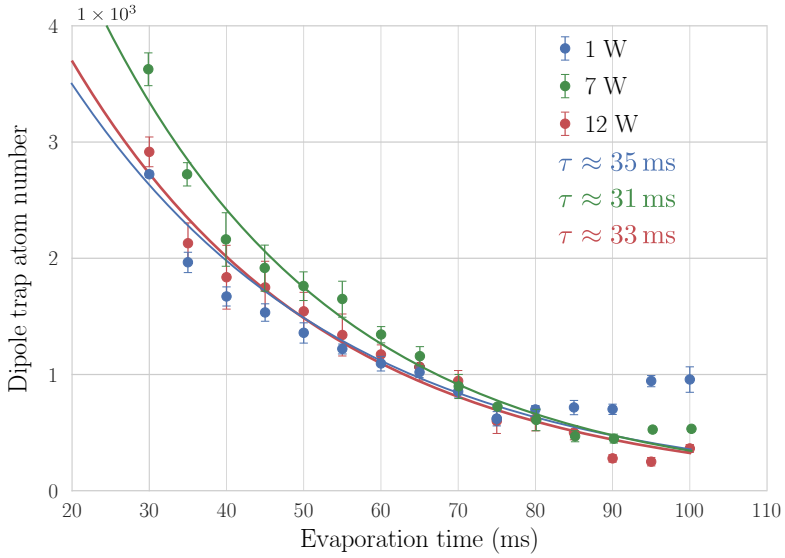


FIGURE 5.30: Dipole trap lifetime measurements at various powers. The errors in the atom number measurements are standard deviations from 3 repetitions for each beam power.

when expressed as a temperature. The atoms loaded in this experiment always have least a small mixture of $F = 3$ and $F = 4$ and so a large two-body loss rate β should be apparent. All of caesium's magnetically trappable states suffer from large spin-relaxation collision coefficients ($\beta^{HFC} = 1.5{-}4 \times 10^{-12}\,\mathrm{cm}^{-3}\,\mathrm{s}^{-1}$) which have historically hampered efforts towards achieving BEC in magnetic traps [99, 100].

As we have shown in the mixture experiment the lifetime of dipole trapped caesium can be greatly improved by first optically pumping the atoms into the maximally spin polarised hyperfine ground state $F = 3, m_F = 3$. For a doubly spin polarised caesium gas the loss rate is purely exponential depending only on collisions with the background gas. Currently, only primitive state preparation is performed by switching off the repumper beam (resonant with the $F = 3 \Rightarrow F' = 3$ transition) approximately $1\,\mathrm{ms}$ before the cooler beam is switched off. This is effective enough to migrate 100% of the trapped atoms into the $F = 3$ state (equally distributed among the Zeeman sublevels) in the absence of the dipole beam and 80% with the dipole beam turned on. Although not yet implemented, the QuILMI chamber does offer enough optical access along the x-axis for us to fully spin polarise the gas using polarised σ^+ pumping light resonant with the $F = 3 \Rightarrow F' = 2$ transition (in the presence of a bias

field provided by the x-axis compensation coils). Using light resonant with the $F = 3 \Rightarrow F' = 2$ transition is favourable over the $F = 3 \Rightarrow F' = 3$ repumper transition because decay from $F = 2$ to $F = 4$ is dipole forbidden and so fewer atoms would need to be repumped out of the $F = 4$ state. A small π component is added to the pumping light in order to prevent the $F = 4, m_F = 2$ from becoming dark.

Since we do not plan to evaporatively cool caesium to quantum degeneracy, a long lifetime is not entirely necessary and the lifetime achieved here is entirely satisfactory for observing atom-photon coupling in the fibre. However, it is still important to understand what is negatively affecting our lifetime. The lifetime measurements plotted in Figure 5.30 show distinctive exponential character with little to no evidence of a two-body loss rate. Because the data was taken using the vertical absorption imaging arrangement, it was necessary to wait for the MOT to fall away from view before taking images so that the MOT atoms would not interfere with the dipole trap atom number measurement (see Figure 5.29 for an example of the MOT appearing below the dipole trap). As a result we had to wait for a minimum of $30\,\mathrm{ms}$ before reliable atom number measurements could be made. It is reasonable to suggest then that the two-body losses occurred before the measurements were taken. Since the curves are exponential in character, we understand that the trap suffers from a high one-body loss rate. This could be caused by the nearby caesium dispensers producing a high background gas pressure in the science chamber, although our vacuum gauge measurements tell us otherwise ($< 1 \times 10^{-9}\,\mathrm{mbar}$). The caesium dispensers do have line-of-sight to the dipole trap however, which would make them particularly effective at knocking atoms out of the trap. As mentioned earlier in this section, it is possible that the vacuum gauge is underestimating the pressure inside the science chamber since it is not directly connected to the spherical octagon. A quick lifetime measurement was performed with the dispensers turned off after the MOT stage revealing no apparent change in the lifetime. Another feasible explanation is that imperfections in the trap shape are allowing atoms to escape. Since increasing the dipole trap power has no noticeable effect on the trap lifetime, we can conclude that insufficient trap depth is not the problem.

The fact that the atoms can be trapped at all at $1\,\mathrm{W}$ puts an upper bound on the waist achieved inside the chamber. Figure 5.31 shows the predicted trap

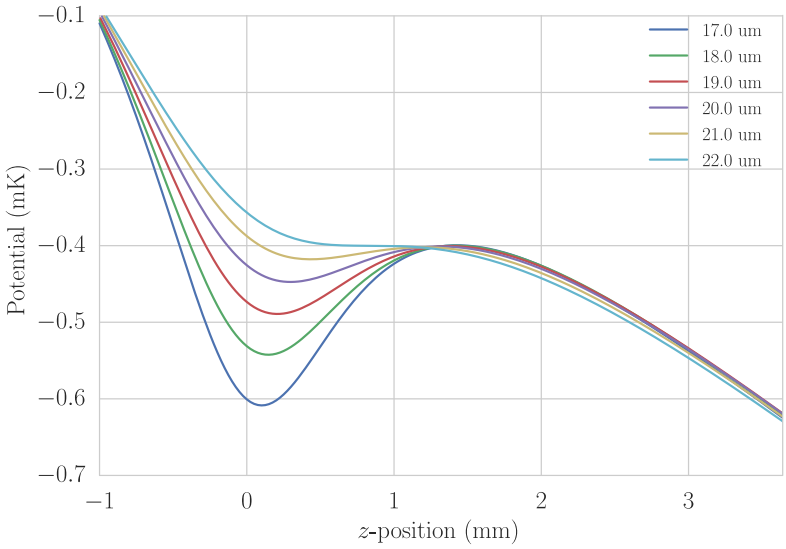


FIGURE 5.31: z-axis trap depths at 1 W at the largest beam waists that still produce a trap. At 22 µm the beam waist is completely open.

depth as a function of the beam waist at 1 W. At a waist of 22 µm, our measured beam waist, the trap is predicted to be completely open yet we can still trap atoms. This can be explained in a few different ways. Figure 5.32 shows a beam waist measurement performed by reflecting the beam out into the laboratory just before the $\lambda/4$ waveplate underneath the chamber revealing that the shape of the potential is non-ideal. The beam profile has multiple lobes that emanate from a central lobe each with a narrower waist than the last[4]. The atoms could feasibly be trapped in these tighter traps. Another hypothesis is that additional lensing is occurring at the large anti-reflection coated CF100 viewport. Finally, the dipole beam could be slightly retroreflected at any of the many optical elements in the path to form a standing wave. If the second hypothesis is assumed we can make an estimate for the final waist at the chip. Since the lowest achievable temperatures in the MOT are approximately 30 µK, the shallowest trap that could feasibly contain these atoms would be ~200 mK corresponding to a waist of 17 µm.

From this analysis, clearly the next important step to made is to ensure that an interference-free dipole potential with the correct waist is formed in the chamber.

[4]This measurement supports the imperfect trap shape explanation for the poor lifetime made in the previous paragraph. It is possible that the lobes provide an escape channel through which the atoms are escaping.

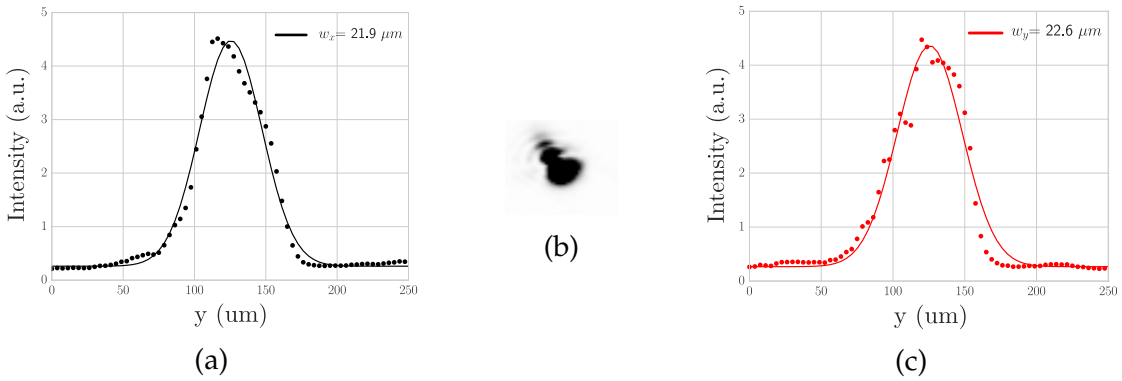


FIGURE 5.32: Results from a beam profile measurement performed using a CCD (AVT Guppy Pro 125-B) mounted on a translation stage. Subfigures (a) and (c) show data points from horizontal and vertical cuts through the central lobe and fits to Gaussian profiles for waist measurements. Subfigure (b) displays the irregular shape of the beam at its waist.

5.3 Coupling between atoms and fibre-guided photons

In order to probe whether atoms have been transferred to the fibre hole, a control system sequence for atom detection in the fibre was developed. After optimising and characterising the dipole beam, it was migrated to the fibre hole for atom-photon coupling experimentation. A probe beam locked to the $F = 4 \Rightarrow F' = 5$ transition is coupled into the fibre. The amount of light coupled in varies depending on the experiment being performed. The total efficiency measured across the entire system (free-space $\rightarrow$ fibre $\rightarrow$ feedthrough $\rightarrow$ void $\rightarrow$ feedthrough) is measured to be 16%. Unfortunately there is no way to measure the power lost at the void in isolation, but assuming 80% coupling at the first air-fibre interface (achieved with a separate length of the same fibre) and 2% losses at each fibre feedthrough, we can estimate the losses at the void to be 21%. The poor efficiency is likely due to the surface roughness caused by the laser drilling procedure (see Figure 5.19). However, this is far better than the efficiencies across the voids made using the FLICE method.

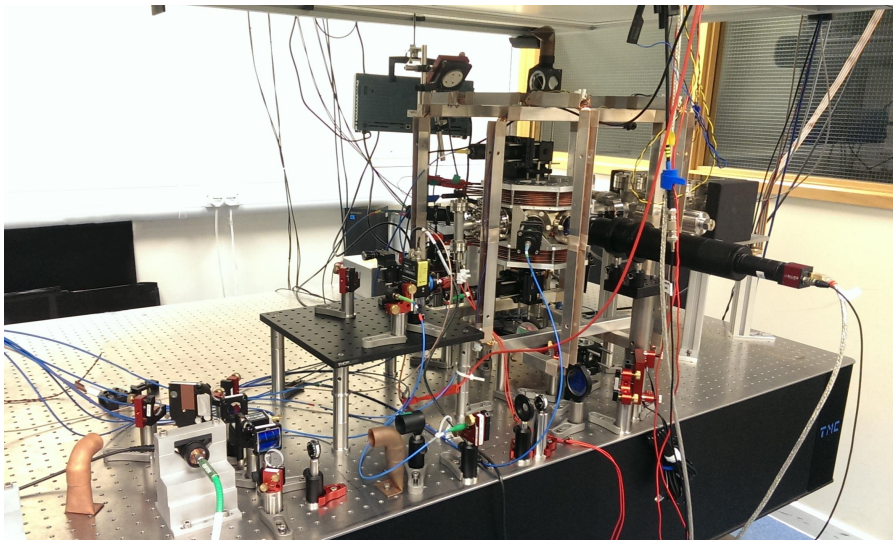


FIGURE 5.33: The QuILMI experiment. The dipole beam path originates from the green fibre outcoupler connected to a custom-built heavy-duty outcoupler mount. The platform supports the waveguide or fibre chip optics.

5.3.1 Detection as reduced atom number

Coupling between the atoms and guided probe light can be detected as a reduction in the trapped atom number in the presence of resonant probe light. The resonant probe light either scattered at the hole or hitting the dipole trap directly should excite atoms out of the trap which can be detected as a reduced atom number. We couple $1\,\mathrm{mW}$ of resonant probe light on the $F = 4 \Rightarrow F' = 5$ transition into the fibre. Figure 5.34 shows the trapped atom number measured on the vertical imaging as a function of the beam exposure time. Clearly the dipole trap lifetime is significantly affected by the presence of resonant light coupled out from the fibre. However, with a poor transfer efficiency estimated at the void (21%) and unclear images (see Figure 5.34), we have no way of telling if the dipole trap is interacting directly with fibre-guided photons in the void or with scattered light. To determine this, we can reduce the probe power and aim to measure a direct absorption signal in the fibre using a single-photon counting module (SPCM).

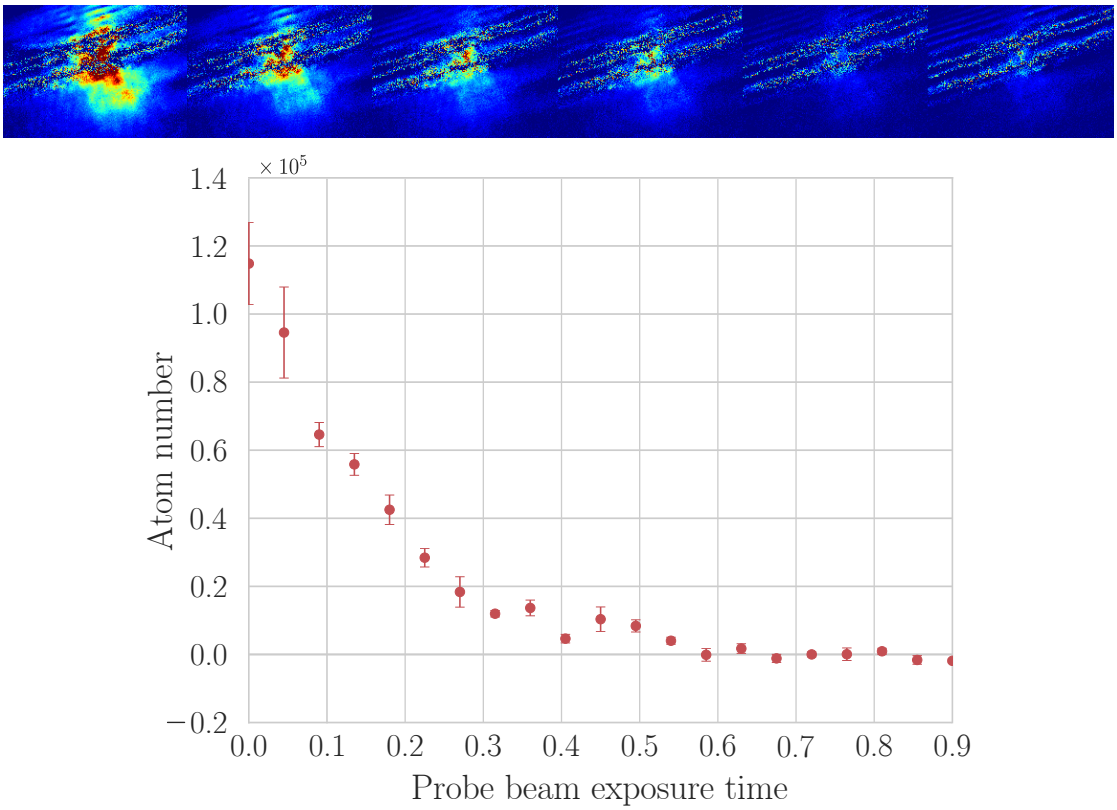


FIGURE 5.34: The atom number measured on the vertical camera as a function of the probe beam exposure time. The lifetime in the trap has been radically reduced as a result of turning on the beam.

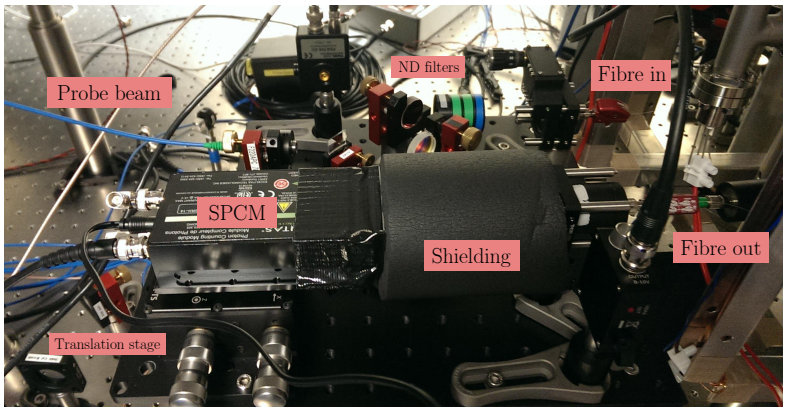


FIGURE 5.35: Experimental setup for experiments involving the single-photon counting module. A schematic is given in Figure 5.13b

5.3.2 Detection as fluorescence absorption on the single-photon counting module

A single-photon counting module (SPCM) allows us to perform highly sensitive measurements of either fluorescence photons that couple into the fibre from atoms trapped in the MOT, or absorption of the probe beam by atoms in the void. A sketch of the experimental setup is shown in Figure 5.13b and a photo is given in Figure 5.35. As before a probe beam resonant on the $6^2S_{1/2}F = 4 \Rightarrow 6^2P_{3/2}F' = 5$ transition is coupled into the fibre, but now a small amount of light is peeled off using a piece of microscope slide to measure the intensity fluctuations. The intensity fluctuations (from the lasers and AOMs) are removed in post-processing by dividing the measured signal with the one measured at the photodiode. The beam is then heavily attenuated (ND8) before being coupled into the fibre. The light from the other end of the fibre is then focused on to an Excelitas single-photon counting module (SPCM-RHEA-14) which sits atop a 3D translation stage for fine tuning. The SPCM is heavily shielded from room light using a combination of duct tape and pipe insulation. Unfortunately, at this point no conclusive evidence of atom-photon coupling has been found. However, the system is in a great position to observe atom-photon coupling in the near future and there is no theoretical reason why it should not be possible with the current setup.

5.4 Next Steps

5.4.1 Reducing the dipole beam waist and shape

As is shown in Figure 5.32 the dipole beam waist ($22\,\mu\mathrm{m}$) is wider than theoretically predicted (Figure 5.14) and the fibre void radius ($15\,\mu\mathrm{m}$). As a result, even with perfect alignment to the void we can expect a significant amount of scattering and beam distortion. To combat this we can use better optical elements, namely larger aspheric lenses or expand the beam more before focusing. Using a beam profiler we can analyse the beam and remove the lobe structure seen in Figure 5.32.

5.4.2 Rotating the chamber

Installing the chip above the MOT has been inconvenient than anticipated. First of all, we have no conclusive method to determine whether the dipole trap has been threaded through the void or not. Narrowing the dipole trap focus should improve alignment, but it is not guaranteed to provide us with more clarity. Secondly, the dipole trap beam optics do not function in the way they were intended. Despite the fact that the beam appears to be collimated, translating the $150\,\mathrm{mm}$ focal length lens underneath the chamber does not translate the trap position as it should making it difficult to place the trap focus in the plane of the fibre. As well as improving the beam shape it will be important to improve the collimation at this point in the dipole beam path.

A possible solution for these problems would be to flip the chamber $180°$ about its y-axis. With enough hands and eyes this should be possible considering the small size of the chamber. With the chip below the MOT the transport of atoms to the hole should be facilitated potentially allowing us to conduct experiments without the dipole trap at all. When using the dipole trap however, we would be able to more easily determine whether the beam is successfully passing through the hole and if atoms can be trapped above the chip. Finally, having the chip closer to the lower viewport means more potential focusing arrangements become available to us which could help with reducing the beam waist.

The chamber could also be flipped $90°$ on its side. In this arrangement the dipole trap would be horizontal with gravity no longer pulling along the weak axis of the dipole trap. Although this would greatly improve the quality of our trap, it would also be difficult to implement. Both the dipole trap and the vertical imaging beam paths would have to be completely reassembled along the horizontal axis. In addition, a new chamber and ion pump support structures would have to be built and installed.

5.4.3 Beyond coupling in the fibre

After observing an initial signal in the fibre, the next step would be to enlarge it by tuning the many parameters at our disposal (MOT loading and alignment, dipole trap loading and alignment, probe frequency and power, timing

etc.). Once the signal is sufficiently large, we should attempt to observe electromagnetically induced transparency (EIT) through the void. To our knowledge would be the first instance of EIT being performed through a fibre on a small ensemble and would be an excellent demonstration of the QuILMI experiment's capabilities to interface light with atoms on a fibre.

For future waveguide chips it will be important to look for ways to enhance the interactions in the void even further. This could be achieved by developing a method of improving the surface roughness of the laser drilled and fliced voids. In the same way that fibre end-faces can be polished using lapping sheets made of polyester with tiny diamond particles glued to it with resin, a void polishing floss could be developed. Its manufacture could be as simple as dipping a narrow thread of plastic into resin and then rolling it in a powder of diamond particles. The plastic thread could even have a square cross-section for the purposes of creating flat void faces. It should also be possible to write a Bragg grating into either a waveguide or fibre. A Bragg grating is a section of waveguide or fibre that reflects a very narrow range of wavelengths and is made by modulating the refractive index along the fibre axis.

Once we have found a way to enhance the coupling strength a logical next step would be to demonstrate the versatility and potential for miniaturisation of the waveguide chip system. It would be straightforward to write a Mach-Zehnder interferometer directly onto the waveguide chip. After simple experiments it would make sense then to move toward the ultimate goal of demonstrating a quantum memory using an atomic ensemble coupled to waveguided light on a chip. An entire experiment capable of Electromagnetically Induced Transparity (EIT) in room temperature vapours is already at our disposal so this extension should be straightforward [101, 102]. A more complicated endeavour would be to generate entangled states using the DLCZ protocol [103, 89, 104].

Chapter 6

Conclusions and outlook

A compact system capable of interfacing cold atoms with light guided by waveguides or fibres on a chip has been planned, developed and constructed. In addition, important steps have been taken with the ^{6}Li-^{133}Cs mixture experiment such that degenerate clouds of $^{6}Li_2$ Feshbach molecules can now be routinely produced. With the addition of a new, meticulously planned dual-species source, the mixture system can resume its course towards realising ultracold mixtures of ^{6}Li and ^{133}Cs .

The design and construction of a highly versatile, well-collimated and thoroughly characterised dual-species oven has been presented. It serves to replace the previous, flawed model and provide atomic beams for years to come. With its tight angular distribution of ~$0.04\,\mathrm{rad}$ (FWHM), source depletion is slow and, more importantly, unuseful flux is kept to a minimum such that our ion pumps can continue to function over the coming years. The oven is also highly tunable: PID temperature controlled lithium and caesium reservoirs allow the axial flux for each species to be tuned across several orders of magnitude. The atomic beams' longitudinal velocity distributions were combined with a differential pumping analysis to obtain predictions for how well the oven will integrate with our existing dual-species Zeeman slower upon installation. For caesium we expect $3.3 \times 10^{9}\,\mathrm{atoms/s}$ to impinge on the MOT at capturable velocities and for lithium we expect $3.9 \times 10^{8}\,\mathrm{atoms/s}$ (at the investigated chamber temperatures).

This thesis has covered the entire development process through which the QuILMI experiment was brought to reality. The QuILMI chamber has largely been the design of the writer. From the shape of the optical dipole trap and the MOT beam intensities right down to the wires chosen for the coils and the screws that hold the chamber together. Although significant help was received

during the construction and operation, the writer was thoroughly involved in every single aspect of the experiment's evolution as can be gleamed from the content of this thesis. The system has been highly optimised and characterised and is in a great position to start performing simple read/write operations. From there, the next step would be more complex quantum-gate operations and a demonstration of the systems scalability by implementing multiple interacting qubits on a chip.

We have paved the way towards an integrated device in which photons and atoms interact strongly. This QuILMI device is on the cusp of a measurement that can demonstrate its enormous potential as a scalable building block for quantum information processing. The next critical steps to be taken have been clearly outlined and it will be no time before the system proves its worth as serious contender among the multitude of candidates for quantum computing.

Appendix A

The Hydrogen Atom

Consisting of only a single proton and accompanying electron, hydrogen has the simplest structure of all the elements and thus has been the most natural starting point for atomic study. The energy of the atom is simply the kinetic energy of the electron (mass m_e and charge $-e$) relative to a stationary proton[1] of charge e plus its potential energy as it moves in the Coulomb potential $V(r)$ of the nucleus. The time-independent Schrödinger equation is written

$$-\frac{\hbar^2}{2m_e}\nabla^2\psi + V(r)\psi = E\psi, \tag{A.1}$$

where ψ is the spatial wave function of the electron. Since the confining potential is spherically symmetric, the wave function ψ ought to be separable meaning it can be written as the product of a radial wave function $R(r)$ and an angular wave function $Y(\theta,\phi)$. In full spherical polar coordinates the Schrödinger equation becomes:

$$-\frac{\hbar^2}{2m_e}\left[\frac{Y}{r^2}\frac{d}{dr}\left(r^2\frac{dR}{dr}\right) + \frac{R}{r^2\sin\theta}\frac{\partial}{\partial\theta}\left(\sin\theta\frac{\partial Y}{\partial\theta}\right) + \frac{R}{r^2\sin^2\theta}\left(\frac{\partial^2 Y}{\partial\phi^2}\right)\right] + VRY = ERY, \tag{A.2}$$

which has the solutions:

$$\psi_{nlm} = \sqrt{\left(\frac{2}{na}\right)^3\frac{(n-l-1)!}{2n[(n+l)!]^3}}e^{-r/na}\left(\frac{2r}{na}\right)^l\left[L^{2l+1}_{n-l-1}(2r/na)\right]Y^m_l(\theta,\phi), \tag{A.3}$$

[1] Of course the nucleus isn't actually stationary, but the effect is very small so I ignore it here. To take it into account one only has to use the reduced mass $m_r = (m_e m_p)/(m_e + m_p)$ instead.

where n is the principle quantum number, l is the azimuthal quantum number, m is the magnetic quantum number, L is an associated Laguerre polynomial and Y is a spherical harmonic. Surface plots of constant probability $|\psi_{nlm}|^2$ are plotted in Figure A.1. The energy associated with each wavefunction is given by the **Bohr formula**:

$$E_n = -\left[\frac{m}{2\hbar^2}\left(\frac{e^2}{4\pi\epsilon_0}\right)^2\right]\frac{1}{n^2} = \frac{E_1}{n^2}, \tag{A.4}$$

which is arguably the most important equation in all of quantum mechanics. With this equation Bohr was able to explain the empirical observations of Rutherford and give a theoretical basis for the **Rydberg formula** which was widely known and accepted but not understood.

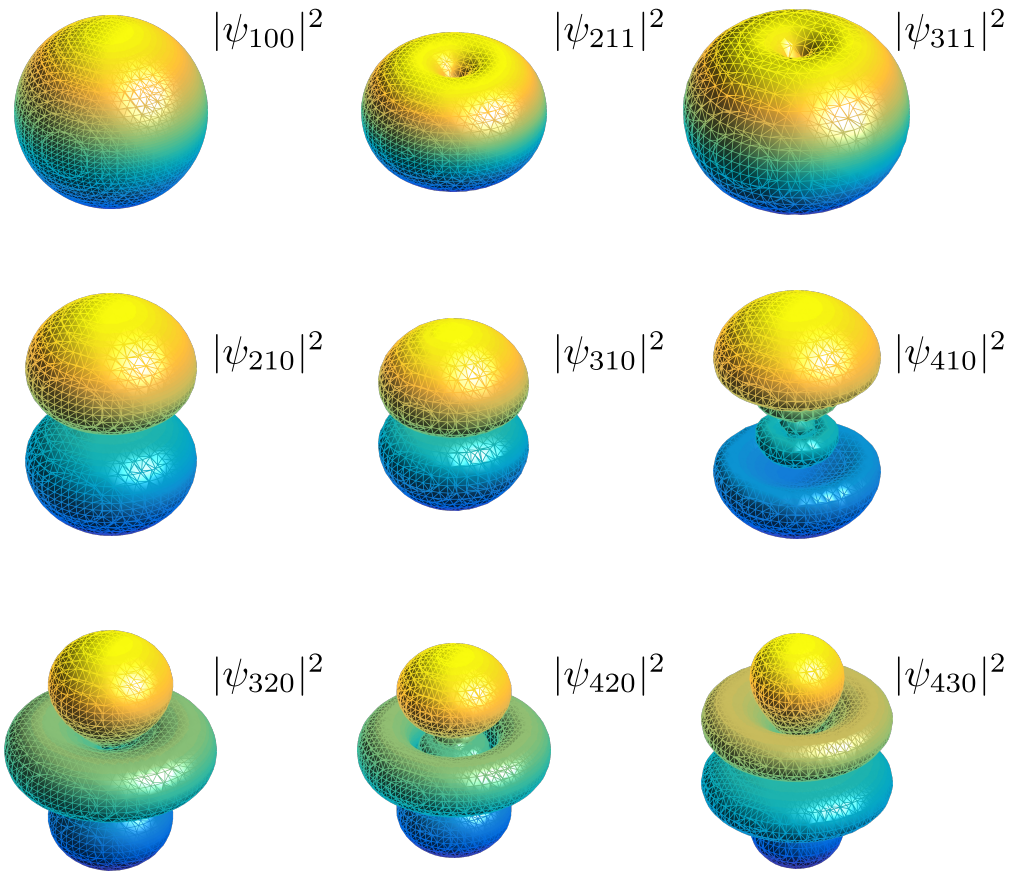


FIGURE A.1: Isosurface plots of a number of interesting-looking hydrogen wave functions. The wavefunctions are labelled by their principal, azimuthal and magnetic quantum numbers.

A.0.1 Fine structure and hyperfine structure

The energy levels predicted by the Bohr formula do not perfectly reflect reality. There remains a relativistic correction to be made and additional structure to be uncovered owing to coupling between the electron's orbital and spin angular momenta. The relativistic correction is needed because we previously used a *classical* expression for the kinetic energy when we wrote the Hamiltonian as the sum of the electron's kinetic and Coulombic potential energy. Using the relativistic formula for the kinetic energy we find a first-order correction of:

$$H'_{\text{rel}} = -\frac{p^4}{8m_e^3c^2}. \tag{A.5}$$

According to first-order perturbation theory the first-order correction to a given energy level is simply the expectation value of the perturbing Hamiltonian in the unperturbed energy state of interest. Hence, for hydrogen the relativistic correction in terms of E_n is:

$$E^1_{\text{rel}} = -\frac{(E_n)^2}{2m_ec^2}\left[\frac{4n}{l+1/2} - 3\right]. \tag{A.6}$$

The electron's orbital angular momentum $\mathbf{L}$ and intrinsic spin angular momentum $\mathbf{S}$ interact with each other and have an associated interaction energy. From the rest frame of the electron, the positive nucleus orbits the electron and produces a magnetic field $\mathbf{B}$ that exerts a torque on the magnetic moment of the electron $\boldsymbol{\mu}$ which tries to align the two. Therefore the spin-orbit Hamiltonian is

$$H'_{\text{so}} = -\boldsymbol{\mu_e} \cdot \mathbf{B}. \tag{A.7}$$

Following through with this analysis, the spin-orbit Hamiltonian can eventually be written as

$$H'_{\text{so}} = \frac{1}{2}\left(\frac{e^2}{4\pi\epsilon_0}\right)\frac{1}{m_e^2c^2r^3}\mathbf{S}\cdot\mathbf{L}, \tag{A.8}$$

where the factor of $1/2$ in front is a kinematic correction known as the **Thomas precession** which serves to correct for the fact that the rest frame of the electron is not an inertial frame[2]. With spin-orbit coupling taken into consideration, the

[2]This can be avoided by performing the analysis in the rest frame of the proton in which the moving magnetic dipole of the electron acquires an electric dipole moment which interacts with the static electric field of the nucleus, but this requires quantum electrodynamics.

Hamiltonian no longer commutes with $\mathbf{L}$ and $\mathbf{S}$ and so from Ehrenfest's theorem we know the electron's spin and orbital angular momenta are no longer conserved quantities. However, the Hamiltonian *does* commute with L^2 and S^2 and the total angular momentum operator $\mathbf{J} = \mathbf{L} + \mathbf{S}$ and so these are conserved quantities and we can use the eigenstates of these operators to perform perturbation theory. Writing the spin-orbit operator $\mathbf{S} \cdot \mathbf{L}$ in terms of the "good" operators and choosing $s = 1/2$, perturbation theory produces a first-order correction of:

$$E^1_{\text{so}} = \frac{(E_n)^2}{m_e c^2} \frac{n[j(j+1) - l(l+1) - 3/4]}{l(l+1/2)(l+1)}. \tag{A.9}$$

Thus the total fine structure correction in terms of E_n is

$$E^1_{\text{fs}} = E^1_{\text{rel}} + E^1_{\text{so}} = \frac{(E_n)^2}{2m_e c^2} \left(3 - \frac{4n}{j+1/2}\right). \tag{A.10}$$

Hence the fine structure energy shift is smaller than the Bohr energy by roughly $E_n/m_e c^2 = 2 \times 10^{-5}$. The fact that the relativistic and spin-orbit coupling corrections are of the same order is entirely coincidental. We say that the fine structure breaks the degeneracy in l since for a given n, different values of l no longer produce the same energy.

The hyperfine structure, due to the interaction between the electron's total angular momentum $\mathbf{J}$ and the nucleus's spin angular momentum $\mathbf{I}$, introduces an even smaller correction by a factor of $\alpha^2 \approx (1/137)^2$, the fine structure constant squared. The hyperfine Hamiltonian describing this interaction is

$$H'_{\text{hfs}} = A_{\text{hfs}} \mathbf{I} \cdot \mathbf{J} + B_{\text{hfs}} \frac{3(\mathbf{I} \cdot \mathbf{J})^2 + \frac{3}{2}(\mathbf{I} \cdot \mathbf{J}) - i(i+i)j(j+1)}{2i(2i-1)j(2j-1)}, \tag{A.11}$$

where A_{hfs} is the magnetic dipole constant and B_{hfs} is the electric quadrupole constant [38]. The first term always applies, but the second is a higher order effect that only contributes when the electron occupies an orbital with a non-spherically symmetric electric field. Looking at the denominator of the last term, clearly it can only apply to states where $j \neq 1/2$ i.e. $j \neq 0$. The dominant term is the magnetic dipole contribution and for most experiments it is satisfactory to keep only this term. In computing the hyperfine energy correction it becomes convenient to work in the basis of the total atomic angular momentum operator $\mathbf{F} = \mathbf{I} + \mathbf{J}$. The hyperfine energy shift in terms of the eigenvalues of $\mathbf{F}$,

I^2 and J^2 is then

$$E_{\text{hfs}} = \frac{1}{2}A_{\text{hfs}}k + \frac{3}{8}B_{\text{hfs}}\frac{k(k+1) - 2i(i+1)j(j+1)}{i(2i-1)j(2j-1)}, \tag{A.12}$$

where $k = f(f+1) - i(i-1) - j(j+1)$. The Hyperfine interaction breaks the degeneracy in j and so the energy levels are split even further. D-line[3] level structure diagrams for ^{6}Li and ^{133}Cs are shown in Figures 2.1 and 2.2. Spectroscopic notation for the different transitions is explained as follows. The first number is the principal quantum number n. The superscript is equal to $2S + 1$ with a capital S to indicate it is the total spin of all the electrons (which for the alkalis is always $1/2$). The capital letter denotes the total orbital angular momentum and the subscript gives the value of J (again capital to indicate the total). The use of letters for angular momentum quantum numbers dates back to the first spectroscopic analyses of atoms in which the observed lines were named sharp, principal, diffuse and fundamental. These lines were later attributed to atomic states of angular momenta 0, 1, 2 and 3 (in units of $\hbar$). For larger angular momenta, the naming convention then follows alphabetical order skipping j in order to avoid confusion with languages which do not differentiate between i and j.

[3]The fine structure doublet is known as the D-line for historical reasons. This is unfortunate and confusing since the orbital angular momentum for the doublet is P not D.

Appendix B

Nufern NuAMP seeding setup

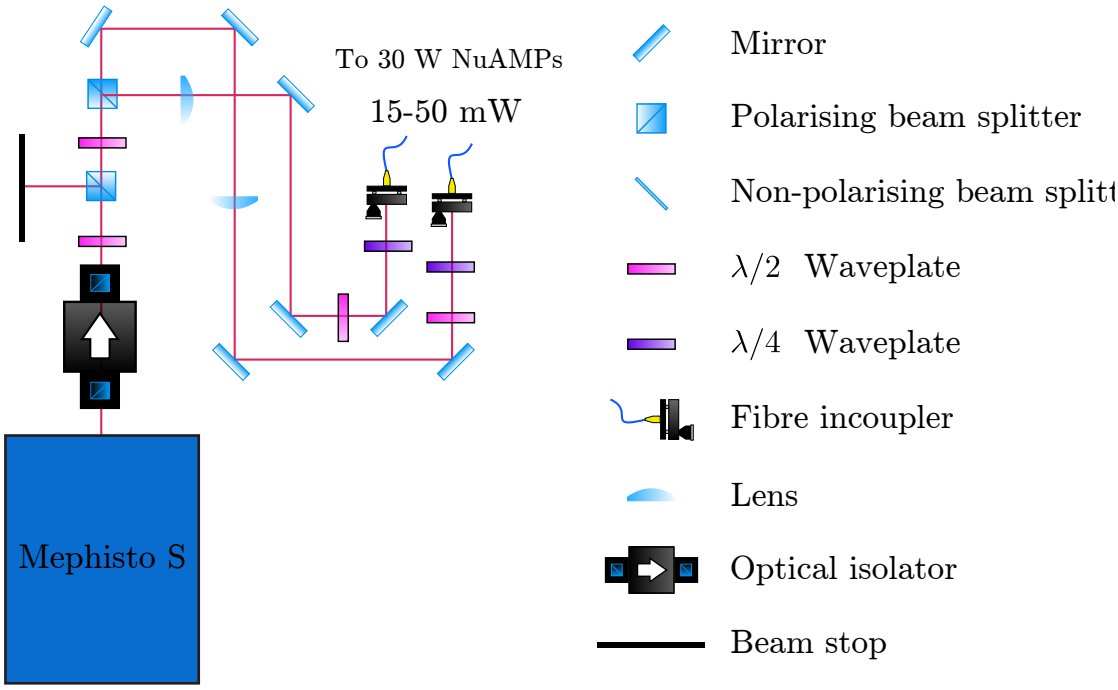


FIGURE B.1: Laser setup for the seeding of two 1064 nm 30 W Nufern NuAMP fibre amplifiers. 500 mW of 1064 nm light, from a Coherent Mephisto S, is divided up, beam shaped and then coupled into polarisation maintaining Thorlabs P3-1064PM-FC-2 fibres which feed into the amplifiers.

Appendix C

Mechanical designs

This appendix contains all of the custom parts that were designed and built by our in-house workshop for the construction of the QuILMI chamber. All of the parts shown are entirely my own design except for the ion pump stand which was designed by the workshop.

C.1 Chip-mounting assembly



FIGURE C.1: CAD drawings made when designing the internal chip-mounting apparatus. The model chip is the fibre chip.

C.2 Coil and optomechanics mounting plates

C.2.1 Top plate

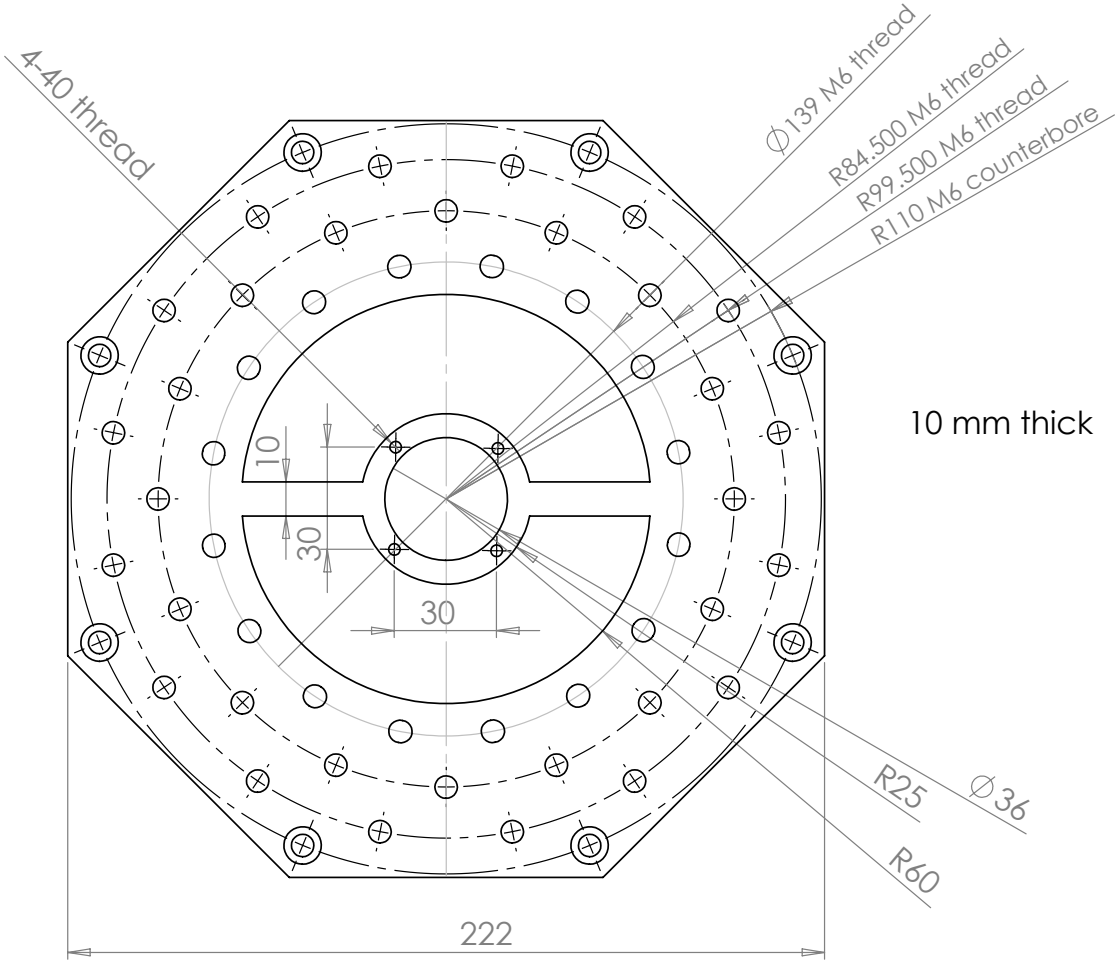


FIGURE C.2: The top coil mounting plate. The M6 counterbores are used to clamp the top MOT coil between this plate and the upper middle plate which fastens to the chamber. The concentric rings of M6 threaded holes are for clamping any additional optical elements. The central ring supports four UNF 4-40 thread holes for the mounting of Thorlabs cage systems.

C.2.2 Bottom plate

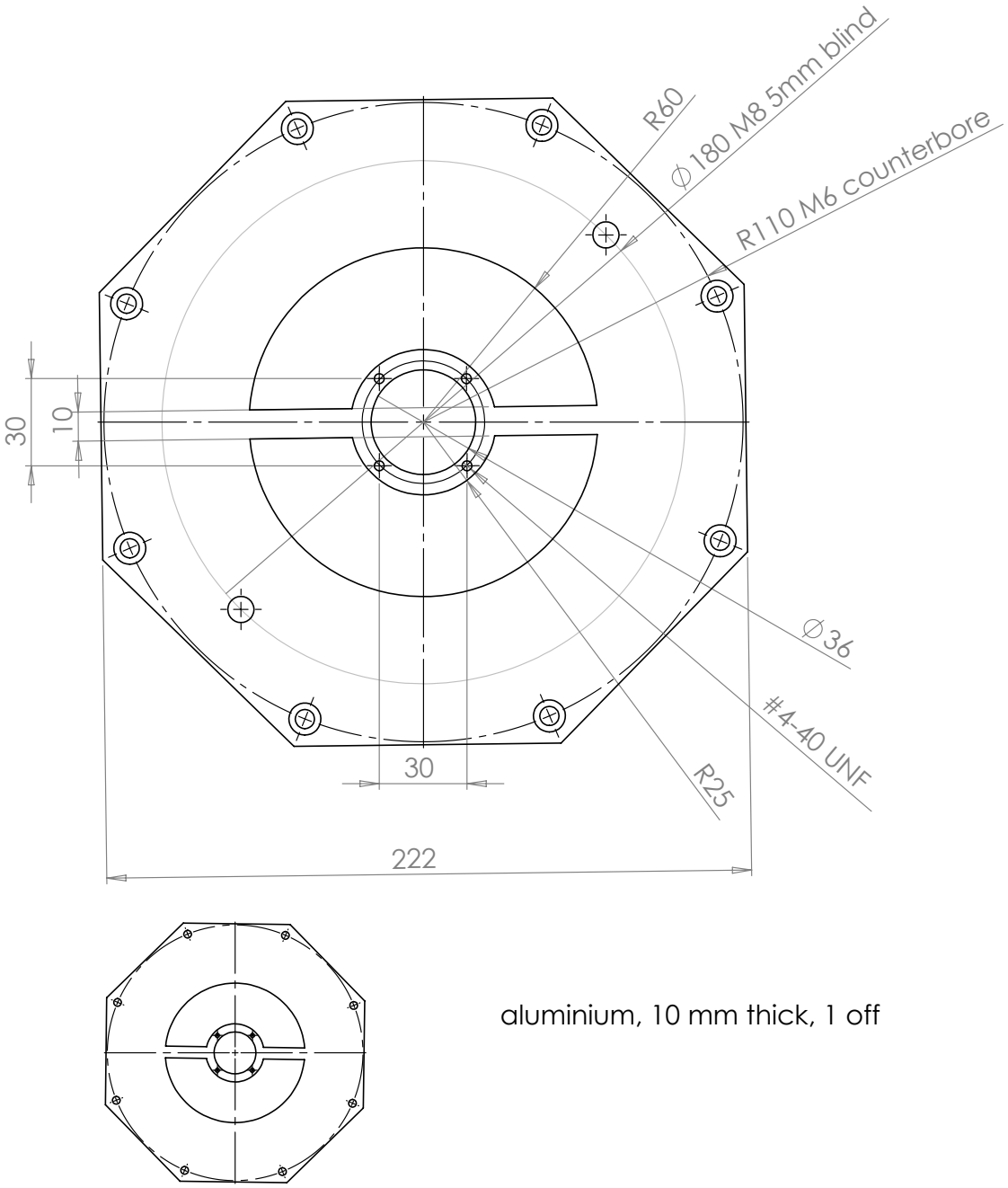


FIGURE C.3: The bottom coil mounting plate. The M6 counterbores are used to clamp the bottom MOT coil between this plate and the lower middle plate which fastens to the chamber. The two M8 threaded holes are for connecting two 2" diameter steel legs. The central ring supports four UNF 4-40 thread holes for the mounting of Thorlabs cage systems.

C.2.3 Middle plate

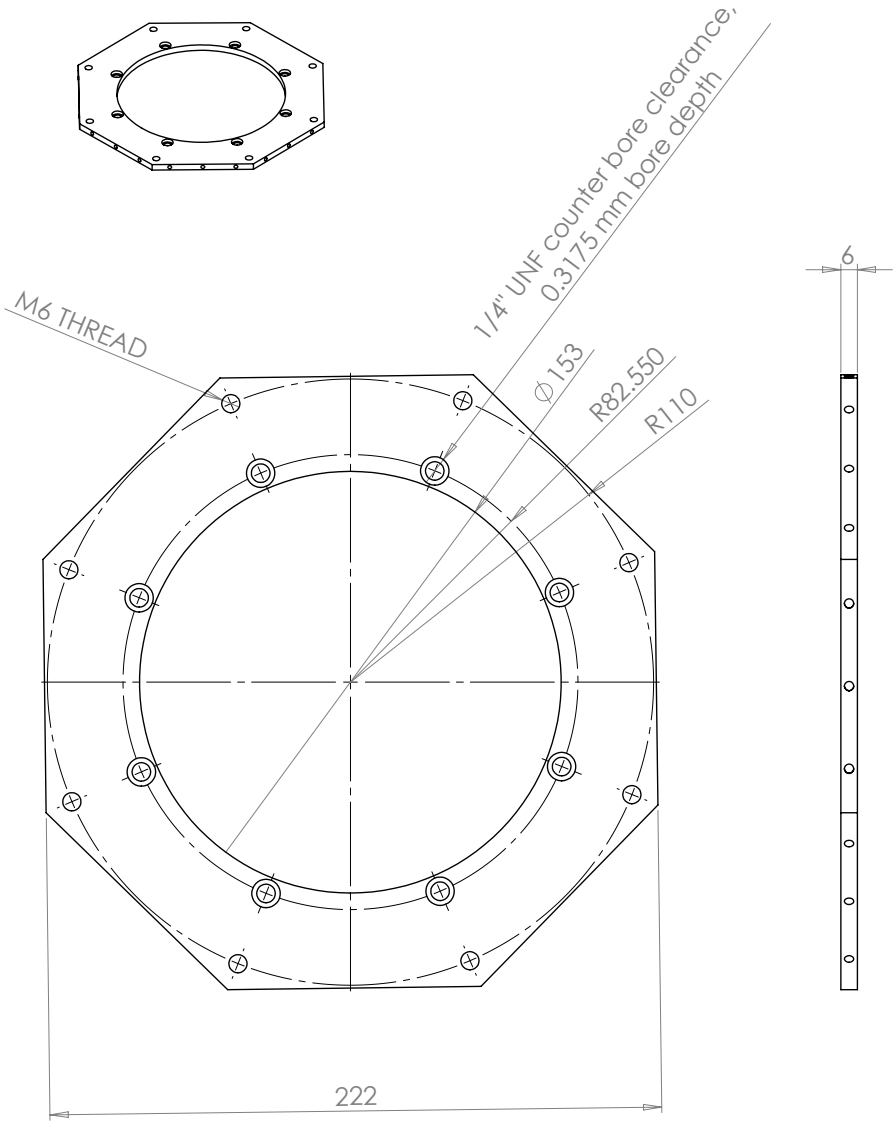


FIGURE C.4: The middle MOT coil mounting plates. Two of these were manufactured, one for the top of the chamber and one underneath the chamber. The outer M6 threaded holes are for connecting the top and bottom plates. The inner ring of 1/4" UNF counter bored holes are used to fasten the plate to the 6" Spherical Octagon (Kimball Physics). Along each edge of the middle coil are M3 threads for mounting window plates.

C.2.4 Window plate

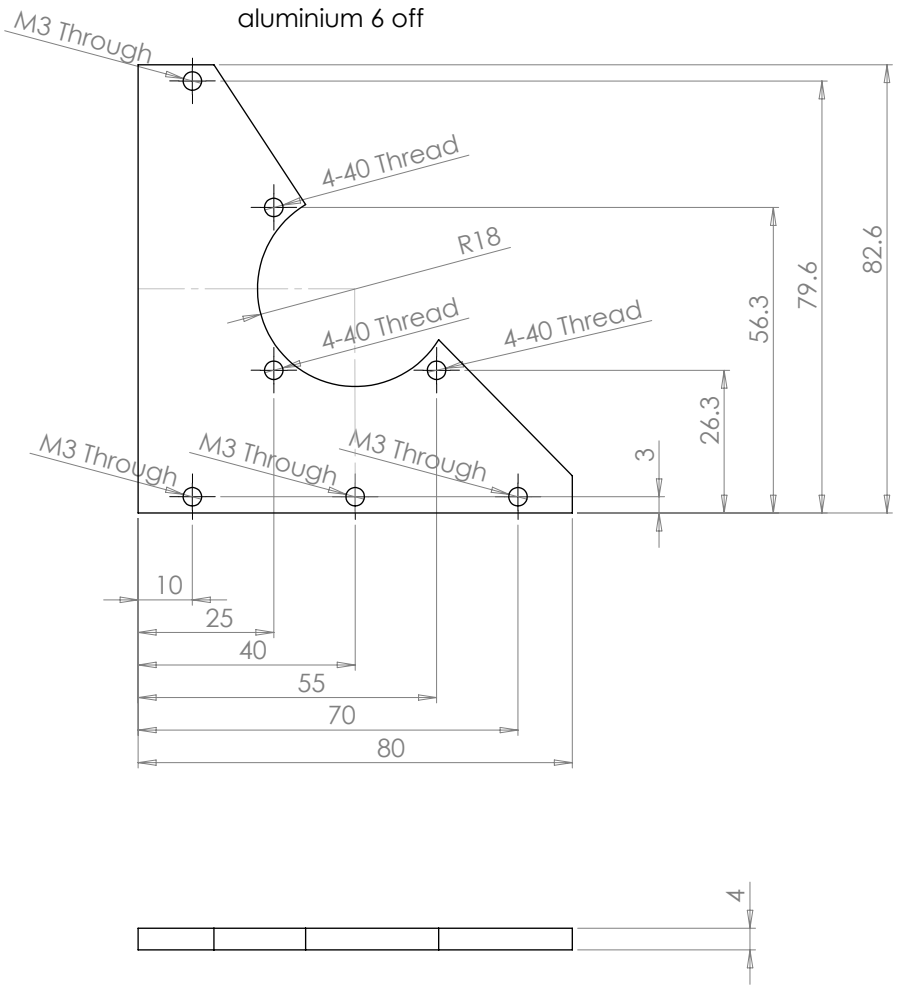


FIGURE C.5: The window plates. With the two middle plates in place these window plates can be installed. Again the central UNF 4-40 threads allow the connection of Thorlabs cage systems. The plates are truncated to allow some visibility into the chamber.

C.3 Fibre feedthrough Teflon ferrule

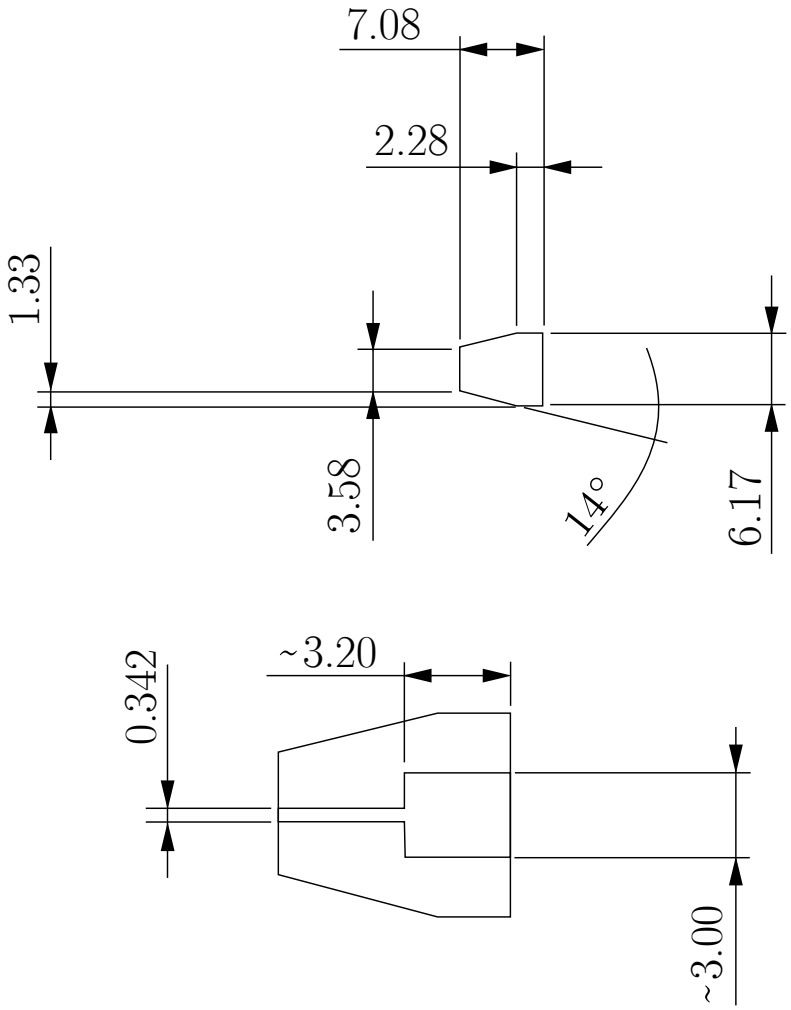


FIGURE C.6: Dimensions of the Teflon ferrules for use with Swagelok ConFlat flanges.

C.4 Compensation coil brackets

Compensation coil brackets for the x and y-axes. The x-axis coil brackets are designed to be smaller than those for the y-axis so they can slot together. These were made by laser cutting the nets shown at the bottom of each figure out of $1\,\mathrm{mm}$ thick aluminium sheets. The sheets were then bent into shape and fastened together to form a total of four brackets which could be assembled together.

C.4.1 Inner compensation coil bracket

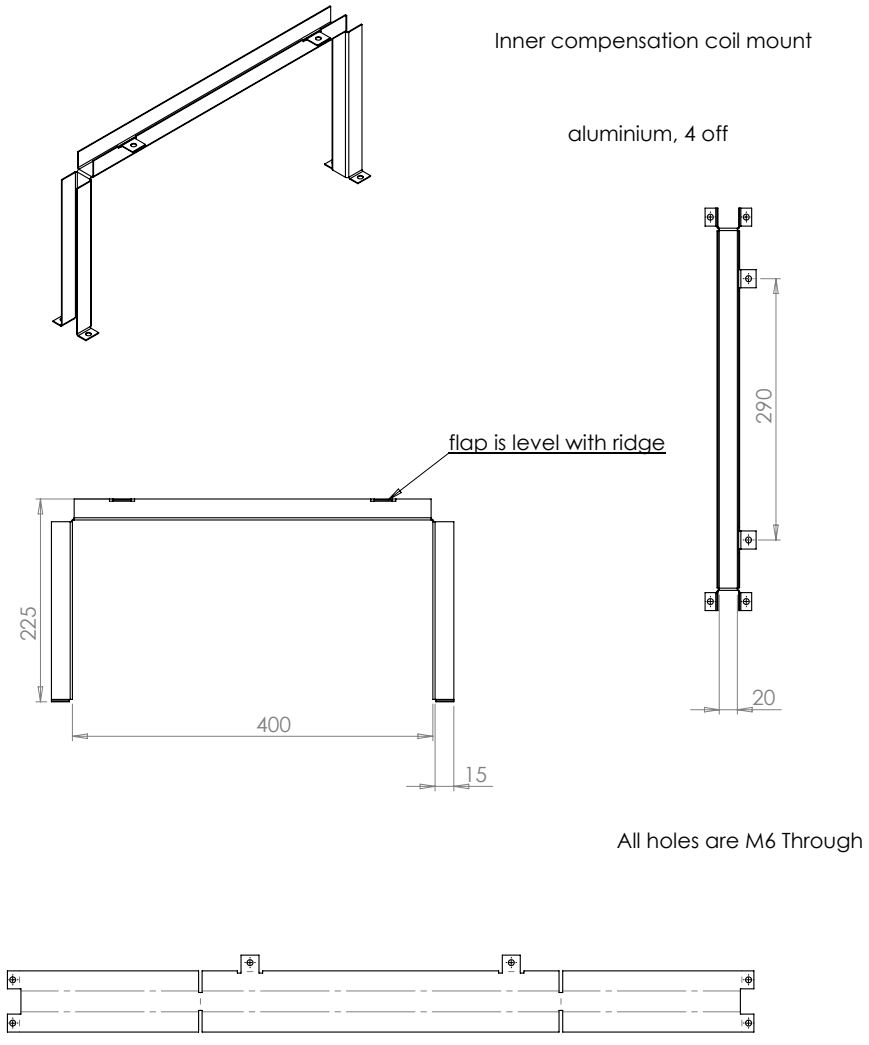


FIGURE C.7: One half of an inner compensation coil bracket. Two fasten together to make one inner coil bracket.

C.4.2 Outer compensation coil bracket

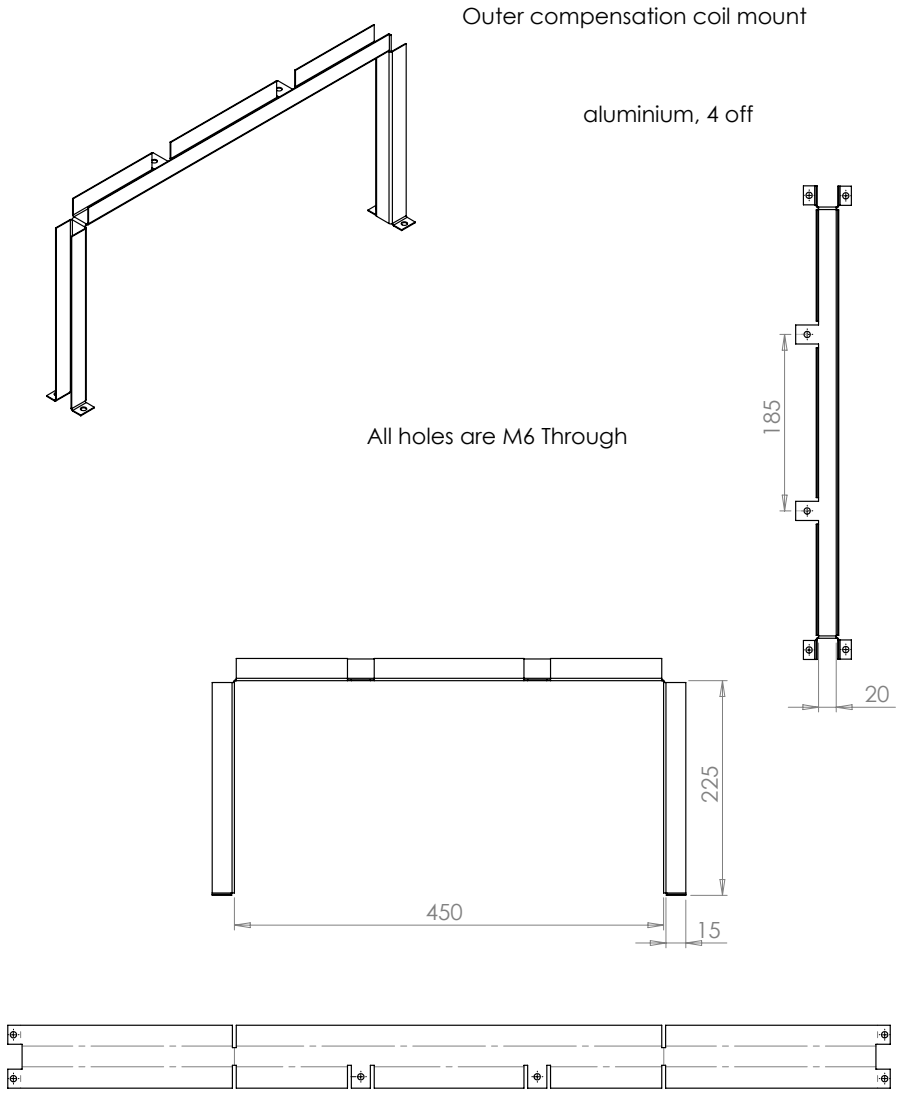


FIGURE C.8: One half of an outer compensation coil bracket. Two fasten together to make one outer coil bracket.

C.4.3 Compensation coil assembly

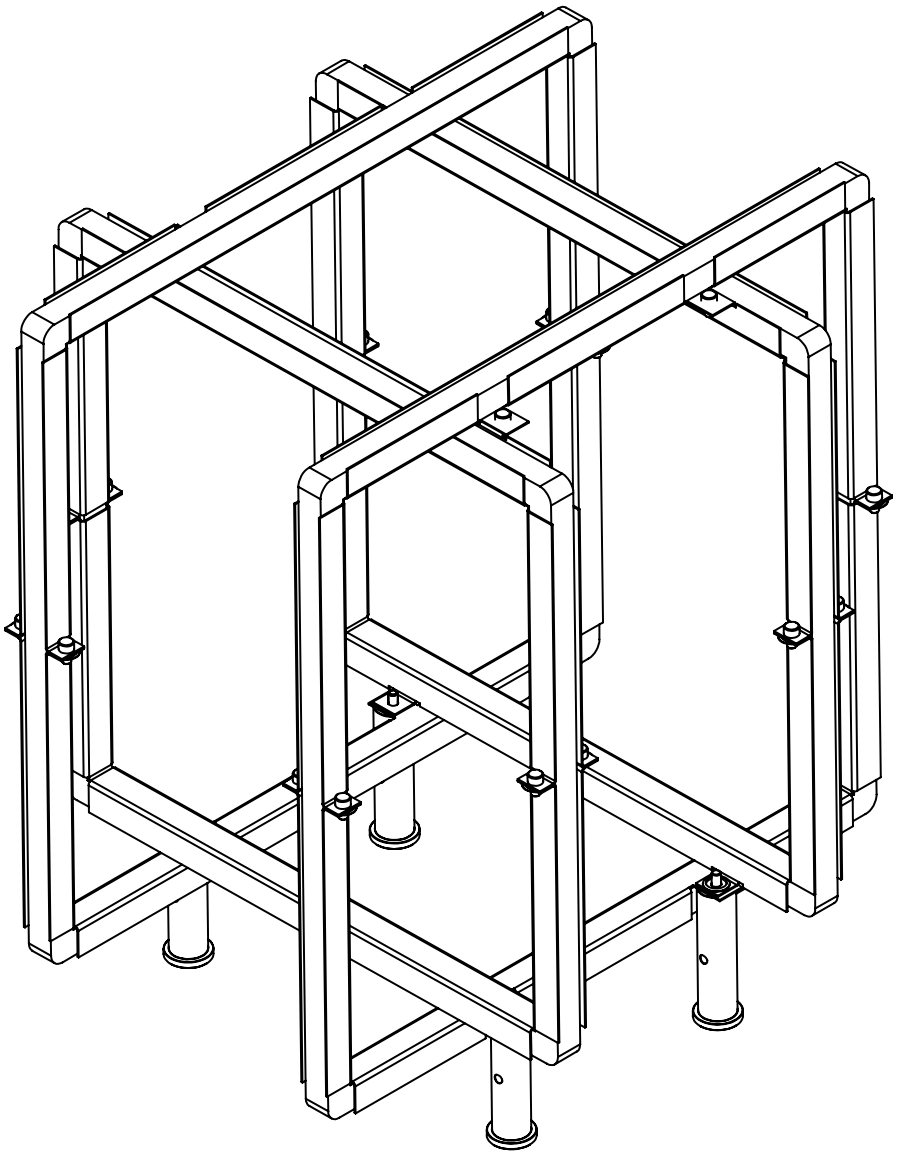


FIGURE C.9: The full compensation coil assembly. The brackets have flaps to secure the inner coils to the outer coils such that each pair of coils is separated by half of their side-length (Helmholtz configuration). The posts at the bottom are 100 mm tall to align the centre of the brackets with the centre of the chamber. Under the stress of the 75 windings of copper wire, the brackets actually buckled with this design so each pair of brackets were eventually welded together.

C.5 Nufern NuAMP outcoupler heavy-duty mount

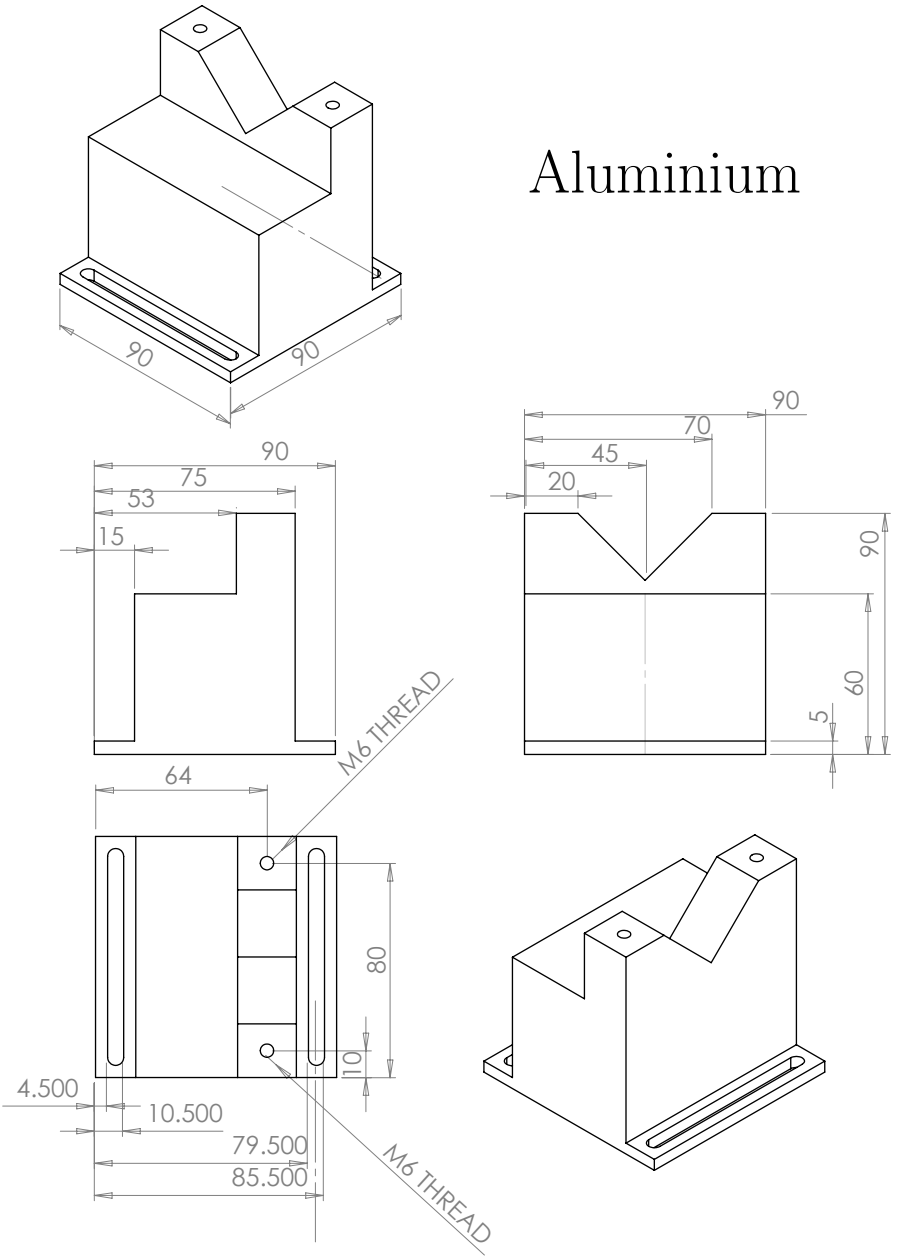


FIGURE C.10: The main body of the NuAMP outcouplers. Two of these were made, one for each 30 W fibre amplifier. The base is thick and heavy to provide ultimate stability.

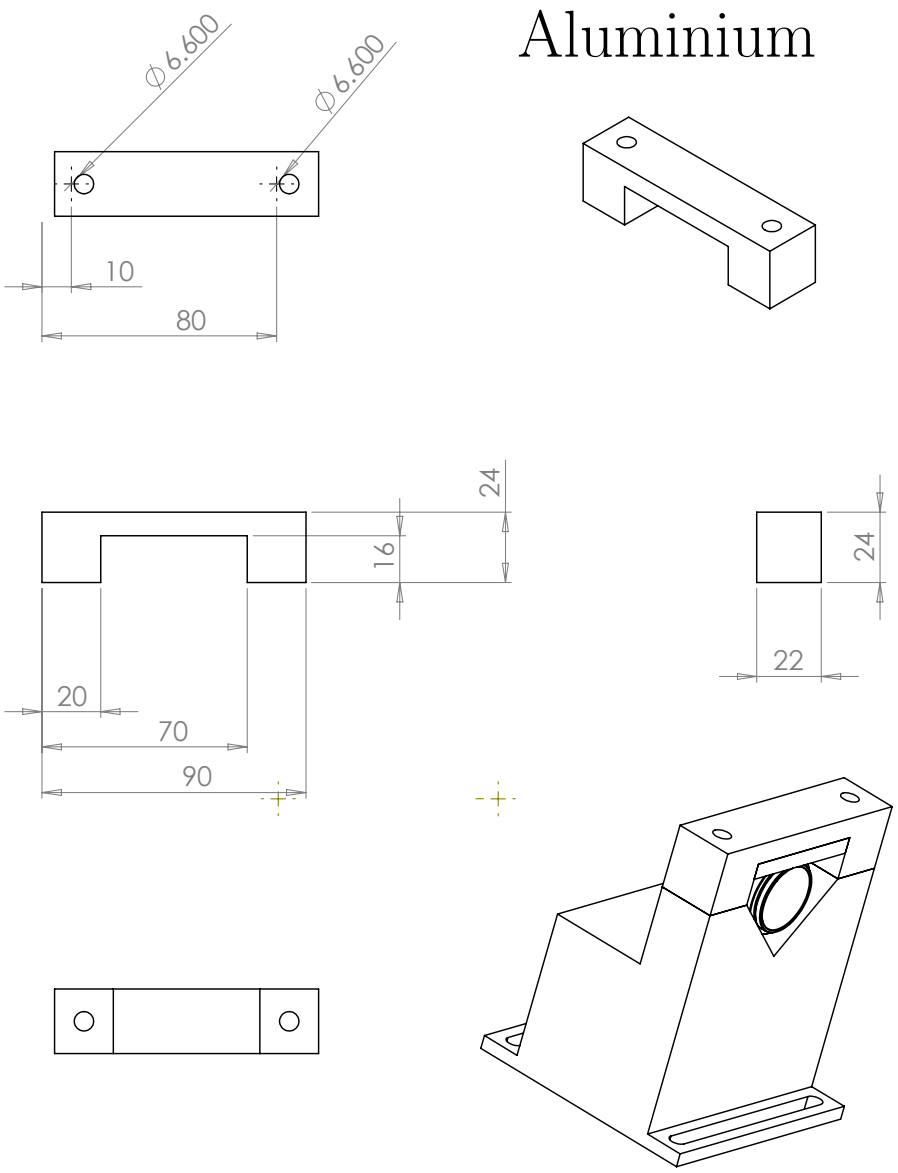


FIGURE C.11: The clamp of the NuAMP outcouplers. A piece of rubber is inserted between the clamp and the outcoupler tube to keep it in place.

C.6 Dichroic mirror holder

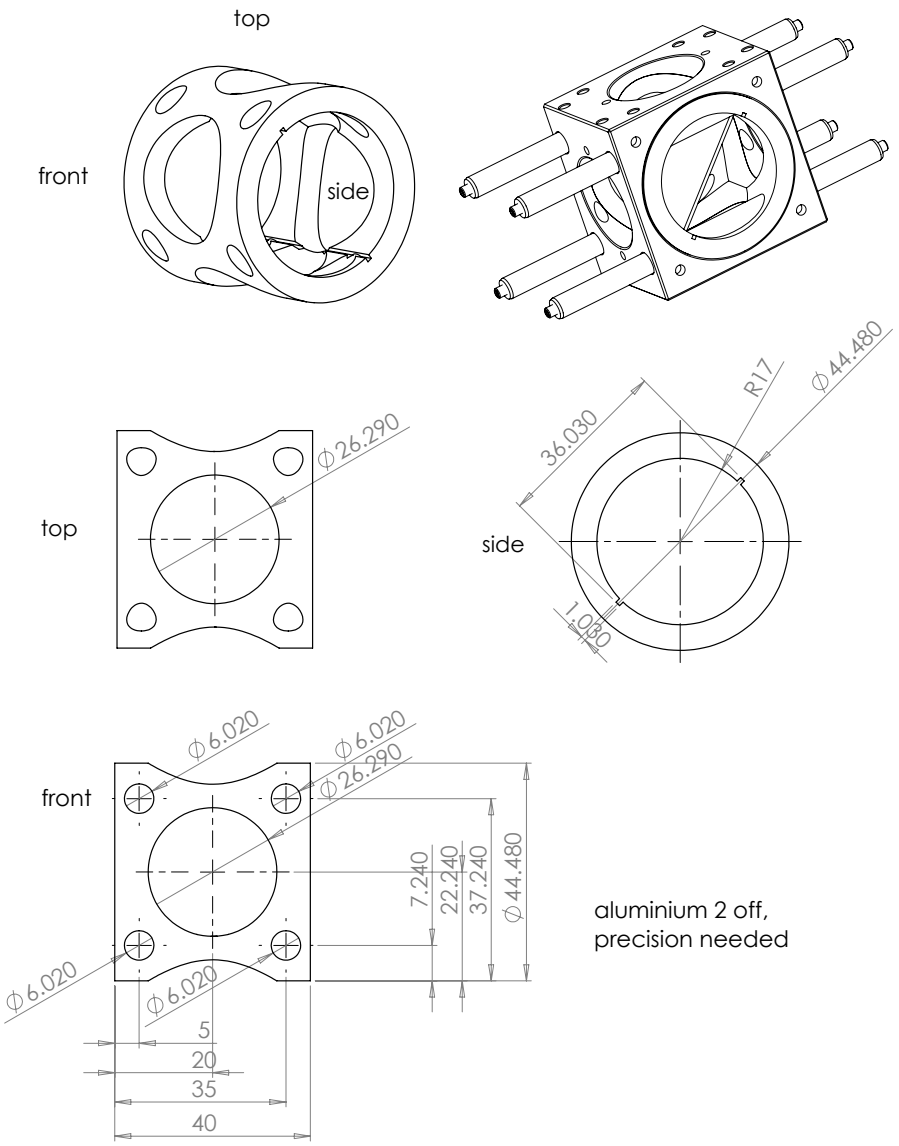


FIGURE C.12: Thorlabs cage cube compatible dichroic mirror holder. Thorlabs do not provide a solution for mounting a dichroic mirror in their cage cubes capable of fully reflecting and transmitting a 1" beam. Hence one was developed to fill this niche. The mirror holder slots easily into the cage cube and is held in place by the cage rods that pass through the cube (Thorlabs c6W). The dichroic mirror (Thorlabs DMLP950R) slots into the ridge cut into the inner face of the holder and is glued in place using two-part epoxy.

C.7 Ion pump stand

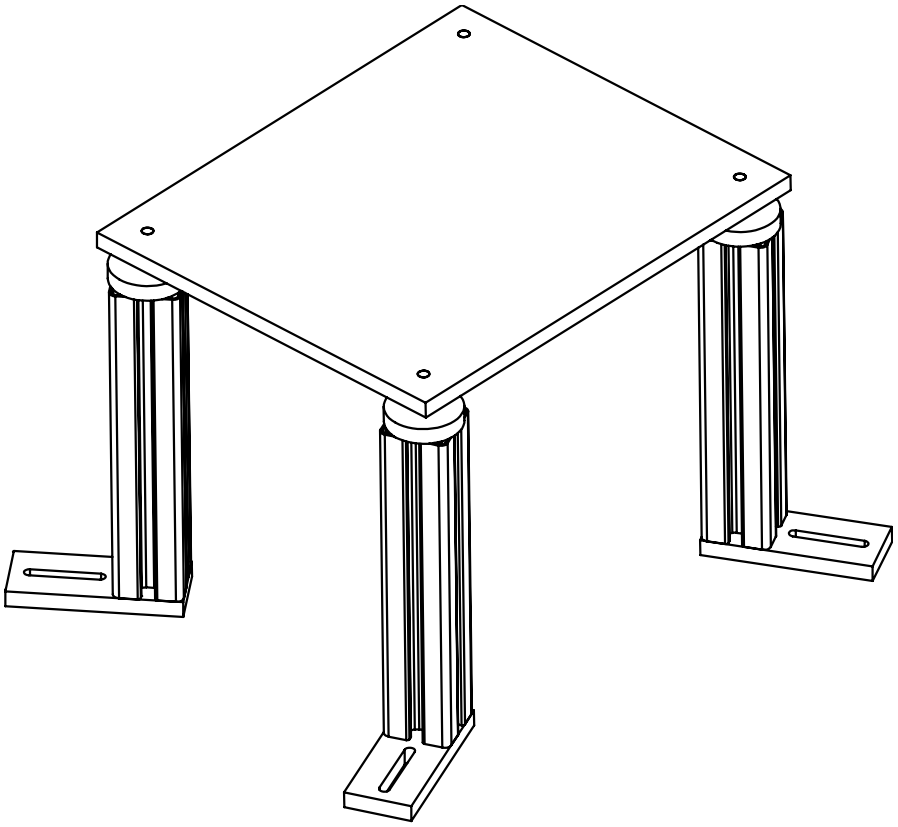


FIGURE C.13: An adjustable table for the Ion pump to sit on. The top plate is a solid piece of aluminium into which four $10\,\mathrm{mm}$ M8 grub bolts are secured. The legs are made out of item profile with an M8 thread cut into the core. The legs screw on and are fastened at the top by a nut. The feet have M6 slots for clamping.

Bibliography

[1] Enakshi Chatterjee. “SATYENDRA NATH BOSE”. In: (1914).

[2] S N Bose. “Planck ’ s Law and Light Quantum Hypothesis.” In: Received (1924), pp. 1–4.

[3] Virendra Singh. “Einstein and the Quantum”. In: i (2005), pp. 1–22.

[4] Albert Einstein. “Über einen die Erzeugung und Verwandlung des Lichtes betreffenden heuristischen Gesichtspunkt”. In: *Annalen der physik* 322.6 (1905), pp. 132–148.

[5] AB Arons and MB Peppard. “Einstein’s Proposal of the Photon Concept - A Translation of the Annalen der Physik Paper of 1905”. In: *American Journal of Physics* 33.5 (1965), pp. 367–374.

[6] Albert Einstein. “Zum gegenwärtigen stand des strahlungsproblems”. In: *Physikalische Zeitschrift* 10 (1909), pp. 185–193.

[7] Max Karl Ernst Ludwig Planck. “Zur theorie des gesetzes der energieverteilung im normalspectrum”. In: *Verhandl. Dtsc. Phys. Ges.* 2 (1900), p. 237.

[8] Albert Einstein. *Quantentheorie des einatomigen idealen Gases*. Preussische Akademie der Wissenschaften, 1924.

[9] Matthias Weidemüller and Claus Zimmermann. *Interactions in ultracold gases: from atoms to molecules*. John Wiley & Sons, 2011.

[10] M H Anderson et al. “Observation of Bose-Einstein Condensation in a Dilute Atomic Vapor”. In: *Science (New York, N.Y.)* 269.5221 (July 1995), pp. 198–201. ISSN: 0036-8075.

[11] Kendall Davis et al. “Evaporative Cooling of Sodium Atoms”. In: *Phys. Rev. Lett.* 74.26 (June 1995), pp. 5202–5205. ISSN: 0031-9007.

[12] K. Davis et al. “Bose-Einstein Condensation in a Gas of Sodium Atoms”. In: *Phys. Rev. Lett.* 75.22 (Nov. 1995), pp. 3969–3973. ISSN: 0031-9007.

[13] W Ketterle, DS Durfee, DM Stamper-Kurn, et al. "Making, probing and understanding Bose-Einstein condensates". In: *arXiv preprint cond-mat/9904034* 5 (1999).

[14] Maciej Lewenstein et al. "Ultracold atomic gases in optical lattices: mimicking condensed matter physics and beyond". In: *Advances in Physics* 56.2 (2007), pp. 243–379.

[15] Dieter Jaksch et al. "Cold bosonic atoms in optical lattices". In: *Physical Review Letters* 81.15 (1998), p. 3108.

[16] Markus Greiner et al. "Quantum phase transition from a superfluid to a Mott insulator in a gas of ultracold atoms." In: *Nature* 415 (2002), p. 39. ISSN: 00280836.

[17] Markus Greiner. "Ultracold quantum gases in three-dimensional optical lattice". PhD thesis. 2003.

[18] Waseem S Bakr et al. "A quantum gas microscope for detecting single atoms in a Hubbard-regime optical lattice." In: *Nature* 462.November (2009), pp. 74–77. ISSN: 0028-0836.

[19] Lawrence W Cheuk et al. "Quantum-gas microscope for fermionic atoms". In: *Physical review letters* 114.19 (2015), p. 193001.

[20] Johanna Elise Bohn. "Towards an ultracold three-component Fermi Gas in a two-dimensional optical lattice". PhD thesis. 2012.

[21] Markus Greiner et al. "Exploring phase coherence in a 2D lattice of Bose-Einstein condensates". In: *Physical Review Letters* 87.16 (2001), p. 160405.

[22] O Morsch et al. "Bloch oscillations and mean-field effects of Bose-Einstein condensates in 1D optical lattices". In: *Physical Review Letters* 87.14 (2001), p. 140402.

[23] Stefan Schmid et al. "Long distance transport of ultracold atoms using a 1D optical lattice". In: *New Journal of Physics* 8.8 (2006), p. 159.

[24] Andreas Wicht et al. "A preliminary measurement of the fine structure constant based on atom interferometry". In: *Physica scripta* 2002.T102 (2002), p. 82.

[25] Pierre Cladé et al. "Determination of the fine structure constant based on Bloch oscillations of ultracold atoms in a vertical optical lattice". In: *Physical review letters* 96.3 (2006), p. 033001.

[26] Achim Peters, Keng Yeow Chung, and Steven Chu. "High-precision gravity measurements using atom interferometry". In: *Metrologia* 38.1 (2001), p. 25.

[27] Remi Geiger et al. "Detecting inertial effects with airborne matter-wave interferometry". In: *Nature communications* 2 (2011), p. 474.

[28] Francesca Ferlaino, Steven Knoop, and Rudolf Grimm. "Ultracold Feshbach Molecules". In: (2008).

[29] Cheng Chin et al. "Feshbach resonances in ultracold gases". In: *Reviews of Modern Physics* 82.June (2010), pp. 1225–1286. ISSN: 00346861.

[30] Elisa Fratini and Pierbiagio Pieri. "Mass imbalance effect in resonant Bose-Fermi mixtures". In: *Physical Review A - Atomic, Molecular, and Optical Physics* 85.6 (2012), pp. 1–11. ISSN: 10502947.

[31] Cindy A Regal et al. "Creation of ultracold molecules from a Fermi gas of atoms." In: *Nature* 424.6944 (July 2003), pp. 47–50. ISSN: 1476-4687.

[32] Lincoln D Carr et al. "Cold and ultracold molecules: science, technology and applications". In: *New Journal of Physics* 11.5 (2009), p. 055049.

[33] J. Deiglmayr et al. "Permanent dipole moment of LiCs in the ground state". In: *Physical Review A - Atomic, Molecular, and Optical Physics* 82.3 (2010). ISSN: 10502947.

[34] Sonali Warriar. "Towards an Ultracold Bose-Fermi Mixture of Cesium and Lithium Atoms". PhD thesis. University of Nottingham, 2013.

[35] Matthew D. Jones. "Preparation of Cold Samples of Caesium-133 and Lithium-6 in a Single Apparatus for Bose-Fermi Mixture Experiments". PhD thesis. University of Nottingham, 2014.

[36] Asaf Paris-mandoki. "A Single Apparatus for the Production of Ultracold Fermionic Lithium and Cold Bosonic Caesium Gases". PhD thesis. 2015.

[37] Michael Gehm. "Properties of Lithium". In: (2003).

[38] Daniel A Steck. "Cesium D line data". In: (2008).

[39] C. J. Foot. *Atomic Physics*. 1st. New York: Oxford University Press, 2005.

[40] Claude Cohen-Tannoudji et al. *Atom-photon interactions: basic processes and applications*. Wiley Online Library, 1992.

[41] C Cohen-Tannoudji, B Diu, and F Laloe. *Quantum Mechanics*. Quantum Mechanics Volumes 1 and 2. Paris: Wiley, 1992. ISBN: 9780471569527.

[42] Cyril Bernard Lucas. *Atomic and Molecular Beams: Production and Collimation*. CRC Press, 2013.

[43] Peter Clausing. "Über die Strahlformung bei der Molekularströmung". In: *Zeitschrift für Physik* 66.7-8 (1930), pp. 471–476.

[44] JA Giordmaine and TC Wang. "Molecular beam formation by long parallel tubes". In: *Journal of Applied Physics* 31.3 (1960), pp. 463–471.

[45] VS Troitskii. "The Mean Free Path of Molecules in a Molecular Beam". In: *Soviet Physics, JETP* 4.2 (1962), p. 23l.

[46] Donald R Olander and Valerie Kruger. "Molecular beam sources fabricated from multichannel arrays. III. The exit density problem". In: *Journal of Applied Physics* 41.7 (1970), pp. 2769–2776.

[47] William Phillips and Harold Metcalf. "Laser Deceleration of an Atomic Beam". In: *Phys. Rev. Lett.* 48.9 (Mar. 1982), pp. 596–599. ISSN: 0031-9007.

[48] Harold J. Metcalf and Peter Van der Straten. *Laser cooling and trapping*. New York: Springer, 1999. ISBN: 0387987282.

[49] Asaf Paris-Mandoki et al. "Versatile cold atom source for multi-species experiments." In: *Rev. Sci. Instrum.* 85.11 (2014), p. 113103. ISSN: 1089-7623.

[50] Hélène Perrin. "Ultra cold atoms and Bose-Einstein condensation for quantum metrology". In: (Sept. 2009), p. 13.

[51] P Jeffery Ungar et al. "Optical molasses and multilevel atoms: theory". In: *JOSA B* 6.11 (1989), pp. 2058–2071.

[52] Steven Chu. "Optical Molasses". In: (1991).

[53] David S Weiss et al. "Optical molasses and multilevel atoms: experiment". In: *JOSA B* 6.11 (1989), pp. 2072–2083.

[54] J. Dalibard and C. Cohen-Tannoudji. "Laser cooling below the Doppler limit by polarization gradients: simple theoretical models". In: *Journal of the Optical Society of America B* 6.11 (Nov. 1989), p. 2023. ISSN: 0740-3224.

[55] Daniel Adam Steck. *Quantum and Atom Optics*.

[56] Oj Luiten, Mw Reynolds, and Jt Walraven. "Kinetic theory of the evaporative cooling of a trapped gas". In: *Phys. Rev. A.* 53.1 (Jan. 1996), pp. 381–389. ISSN: 1050-2947.

[57] E Tiesinga, BJ Verhaar, and HTC Stoof. "Threshold and resonance phenomena in ultracold ground-state collisions". In: *Physical Review A* 47.5 (1993), p. 4114.

[58] Eric Braaten et al. "Three-Body Recombination of Li 6 Atoms with Large Negative Scattering Lengths". In: *Physical review letters* 103.7 (2009), p. 073 202.

[59] M. Lysebo and L. Veseth. "Ab initio calculation of Feshbach resonances in cold atomic collisions: s- and p-wave Feshbach resonances in L6i2". In: *Phys. Rev. A.* 79.6 (June 2009). ISSN: 1050-2947.

[60] S. Jochim et al. "Magnetic field control of elastic scattering in a cold gas of fermionic lithium atoms". In: *Phys. Rev. Lett.* 89.27 (2002), p. 273202.

[61] G. Edward Marti et al. "Two-element Zeeman slower for rubidium and lithium". In: *Phys. Rev. A.* 81.4 (Apr. 2010), p. 043424. ISSN: 1050-2947.

[62] C. a. Stan and W. Ketterle. "Multiple species atom source for laser-cooling experiments". In: *Review of Scientific Instruments* 76.2005 (2005), pp. 6–11. ISSN: 00346748.

[63] Marc Repp. "Interspecies Feshbach Resonances in an Ultracold, Optically Trapped Bose-Fermi Mixture of Cesium and Lithium". In: (2013).

[64] A Derevianko, JF Babb, and A Dalgarno. "High-precision calculations of van der Waals coefficients for heteronuclear alkali-metal dimers". In: *Physical Review A* 63.5 (2001), p. 052704.

[65] S Bali et al. "Quantum-diffractive background gas collisions in atom-trap heating and loss". In: *Physical Review A* 60.1 (1999), R29.

[66] RJ Pickup. "Inorganic chemistry of the main group elements". In: *Chromatographia* 44.1 (1997), pp. 101–101.

[67] FJ Smith. "The limits of miscibility in the lithium-potassium system". In: *Journal of the Less Common Metals* 35.1 (1974), pp. 147–151.

[68] Thorsten Köhler, Krzysztof Góral, and Paul Julienne. "Production of cold molecules via magnetically tunable Feshbach resonances". In: *Rev. Mod. Phys.* 78.4 (Dec. 2006), pp. 1311–1361. ISSN: 0034-6861.

[69] Cheng Chin and Rudolf Grimm. "Thermal equilibrium and efficient evaporation of an ultracold atom-molecule mixture". In: *Physical Review A* 69.3 (Mar. 2004), p. 033612. ISSN: 1050-2947.

[70] S J M Kuppens et al. "Loading an optical dipole trap". In: *Phys. Rev. A.* 62.1 (June 2000), pp. 1–13. ISSN: 1050-2947.

[71] Nathan Welch. "Non-Equilibrium Dynamics of Bose-Einstein Condensates". PhD thesis. University of Nottingham, 2015.

[72] Andrew Kerman et al. "Beyond Optical Molasses: 3D Raman Sideband Cooling of Atomic Cesium to High Phase-Space Density". In: *Phys. Rev. Lett.* 84.3 (Jan. 2000), pp. 439–442. ISSN: 0031-9007.

[73] D. Rio Fernandes et al. "Sub-Doppler laser cooling of fermionic ^{40}K atoms in three-dimensional gray optical molasses". In: *EPL (Europhysics Letters)* 100.6 (2012), p. 63001. ISSN: 0295-5075.

[74] Andrew T. Grier et al. "Λ -enhanced sub-Doppler cooling of lithium atoms in D 1 gray molasses". In: *Physical Review A* 87.6 (2013), p. 063411. ISSN: 1050-2947.

[75] A. Burchianti et al. "Efficient all-optical production of large Li6 quantum gases using D1 gray-molasses cooling". In: *Phys. Rev. A.* 90.4 (Oct. 2014), p. 043408. ISSN: 1050-2947.

[76] Stephan Dürr. "Introduction to Physical Implementations of Quantum Information Processing". In: (Mar. 2013), pp. 1–24.

[77] Paul Benioff. "The computer as a physical system: A microscopic quantum mechanical Hamiltonian model of computers as represented by Turing machines". In: *Journal of Statistical Physics* 22.5 (1980), pp. 563–591.

[78] Yuri Manin. "Computable and Uncomputable (in Russian)". In: *Sovetskoye Radio* (1980).

[79] Peter W Shor. "Introduction to quantum algorithms". In: *Proceedings of Symposia in Applied Mathematics*. Vol. 58. 2002, pp. 143–160.

[80] Peter W Shor. "Algorithms for quantum computation: Discrete logarithms and factoring". In: *Foundations of Computer Science, 1994 Proceedings., 35th Annual Symposium on*. IEEE. 1994, pp. 124–134.

[81] Richard P Feynman. "Simulating physics with computers". In: *International journal of theoretical physics* 21.6 (1982), pp. 467–488.

[82] Emanuel Knill, Raymond Laflamme, and Gerald J Milburn. "A scheme for efficient quantum computation with linear optics". In: *nature* 409.6816 (2001), pp. 46–52.

[83] Nicolas Gisin et al. "Quantum cryptography". In: *Reviews of modern physics* 74.1 (2002), p. 145.

[84] William K Wootters and Wojciech H Zurek. "A single quantum cannot be cloned". In: *Nature* 299.5886 (1982), pp. 802–803.

[85] Martin Mücke et al. "Electromagnetically induced transparency with single atoms in a cavity". In: *Nature* 465.7299 (2010), pp. 755–758.

[86] Sean D Barrett, Peter P Rohde, and Thomas M Stace. "Scalable quantum computing with atomic ensembles". In: *New Journal of Physics* 12.9 (2010), p. 093032.

[87] Joshua Nunn. "Quantum Memory in Atomic Ensembles". PhD thesis. 2008.

[88] L Jiang, JM Taylor, and MD Lukin. "Fast and robust approach to long-distance quantum communication with atomic ensembles". In: *Physical Review A* 76.1 (2007), p. 012301.

[89] Nicolas Sangouard et al. "Robust and efficient quantum repeaters with atomic ensembles and linear optics". In: *Physical Review A* 77.6 (2008), p. 062301.

[90] Andrew Steane. "The ion trap quantum information processor". In: *Applied Physics B: Lasers and Optics* 64.6 (1997), pp. 623–643.

[91] Sougato Bose. "Quantum Communication Through Spin Chain Dynamics: An Introductory Overview". In: (2008).

[92] Shiro Saito et al. "Towards realizing a quantum memory for a superconducting qubit: Storage and retrieval of quantum states". In: *Physical review letters* 111.10 (2013), p. 107008.

[93] Michel H Devoret and Robert J Schoelkopf. "Superconducting circuits for quantum information: an outlook". In: *Science* 339.6124 (2013), pp. 116 9–1174.

[94] MV Gurudev Dutt et al. "Quantum register based on individual electronic and nuclear spin qubits in diamond". In: *Science* 316.5829 (2007), pp. 1312–1316.

[95] L Childress et al. "Coherent dynamics of coupled electron and nuclear spin qubits in diamond". In: *Science* 314.5797 (2006), pp. 281–285.

[96] Alexander I Lvovsky, Barry C Sanders, and Wolfgang Tittel. "Optical quantum memory". In: *Nature photonics* 3.12 (2009), pp. 706–714.

[97] Eric RI Abraham and Eric A Cornell. "Teflon feedthrough for coupling optical fibers into ultrahigh vacuum systems". In: *Applied Optics* 37.10 (1998), pp. 1762–1763.

[98] Rudolf Grimm, Matthias Weidemüller, and Yurii B Ovchinnikov. "Optical dipole traps for neutral atoms". In: (Feb. 1999), p. 39.

[99] J. Söding et al. "Giant Spin Relaxation of an Ultracold Cesium Gas". In: *Phys. Rev. Lett.* 80.9 (Mar. 1998), pp. 1869–1872. ISSN: 0031-9007.

[100] D Guéry-Odelin et al. "Is Bose-Einstein condensation of atomic cesium possible?" In: *Europhys. Lett.* 44.1 (Oct. 1998), pp. 25–30. ISSN: 0295-5075.

[101] Danielle A Braje et al. "Frequency mixing using electromagnetically induced transparency in cold atoms". In: *Physical review letters* 93.18 (2004), p. 183601.

[102] Michael M Kash et al. "Ultraslow group velocity and enhanced nonlinear optical effects in a coherently driven hot atomic gas". In: *Physical Review Letters* 82.26 (1999), p. 5229.

[103] L-M Duan et al. "Long-distance quantum communication with atomic ensembles and linear optics". In: *Nature* 414.6862 (2001), pp. 413–418.

[104] Lene Vestergaard Hau et al. “Light speed reduction to 17 metres per second in an ultracold atomic gas”. In: *Nature* 397.February (1999), pp. 594–598.